Theoretical and Computational Aspects of Scattering from Rough Surfaces: Two-dimensional Surfaces

J. DeSanto, G. Erdmann, W. Hereman,
B. Krause, M. Misra, and E. Swim

MCS-00-03 June 2000

Technical Report # 4 MURI Project
AFOSR Grant # F49620-96-1-0039

Report of Work in Progress

Department of Mathematical and Computer Sciences
Colorado School of Mines
Golden, CO 80401-1887, USA
Phone: (303) 273-3860
Fax: (303) 273-3875
Email: jdesanto@mines.edu

Contents

1 Introduction and Notation **2**

2 Derivation of Spectral-Coordinate (SC) Equations in 2D: Region V_1 **4**

3 Derivation of Spectral-Coordinate (SC) Equations in 2D: Region V_2 **7**

4 Conditions at the Interface **10**

5 Summary of Equations Using the Boundary Unknowns **10**

6 Evaluate $S_1^{\pm}$: Scattered Field and Incident Field Expansions **11**

7 Evaluate $S_2^{\pm}$: Transmitted Field Expansion **13**

8 Snell's Law and Summary of Equations **14**

9 Dirichlet Problem **17**

10 Neumann Problem **18**

11 Flux Conservation **19**

12 Reduction to a Periodic Surface **21**

13 Equations for a Periodic Surface **23**

14 Energy Balance **25**

15 Numerical Methods **25**

16 Introduction and Outline of the Computational Results **29**

17 Dirichlet Computations **31**

17.1 Example 1 Case A, No Grazing 32
17.2 Example 1 Case B, Near-Grazing Incidence/Reflection 39
17.3 Example 2 Case A, No Grazing 47
17.4 Example 2 Case B, Near-Grazing Incidence/Reflection 52
17.5 Example 3 Case A, No Grazing 58
17.6 Example 3 Case B, Near-Grazing Incidence/Reflection 63
17.7 Example 4 Case A, $L_1 > L_2$ 68
17.8 Example 4 Case B, $L_1 >> L_2$ 74
17.9 Saw-tooth Surface 80
17.10Suite of ϕ^i values (azimuthal angles of incidence) 87
17.11Maximum Roughness with respect to incident polar angle θ^i 89
17.12Maximum Roughness with respect to λ/L 92
17.13Complexity Analysis: Square Systems using Gaussian Elimination 94

17.14Complexity Analysis: Non-Square Systems using Pseudo-inverse 96

18 Neumann Computations **98**
18.1 Example 1 Case A, No Grazing 99
18.2 Example 1 Case B, Near-Grazing Incidence/Reflection 102
18.3 Example 2 Case A, No Grazing 105
18.4 Example 2 Case B, Near-Grazing Incidence/Reflection 108
18.5 Example 3 Case A, No Grazing 111
18.6 Example 3 Case B, Near-Grazing Incidence/Reflection 114
18.7 Maximum Roughness with respect to incident polar angle θ^i 117
18.8 Maximum Roughness with respect to λ/L 120
18.9 Complexity Analysis: Square Systems using Gaussian Elimination 122
18.10Complexity Analysis: Non-Square Systems using Pseudo-inverse 124

19 Transmission Interface Computations **126**
19.1 Example 1 Case A 127
19.2 Example 1 Case B 134
19.3 Example 2 Case A 141
19.4 Example 2 Case B 148
19.5 Example 3 Case A 155
19.6 Example 3 Case B 157
19.7 Suite of ϕ^i Values, Azimuthal Angle of Incidence 159
19.8 Suite of κ Values 162
19.9 Suite of ρ Values 165
19.10Maximum Roughness with Respect to Incident Polar Angle θ^i 168
19.11Maximum Roughness with Respect to ρ 171
19.12Maximum Roughness with Respect to ρ at Near-Grazing Incidence 172
19.13Maximum Roughness with Respect to κ 174
19.14Maximum Roughness with Respect to κ at Near-Grazing Incidence 176
19.15Complexity Analysis: Square Systems using Gaussian Elimination 178
19.16Complexity Analysis: Non-Square Systems using Pseudo-inverse 180

20 Summary and Conclusions **182**

Abstract

We consider the scattering from and transmission through a two-dimensional rough surface. From our previous work on scattering from one-dimensional surfaces we have learned that the spectral-coordinate (SC) method was the fastest method we have available. Most computational studies of scattering from two-dimensional surfaces require a large memory and a long calculation time unless some approximations are used in the theoretical development. Here by using the SC method we are able to solve exact theoretical equations with a minimum of calculation time. This is necessary in order to compute the many examples we present.

We first derive (in PART I) in detail the SC equations for scattering from two-dimensional *infinite* surfaces in both the reflected and transmitted regimes. A coupled system of equations for the boundary unknowns (surface field and its normal derivative) result as well as two equations to evaluate the scattered and transmitted fields once we have solved for the boundary unknowns. Special cases for the perfectly reflecting Dirichlet and Neumann boundary value problems are also presented as in the flux-conservation relation for the full transmission problem.

The equations are reduced to those for a two-dimensional periodic surface in PART II and we discuss the numerical methods for their solution. This requires one-dimensional strings from both the two-dimensional coordinate samples on the surface as well as from the two-dimensional spectral Bragg mode sampling both above and below the rough interface.

The SC equations for the two-dimensional periodic surfaces are solved in PART III. Computations are done for both Dirichlet and Neumann problems as well as the full transmission problem. Various periodic sinusoidal surface examples are studied as well as a saw-tooth surface. The surfaces vary in roughness as well as period and are investigated under no grazing and near-grazing conditions. Extensive computations are included in terms of the maximum roughness slope which can be computed using the method with a fixed maximum error as a function of azimuthal angle of incidence, polar angle of incidence, wavelength to period ratio, density (or dielectric constant) ratio and wavenumber ratio. Further extensive suites of computations are included as these parameters vary over a wide range of values. We also briefly include a study of the complexity analysis as we solve both square and non-square systems.

Although we have presented the derivation of the spectral coordinate equations for two-dimensional full electromagnetic problems previously [5], this is the first presentation of the two-dimensional scalar equations and their computational solution.

PART I: THEORETICAL DEVELOPMENT FOR AN INFINITE SURFACE

1 Introduction and Notation

In previous reports [6, 7] and a paper [8] we presented the theoretical and computational results of scattering from one-dimensional rough surfaces. Many different methods were studied. They were all exact theoretical developments which were discretized and solved as matrix systems. They were characterized by the space in which the rows and columns of the matrices were sampled, either coordinate space (C) or spectral space (S). The coordinate-coordinate (CC) method was the usual method of moments. The spectral-coordinate (SC) method used the Weyl representation of the free-space Green's function to generate equations in a mixed spectral and coordinate representation, and the spectral-spectral (SS) method had the equations fully in the spectral space. The results of our one-dimensional scattering confirmed that the SC method was the fastest method (usually by several orders of magnitude) in terms of fill time, i. e. the time necessary to create the matrix. This is not a minor point for the rapid solution of matrix systems. Once the linear systems were created, the solution time for each of the methods was comparable. The reason that the fill time of the SC method was so short is easily explained. The matrix is created by sampling a simple exponential function. The function can be highly oscillatory but this presents no difficulty for SC. The CC method requires an infinite sum over these functions (to form the periodic Green's function for example) and the SS method a surface integral over these same functions. Both of the latter can be very time consuming computations. The SC method was designed to avoid this complexity. The price of the SC method comes in the fact that for large slopes the method becomes ill-conditioned. As yet we have not found a consistent way to overcome this ill-conditioning so that the dramatic time advantage we get in extending the SC method to computations from two-dimensional surfaces must be tempered to stay within parametric surface variability to ensure convergence.

Our computations are thus limited by maximum roughness and we quantify these limitations. On the other hand, extensive computations reveal that the SC method is quite robust in terms of its ability to produce highly accurate results over a wide range of incident angles (including near-grazing incidence and reflection), surface period, and two orders of magnitude variability in density and wavenumber ratios for the two homogeneous media the surface separates.

Our methods have been developed to treat the scattering from two-dimensional surfaces. Kim *et al.* [9] based their approach on previous work of ours [3, 4] involving spectral methods. They differed from our work by expanding the boundary unknowns in a two-dimensional Fourier series, producing a spectral-Fourier method. For this expansion, the matrix elements were again integrals over rapidly oscillating functions and they limited their work to Dirichlet and Neumann problems and further limited their results to shallow surfaces. Our surface heights are much larger and we have focused the results on maximum roughness which we define here to be essentially maximum slope divided by π. Kinsman [10] refers to this as steepness for one-dimensional waves. Tran and Maradudin [11] use the Liouville-Neumann expansion on integral equations to treat random surface scattering. The iterative expansion

cuts down on solution time but has limitations on the size involved in the expansion parameter. Our method uses exact inversion. A method of Boag *et al.* [1] sets up fictitious patch sources displaced from the surface. The amplitudes of these sources are adjusted to match the boundary conditions at selected points on the surface. Our method computes the surface sources directly. Wagner *et al.* [12] developed the fast multipole method as an approximate analytical tool to speed up the computations. A special case of normal incidence is studied in terms of approximately computing the Mueller matrix for the scattering process [2]. All these authors point out the difficulties of computing any fully two-dimensional scattering problem, and all are faced with fill-time questions which our SC method enables us to resolve.

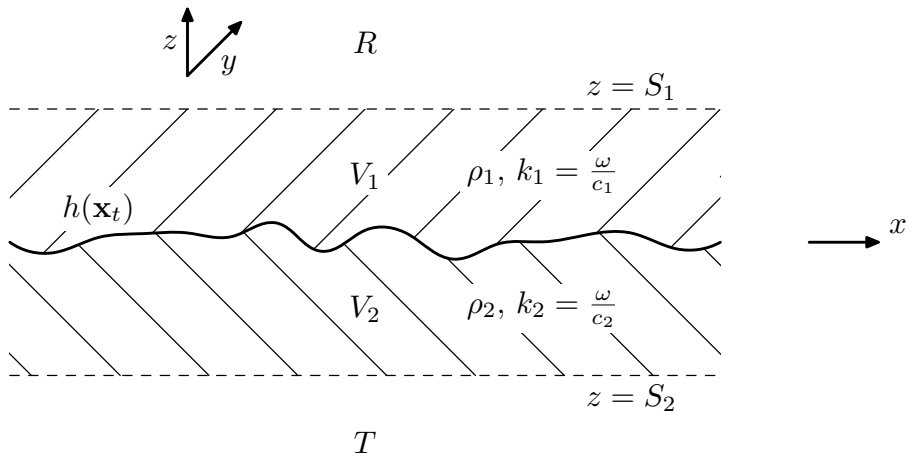

Figure 1: Illustration of the geometry and region parameters. The infinite rough surface $h(\mathbf{x}_t)$ separates two homogeneous half-spaces defined by constant densities ρ_j, wavenumbers k_j and wave speeds $c_j\,(j = 1, 2)$. ω is circular frequency and the constant planes $z = S_j$ refer to the highest $(j = 1)$ and lowest $(j = 2)$ rough surface excursion. The regions R, V_1, V_2 and T are defined in the text.

In Figure 1 we illustrate the geometry and definitions for the derivation of the spectral-coordinate method in 2 dimensions. In what follows $\mathbf{x} = (x, y, z) = (\mathbf{x}_t, z)$ denotes a vector in the 3 dimensional Cartesian space. Obviously, $\mathbf{x}_t = (x, y)$. The $z-$axis points vertically upwards, the $x-$axis points towards the right, and the $y-$axis is such that (x, y, z) form a right-handed coordinate system. The two-dimensional surface is specified by $z = h(\mathbf{x}_t)$. So, $\mathbf{x}_h = (\mathbf{x}_t, h(\mathbf{x}_t))$ is a position vector on the surface.

There are 4 regions of interest: R, V_1, V_2 and T. They are defined as follows:

- For region $R : z \geq S_1$. The value S_1 is assumed to be above the highest surface excursion.
- For region $V_1 : h(\mathbf{x}_t) < z \leq S_1$.
- For region $V_2 : S_2 \leq z < h(\mathbf{x}_t)$.
- For region $T : z \leq S_2$, where S_2 is below the lowest surface excursion.

ψ is the symbol for the acoustic velocity potential which satisfies the appropriate Helmholtz equation in different regions.

Note that the derivation is analogous to the electromagnetic case discussed previously in [5]. Further, the relation of acoustic and electromagnetic boundary value problems can be found in [7, Appendix B].

2 Derivation of Spectral-Coordinate (SC) Equations in 2D: Region V_1

In region V_1 the density is ρ_1, and the wave number of the incident sound wave is $k_1 = \omega/c_1$.

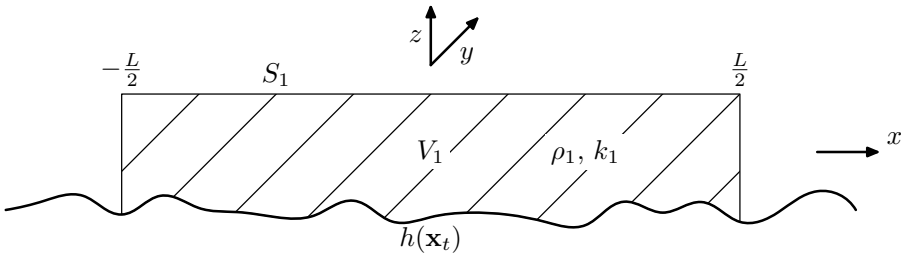

Figure 2: V_1 is the region between the rough surface and the highest surface excursion. This region is bounded by $h(\mathbf{x}_t)$ and S_1 vertically and $\pm\frac{L}{2}$ horizontally. In the derivation of the equations we let $L \to \infty$ for the results through Section 11.

Figure 2 illustrates region V_1. The shaded area is defined by $h(\mathbf{x}_t) < z \leq S_1$ and $-\frac{L}{2} \leq x, y \leq \frac{L}{2}$. V_1 is specified by the *characteristic function*

$$\theta_1(\mathbf{x}) = \begin{cases} 1, & \mathbf{x} \in V_1, \\ 0, & \mathbf{x} \notin V_1, \end{cases} \tag{2.1}$$

which is given by

$$\theta_1(\mathbf{x}) = \theta(z - h(\mathbf{x}_t))\theta(S_1 - z)\theta_+(\mathbf{x}_t), \tag{2.2}$$

where θ is the Heaviside function and

$$\theta_+(\mathbf{x}_t) = \theta(x + \frac{L}{2})\theta(\frac{L}{2} - x)\theta(y + \frac{L}{2})\theta(\frac{L}{2} - y). \tag{2.3}$$

The vector derivative of θ_1 is

$$\partial_l \theta_1(\mathbf{x}) = n_l(\mathbf{x}_t)\delta(z - h)\theta_+ - \delta_{l_3}\delta(z - S_1)\theta_+ + \theta(z - h)\delta(S_1 - z)\partial_l\theta_+, \tag{2.4}$$

with

$$\begin{aligned} \partial_l\theta_+ \;=\; & \delta_{l_1}\delta(x + \frac{L}{2})\theta(y + \frac{L}{2})\theta(\frac{L}{2} - y) - \delta_{l_1}\delta(x - \frac{L}{2})\theta(y + \frac{L}{2})\theta(\frac{L}{2} - y) \\ & + \delta_{l_2}\delta(y + \frac{L}{2})\theta(x + \frac{L}{2})\theta(\frac{L}{2} - x) - \delta_{l_2}\delta(y - \frac{L}{2})\theta(x + \frac{L}{2})\theta(\frac{L}{2} - x). \end{aligned} \tag{2.5}$$

Here

$$n_l(\mathbf{x}_t) = \delta_{l_3} - h_x\delta_{l_1} - h_y\delta_{l_2} \tag{2.6}$$

is a non-unit normal. Furthermore, the field ψ is given by $\psi^{(1)}(\mathbf{x}) \in V_1$.

Assume that $\psi^{(1)}(\mathbf{x})$ is source free in V_1 and therefore satisfies the Helmholtz equation

$$(\partial_l\partial_l + k_1^2)\psi^{(1)}(\mathbf{x}) = 0. \tag{2.7}$$

Planar wave states are defined in V_1 as

$$\phi_1^{\pm}(\mathbf{x}) = \exp[ik_1\mathbf{M}^{\pm}\cdot\mathbf{x}], \tag{2.8}$$

where $\mathbf{M}^{\pm} = (-\mathbf{M}_t, \pm M_z)$, $\mathbf{M}_t = (M_x, M_y)$, and

$$M_z = \begin{cases} +\sqrt{1-M_t^2}, & M_t^2 < 1, \\ +i\sqrt{M_t^2-1}, & M_t^2 > 1. \end{cases}$$

They satisfy the same Helmholtz equation

$$(\partial_l\partial_l + k_1^2)\phi_1^{\pm}(\mathbf{x}) = 0. \tag{2.9}$$

From (2.7) and (2.9) we obtain the following *vector identity*:

$$\partial_l[\partial_l\phi_1^{\pm}(\mathbf{x})\psi^{(1)}(\mathbf{x}) - \phi_1^{\pm}(\mathbf{x})\partial_l\psi^{(1)}(\mathbf{x})] = 0. \tag{2.10}$$

Multiplying (2.10) by $\theta_1(\mathbf{x})$ and integrating over all space in $\mathbf{x}$ we get

$$\int\int\int_{-\infty}^{\infty} \theta_1(\mathbf{x})\ \partial_l[\partial_l\phi_1^{\pm}(\mathbf{x})\psi^{(1)}(\mathbf{x}) - \phi_1^{\pm}(\mathbf{x})\partial_l\psi^{(1)}(\mathbf{x})]\, d\mathbf{x} = 0. \tag{2.11}$$

Integrating (2.11) by parts results in

$$\int\int\int_{-\infty}^{\infty} [\partial_l\phi_1^{\pm}(\mathbf{x})\psi^{(1)}(\mathbf{x}) - \phi_1^{\pm}(\mathbf{x})\partial_l\psi^{(1)}(\mathbf{x})]\ \partial_l\theta_1(\mathbf{x})\, d\mathbf{x} = 0. \tag{2.12}$$

Note that the partially integrated term drops because $\theta_1(\mathbf{x})$ defines a bounded region.

Next evaluate the integrals in (2.12). Using $\partial_l\theta_1(\mathbf{x})$ from (2.4) we have to consider three types of integrals:

1. An integral over h;
2. An integral over $z = S_1$;
3. 'Edge' or side integrals involving $\partial_l\theta_+$.

Also, we will normalize the integrals to a per unit length by dividing them all by L^2. (Equivalently, we could put a factor $1/L^2$ in the plane wave definition).

The result is

$$\mathcal{U}^{\pm}(L) = S_1^{\pm}(L) - E_1^{\pm}(L), \tag{2.13}$$

where $\mathcal{U}^{\pm}(L)$ are integrals on the upper side of h. Hence,

$$\mathcal{U}^{\pm}(L) = \frac{1}{L^2}\int\int_{-\frac{L}{2}}^{\frac{L}{2}} [n_l\partial_l\phi_1^{\pm}(\mathbf{x}_h)\psi^{(1)}(\mathbf{x}_h) - \phi_1^{\pm}(\mathbf{x}_h)n_l\partial_l\psi^{(1)}(\mathbf{x}_h)]\, d\mathbf{x}_t, \tag{2.14}$$

where $\phi_1^{\pm}(\mathbf{x}_h) = \lim_{z\to h^+}\phi_1^{\pm}(\mathbf{x})$ and $n_l\partial_l\psi^{(1)}(\mathbf{x}_h) = \lim_{z\to h^+} n_l\partial_l\psi^{(1)}(\mathbf{x})$. $S_1^{\pm}(L)$ are the integrals over $z = S_1$ and are given by

$$S_1^{\pm}(L) = \frac{1}{L^2}\int\int_{-\frac{L}{2}}^{\frac{L}{2}} [\frac{\partial}{\partial z}\phi_1^{\pm}(\mathbf{x}_1)\psi^{(1)}(\mathbf{x}_1) - \phi_1^{\pm}(\mathbf{x}_1)\frac{\partial}{\partial z}\psi^{(1)}(\mathbf{x}_1)]\, d\mathbf{x}_t, \tag{2.15}$$

where $\mathbf{x}_1 = (\mathbf{x}_t, S_1)$. Finally, $E_1^{\pm}(L)$ are the integrals on the 'edge', given by

$$E_1^{\pm}(L) = \frac{1}{L^2}\int_{h(\mathbf{x}_t)}^{S_1} dz \int\int_{-\frac{L}{2}}^{\frac{L}{2}} [\partial_l\phi_1^{\pm}(\mathbf{x})\psi^{(1)}(\mathbf{x}) - \phi_1^{\pm}(\mathbf{x})\partial_l\psi^{(1)}(\mathbf{x})]\partial_l\theta_+\, d\mathbf{x}_t. \tag{2.16}$$

Note that the limits for the integration with respect to z come from the $\partial_l\theta_+$ part of $\partial_l\theta_1$.

For the edge integrals we note the following:

1. For $E_1^{\pm}$ in (2.16), $\partial_l\theta_+$ yields at least one delta function in x and y and so one horizontal integral can be carried out. One integral of order L remains. Then,
2. For bounded functions $\phi_1^{\pm}, \psi^{(1)}, ...$ an estimate of $E_1^{\pm}(L)$ yields $E_1^{\pm}(L) \sim O(\frac{1}{L})$.
3. The other integrals behave like $\mathcal{U}^{\pm}(L) \sim O(1)$ and $S_1^{\pm}(L) \sim O(1)$ for L large.
4. In the limit of large L, $E_1^{\pm}(L) \to 0$ relative to $\mathcal{U}^{\pm}(L)$, and$S_1^{\pm}(L)$, and thus edge integrals are dropped. For any large finite value of L we assume that these integrals can be as small as we want. For periodic surfaces (which we introduce later) the edge integrals cancel exactly using Floquet boundary conditions.

If we define the remaining limits as

$$\mathcal{U}^{\pm} = \lim_{L\to\infty} L^2\mathcal{U}^{\pm}(L), \tag{2.17}$$

and

$$S_1^{\pm} = \lim_{L\to\infty} L^2 S_1^{\pm}(L), \tag{2.18}$$

then the equations reduce to

$$\mathcal{U}^{\pm} = S_1^{\pm}, \tag{2.19}$$

where

$$\mathcal{U}^{\pm} = \int\int_{-\infty}^{\infty} [n_l\partial_l\phi_1^{\pm}(\mathbf{x}_h)\psi^{(1)}(\mathbf{x}_h) - \phi_1^{\pm}(\mathbf{x}_h)n_l\partial_l\psi^{(1)}(\mathbf{x}_h)]\, d\mathbf{x}_t, \tag{2.20}$$

and

$$S_1^{\pm} = \int\int_{-\infty}^{\infty} [\frac{\partial}{\partial z}\phi_1^{\pm}(\mathbf{x}_1)\psi^{(1)}(\mathbf{x}_1) - \phi_1^{\pm}(\mathbf{x}_1)\frac{\partial}{\partial z}\psi^{(1)}(\mathbf{x}_1)]\, d\mathbf{x}_t. \tag{2.21}$$

We note that:

1. Equation (2.19) relates integrals on $z = h$ to those on $z = S_1$, a kind of analytic continuation.

2. $\mathcal{U}^{\pm}$ and $S_1^{\pm}$ are functions of the spectral parameter $\mathbf{M}^{\pm}$ through $\phi_1^{\pm}$ from (2.8). We have suppressed it. Indeed, using (2.8),

$$n_l \partial_l \phi_1^{\pm}(\mathbf{x}_h) = ik_1 n_l M_l^{\pm} \phi_1^{\pm}(\mathbf{x}_h), \tag{2.22}$$

and

$$\frac{\partial}{\partial z}\phi_1^{\pm}(\mathbf{x}_1) = ik_1(\pm M_z)\phi_1^{\pm}(\mathbf{x}_1), \tag{2.23}$$

so that (2.20) and (2.21) are (after ik_1 is factored out)

$$\mathcal{U}^{\pm} = ik_1 \int\int_{-\infty}^{\infty} \phi_1^{\pm}(\mathbf{x}_h)\, [n_l M_l^{\pm} \psi^{(1)}(\mathbf{x}_h) - \frac{1}{ik_1} n_l \partial_l \psi^{(1)}(\mathbf{x}_h)]\, d\mathbf{x}_t, \tag{2.24}$$

and

$$S_1^{\pm} = ik_1 \int\int_{-\infty}^{\infty} \phi_1^{\pm}(\mathbf{x}_1)\, [\pm M_z \psi^{(1)}(\mathbf{x}_1) - \frac{1}{ik_1}\frac{\partial}{\partial z}\psi^{(1)}(\mathbf{x}_1)]\, d\mathbf{x}_t, \tag{2.25}$$

which we use along with (2.19).

3 Derivation of Spectral-Coordinate (SC) Equations in 2D: Region V_2

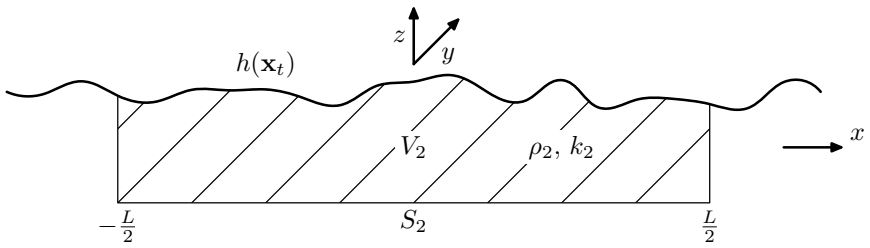

Figure 3: V_2 is the region between the rough surface and the lowest surface excursion. This region is bounded by $h(\mathbf{x}_t)$ and S_2 vertically and $\pm\frac{L}{2}$ horizontally. In the derivation of the equations $L \to \infty$ for the results through Section 11.

Figure 3 illustrates region V_2. In V_2 the density is ρ_2 and the wavenumber is k_2. The shaded area is defined by $S_2 \le z < h(\mathbf{x}_t)$ and $-\frac{L}{2} \le x, y \le \frac{L}{2}$. V_2 is specified by the *characteristic function*

$$\theta_2(\mathbf{x}) = \begin{cases} 1, & \mathbf{x} \in V_2, \\ 0, & \mathbf{x} \notin V_2. \end{cases} \tag{3.1}$$

We define

$$\theta_2(\mathbf{x}) = \theta(h(\mathbf{x}_t - z))\theta(z - S_2)\theta_+(\mathbf{x}_t), \tag{3.2}$$

where θ is the Heaviside function and θ_+ is given in (2.3). The vector derivative of θ_2 is

$$\partial_l \theta_2(\mathbf{x}) = -n_l(\mathbf{x}_t)\delta(z - h)\theta_+ + \delta_{l_3}\delta(z - S_2)\theta_+ + \theta(h - z)\delta(z - S_2)\partial_l\theta_+, \tag{3.3}$$

with $n_l(\mathbf{x}_t)$ in (2.6) and $\partial_l\theta_+$ in (2.5). Furthermore, the field ψ is replaced by $\psi^{(2)}(\mathbf{x}) \in V_2$.

Assuming that $\psi^{(2)}(\mathbf{x})$ is source free in V_2, it satisfies the Helmholtz equation

$$(\partial_l\partial_l + k_2^2)\psi^{(2)}(\mathbf{x}) = 0. \tag{3.4}$$

In V_2 plane wave states are defined as

$$\phi_2^{\pm}(\mathbf{x}) = \exp[ik_2\mathbf{P}^{\pm}\cdot\mathbf{x}], \tag{3.5}$$

where $\mathbf{P}^{\pm} = (-\mathbf{P}_t, \pm P_z)$, $\mathbf{P}_t = (P_x, P_y)$, and

$$P_z = \begin{cases} +\sqrt{1-P_t^2}, & P_t^2 < 1, \\ +i\sqrt{P_t^2-1}, & P_t^2 > 1. \end{cases}$$

These satisfy the same Helmholtz equation

$$(\partial_l\partial_l + k_2^2)\phi_2^{\pm}(\mathbf{x}) = 0. \tag{3.6}$$

From (3.4) and (3.6) we obtain the following *vector identity*:

$$\partial_l[\partial_l\phi_2^{\pm}(\mathbf{x})\psi^{(2)}(\mathbf{x}) - \phi_2^{\pm}(\mathbf{x})\partial_l\psi^{(2)}(\mathbf{x})] = 0. \tag{3.7}$$

Multiplying (3.7) by $\theta_2(\mathbf{x})$ and integrating over all space in $\mathbf{x}$ we get

$$\int\int\int_{-\infty}^{\infty} \theta_2(\mathbf{x})\ \partial_l[\partial_l\phi_2^{\pm}(\mathbf{x})\psi^{(2)}(\mathbf{x}) - \phi_2^{\pm}(\mathbf{x})\partial_l\psi^{(2)}(\mathbf{x})]\, d\mathbf{x} = 0. \tag{3.8}$$

Integrating (3.8) by parts results in

$$\int\int\int_{-\infty}^{\infty} [\partial_l\phi_2^{\pm}(\mathbf{x})\psi^{(2)}(\mathbf{x}) - \phi_2^{\pm}(\mathbf{x})\partial_l\psi^{(2)}(\mathbf{x})]\ \partial_l\theta_2(\mathbf{x})\, d\mathbf{x} = 0. \tag{3.9}$$

Again the partially integrated term drops because $\theta_2(\mathbf{x})$ defines a bounded region.

Using $\partial_l\theta_2(\mathbf{x})$ from (3.3) we have to evaluate three types of integrals:

1. An integral over h;
2. An integral over $z = S_2$;
3. 'Edge' or side integrals involving $\partial_l\theta_+$.

As for region V_1, we will normalize the integrals to a per unit length by dividing them all by L^2. The result is

$$\mathcal{L}^{\pm}(L) = S_2^{\pm}(L) + E_2^{\pm}(L), \tag{3.10}$$

where $\mathcal{L}^{\pm}(L)$ are integrals on the lower side of h. Hence,

$$\mathcal{L}^{\pm}(L) = \frac{1}{L^2}\int\int_{-\frac{L}{2}}^{\frac{L}{2}} [n_l\partial_l\phi_2^{\pm}(\mathbf{x}_h)\psi^{(2)}(\mathbf{x}_h) - \phi_2^{\pm}(\mathbf{x}_h)n_l\partial_l\psi^{(2)}(\mathbf{x}_h)]\, d\mathbf{x}_t, \tag{3.11}$$

where $\phi_2^{\pm}(\mathbf{x}_h) = \lim_{z\to h^-} \phi_2^{\pm}(\mathbf{x})$ and $n_l\partial_l\psi^{(2)}(\mathbf{x}_h) = \lim_{z\to h^-} n_l\partial_l\psi^{(2)}(\mathbf{x})$, both limits from below.

$S_2^{\pm}(L)$ are the integrals over $z = S_2$ which are

$$S_2^{\pm}(L) = \frac{1}{L^2}\int\int_{-\frac{L}{2}}^{\frac{L}{2}} [\frac{\partial}{\partial z}\phi_2^{\pm}(\mathbf{x}_2)\psi^{(2)}(\mathbf{x}_2) - \phi_2^{\pm}(\mathbf{x}_2)\frac{\partial}{\partial z}\psi^{(2)}(\mathbf{x}_2)]\, d\mathbf{x}_t, \tag{3.12}$$

where $\mathbf{x}_2 = (\mathbf{x}_t, S_2)$, and $E_2^{\pm}(L)$ are the integrals on the 'edge' given by

$$E_2^{\pm}(L) = \frac{1}{L^2}\int_{S_2}^{h(\mathbf{x}_t)} dz \int\int_{-\frac{L}{2}}^{\frac{L}{2}} [\partial_l\phi_2^{\pm}(\mathbf{x})\psi^{(2)}(\mathbf{x}) - \phi_2^{\pm}(\mathbf{x})\partial_l\psi^{(2)}(\mathbf{x})]\partial_l\theta_+\, d\mathbf{x}_t. \tag{3.13}$$

The limits of integration with respect to z come from the $\partial_l\theta_+$ part of $\partial_l\theta_2$. The edge integrals vanish using the same limit argument as in Section 2. If we define

$$\mathcal{L}^{\pm} = \lim_{L\to\infty} L^2\mathcal{L}^{\pm}(L), \tag{3.14}$$

and

$$S_2^{\pm} = \lim_{L\to\infty} L^2 S_2^{\pm}(L), \tag{3.15}$$

then the equations reduce to

$$\mathcal{L}^{\pm} = S_2^{\pm}, \tag{3.16}$$

where

$$\mathcal{L}^{\pm} = \int\int_{-\infty}^{\infty} [n_l\partial_l\phi_2^{\pm}(\mathbf{x}_h)\psi^{(2)}(\mathbf{x}_h) - \phi_2^{\pm}(\mathbf{x}_h)n_l\partial_l\psi^{(2)}(\mathbf{x}_h)]\, d\mathbf{x}_t, \tag{3.17}$$

and

$$S_2^{\pm} = \int\int_{-\infty}^{\infty} [\frac{\partial}{\partial z}\phi_2^{\pm}(\mathbf{x}_2)\psi^{(2)}(\mathbf{x}_2) - \phi_2^{\pm}(\mathbf{x}_2)\frac{\partial}{\partial z}\psi^{(2)}(\mathbf{x}_2)]\, d\mathbf{x}_t. \tag{3.18}$$

We note the following:

1. Equation (3.16) relates integrals on $z = h$ to those on $z = S_2$, a kind of lower region analytic continuation.

2. $\mathcal{L}^{\pm}$ and $S_2^{\pm}$ are functions of the spectral parameter $\mathbf{P}^{\pm}$ through $\phi_2^{\pm}$ from (3.5). We have suppressed it. Indeed, using (3.5),

$$n_l\partial_l\phi_2^{\pm}(\mathbf{x}_h) = ik_2 n_l {P_l}^{\pm}\phi_2^{\pm}(\mathbf{x}_h), \tag{3.19}$$

and

$$\frac{\partial}{\partial z}\phi_2^{\pm}(\mathbf{x}_2) = ik_2(\pm P_z)\phi_2^{\pm}(\mathbf{x}_2), \tag{3.20}$$

so that (3.17) and (3.18) are (after ik_2 is factored out)

$$\mathcal{L}^{\pm} = ik_2\int\int_{-\infty}^{\infty} \phi_2^{\pm}(\mathbf{x}_h)\, [n_l P_l^{\pm}\psi^{(2)}(\mathbf{x}_h) - \frac{1}{ik_2}n_l\partial_l\psi^{(2)}(\mathbf{x}_h)]\, d\mathbf{x}_t, \tag{3.21}$$

and

$$S_2^{\pm} = ik_2\int\int_{-\infty}^{\infty} \phi_2^{\pm}(\mathbf{x}_2)\, [\pm P_z\psi^{(2)}(\mathbf{x}_2) - \frac{1}{ik_2}\frac{\partial}{\partial z}\psi^{(2)}(\mathbf{x}_2)]\, d\mathbf{x}_t, \tag{3.22}$$

which we use in (3.16).

4 Conditions at the Interface

If the ψ fields have the dimensions of a velocity potential then the following continuity conditions are valid at the interface. First, continuity of pressure which becomes

$$\rho_1 \psi^{(1)}(\mathbf{x}_h) = \rho_2 \psi^{(2)}(\mathbf{x}_h), \tag{4.1}$$

and, second, continuity of the normal velocity component which is

$$n_l \partial_l \psi^{(1)}(\mathbf{x}_h) = n_l \partial_l \psi^{(2)}(\mathbf{x}_h). \tag{4.2}$$

If we define $\psi(\mathbf{x}_h) = \psi^{(1)}(\mathbf{x}_h)$ then

$$\psi^{(2)}(\mathbf{x}_h) = \frac{1}{\rho}\psi(\mathbf{x}_h), \quad \rho = \frac{\rho_2}{\rho_1}. \tag{4.3}$$

If we scale out the factor ik_1 in the normal derivative and define N as

$$n_l \partial_l \psi^{(1)}(\mathbf{x}_h) = ik_1 N(\mathbf{x}_h), \tag{4.4}$$

then by (4.2) we also have

$$n_l \partial_l \psi^{(2)}(\mathbf{x}_h) = ik_1 N(\mathbf{x}_h). \tag{4.5}$$

This defines the two *boundary unknowns* $\psi(\mathbf{x}_h)$ and $N(\mathbf{x}_h)$. The relation of these scalar boundary value problems to those in electromagnetism is discussed in [7, Appendix B].

5 Summary of Equations Using the Boundary Unknowns

Using all the definitions in Section 4, we get that equations (2.19), (2.24), and (2.25) are

$$\mathcal{U}^{\pm} = S_1^{\pm}, \tag{5.1}$$

with

$$\mathcal{U}^{\pm} = ik_1 \int\int_{-\infty}^{\infty} \phi_1^{\pm}(\mathbf{x}_h)\, [n_l M_l^{\pm} \psi(\mathbf{x}_h) - N(\mathbf{x}_h)]\, d\mathbf{x}_t, \tag{5.2}$$

and

$$S_1^{\pm} = ik_1 \int\int_{-\infty}^{\infty} \phi_1^{\pm}(\mathbf{x}_1)\, [\pm M_z \psi^{(1)}(\mathbf{x}_1) - \frac{1}{ik_1}\frac{\partial}{\partial z}\psi^{(1)}(\mathbf{x}_1)]\, d\mathbf{x}_t. \tag{5.3}$$

From Section 3, equations (3.16), (3.21), and (3.22) become

$$\mathcal{L}^{\pm} = S_2^{\pm}, \tag{5.4}$$

with ($\kappa = \frac{k_2}{k_1}$)

$$\mathcal{L}^{\pm} = ik_2 \int\int_{-\infty}^{\infty} \phi_2^{\pm}(\mathbf{x}_h)\, [\frac{1}{\rho} n_l P_l^{\pm} \psi(\mathbf{x}_h) - \frac{1}{\kappa} N(\mathbf{x}_h)]\, d\mathbf{x}_t, \tag{5.5}$$

and

$$S_2^{\pm} = ik_2 \int\int_{-\infty}^{\infty} \phi_2^{\pm}(\mathbf{x}_2)\, [\pm P_z \psi^{(2)}(\mathbf{x}_2) - \frac{1}{ik_2}\frac{\partial}{\partial z}\psi^{(2)}(\mathbf{x}_2)]\, d\mathbf{x}_t. \tag{5.6}$$

Of the four above equations, two are used to *solve* for ψ and N on the boundary $\mathbf{x}_h$; the two other equations are used to *evaluate* the reflection and transmission amplitudes after ψ and N are known on h. First we evaluate equations (5.3) and (5.6). Although the wavenumber scaling on the $S_1^{\pm}$ and $S_2^{\pm}$ appears awkward we have set it up to benefit from cancellations later.

6 Evaluate $S_1^{\pm}$: Scattered Field and Incident Field Expansions

We start with the evaluation of $S_1^{\pm}$ where $\psi^{(1)}$ is the sum of the incident and scattered fields. In region R : Above the highest surface excursion in region R we can write the total field $\psi^{(1)}(\mathbf{x})$ as the sum of incident and scattered fields, the latter of which is written as a superposition of purely upgoing waves using a spectral expansion

$$\psi^{(1)} \rightarrow \psi_R(\mathbf{x}) = \psi^{(0)}(\mathbf{x}) + \psi^{\mathrm{SC}}(\mathbf{x}), \tag{6.1}$$

where

$$\psi^{\mathrm{SC}}(\mathbf{x}) = \int\int R(\boldsymbol{\alpha}_t) e^{ik_1 \boldsymbol{\alpha}\cdot\mathbf{x}}\, d\boldsymbol{\alpha}_t, \tag{6.2}$$

with

$$\boldsymbol{\alpha} = (\boldsymbol{\alpha}_t, \alpha_z), \tag{6.3}$$

$$\alpha_z = \begin{cases} +\sqrt{1-\alpha_t^2}, & \alpha_t^2 < 1, \\ +i\sqrt{\alpha_t^2 - 1}, & \alpha_t^2 > 1. \end{cases} \tag{6.4}$$

Note that we only consider upgoing waves. $\psi^{(0)}(\mathbf{x})$ is the *incident field* which we will define later in this section.

Computing the $z-$derivative of (6.1), i. e.

$$\frac{\partial}{\partial z}\psi_R(\mathbf{x}) = \frac{\partial}{\partial z}\psi^{(0)}(\mathbf{x}) + \int\int R(\boldsymbol{\alpha}_t) ik_1\alpha_z e^{ik_1\boldsymbol{\alpha}\cdot\mathbf{x}}\, d\boldsymbol{\alpha}_t, \tag{6.5}$$

and using (5.3), we can write $S_1^{\pm}$ as the sum of two terms

$$S_1^{\pm} = S_1^{\pm(0)} + S_1^{\pm(\mathrm{SC})}, \tag{6.6}$$

with

$$S_1^{\pm(0)} = ik_1 \int\int_{-\infty}^{\infty} \phi_1^{\pm}(\mathbf{x}_1)\, [\pm M_z \psi^{(0)}(\mathbf{x}_1) - \frac{1}{ik_1}\frac{\partial}{\partial z}\psi^{(0)}(\mathbf{x}_1)]\, d\mathbf{x}_t, \tag{6.7}$$

and

$$S_1^{\pm(\mathrm{SC})} = ik_1 \int\int_{-\infty}^{\infty} \phi_1^{\pm}(\mathbf{x}_1)\, [\pm M_z \psi^{\mathrm{SC}}(\mathbf{x}_1) - \frac{1}{ik_1}\frac{\partial}{\partial z}\psi^{\mathrm{SC}}(\mathbf{x}_1)]\, d\mathbf{x}_t. \tag{6.8}$$

Next, using

$$\pm M_z \psi^{\mathrm{SC}}(\mathbf{x}_1) - \frac{1}{ik_1}\frac{\partial}{\partial z}\psi^{\mathrm{SC}}(\mathbf{x}_1) = \int\int R(\boldsymbol{\alpha}_t) e^{ik_1\boldsymbol{\alpha}\cdot\mathbf{x}_1} [\pm M_z - \alpha_z]\, d\boldsymbol{\alpha}_t, \tag{6.9}$$

equation (6.8) can be rewritten as

$$S_1^{\pm(\mathrm{SC})} = ik_1 \int\int R(\boldsymbol{\alpha}_t)\, (\pm M_z - \alpha_z)\, [\int\int_{-\infty}^{\infty} \phi_1^{\pm}(\mathbf{x}_1) e^{ik_1\boldsymbol{\alpha}\cdot\mathbf{x}_1}\, d\mathbf{x}_t]\, d\boldsymbol{\alpha}_t. \tag{6.10}$$

With (2.8), the second double integral in (6.10) can be recast as

$$\begin{aligned}\int\int_{-\infty}^{\infty}\phi_1^{\pm}(\mathbf{x}_1)e^{ik_1\boldsymbol{\alpha}\cdot\mathbf{x}_1}\,d\mathbf{x}_t &= \int\int_{-\infty}^{\infty}e^{ik_1[\mathbf{M}^{\pm}+\boldsymbol{\alpha}]\cdot\mathbf{x}_1}\,d\mathbf{x}_t\\ &= e^{ik_1(\pm M_z+\alpha_z)S_1}\int\int_{-\infty}^{\infty}e^{ik_1[\boldsymbol{\alpha}_t-\mathbf{M}_t]\cdot\mathbf{x}_t}\,d\mathbf{x}_t\\ &= \frac{(2\pi)^2}{k_1^2}\,e^{ik_1(\pm M_z+\alpha_z)S_1}\,\delta(\boldsymbol{\alpha}_t-\mathbf{M}_t). \qquad (6.11)\end{aligned}$$

Inserting this result in (6.10), we obtain

$$S_1^{\pm(\mathrm{SC})}=\frac{ik_1(2\pi)^2}{k_1^2}\int\int R(\boldsymbol{\alpha}_t)\,(\pm M_z-\alpha_z)\,e^{ik_1(\pm M_z+\alpha_z)S_1}\,\delta(\boldsymbol{\alpha}_t-\mathbf{M}_t)\,d\boldsymbol{\alpha}_t. \qquad (6.12)$$

To achieve further simplification we note that when $\boldsymbol{\alpha}_t=\mathbf{M}_t$:

$$\begin{aligned}\pm M_z-\alpha_z &= \pm\sqrt{1-M_t^2}-\sqrt{1-\alpha_t^2}|_{\boldsymbol{\alpha}_t=\mathbf{M}_t}\\ &= \begin{cases}0\\ -2M_z,\end{cases} \qquad (6.13)\end{aligned}$$

and

$$\pm M_z+\alpha_z|_{\boldsymbol{\alpha}_t=\mathbf{M}_t}=\begin{cases}2M_z\\ 0.\end{cases} \qquad (6.14)$$

Thus,

$$S_1^{\pm(\mathrm{SC})}=ik_1[\frac{-2(2\pi)^2M_z}{k_1^2}]\begin{cases}0\\ R(\mathbf{M}_t).\end{cases} \qquad (6.15)$$

Note that the upgoing wave expansion for the scattered field and $\phi_1^{\pm}$ projects out 0 for the ϕ_1^{+}, which itself is *upgoing* and projects out the reflection coefficients R for ϕ_1^{-} which is *downgoing*.

We continue with the evaluation of the incident field $S_1^{\pm(0)}$. An arbitrary incident field can be spectrally expanded as

$$\psi^{(0)}(\mathbf{x})=\int\int I(\boldsymbol{\beta}_t)e^{ik_1\boldsymbol{\beta}\cdot\mathbf{x}}\,d\boldsymbol{\beta}_t, \qquad (6.16)$$

where

$$\boldsymbol{\beta}=(\boldsymbol{\beta}_t,-\beta_z),\quad \beta_z=+\sqrt{1-\beta_t^2}. \qquad (6.17)$$

The sign in $-\beta_z$ indicates a *downgoing* wave superposition (i.e. in the negative z direction).

If in (6.7) on the surface S_1, we use

$$\pm M_z\psi^{(0)}(\mathbf{x}_1)-\frac{1}{ik_1}\frac{\partial}{\partial z}\psi^{(0)}(\mathbf{x}_1)=\int\int I(\boldsymbol{\beta}_t)e^{ik_1\boldsymbol{\beta}\cdot\mathbf{x}_1}[\pm M_z+\beta_z]\,d\boldsymbol{\beta}_t, \qquad (6.18)$$

then equation (6.7) can be rewritten as

$$S_1^{\pm(0)}=ik_1\int\int I(\boldsymbol{\beta}_t)\,(\pm M_z+\beta_z)\,[\int\int_{-\infty}^{\infty}\phi_1^{\pm}(\mathbf{x}_1)e^{ik_1\boldsymbol{\beta}\cdot\mathbf{x}_1}\,d\mathbf{x}_t]\,d\boldsymbol{\beta}_t. \qquad (6.19)$$

The second double integral in (6.19) can be recast as

$$\begin{aligned}\int\int_{-\infty}^{\infty}\phi_1^{\pm}(\mathbf{x}_1)e^{ik_1\boldsymbol{\beta}\cdot\mathbf{x}_1}\,d\mathbf{x}_t &= e^{ik_1(\pm M_z-\beta_z)S_1}\int\int_{-\infty}^{\infty}e^{ik_1[\boldsymbol{\beta}_t-\mathbf{M}_t]\cdot\mathbf{x}_t}\,d\mathbf{x}_t\\ &= \frac{(2\pi)^2}{k_1^2}\,e^{ik_1(\pm M_z-\beta_z)S_1}\,\delta(\boldsymbol{\beta}_t-\mathbf{M}_t), \qquad (6.20)\end{aligned}$$

which leads to

$$S_1^{\pm(0)} = \frac{ik_1(2\pi)^2}{k_1^2} \int\int I(\boldsymbol{\beta}_t)\,(\pm M_z + \beta_z)\, e^{ik_1(\pm M_z - \beta_z)S_1}\, \delta(\boldsymbol{\beta}_t - \mathbf{M}_t)\, d\boldsymbol{\beta}_t. \tag{6.21}$$

When $\boldsymbol{\beta}_t = \mathbf{M}_t$:

$$\pm M_z + \beta_z = \begin{cases} 2M_z \\ 0, \end{cases} \tag{6.22}$$

and

$$\pm M_z - \beta_z = \begin{cases} 0 \\ -2M_z. \end{cases} \tag{6.23}$$

Thus,

$$S_1^{\pm(0)} = ik_1[\frac{2(2\pi)^2 M_z}{k_1^2}] \begin{cases} I(\mathbf{M}_t) \\ 0. \end{cases} \tag{6.24}$$

Note that this time the projection goes the other way. The incident field which is *downgoing* is projected out by upgoing ϕ_1^+; and 0 is projected out by downgoing ϕ_1^-.

Now we combine the results. First, substitute (6.15) and (6.24) into the right hand side of $\mathcal{U}^\pm = S_1^\pm = S_1^{\pm(0)} + S_1^{\pm(\mathrm{SC})}$, which yields

$$\mathcal{U}^\pm = ik_1[\frac{2(2\pi)^2 M_z}{k_1^2}] \begin{cases} I(\mathbf{M}_t) \\ -R(\mathbf{M}_t). \end{cases} \tag{6.25}$$

Second, use the expression for $\mathcal{U}^\pm$ in (5.2). The final result are the two equations:

$$\int\int_{-\infty}^{\infty} \phi_1^\pm(\mathbf{x}_h)\, [n_l M_l^\pm \psi(\mathbf{x}_h) - N(\mathbf{x}_h)]\, d\mathbf{x}_t = \frac{2(2\pi)^2 M_z}{k_1^2} \begin{cases} I(\mathbf{M}_t) \\ -R(\mathbf{M}_t). \end{cases} \tag{6.26}$$

The top equation will be used in the solution of the boundary unknowns and the bottom equation in the evaluation of the reflection coefficient R and thus the reflected field by (6.2).

7 Evaluate $S_2^\pm$: Transmitted Field Expansion

To evaluate the transmitted field $S_2^\pm$, expand $\psi^{(2)}(\mathbf{x}) \to \psi_{\mathrm{T}}(\mathbf{x})$ in the region $z \le S_2$ as a spectral expansion of *downgoing* waves (like the incident field expansion).

Using

$$\psi^{(2)}(\mathbf{x}) \to \psi_T(\mathbf{x}) = \int\int \tilde{T}(\boldsymbol{\gamma}_t) e^{ik_2 \boldsymbol{\gamma}\cdot\mathbf{x}}\, d\boldsymbol{\gamma}_t, \quad z \le S_2, \tag{7.1}$$

where

$$\boldsymbol{\gamma} = (\boldsymbol{\gamma}_t, -\gamma_z), \tag{7.2}$$

$$\gamma_z = \begin{cases} +\sqrt{1-\gamma_t^2}, & \gamma_t^2 < 1, \\ +i\sqrt{\gamma_t^2 - 1}, & \gamma_t^2 > 1, \end{cases} \tag{7.3}$$

we compute

$$\pm P_z \psi^{(2)}(\mathbf{x}_2) - \frac{1}{ik_2}\frac{\partial}{\partial z}\psi^{(2)}(\mathbf{x}_2) = \int\int \tilde{T}(\boldsymbol{\gamma}_t) e^{ik_2 \boldsymbol{\gamma}\cdot\mathbf{x}_2}\, [\pm P_z + \gamma_z]\, d\boldsymbol{\gamma}_t, \tag{7.4}$$

and substitute it into (5.6). We obtain

$$S_2^{\pm} = ik_2 \int\int \tilde{T}(\boldsymbol{\gamma}_t)\,(\pm P_z + \gamma_z)\,[\int\int_{-\infty}^{\infty} \phi_2^{\pm}(\mathbf{x}_2) e^{ik_2 \boldsymbol{\gamma}\cdot\mathbf{x}_2}\,d\mathbf{x}_t]\,d\boldsymbol{\gamma}_t. \tag{7.5}$$

Now, using (3.5), we compute

$$\begin{aligned} \int\int_{-\infty}^{\infty} \phi_2^{\pm}(\mathbf{x}_2) e^{ik_2 \boldsymbol{\gamma}\cdot\mathbf{x}_2}\,d\mathbf{x}_t &= \int\int_{-\infty}^{\infty} e^{ik_2[\mathbf{P}^{\pm}+\boldsymbol{\gamma}]\cdot\mathbf{x}_2}\,d\mathbf{x}_t \\ &= \frac{(2\pi)^2}{k_2^2}\, e^{ik_2(\pm P_z - \gamma_z)S_2}\,\delta(\boldsymbol{\gamma}_t - \mathbf{P}_t). \end{aligned} \tag{7.6}$$

Inserting this result in (7.5), we obtain

$$S_2^{\pm} = \frac{ik_2(2\pi)^2}{k_2^2} \int\int \tilde{T}(\boldsymbol{\gamma}_t)\,(\pm P_z + \gamma_z)\, e^{ik_2(\pm P_z - \gamma_z)S_2}\,\delta(\boldsymbol{\gamma}_t - \mathbf{P}_t)\,d\boldsymbol{\gamma}_t. \tag{7.7}$$

When $\boldsymbol{\gamma}_t = \mathbf{P}_t$:

$$\pm P_z + \gamma_z = \begin{cases} 2P_z \\ 0, \end{cases} \tag{7.8}$$

and

$$\pm P_z - \gamma_z = \begin{cases} 0 \\ -2P_z. \end{cases} \tag{7.9}$$

Thus,

$$S_2^{\pm} = ik_2[\frac{2(2\pi)^2 P_z}{k_2^2}] \begin{cases} \tilde{T}(\mathbf{P}_t) \\ 0. \end{cases} \tag{7.10}$$

Using the above results in (3.16) we obtain

$$\int\int_{-\infty}^{\infty} \phi_2^{\pm}(\mathbf{x}_h)\,[\frac{1}{\rho} n_l P_l^{\pm}\psi(\mathbf{x}_h) - \frac{1}{\kappa} N(\mathbf{x}_h)]\,d\mathbf{x}_t = \frac{2(2\pi)^2 P_z}{k_2^2} \begin{cases} \tilde{T}(\mathbf{P}_t) \\ 0. \end{cases} \tag{7.11}$$

Note the analogy with (6.26). The zero on the right hand side of (7.11) illustrates that there is no incident field from the region below the surface.

8 Snell's Law and Summary of Equations

The equations to be solved for the boundary unknowns ψ and N are the "+" sign equation in (6.26):

$$\int\int_{-\infty}^{\infty} \phi_1^{+}(\mathbf{x}_h)\,[n_l M_l^{+}\psi(\mathbf{x}_h) - N(\mathbf{x}_h)]\,d\mathbf{x}_t = \frac{2M_z(2\pi)^2}{k_1^2}\, I(\mathbf{M}_t), \tag{8.1}$$

and the "–" sign equation in (7.11):

$$\int\int_{-\infty}^{\infty} \phi_2^{-}(\mathbf{x}_h)\,[\frac{1}{\rho} n_l P_l^{-}\psi(\mathbf{x}_h) - \frac{1}{\kappa} N(\mathbf{x}_h)]\,d\mathbf{x}_t = 0. \tag{8.2}$$

Given the boundary unknowns, the reflection and transmission amplitudes follow from the "–" sign equation in (6.26)

$$\int\int_{-\infty}^{\infty} \phi_1^{-}(\mathbf{x}_h)\,[n_l M_l^{-}\psi(\mathbf{x}_h) - N(\mathbf{x}_h)]\,d\mathbf{x}_t = -\frac{2M_z(2\pi)^2}{k_1^2}\, R(\mathbf{M}_t), \tag{8.3}$$

and the "+" sign equation in (7.11):

$$\int\int_{-\infty}^{\infty} \phi_2^+(\mathbf{x}_h)\,[\frac{1}{\rho} n_l P_l^+ \psi(\mathbf{x}_h) - \frac{1}{\kappa} N(\mathbf{x}_h)]\,d\mathbf{x}_t = \frac{2P_z(2\pi)^2}{k_2^2}\,\tilde{T}(\mathbf{P}_t), \tag{8.4}$$

where

$$n_l M_l^{\pm} = \pm M_z + h_x M_x + h_y M_y, \tag{8.5}$$

and, similarly,

$$n_l P_l^{\pm} = \pm P_z + h_x P_x + h_y P_y. \tag{8.6}$$

In (2.8) and (3.5) we defined the plane wave states:

For $\phi_1^{\pm}$:

$$\phi_1^{\pm}(\mathbf{x}_h) = e^{ik_1 \mathbf{M}^{\pm}\cdot\mathbf{x}_h}, \tag{8.7}$$

where

$$\mathbf{M}^{\pm}\cdot\mathbf{x}_h = -\mathbf{M}_t\cdot\mathbf{x}_t \pm M_z h(\mathbf{x}_t), \tag{8.8}$$

and

$$M_z = \begin{cases} +\sqrt{1-M_t^2}, & M_t^2 < 1, \\ +i\sqrt{M_t^2-1}, & M_t^2 > 1. \end{cases} \tag{8.9}$$

For $\phi_2^{\pm}$:

$$\phi_2^{\pm}(\mathbf{x}_h) = e^{ik_2 \mathbf{P}^{\pm}\cdot\mathbf{x}_h}, \tag{8.10}$$

where

$$\mathbf{P}^{\pm}\cdot\mathbf{x}_h = -\mathbf{P}_t\cdot\mathbf{x}_t \pm P_z h(\mathbf{x}_t), \tag{8.11}$$

and

$$P_z = \begin{cases} +\sqrt{1-P_t^2}, & P_t^2 < 1, \\ +i\sqrt{P_t^2-1}, & P_t^2 > 1. \end{cases} \tag{8.12}$$

The incident field is given in (6.16):

$$\psi^{(0)}(\mathbf{x}) = \int\int I(\boldsymbol{\beta}_t) e^{ik_1 \boldsymbol{\beta}\cdot\mathbf{x}}\,d\boldsymbol{\beta}_t, \tag{8.13}$$

where

$$\boldsymbol{\beta} = (\boldsymbol{\beta}_t, -\beta_z), \quad \beta_z = +\sqrt{1-\beta_t^2}. \tag{8.14}$$

The scattered field is given in (6.1):

$$\psi^{\mathrm{SC}}(\mathbf{x}) = \int\int R(\boldsymbol{\alpha}_t) e^{ik_1 \boldsymbol{\alpha}\cdot\mathbf{x}}\,d\boldsymbol{\alpha}_t, \tag{8.15}$$

where

$$\boldsymbol{\alpha} = (\boldsymbol{\alpha}_t, \alpha_z), \tag{8.16}$$

$$\alpha_z = \begin{cases} +\sqrt{1-\alpha_t^2}, & \alpha_t^2 < 1, \\ +i\sqrt{\alpha_t^2-1}, & \alpha_t^2 > 1. \end{cases} \tag{8.17}$$

The transmitted field is given in (7.1) and written here as

$$\psi_T(\mathbf{x}) = \int\int \tilde{T}(\mathbf{P}_t) e^{ik_2 \mathbf{P}\cdot\mathbf{x}}\, d\mathbf{P}_t, \qquad z \le S_2, \tag{8.18}$$

where

$$\mathbf{P} = (\mathbf{P}_t, -P_z), \tag{8.19}$$

$$P_z = \begin{cases} +\sqrt{1-P_t^2}, & P_t^2 < 1, \\ +i\sqrt{P_t^2-1}, & P_t^2 > 1. \end{cases} \tag{8.20}$$

Snell's law (conservation of ray parameter) is given by

$$\begin{aligned} k_1 \mathbf{M}_t &= k_2 \mathbf{P}_t, \\ P_x &= \frac{1}{\kappa} M_x, \\ P_y &= \frac{1}{\kappa} M_y, \\ P_z &= \sqrt{1 - \frac{1}{\kappa^2} M_t^2} = \frac{1}{\kappa}\sqrt{\kappa^2 - M_t^2}. \end{aligned} \tag{8.21}$$

This allows one to rewrite ϕ_2^- as a function of k_1 and the ratio κ

$$\begin{aligned} \phi_2^-(\mathbf{x}_h) &= e^{ik_2 \mathbf{P}^-\cdot\mathbf{x}_h} \\ &= e^{-ik_2 \mathbf{P}_t\cdot\mathbf{x}_t} e^{-ik_2 P_z h(\mathbf{x}_t)} \\ &= e^{-ik_1 \mathbf{M}_t\cdot\mathbf{x}_t} e^{-ik_1\sqrt{\kappa^2 - M_t^2} h(\mathbf{x}_t)}. \end{aligned} \tag{8.22}$$

The first exponential terms in the latter product correspond to conservation of horizontal wave number or ray parameter.

Using (8.6) and (8.21), equation (8.2) can be rewritten as

$$\int\int_{-\infty}^{\infty} \phi_2^-(\mathbf{x}_h)\, [\frac{1}{\rho}(-\sqrt{\kappa^2 - M_t^2} + h_x M_x + h_y M_y)\psi(\mathbf{x}_h) - N(\mathbf{x}_h)]\, d\mathbf{x}_t = 0. \tag{8.23}$$

Note that with respect to the solution of (8.1) and (8.2), it should be clear that if the sampling of $\mathbf{M}_t$ is to be maintained then (8.23) should be used. It is not necessary since P_x, P_y generate a sampled set of equations. Further, if we define the transmitted field as

$$\psi_T(\mathbf{x}) = \int\int T(\mathbf{M}_t) e^{ik_1(\mathbf{M}_t\cdot\mathbf{x}_t - \sqrt{\kappa^2 - M_t^2} z)}\, d\mathbf{M}_t, \tag{8.24}$$

using the wave number k_1, then from (8.18), (8.21) and the result

$$\tilde{T}(\mathbf{P}_t) = \kappa^2 T(\mathbf{M}_t), \tag{8.25}$$

equation (8.4) can be written as

$$\int\int_{-\infty}^{\infty} \phi_2^+(\mathbf{x}_h)\, [\frac{1}{\rho}(\sqrt{\kappa^2 - M_t^2} + h_x M_x + h_y M_y)\psi(\mathbf{x}_h) - N(\mathbf{x}_h)]\, d\mathbf{x}_t = \frac{2(2\pi)^2}{k_1^2} \begin{cases} T(\mathbf{M}_t) \\ 0, \end{cases} \tag{8.26}$$

which is appropriate for the $\mathbf{M}_t$ sampling.

The result is that equations (8.1) and (8.2) (or (8.23)) are used to solve for the boundary unknowns ψ and N, equation (8.3) is used to evaluate the reflection amplitudes (and thus the scattered field from (8.15)), and (8.4) (with (8.18)) or (8.26) (with (8.24)) to evaluate the transmitted field.

For simplicity we introduce two square root notations used henceforth. They correspond to region V_1.

$$m_1(\mathbf{M}_t) = \sqrt{1 - M_t^2}, \tag{8.27}$$

and to region V_2.

$$m_2(\mathbf{M}_t) = \sqrt{\kappa^2 - M_t^2}. \tag{8.28}$$

The term $n_l M_l^{\pm}$ occurs frequently in the subsequent analysis and using (8.27) with (8.5) it is given by

$$n_l M_l^{\pm} = \pm m_1(\mathbf{M}_t) + h_x M_x + h_y M_y. \tag{8.29}$$

Further, we confine many of our results to single plane wave incidence. The spectral amplitude in (8.13) can be written as

$$I(\mathbf{M}_t) = \delta(\mathbf{M}_t - \boldsymbol{\alpha}_t^{(0)}), \tag{8.30}$$

where

$$\alpha_x^{(0)} = \cos\phi^{\mathrm{i}} \sin\theta^{\mathrm{i}}, \quad \alpha_y^{(0)} = \sin\phi^{\mathrm{i}} \sin\theta^{\mathrm{i}}, \tag{8.31}$$

and

$$m_1(\boldsymbol{\alpha}_t^{(0)}) = \cos\theta^{\mathrm{i}}, \tag{8.32}$$

in terms of incident polar (θ^{i}) and azimutal (ϕ^{i}) angles.

9 Dirichlet Problem

From Section 8, there are no equations from V_2 since we have perfect reflection and

$$\psi(\mathbf{x}_h) = 0. \tag{9.1}$$

The equation to solve is (8.1), a first-kind integral equation for N, which becomes using (8.27)

$$\int\int_{-\infty}^{\infty} \phi_1^+(\mathbf{x}_h)\; N(\mathbf{x}_h)\, d\mathbf{x}_t = -\frac{2m_1(\mathbf{M}_t)(2\pi)^2}{k_1^2}\, I(\mathbf{M}_t), \tag{9.2}$$

and we get the reflection coefficient for the Dirichlet problem $R^{(\mathrm{D})}$ from (8.3)

$$\int\int_{-\infty}^{\infty} \phi_1^-(\mathbf{x}_h)\; N(\mathbf{x}_h)\, d\mathbf{x}_t = \frac{2m_1(\mathbf{M}_t)(2\pi)^2}{k_1^2}\, R^{(\mathrm{D})}(\mathbf{M}_t). \tag{9.3}$$

We have suppressed the spectral dependence of the kernels of these equations. We can make this explicit by defining the kernels as

$$\begin{aligned} k_{\mathrm{D}}^{\pm}(\mathbf{M}_t, \mathbf{x}_t) &= \phi^{\pm}(\mathbf{x}_h) \\ &= e^{-ik_1 \mathbf{M}_t \cdot \mathbf{x}_t}\, e^{\pm ik_1 m_1(\mathbf{M}_t) h(\mathbf{x}_t)}. \end{aligned} \tag{9.4}$$

Equations (9.2) and (9.3) can thus be written in canonical form as

$$\int\int_{-\infty}^{\infty} k_{\mathrm{D}}^{\pm}(\mathbf{M}_t, \mathbf{x}_t)\, N(\mathbf{x}_h)\, d\mathbf{x}_t = D^{\pm}(\mathbf{M}_t), \tag{9.5}$$

where the terms on the right-hand side are defined as

$$D^{\pm}(\mathbf{M}_t) = \frac{2m_1(\mathbf{M}_t)(2\pi)^2}{k_1^2} \begin{cases} -I(\mathbf{M}_t) \\ R^{(\mathrm{D})}(\mathbf{M}_t). \end{cases} \tag{9.6}$$

We solve the equation with the "+" sign for $N(\mathbf{x}_h)$, and then evaluate the equation with the "–" sign for $R^{(\mathrm{D})}(\mathbf{M}_t)$. For the Dirichlet problem the solution was discussed in [6, 8] for the one dimensional surface. Note that the kernels $k_{\mathrm{D}}^{\pm}$ are functions of a spectral argument $\mathbf{M}_t$ and a coordinate argument $\mathbf{x}_t$, the former leading to row discretization and the latter to column discretization to form the resulting matrix inversion problem we solve, as well as the designation of the method as spectral-coordinated (SC).

10 Neumann Problem

From Section 8, there again are no equations from the region V_2 since we have perfect reflection and the boundary condition

$$N(\mathbf{x}_h) = 0. \tag{10.1}$$

Solve for ψ using (8.1), which is a first-kind integral equation

$$\int\int_{-\infty}^{\infty} \phi_1^{+}(\mathbf{x}_h)\; n_l M_l^{+}\, \psi(\mathbf{x}_h)\, d\mathbf{x}_t = \frac{2m_1(\mathbf{M}_t)(2\pi)^2}{k_1^2}\, I(\mathbf{M}_t), \tag{10.2}$$

and evaluate the Neumann reflection coefficient $R^{(\mathrm{N})}$ from (8.3):

$$\int\int_{-\infty}^{\infty} \phi_1^{-}(\mathbf{x}_h)\; n_l M_l^{-}\, \psi(\mathbf{x}_h)\, d\mathbf{x}_t = -\frac{2m_1(\mathbf{M}_t)(2\pi)^2}{k_1^2}\, R^{(\mathrm{N})}(\mathbf{M}_t), \tag{10.3}$$

The equations can be combined with the spectral dependence explicit as

$$\int\int_{-\infty}^{\infty} k_{\mathrm{N}}^{\pm}(\mathbf{M}_t, \mathbf{x}_t)\, \psi(\mathbf{x}_h)\, d\mathbf{x}_t = N^{\pm}(\mathbf{M}_t), \tag{10.4}$$

where

$$k_{\mathrm{N}}^{\pm}(\mathbf{M}_t, \mathbf{x}_t) = \phi_1^{\pm}(\mathbf{x}_h)\; n_l M_l^{\pm}, \tag{10.5}$$

or

$$k_{\mathrm{N}}^{\pm}(\mathbf{M}_t, \mathbf{x}_t) = k_{\mathrm{D}}^{\pm}(\mathbf{M}_t, \mathbf{x}_h)\; n_l M_l^{\pm}, \tag{10.6}$$

and

$$N^{\pm}(\mathbf{M}_t) = \frac{2m_1(\mathbf{M}_t)(2\pi)^2}{k_1^2} \begin{cases} I(\mathbf{M}_t) \\ -R^{(\mathrm{N})}(\mathbf{M}_t). \end{cases} \tag{10.7}$$

Here $N^{+} = -D^{+}$. We solve (10.4) with the "+" sign for $\psi(\mathbf{x}_h)$, and evaluate the equation with the "–" sign for $R^{(\mathrm{N})}(\mathbf{M}_t)$. Solution methods are similar to those described in [6, 8] for the Dirichlet problem in one dimension. The kernels $k_{\mathrm{N}}^{\pm}$ are also functions of spectral and coordinate variables as in Section 9 and this is the SC method for the Neumann problem.

11 Flux Conservation

For any complex field $\phi(\mathbf{x})$ the z-component of flux is defined as

$$J_z(\mathbf{x}) = \rho_B \, [\phi(\mathbf{x}) \frac{\partial}{\partial z} \overline{\phi}(\mathbf{x}) - \overline{\phi}(\mathbf{x}) \frac{\partial}{\partial z} \phi(\mathbf{x})], \tag{11.1}$$

where ρ_B is the density of the medium and the overbar is complex conjugation.

A spectral representation of ϕ is

$$\phi(\mathbf{x}) = \int \int B(\boldsymbol{\epsilon}_t) \, e^{ik\boldsymbol{\epsilon}\cdot\mathbf{x}} \, d\boldsymbol{\epsilon}_t, \tag{11.2}$$

where

$$\boldsymbol{\epsilon} = (\boldsymbol{\epsilon}_t, \epsilon_z), \tag{11.3}$$

$$\epsilon_z = \begin{cases} +\sqrt{1-\epsilon_t^2}, & \epsilon_t^2 < 1, \\ +i\sqrt{\epsilon_t^2 - 1}, & \epsilon_t^2 > 1. \end{cases} \tag{11.4}$$

We can thus write

$$J_z(\mathbf{x}) = \rho_B \int \int \int \int d\boldsymbol{\epsilon}_t \, d\boldsymbol{\epsilon}_t' \, B(\boldsymbol{\epsilon}_t) \, \overline{B}(\boldsymbol{\epsilon}_t') \, \{-ik\overline{\epsilon}_z' - ik\epsilon_z\} \, e^{ik(\boldsymbol{\epsilon}_t - \boldsymbol{\epsilon}_t')\cdot\mathbf{x}_t} \, e^{ik(\epsilon_z - \overline{\epsilon}_z')z}. \tag{11.5}$$

The flux through an area L^2 is

$$\hat{J}_z = \int \int_{-\frac{L}{2}}^{\frac{L}{2}} J_z(\mathbf{x}) \, d\mathbf{x}_t. \tag{11.6}$$

In the limit as $L \to \infty$ this becomes

$$\hat{J}_z(z) = -\frac{8i\pi^2}{k} \, \rho_B \int \int |B(\boldsymbol{\epsilon}_t)|^2 \, (\mathrm{Re}\ \epsilon_z) \, d\boldsymbol{\epsilon}_t, \tag{11.7}$$

which is independent of z and where only the real part of the z-component ϵ_z appears in the integrals.

For the scattered field replace ϵ_z by $\alpha_z = m_1$ from (8.15) and (8.27), and k by k_1 in (11.7), so that

$$\hat{J}_z^{\mathrm{SC}} = -\frac{8i\pi^2}{k_1} \, \rho_1 \int \int |R(\boldsymbol{\alpha}_t)|^2 \, (\mathrm{Re}\ m_1(\boldsymbol{\alpha}_t)) \, d\boldsymbol{\alpha}_t, \tag{11.8}$$

and for the incident field replace ϵ_z by $-\beta_z = -m_1$ from (8.13) and (8.27), and k by k_1 in (11.7), so that

$$\hat{J}_z^{\mathrm{i}} = -\frac{8i\pi^2}{k_1} \, \rho_1 \int \int |I(\boldsymbol{\beta}_t)|^2 \, (-\mathrm{Re}\ m_1(\boldsymbol{\beta}_t)) \, d\boldsymbol{\beta}_t. \tag{11.9}$$

For the transmitted field replace ϵ_z by $-m_2(\mathbf{M}_t)$ from (8.24) and (8.28), ρ_B by ρ_2 and (still) k by k_1 in (11.7), to get

$$\hat{J}_z^{\mathrm{T}} = -\frac{8i\pi^2}{k_1} \, \rho_2 \int \int |T(\mathbf{M}_t)|^2 \, (-\mathrm{Re}\ m_2(\mathbf{M}_t)) \, d\mathbf{M}_t. \tag{11.10}$$

The overall energy flux conservation is

$$\hat{J}_z^{\mathrm{i}} + \hat{J}_z^{\mathrm{SC}} = \hat{J}_z^{\mathrm{T}}, \tag{11.11}$$

which yields

$$\begin{aligned}\int\int |I(\boldsymbol{\beta}_t)|^2 \,(\mathrm{Re}\; m_1(\boldsymbol{\beta}_t))\, d\boldsymbol{\beta}_t = \int\int |R(\boldsymbol{\alpha}_t)|^2 (\mathrm{Re}\; m_1(\boldsymbol{\alpha}_t))\, d\boldsymbol{\alpha}_t \\ +\rho \int\int |T(\mathbf{M}_t)|^2 \,(\mathrm{Re}\; m_2(\mathbf{M}_t))\, d\mathbf{M}_t.\end{aligned} \tag{11.12}$$

This is used as a check in our computations. For a single plane wave incident on a periodic surface see Section 14.

PART II: THEORETICAL DEVELOPMENT FOR A PERIODIC SURFACE

12 Reduction to a Periodic Surface

In this section we reduce the equations in Section 8 to those for a periodic surface of period L_1 in x and period L_2 in y. Equation (8.1) is

$$\int\int_{-\infty}^{\infty} [n_1^+(\mathbf{M}_t, \mathbf{x}_t)\psi(\mathbf{x}_h) - N(\mathbf{x}_h)]\; e^{-ik_1\mathbf{M}_t\cdot\mathbf{x}_t}\; e^{ik_1 m_1(\mathbf{M}_t)h(\mathbf{x}_t)}\, d\mathbf{x}_t = F^{\rm in}(\mathbf{M}_t), \tag{12.1}$$

where

$$n_1^+(\mathbf{M}_t, \mathbf{x}_t) = m_1(\mathbf{M}_t) + \mathbf{M}_t \cdot \mathbf{h}_t, \tag{12.2}$$

$$\mathbf{M}_t = (M_x, M_y), \tag{12.3}$$

and

$$F^{\rm in}(\mathbf{M}_t) = \frac{2(2\pi)^2}{k_1^2} m_1(\mathbf{M}_t) I(\mathbf{M}_t). \tag{12.4}$$

Similarly, (8.23) becomes

$$\int\int_{-\infty}^{\infty} [n_2^-(\mathbf{M}_t, \mathbf{x}_t)\psi(\mathbf{x}_h) + \rho N(\mathbf{x}_h)]\; e^{-ik_1\mathbf{M}_t\cdot\mathbf{x}_t}\; e^{-ik_1 m_2(\mathbf{M}_t)h(\mathbf{x}_t)}\, d\mathbf{x}_t = 0, \tag{12.5}$$

where

$$n_2^-(\mathbf{M}_t, \mathbf{x}_t) = m_2(\mathbf{M}_t) - \mathbf{M}_t \cdot \mathbf{h}_t. \tag{12.6}$$

Floquet conditions on the surface fields

$$\begin{Bmatrix}\psi \\ N\end{Bmatrix}(x + L_1, y + L_2) = e^{ik_1 \boldsymbol{\alpha}_t^{(0)}\cdot\mathbf{L}_t} \begin{Bmatrix}\psi \\ N\end{Bmatrix}(x, y), \tag{12.7}$$

where

$$\boldsymbol{\alpha}_t^{(0)} = (\alpha_x^{(0)}, \alpha_y^{(0)}), \quad \mathbf{L}_t = (L_1, L_2), \tag{12.8}$$

yield a sum over an infinite number of finite cells (p, q run from $-\infty$ to ∞) from (12.1):

$$L_1 L_2 \sum_p \sum_q I_{p\,q}^{(1)}(\mathbf{M}_t) = F^{\rm in}(\mathbf{M}_t), \tag{12.9}$$

where

$$I_{p\,q}^{(1)}(\mathbf{M}_t) = \frac{1}{L_1 L_2} \int_{(2p-1)L_1/2}^{(2p+1)L_1/2} dx \int_{(2q-1)L_2/2}^{(2q+1)L_2/2} dy\; [n_1^+(\mathbf{M}_t, \mathbf{x}_t)\psi(\mathbf{x}_h) - N(\mathbf{x}_h)] \cdot \\ \cdot\, e^{-ik_1\mathbf{M}_t\cdot\mathbf{x}_t}\; e^{ik_1 m_1(\mathbf{M}_t)h(\mathbf{x}_t)}. \tag{12.10}$$

If we change variables to $x' = x - pL_1$ and $y' = y - qL_2$, and note that $n_1^+(\mathbf{M}_t, \mathbf{x}_t)$ is periodic, we can then use the Floquet conditions (12.7) on ψ and N to write

$$I_{p\,q}^{(1)}(\mathbf{M}_t) = e^{ik_1\alpha_x^{(0)} pL_1}\, e^{ik_1\alpha_y^{(0)} qL_2}\, e^{-ik_1\mathbf{M}_t\cdot(pL_1, qL_2)}\; I_{0\,0}^{(1)}(\mathbf{M}_t). \tag{12.11}$$

Then (12.9) becomes

$$L_1 L_2 \; I^{(1)}_{0\,0}(\mathbf{M}_t) \sum_p e^{ik_1(\alpha_x^{(0)} - M_x)pL_1} \sum_q e^{ik_1(\alpha_y^{(0)} - M_y)qL_2} = F^{\text{in}}(\mathbf{M}_t). \tag{12.12}$$

These are just Poisson sums:

$$L_1 L_2 \; I^{(1)}_{0\,0}(\mathbf{M}_t) \frac{\lambda_1}{L_1} \sum_{j=-\infty}^{\infty} \delta(M_x - \alpha_{jx}) \;\; \frac{\lambda_1}{L_2} \sum_{j'=-\infty}^{\infty} \delta(M_y - \alpha_{j'y}) = F^{\text{in}}(\mathbf{M}_t), \tag{12.13}$$

where

$$\alpha_{jx} = \alpha_x^{(0)} + j\frac{\lambda_1}{L_1}, \quad \text{and} \quad \alpha_{j'y} = \alpha_y^{(0)} + j'\frac{\lambda_1}{L_2}, \tag{12.14}$$

are the Bragg equations in the 2 dimensions.

The result of (12.12) is thus

$$I^{(1)}_{0\,0}(\mathbf{M}_t) \sum_{j=-\infty}^{\infty} \delta(M_x - \alpha_{jx}) \sum_{j'=-\infty}^{\infty} \delta(M_y - \alpha_{j'y}) = \frac{1}{\lambda_1^2} F^{\text{in}}(\mathbf{M}_t). \tag{12.15}$$

The same sequence of operations applied to (12.5) yields

$$I^{(2)}_{0\,0}(\mathbf{M}_t) \sum_{j=-\infty}^{\infty} \delta(M_x - \alpha_{jx}) \sum_{j'=-\infty}^{\infty} \delta(M_y - \alpha_{j'y}) = 0, \tag{12.16}$$

where

$$I^{(2)}_{0\,0}(\mathbf{M}_t) = \frac{1}{L_1 L_2} \int_{-L_1/2}^{L_1/2} dx \int_{-L_2/2}^{L_2/2} dy \quad [n_2^-(\mathbf{M}_t, \mathbf{x}_t)\psi(\mathbf{x}_h) + \rho N(\mathbf{x}_h)] \; e^{-ik_1 \mathbf{M}_t \cdot \mathbf{x}_t} \; e^{-ik_1 m_2(\mathbf{M}_t) h(\mathbf{x}_t)}. \tag{12.17}$$

Integrating (12.15) and (12.16), using the following integration scheme,

$$\lim_{\epsilon_j \to 0} \int_{\alpha_{px} - \epsilon_1 \frac{\lambda_1}{L_1}}^{\alpha_{px} + \epsilon_1 \frac{\lambda_1}{L_1}} dM_x \int_{\alpha_{qy} - \epsilon_2 \frac{\lambda_1}{L_2}}^{\alpha_{qy} + \epsilon_2 \frac{\lambda_1}{L_2}} dM_y \quad 0 < \epsilon_j < 1, \quad j = 1, 2, \tag{12.18}$$

these equations become

$$I^{(1)}_{0\,0}(\alpha_{jx}, \alpha_{j'y}) = \frac{1}{\lambda_1^2} \int_{\alpha_{px} - \epsilon_1 \frac{\lambda_1}{L_1}}^{\alpha_{px} + \epsilon_1 \frac{\lambda_1}{L_1}} dM_x \int_{\alpha_{qy} - \epsilon_2 \frac{\lambda_1}{L_2}}^{\alpha_{qy} + \epsilon_2 \frac{\lambda_1}{L_2}} dM_y \; F^{\text{in}}(\mathbf{M}_t), \tag{12.19}$$

and

$$I^{(2)}_{0\,0}(\alpha_{jx}, \alpha_{j'y}) = 0. \tag{12.20}$$

For a single plane wave incidence, from Section 8,

$$\begin{aligned} F^{\text{in}}(\mathbf{M}_t) &= \frac{2(2\pi)^2}{k_1^2} m_1(\mathbf{M}_t)\, I(\mathbf{M}_t) \\ &= \frac{2(2\pi)^2}{k_1^2} m_1(\mathbf{M}_t)\; \delta(\mathbf{M}_t - \boldsymbol{\alpha}_t^{(0)}) \\ &= \frac{2(2\pi)^2}{k_1^2} m_1(\mathbf{M}_t)\; \delta(M_x - \alpha_x^{(0)})\, \delta(M_y - \alpha_y^{(0)}). \end{aligned} \tag{12.21}$$

Equations (12.19) become

$$I_{0\,0}^{(1)}(\alpha_{jx},\alpha_{j'y}) = 2m_1(\boldsymbol{\alpha}_t^{(0)})\,\delta_{j0}\,\delta_{j'0}. \tag{12.22}$$

The equations to solve are (12.22) and (12.20), which are explicitly,

$$\frac{1}{L_1L_2}\int_{-L_1/2}^{L_1/2} dx\ \int_{-L_2/2}^{L_2/2} dy\ [(m_1(\alpha_{jx},\alpha_{j'y}) + \alpha_{jx}h_x + \alpha_{j'y}h_y)\,\psi(\mathbf{x}_h) - N(\mathbf{x}_h)]\cdot$$
$$\cdot\, e^{-ik_1(\alpha_{jx}x+\alpha_{j'y}y)}\, e^{ik_1m_1(\alpha_{jx},\alpha_{j'y})h(\mathbf{x}_t)} = 2m_1(\boldsymbol{\alpha}_t^{(0)})\delta_{j0}\delta_{j'0}, \tag{12.23}$$

$$\frac{1}{L_1L_2}\int_{-L_1/2}^{L_1/2} dx\ \int_{-L_2/2}^{L_2/2} dy\ [(m_2(\alpha_{jx},\alpha_{j'y}) - \alpha_{jx}h_x - \alpha_{j'y}h_y)\,\psi(\mathbf{x}_h) + \rho N(\mathbf{x}_h)]\cdot$$
$$\cdot\, e^{-ik_1(\alpha_{jx}x+\alpha_{j'y}y)}\, e^{-ik_1m_2(\alpha_{jx},\alpha_{j'y})h(\mathbf{x}_t)} = 0. \tag{12.24}$$

Note that

$$m_1(\alpha_{jx},\alpha_{j'y}) = \sqrt{1-\alpha_{jx}^2-\alpha_{j'y}^2}, \tag{12.25}$$

and

$$m_2(\alpha_{jx},\alpha_{j'y}) = \sqrt{\kappa^2-\alpha_{jx}^2-\alpha_{j'y}^2}. \tag{12.26}$$

13 Equations for a Periodic Surface

For a periodic surface the reflected and transmitted fields are discrete infinite sums of Bragg waves. These can be written using (8.15)

$$\psi^{\mathrm{SC}}(\mathbf{x}) = \int\int R(\mathbf{M}_t)\, e^{ik_1\mathbf{M}_t\cdot\mathbf{x}_t}\, e^{ik_1m_1(\mathbf{M}_t)z}\, d\mathbf{M}_t, \tag{13.1}$$

where here

$$R(\mathbf{M}_t) = \sum_{j=-\infty}^{\infty}\sum_{j'=-\infty}^{\infty} A_{jj'}\,\delta(M_x-\alpha_{jx})\,\delta(M_y-\alpha_{j'y}), \tag{13.2}$$

so that

$$\psi^{\mathrm{SC}}(\mathbf{x}) = \sum_{j=-\infty}^{\infty}\sum_{j'=-\infty}^{\infty} A_{jj'}\, e^{ik_1(\alpha_{jx}x+\alpha_{j'y}y)}\, e^{ik_1m_1(\alpha_{jx},\alpha_{j'y})z}. \tag{13.3}$$

Using (8.24)

$$\psi_T(\mathbf{x}) = \int\int T(\mathbf{M}_t)\, e^{ik_1\mathbf{M}_t\cdot\mathbf{x}_t}\, e^{-ik_1m_2(\mathbf{M}_t)z}\, d\mathbf{M}_t, \tag{13.4}$$

we have

$$T(\mathbf{M}_t) = \sum_{j=-\infty}^{\infty}\sum_{j'=-\infty}^{\infty} B_{jj'}\,\delta(M_x-\alpha_{jx})\,\delta(M_y-\alpha_{j'y}), \tag{13.5}$$

which yields

$$\psi_T(\mathbf{x}) = \sum_{j=-\infty}^{\infty}\sum_{j'=-\infty}^{\infty} B_{jj'}\, e^{ik_1(\alpha_{jx}x+\alpha_{j'y}y)}\, e^{-ik_1m_2(\alpha_{jx},\alpha_{j'y})z}. \tag{13.6}$$

Equations (8.3) and (8.26) (upper equation) reduce to

$$L_1L_2\ J_{0\,0}^{(1)}(\mathbf{M}_t)\ \sum_p e^{ik_1(\alpha_x^{(0)}-M_x)pL_1}\ \sum_q e^{ik_1(\alpha_y^{(0)}-M_y)qL_2} = \frac{2(2\pi)^2}{k_1^2}\, m_1(\mathbf{M}_t)\, R(\mathbf{M}_t), \tag{13.7}$$

and

$$L_1L_2\ J_{0\,0}^{(2)}(\mathbf{M}_t)\ \sum_p e^{ik_1(\alpha_x^{(0)}-M_x)pL_1}\ \sum_q e^{ik_1(\alpha_y^{(0)}-M_y)qL_2} = \rho\frac{2(2\pi)^2}{k_1^2}\, m_2(\mathbf{M}_t)\, T(\mathbf{M}_t), \tag{13.8}$$

where

$$J_{0\,0}^{(1)}(\mathbf{M}_t) = \frac{1}{L_1L_2}\int_{-L_1/2}^{L_1/2} dx \int_{-L_2/2}^{(L_2/2} dy\ [(m_1(\mathbf{M}_t) - \mathbf{M}_t\cdot h_t)\psi(\mathbf{x}_h) + N(\mathbf{x}_h)] \\ e^{-ik_1\mathbf{M}_t\cdot\mathbf{x}_t}\ e^{-ik_1m_2(\mathbf{M}_t)h(\mathbf{x}_t)}, \tag{13.9}$$

and

$$J_{0\,0}^{(2)}(\mathbf{M}_t) = \frac{1}{L_1L_2}\int_{-L_1/2}^{L_1/2} dx \int_{-L_2/2}^{(L_2/2} dy\ [(m_2(\mathbf{M}_t) + \mathbf{M}_t\cdot h_t)\psi(\mathbf{x}_h) - \rho N(\mathbf{x}_h)] \\ e^{-ik_1\mathbf{M}_t\cdot\mathbf{x}_t}\ e^{ik_1m_2(\mathbf{M}_t)h(\mathbf{x}_t)}. \tag{13.10}$$

Next, use the Poisson sum evaluation and integration as in Section 12, to get the explicit equations that must be evaluated

$$J_{0\,0}^{(1)}(\alpha_{jx},\alpha_{j'y}) = 2m_1(\alpha_{jx},\alpha_{j'y})\, A_{jj'}, \tag{13.11}$$

and

$$J_{0\,0}^{(2)}(\alpha_{jx},\alpha_{j'y}) = 2\rho m_2(\alpha_{jx},\alpha_{j'y})\, B_{jj'}, \tag{13.12}$$

where

$$J_{0\,0}^{(1)}(\alpha_{jx},\alpha_{j'y}) = \frac{1}{L_1L_2}\int_{-L_1/2}^{L_1/2} dx \int_{-L_2/2}^{L_2/2} dy\,[(m_1(\alpha_{jx},\alpha_{j'y}) - \alpha_{jx}h_x - \alpha_{j'y}h_y)\,\psi(\mathbf{x}_h) + N(\mathbf{x}_h)]\cdot \\ \cdot\, e^{-ik_1(\alpha_{jx}x+\alpha_{j'y}y)}\, e^{-ik_1m_1(\alpha_{jx},\alpha_{j'y})h(\mathbf{x}_t)}, \tag{13.13}$$

and

$$J_{0\,0}^{(2)}(\alpha_{jx},\alpha_{j'y}) = \frac{1}{L_1L_2}\int_{-L_1/2}^{L_1/2} dx \int_{-L_2/2}^{L_2/2} dy[(m_2(\alpha_{jx},\alpha_{j'y}) + \alpha_{jx}h_x + \alpha_{j'y}h_y)\,\psi(\mathbf{x}_h) - \rho N(\mathbf{x}_h)]\cdot \\ \cdot\, e^{-ik_1(\alpha_{jx}x+\alpha_{j'y}y)}\, e^{ik_1m_2(\alpha_{jx},\alpha_{j'y})h(\mathbf{x}_t)}. \tag{13.14}$$

The procedure is to compute the boundary unknowns $\psi(\mathbf{x}_h)$ and $N(\mathbf{x}_h)$ using (12.23) and (12.24) and use them in (13.13) and (13.14) to compute the scattered amplitudes by (13.11) and the transmission amplitudes from (13.12). The scattered and transmitted fields are then found from (13.3) and (13.6).

14 Energy Balance

The flux conservation or energy balance follows from the results in Section 11. The major difference is that the reflection and transmission coefficients are discrete sums as in (13.2) and (13.5). For a single plane wave as defined in (8.30)-(8.32) with amplitude D it can easily be shown that the energy balance result is analogous to (11.12) and given by

$$D^2 m_1(\alpha_x^{(0)}, \alpha_y^{(0)}) = \sum_{j,j'} |A_{jj'}|^2 \left(\text{Re } m_1(\alpha_{jx}, \alpha_{j'y})\right) + \rho \sum_{p,p'} |B_{pp'}|^2 \left(\text{Re } m_2(\alpha_{px}, \alpha_{p'y})\right), \tag{14.1}$$

where the summations extend over all j, j' values such that m_1 (defined in (12.25)) is real and all p, p' values such that m_2 (defined in (12.26)) is real, i.e. over all real scattered and transmitted Bragg orders. This is used as a check in our calculations as follows: Set $D = 1$ in (14.1) and divide the equation by $m_1(\alpha_x^{(0)}, \alpha_y^{(0)})$ so the left hand side of (14.1) is 1 and the resulting right hand side is called the normalized energy. The resulting error is

$$\text{Error } = \log_{10} |1 - \text{ Normalized Energy}|. \tag{14.2}$$

We have effectively scaled the incident energy to 1, and the normalized energy is the total energy in the scattered and transmitted fields.

15 Numerical Methods

In this section we summarize the equations and the computational methodology.

For a periodic transmission interface, the two coupled integral equations which we solve are from (12.23) and (12.24):

$$\frac{1}{L_1 L_2} \int_{-L_1/2}^{L_1/2} dx \int_{-L_2/2}^{L_2/2} dy [(m_1(\alpha_{jx}, \alpha_{j'y}) + \alpha_{jx} h_x(\mathbf{x}_t) + \alpha_{j'y} h_y(\mathbf{x}_t))\, \psi(\mathbf{x}_h) - N(\mathbf{x}_h)] \\ e^{-ik_1(\alpha_{jx}x + \alpha_{j'y}y)}\, e^{ik_1 m_1(\alpha_{jx}, \alpha_{j'y}) h(\mathbf{x}_t)} = 2m_1(\boldsymbol{\alpha}_t^{(0)}) \delta_{j0} \delta_{j'0}, \tag{15.1}$$

and

$$\frac{1}{L_1 L_2} \int_{-L_1/2}^{L_1/2} dx \int_{-L_2/2}^{L_2/2} dy [(m_2(\alpha_{jx}, \alpha_{j'y}) - \alpha_{jx} h_x(\mathbf{x}_t) - \alpha_{j'y} h_y(\mathbf{x}_t))\, \psi(\mathbf{x}_h) + \rho N(\mathbf{x}_h)] \\ e^{-ik_1(\alpha_{jx}x + \alpha_{j'y}y)}\, e^{-ik_1 m_2(\alpha_{jx}, \alpha_{j'y}) h(\mathbf{x}_t)} = 0. \tag{15.2}$$

where (to summarize all the notations),

$$\mathbf{x}_t = (x, y), \tag{15.3}$$

$$\mathbf{x}_h = (\mathbf{x}_t, h(\mathbf{x}_t)), \tag{15.4}$$

$$h_x(\mathbf{x}_t) = \frac{\partial h}{\partial x}(\mathbf{x}_t), \tag{15.5}$$

$$h_y(\mathbf{x}_t) = \frac{\partial h}{\partial y}(\mathbf{x}_t), \tag{15.6}$$

$$\alpha_x^{(0)} = \cos\phi^{\mathrm{i}}\sin\theta^{\mathrm{i}}, \tag{15.7}$$

$$\alpha_y^{(0)} = \sin\phi^{\mathrm{i}}\sin\theta^{\mathrm{i}}, \tag{15.8}$$

$$\boldsymbol{\alpha}_t^{(0)} = (\alpha_x^{(0)}, \alpha_y^{(0)}), \tag{15.9}$$

$$\alpha_{jx} = \alpha_x^{(0)} + j\frac{\lambda}{L_1}, \tag{15.10}$$

$$\alpha_{j'y} = \alpha_y^{(0)} + j'\frac{\lambda}{L_2}, \tag{15.11}$$

$$m_1(\alpha_{jx}, \alpha_{j'y}) = \sqrt{1 - \alpha_{jx}^2 - \alpha_{j'y}^2}, \tag{15.12}$$

and

$$m_2(\alpha_{jx}, \alpha_{j'y}) = \sqrt{\kappa^2 - \alpha_{jx}^2 - \alpha_{j'y}^2}. \tag{15.13}$$

The equations are thus already discrete in spectral space.

The integral equations are then discretized over the rough surface in coordinate space to give (w_p are weight functions)

$$\begin{aligned}
&\sum_{q=1}^{M}\sum_{p=1}^{N}\left[\left(m_1(\alpha_{jx}, \alpha_{j'y}) + \alpha_{jx}h_x(x_p, y_q) + \alpha_{j'y}h_y(x_p, y_q)\right)\psi(x_p, y_q, h(x_p, y_q))\right.\\
&\quad\left. - N(x_p, y_q, h(x_p, y_q))\right] e^{-ik_1\alpha_{jx}x_p}\, e^{-ik_1\alpha_{j'y}y_q}\, e^{ik_1 m_1(\alpha_{jx},\alpha_{j'y})h(x_p,y_q)}\, w_p w_q\\
&\quad = 2L_1L_2 m_1(\boldsymbol{\alpha}_t^{(0)})\,\delta_{j0}\,\delta_{j'0},
\end{aligned} \tag{15.14}$$

and

$$\begin{aligned}
&\sum_{q=1}^{M}\sum_{p=1}^{N}\left[\left(m_2(\alpha_{jx}, \alpha_{j'y}) - \alpha_{jx}h_x(x_p, y_q) - \alpha_{j'y}h_y(x_p, y_q)\right)\psi(x_p, y_q, h(x_p, y_q))\right.\\
&\left. + \rho N(x_p, y_q, h(x_p, y_q))\right] e^{-ik_1\alpha_{jx}x_p}\, e^{-ik_1\alpha_{j'y}y_q}\, e^{-ik_1 m_2(\alpha_{jx},\alpha_{j'y})h(x_p,y_q)}\, w_p w_q = 0.
\end{aligned} \tag{15.15}$$

These integral equations can be written as matrix equations by defining the following matrices:

$$\mathbf{M1}_{jj',pq} = e^{-ik_1\alpha_{jx}x_p}\, e^{-ik_1\alpha_{j'y}y_q}\, e^{ik_1 m_1(\alpha_{jx},\alpha_{j'y})h(x_p,y_q)}\, w_p w_q, \tag{15.16}$$

$$\mathbf{K1}_{jj',pq} = \left[\left(m_1(\alpha_{jx}, \alpha_{j'y}) + \alpha_{jx}h_x(x_p, y_q) + \alpha_{j'y}h_y(x_p, y_q)\right]\mathbf{M1}_{jj',pq} \right. \tag{15.17}$$

$$\mathbf{M2}_{jj',pq} = e^{-ik_1\alpha_{jx}x_p}\, e^{-ik_1\alpha_{j'y}y_q}\, e^{-ik_1 m_2(\alpha_{jx},\alpha_{j'y})h(x_p,y_q)}\, w_p w_q, \tag{15.18}$$

$$\mathbf{K2}_{jj',pq} = \left[m_2(\alpha_{jx}, \alpha_{j'y}) - \alpha_{jx}h_x(x_p, y_q) - \alpha_{j'y}h_y(x_p, y_q)\right]\mathbf{M2}_{jj',pq}. \tag{15.19}$$

The indices jj' and pq are strung out and act as one index each using the schematic defined in Table 1 at the end of this section.

The vectors $\mathbf{b}$, $\mathbf{\Psi}$and $\mathbf{N}$ are defined as

$$b_{jj'} = 2L_1L_2 m_1(\boldsymbol{\alpha}_t^{(0)})\delta_{j0}\delta_{j'0}, \tag{15.20}$$

$$\psi_{pq} = \psi(x_p, y_q, h(x_p, y_q)), \tag{15.21}$$

$$N_{pq} = N(x_p, y_q, h(x_p, y_q)), \tag{15.22}$$

so the whole system can be expressed as

$$\left[\begin{array}{c} \mathbf{K1} \\ \mathbf{K2} \end{array}\right] \mathbf{\Psi} + \left[\begin{array}{c} -\mathbf{M1} \\ \rho\mathbf{M2} \end{array}\right] \mathbf{N} = \left[\begin{array}{c} \mathbf{b} \\ \mathbf{0} \end{array}\right], \tag{15.23}$$

or

$$\left[\begin{array}{cc} \mathbf{K1} & -\mathbf{M1} \\ \mathbf{K2} & \rho\mathbf{M2} \end{array}\right] \left[\begin{array}{c} \mathbf{\Psi} \\ \mathbf{N} \end{array}\right] = \left[\begin{array}{c} \mathbf{b} \\ \mathbf{0} \end{array}\right]. \tag{15.24}$$

The reported system size is the size of the matrix

$$\left[\begin{array}{cc} \mathbf{K1} & -\mathbf{M1} \\ \mathbf{K2} & \rho\mathbf{M2} \end{array}\right]. \tag{15.25}$$

When $\kappa \neq 1$, the system is not square. For this case, a single equation is used for the current, and a Dirichlet to Neumann map is used for the field to yield

$$\mathbf{N} = -\left[\mathbf{M1} + \mathbf{K1}\mathbf{K2}^{-1}\rho\mathbf{M2}\right]^{-1}\mathbf{b}, \tag{15.26}$$

and

$$\mathbf{\Psi} = \mathbf{K1}^{-1}[\mathbf{b} + \mathbf{M1}\mathbf{N}]. \tag{15.27}$$

The pseudo inverse is used for all inverses. Finally, reported condition numbers are the condition numbers of the matrix

$$\left[\begin{array}{cc} \mathbf{K1} & -\mathbf{M1} \\ \mathbf{K2} & \rho\mathbf{M2} \end{array}\right]. \tag{15.28}$$

Coordinate Index	p	q
1	1	1
2	1	2
3	1	3
.	.	.
.	.	.
.	.	.
M	1	M
M+1	2	1
M+2	2	2
M+3	2	3
.	.	.
.	.	.
.	.	.
$M \cdot N$	$N\cdot$	M

Table 1: A schematic representation of the labelling scheme to write the two dimensional coordinate sampling indices p (N samples in x) and q (M samples in y). The total of $M \cdot N$ coordinate samples are strung out in a coordinate sample line running from 1 to $M \cdot N$.

Spectral Index	j	j'
1	$j$min	j'min
2	$j$min	j'min+1
3	$j$min	j'min+2
.	.	.
.	.	.
.	.	.
m	$j$min	j'max
$m+1$	$j$min+1	j'min
$m+2$	$j$min+1	j'min+1
$m+3$	$j$min+1	j'min+2
.	.	.
.	.	.
.	.	.
n	$j$max	j'max

Table 2: A schematic representation of the labelling scheme to write the total numbers of real Bragg modes as n. The indices j and j' each run from a minimum to a maximum value for which the right hand sides of (15.10) and (15.11) do not exceed a magnitude of one for m_1 in (15.12) or a magnitude of κ for m_2 in (15.13). The mode j refers to the $x-$direction and j' to the $y-$direction.

PART III: COMPUTATIONAL RESULTS FOR PERIODIC SURFACES

16 Introduction and Outline of the Computational Results

In Sections 17-19 we present the computational results for scattering from many examples of surfaces periodic in two dimensions. All the results were generated using the two-dimensional spectral-coordinate (SC) method developed in PART II. Most computations were performed using MATLAB 5.2 on a Sun SPARC station 20. Some computations were done using MATLAB 5.3 on a customized Pentium III-500 MHz PC. These latter computations will be clearly indicated in the figure captions.

The objective of this study was to provide results for a broad suite of parameter values in order to assess the computational speed and accuracy of the SC method for two-dimensional scattering. Various surface examples and cases were presented where the surface periods, heights and slopes were varied as were the incident polar and azimuthal angles. In addition, for fixed error, the maximum roughness (related to largest slope) was studied as the incident polar angle was varied from 0° (vertical incidence) to 89.99° (near grazing incidence) and as the ratio of wavelength to surface period (both $x-$and $y-$periods the same) varied over three orders of magnitude.

The number of spectral samples was generally fixed by the number of real Bragg modes although we also present many examples where we increased the spectral sampling by adding non-radiating (surface wave) modes. To form a square matrix in our SC development requires the same number of coordinate samples and we studied the convergence behavior of increasingly larger square systems as well as non-square systems where more coordinate than spectral samples were chosen. Complexity analysis of both square and non-square systems was also studied.

In Section 17 the results for the perfectly reflecting Dirichlet boundary value problem are presented. The equations on which the results are based are found in Section 9. In addition to the sinusoidal surface examples we also present results for a saw-tooth surface in Sec. 17.9. For the sinusoidal surfaces we present four examples in Secs. 17.1-17.8 each with no grazing and near-grazing conditions. The examples were representative, all converged very well even for very large slopes, high condition numbers, and under near-grazing conditions. In Sec. 17.10 we study convergence as a function of ϕ^i, the azimuthal angle of incidence. In Secs. 17.11 and 17.12 we fix an upper bound on the error and study the maximum roughness (slope) attainable with respect to incident polar angle (Sec. 17.11) and wavenumber to surface period ratio (Sec. 17.12). Finally, we briefly remark on the complexity analysis for both square (Sec. 17.13) and non-square systems (Sec. 17.14).

In Section 18 the results for the perfectly reflecting Neumann boundary value problem are presented using the theoretical results in Section 10. Three examples of sinusoidal surfaces are treated for no grazing and near-grazing conditions in Secs. 18.1 through 18.6. Again, the examples were representative and nearly all converged well under large slope and near-grazing conditions and for large condition numbers. The only case where difficulty was encountered was when both heights and slopes were large with accompanying grazing incidence and re-

flection. In Secs. 18.7 and 18.8 we fix an upper bound on the error and study the maximum roughness (slope) attainable with respect to incident polar angle (Sec. 18.7) and wavenumber to surface period ratio (Sec. 18.8). Finally, we briefly remark on the complexity analysis for both square (Sec. 18.9) and non-square systems (Sec. 18.10).

In Section 19 we present the results for the rough interface where we have transmission. We treat several examples of surfaces in Secs. 19.1 to 19.6. We study convergence as a function of ϕ^i, the azimuthal angle of incidence (Sec. 19.7), as a function of κ, the ratio of wavenumbers (Sec. 19.8), and as a function of ρ, the density or electromagnetic parameter ratio (Sec. 19.9). Fixing an upper bound on the error we present results of the maximum roughness (slope) attainable as a function of θ^i, the polar angle of incidence (Sec. 19.10), as a function of ρ (Sec. 19.11), as a function of ρ for near-grazing incidence (Sec. 19.12), as a function of κ (Sec. 19.13), and as a function of κ for near-grazing incidence (Sec. 19.14).

We briefly discuss the complexity analysis for square systems using Gaussian elimination (Sec. 19.15) and for non-square systems using pseudo-inverse methods (Sec. 19.16).

17 Dirichlet Computations

In this section we present results for the perfectly reflecting Dirichlet boundary value problem based on the theoretical development in Section 9. This corresponds electromagnetically to TE-polarization. Four sinusoidal surface examples are presented in Secs. 17.1-17.8 under both non-grazing and near-grazing conditions.

In Example 1 the wavelength was much less than the surface periods. In Example 2 the wavelength was approximately equal to the surface periods, and in Example 3 the wavelength was much greater than the surface periods. Example 4 was similar to Example 1 except one period was twice the other (Case A) and twenty times the other (Case B). In addition to the sinusoidal examples we present a saw-tooth surface example in Sec. 17.9.

We present both tabular and visual representations of the computations. In the tables the number of spectral and coordinate samples is indicated as well as the overall matrix size for both square and non-square matrices. The number of real Bragg modes fixes the number of real spectral samples. Occasionally we explore the effect of adding additional non-radiating modes to the spectral sampling. Basically, for a square system, the number of coordinate samples equals the number of spectral samples. If the system is not square then the number of coordinate samples has been increased. The computational procedure is outlined in Section 15. In addition, the tables contain sampling distances in the $x-$ and $y-$ directions as a function of wavelength as well as the fill time (times in seconds necessary to compute each term in the matrix), linear solution time (times in seconds necessary to invert the matrix, compute the boundary unknown functions and the resulting scattered field), the condition number of the matrix and the error in the computations (see Section 14 for the definition of error). The graphical presentation for the examples consists in plotting the real part and magnitude of the surface boundary unknown (here the normal derivative or surface current N) as well as the real part and magnitude of the scattered field on hemispheres of radii R above the surface where R is related to the surface period and on planes a distance H above the surface where H is also related to the surface period. Plots of the spectral orders are also included.

In Sec. 17.10 we present an example where we vary the incident azimuthal angle from 0° to 90°. In Secs. 17.11 and 17.12 we fix the error in the computations to be less than -2 and plot the maximum value of roughness d/L with respect to incident polar angle θ^i (Sec. 17.11) and wavelength to period ratio λ/L (Sec. 17.12).

A brief discussion of the complexity analysis for the solution of these systems of equations is presented in Sec. 17.13 for square systems using Gaussian elimination and in Sec. 17.14 for non-square systems using pseudo-inverse techniques.

17.1 Example 1 Case A, No Grazing

The parameters for this case are presented in Tables 3 and 4 for square and non-square systems respectively.

$S(x,y)$	$-(d/2)\cos(2\pi x/L_1)\cos(2\pi y/L_2)$
(L_1, L_2)	(1,1)
$(d/L_1, d/L_2)$	(.075,.075)
$(\lambda/L_1, \lambda/L_2)$	(.12,.12)
Radiating Orders	218
θ^i	20°
ϕ^i	15°

Matrix Size	Number of Samples				$\lambda/\Delta x$	$\lambda/\Delta y$	Fill Time (s)	Linear Solution Time (s)	Condition Number	Error
	Coord.		Spectral							
	x	y	j	j'						
289 × 289	17	17	17	17	2.0400	2.0400	3.0100	5.4000	12.9112	-5.9342
324 × 324	18	18	18	18	2.1600	2.1600	3.6800	7.5600	20.4592	-7.2897
361 × 361	19	19	19	19	2.2800	2.2800	4.4900	10.2200	31.6313	-7.6609
400 × 400	20	20	20	20	2.4000	2.4000	5.3300	13.7000	47.8785	-8.6434
441 × 441	21	21	21	21	2.5200	2.5200	6.4900	18.0800	71.5582	-8.5985
484 × 484	22	22	22	22	2.6400	2.6400	7.6400	23.9900	105.5270	-9.6605
529 × 529	23	23	23	23	2.7600	2.7600	9.1000	31.0000	154.5561	-9.6695
576 × 576	24	24	24	24	2.8800	2.8800	10.7400	41.7200	224.3060	-10.8312
625 × 625	25	25	25	25	3.0000	3.0000	12.6900	52.6900	324.2507	-10.8692
676 × 676	26	26	26	26	3.1200	3.1200	14.4800	68.1100	465.5978	-12.4765
729 × 729	27	27	27	27	3.2400	3.2400	17.1000	86.2500	667.0382	-12.5681

Table 3: Parameters and computational results for the Dirichlet problem, Example 1, Case A. Angle parameters were chosen to avoid grazing incidence and reflection. Only square systems were considered. The table is mostly self-explanatory with additional definitions in Section 16. The wavelength λ is much less than either of the (here) equal periods. Convergence is very good for all cases considered.

Matrix Size	Number of Samples Coord. x	Coord. y	Spectral j	Spectral j'	$\lambda/\Delta x$	$\lambda/\Delta y$	Fill Time (s)	Linear Solution Time (s)	Condition Number	Error
289 × 324	18	18	17	17	2.1600	2.1600	3.2900	249.8100	6.5844	-6.3604
289 × 361	19	19	17	17	2.2800	2.2800	3.5500	281.1500	5.0713	-6.3555
289 × 400	20	20	17	17	2.4000	2.4000	3.8400	337.6500	4.8837	-6.3541
289 × 441	21	21	17	17	2.5200	2.5200	4.1200	397.6500	4.8406	-6.3540
289 × 484	22	22	17	17	2.6400	2.6400	4.4100	465.7800	4.8385	-6.3540
324 × 289	17	17	18	18	2.0400	2.0400	3.4500	235.4800	18.2621	-5.8827
361 × 289	17	17	19	19	2.0400	2.0400	3.8900	250.5900	20.4573	-5.1014
400 × 289	17	17	20	20	2.0400	2.0400	4.3100	270.2100	24.5656	-5.1073
441 × 289	17	17	21	21	2.0400	2.0400	4.8400	283.1500	27.2566	-3.4552
484 × 289	17	17	22	22	2.0400	2.0400	5.2900	301.9800	30.9791	-3.4550

Table 4: Parameters and computational results for the Dirichlet problem, Example 1, Case A. Angle parameters were chosen to avoid grazing incidence and reflection. Only non-square systems are included by using additional coordinate-based sampling. Error numbers were still quite good but not nearly as good as the square systems in Table 3. Undersampling in coordinate space caused the error to deteriorate.

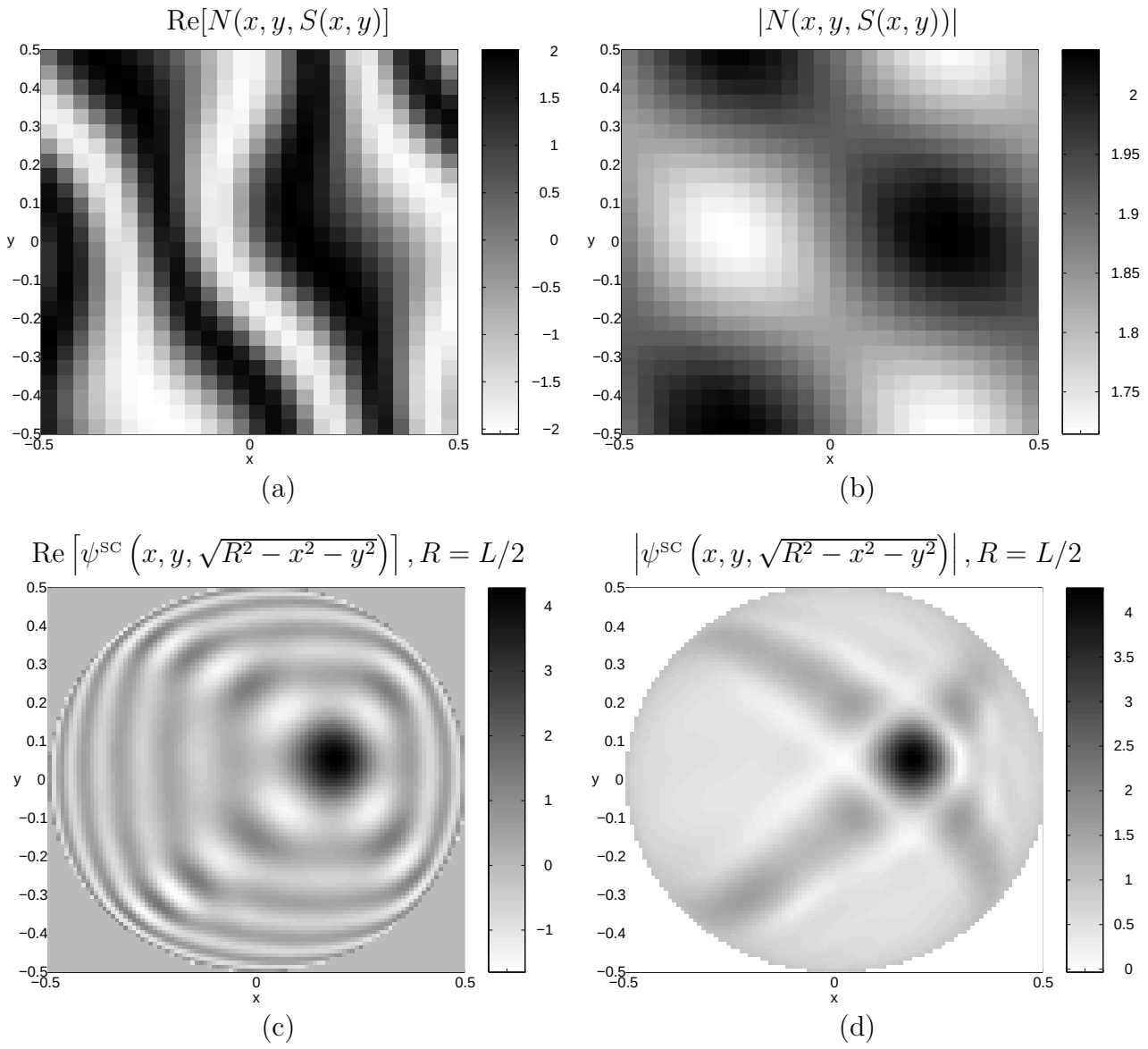

Figure 4: Example 1, Case A for the Dirichlet problem and a matrix size of 729×729. Real part (a) and magnitude (b) of the surface current or normal derivative N and the real part (c) and magnitude (d) of the scattered field plotted on a hemisphere of radius $R = L/2$ ($L = L_1 = L_2$) looking down from above. The resolution is 100×100.

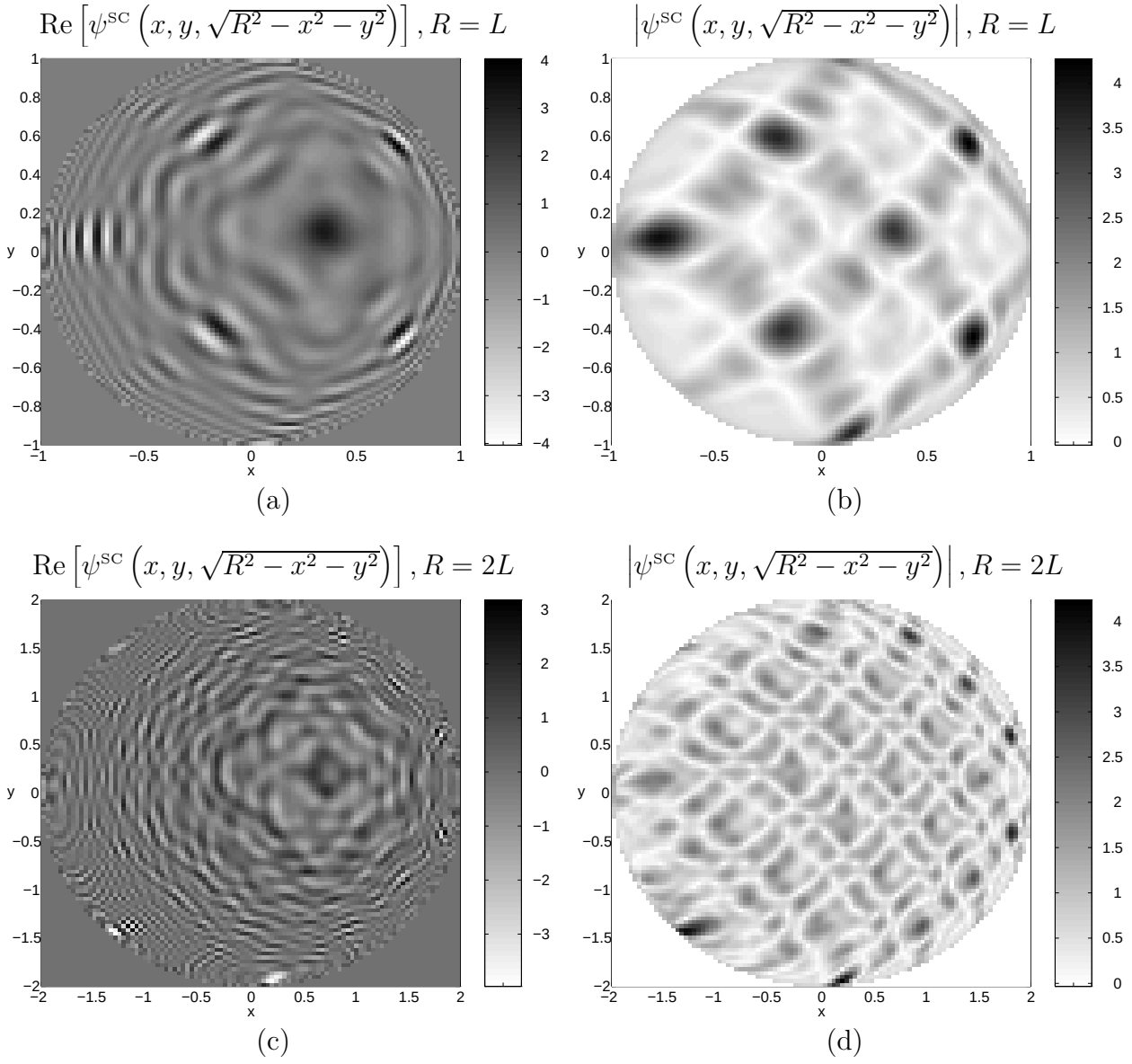

Figure 5: Example 1, Case A for the Dirichlet problem and a matrix size of 729×729. Real part and magnitude of the scattered field plotted on hemispheres of radius $R = L$ in (a) and (b) and $R = 2L$ in (c) and (d). Here $L = L_1 = L_2$ and the resolution is 100×100.

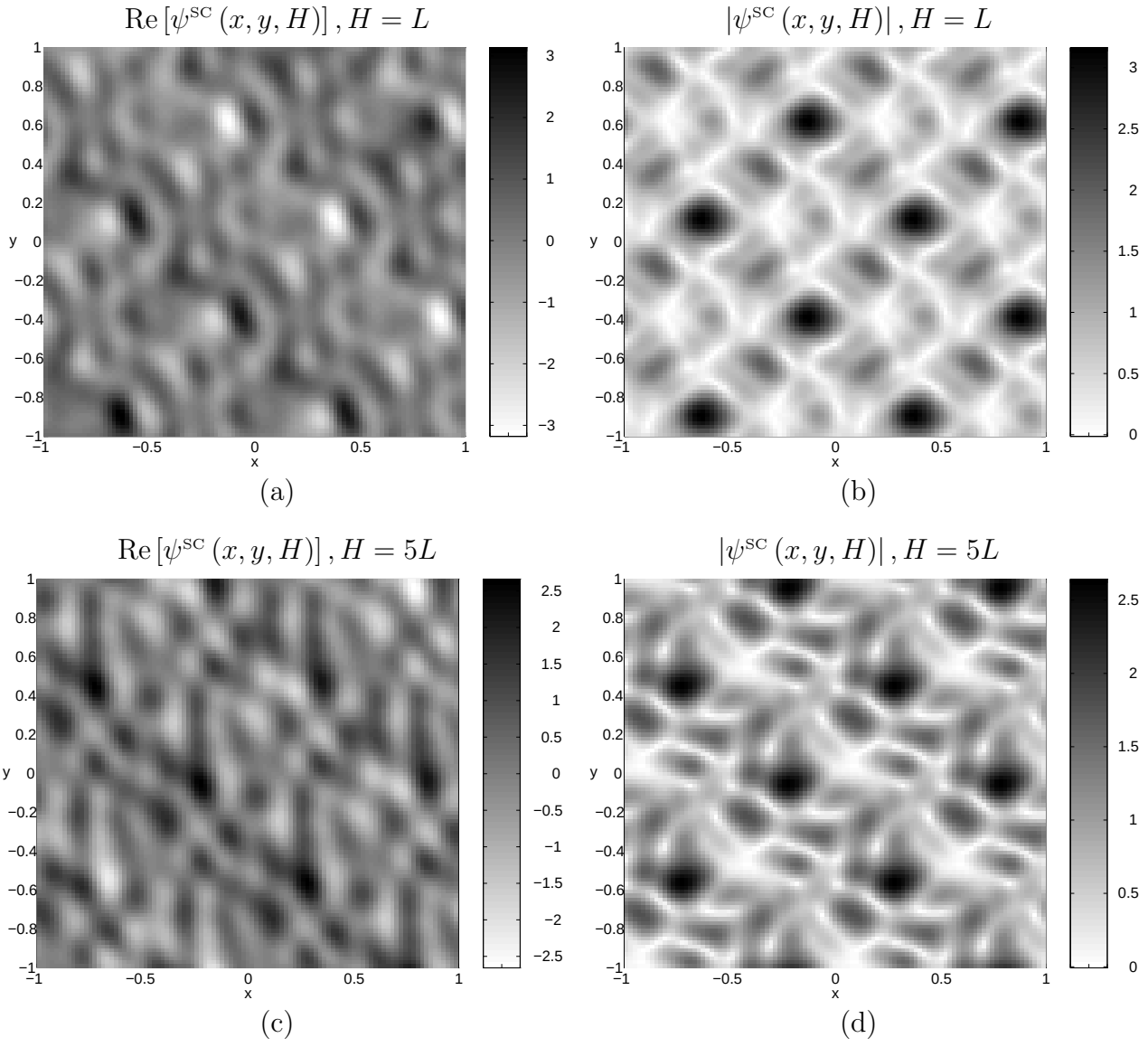

Figure 6: Example 1, Case A for the Dirichlet problem and a matrix size of 729×729. Real part and magnitude of the scattered field plotted on horizontal planes a distance $H = L$ above the surface in (a) and (b), and $H = 5L$ above the surface in (c) and (d). Here $L = L_1 = L_2$. The resolution is 100×100. The real parts can be quite blurry whereas the magnitudes are much sharper.

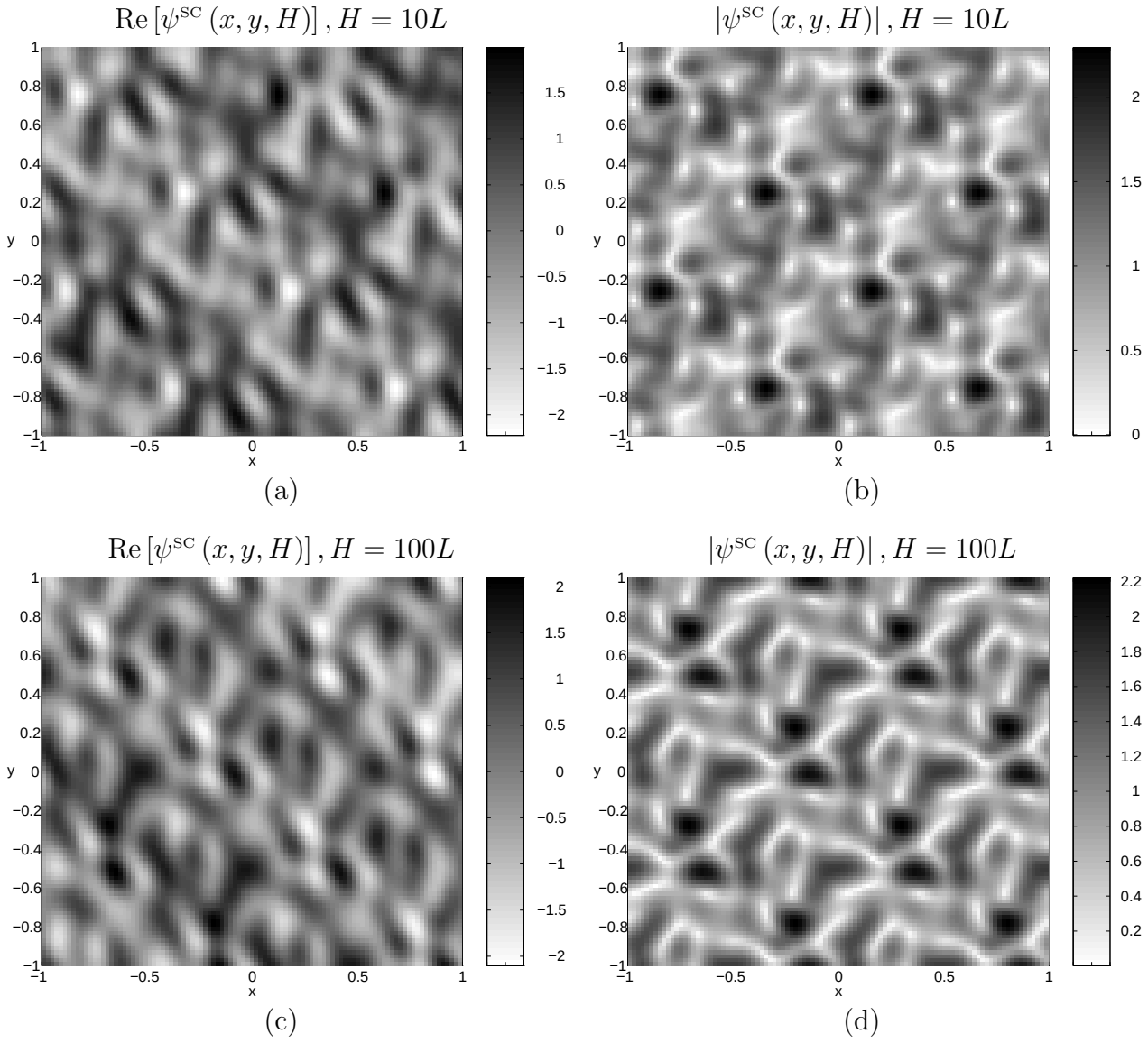

Figure 7: Example 1, Case A for the Dirichlet problem and a matrix size of 729×729. Real part and magnitude of the scattered field plotted on horizontal planes a distance $H = 10L$ above the surface in (a) and (b), and $H = 100L$ above the surface in (c) and (d). Here $L = L_1 = L_2$. The resolution is 100×100. The real parts can be quite blurry whereas the magnitudes are much sharper.

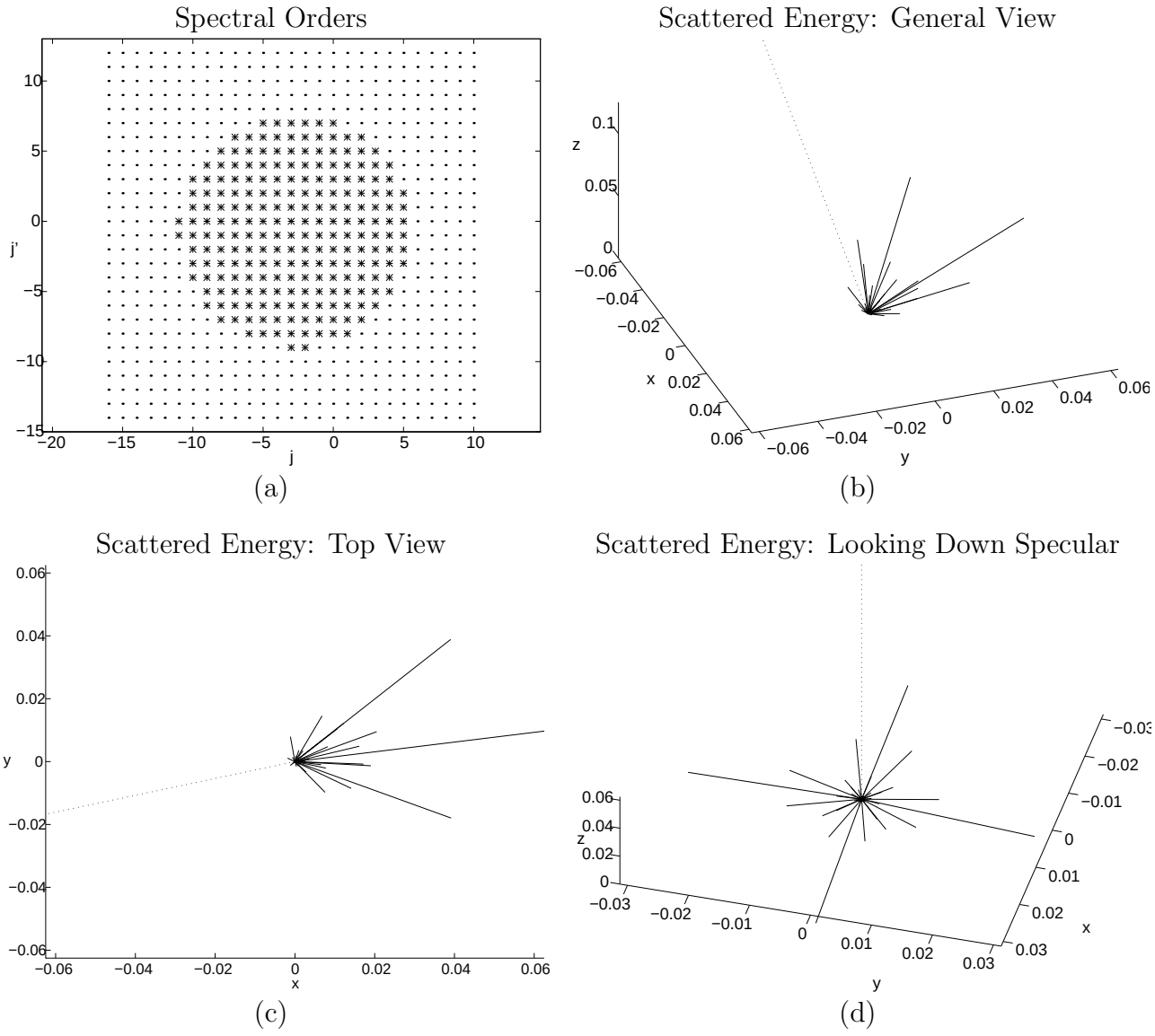

Figure 8: Example 1, Case A for the Dirichlet problem and a matrix size of 729×729. (a) Spectral orders with 27 samples in j and j'; stars refer to radiating modes, dots to non-radiating modes. Scattered energy distribution viewed from (b) $\theta = 40°, \phi = -20°$, (c) $\theta = 0°, \phi = -90°$, and (d) $\theta = 20°, \phi = 15°$. Dashed line is incident field, solid lines are scattered Bragg modes. The magnitudes of the lines are proportional to the energy.

17.2 Example 1 Case B, Near-Grazing Incidence/Reflection

$S(x,y)$	$-(d/2)\cos(2\pi x/L_1)\cos(2\pi y/L_2)$
(L_1, L_2)	(1,1)
$(d/L_1, d/L_2)$	(.075,.075)
$(\lambda/L_1, \lambda/L_2)$	(.12,.12)
Radiating Orders	220
θ^i	75°
ϕ^i	15°

Matrix Size	Number of Samples				$\lambda/\Delta x$	$\lambda/\Delta y$	Fill Time (s)	Linear Solution Time (s)	Condition Number	Error
	Coord.		Spectral							
	x	y	j	j'						
289 × 289	17	17	17	17	2.0400	2.0400	3.0300	5.4900	12.7476	-2.0498
324 × 324	18	18	18	18	2.1600	2.1600	3.6700	7.5800	21.3189	-3.2254
361 × 361	19	19	19	19	2.2800	2.2800	4.5600	10.2800	31.3239	-3.2300
400 × 400	20	20	20	20	2.4000	2.4000	5.8200	14.6800	49.5966	-4.2416
441 × 441	21	21	21	21	2.5200	2.5200	6.9900	19.7400	70.9439	-4.2266
484 × 484	22	22	22	22	2.6400	2.6400	8.7500	27.6500	108.9295	-5.2112
529 × 529	23	23	23	23	2.7600	2.7600	9.0700	31.1600	153.3484	-5.2294
576 × 576	24	24	24	24	2.8800	2.8800	11.4300	42.3800	230.9881	-6.1944
625 × 625	25	25	25	25	3.0000	3.0000	12.5100	53.5300	321.8926	-6.2196
676 × 676	26	26	26	26	3.1200	3.1200	14.9000	74.1900	478.6422	-7.1775
729 × 729	27	27	27	27	3.2400	3.2400	17.3100	88.7600	662.4547	-7.2064

Table 5: Parameters and computational results for the Dirichlet problem, Example 1, Case B. Angle parameters were chosen so that near-grazing incidence and reflection occurred as evidenced by the 220 radiating orders (compare with Table 3). Only square systems were included. Convergence was very good for all cases considered.

Matrix Size	Number of Samples Coord. x	Coord. y	Spectral j	Spectral j'	$\lambda/\Delta x$	$\lambda/\Delta y$	Fill Time (s)	Linear Solution Time (s)	Condition Number	Error
289 × 324	18	18	17	17	2.1600	2.1600	4.0500	278.0100	6.4380	-0.9317
289 × 361	19	19	17	17	2.2800	2.2800	3.5200	286.8000	4.7637	-0.9148
289 × 400	20	20	17	17	2.4000	2.4000	4.5400	350.5100	4.5491	-0.9145
289 × 441	21	21	17	17	2.5200	2.5200	4.1500	414.2700	4.4831	-0.9145
289 × 484	22	22	17	17	2.6400	2.6400	4.6400	545.0200	4.4805	-0.9145
324 × 289	17	17	18	18	2.0400	2.0400	3.5500	237.5600	18.6666	-1.6141
361 × 289	17	17	19	19	2.0400	2.0400	3.8000	255.1200	20.2728	-0.1814
400 × 289	17	17	20	20	2.0400	2.0400	4.2700	266.5200	25.0452	-0.1773
441 × 289	17	17	21	21	2.0400	2.0400	4.7700	298.6400	27.0235	-0.1600
484 × 289	17	17	22	22	2.0400	2.0400	6.3300	320.9800	31.4774	-0.1598

Table 6: Parameters and computational results for the Dirichlet problem, Example 1, Case B. Angle parameters were chosen so that near-grazing incidence and reflection occurred as evidenced by the 220 radiating orders (compare with Table 4). Only non-square systems were included and the energy checks were quite poor.

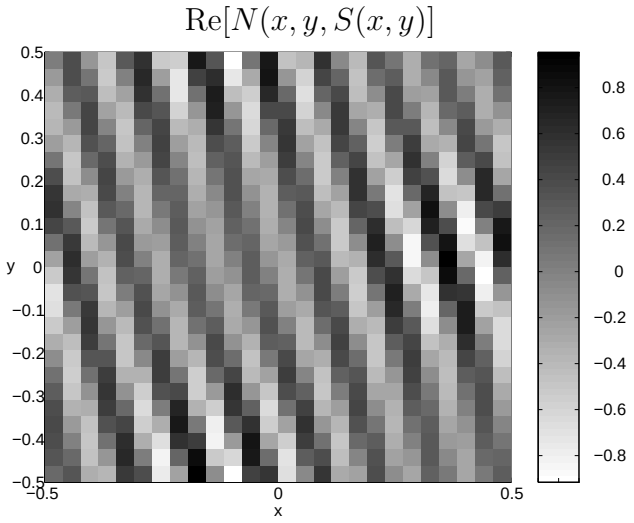

(a)

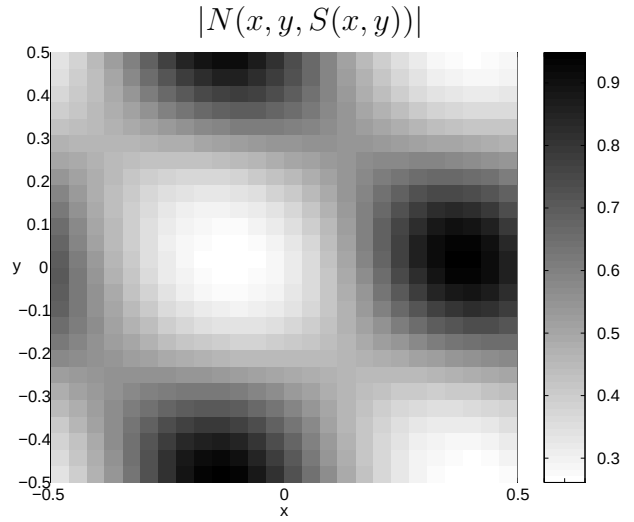

(b)

Figure 9: Example 1, Case B for the Dirichlet problem and a matrix size of 729×729 with an error of -7.2064. Real part (a) and magnitude (b) of the surface current or normal derivative N.

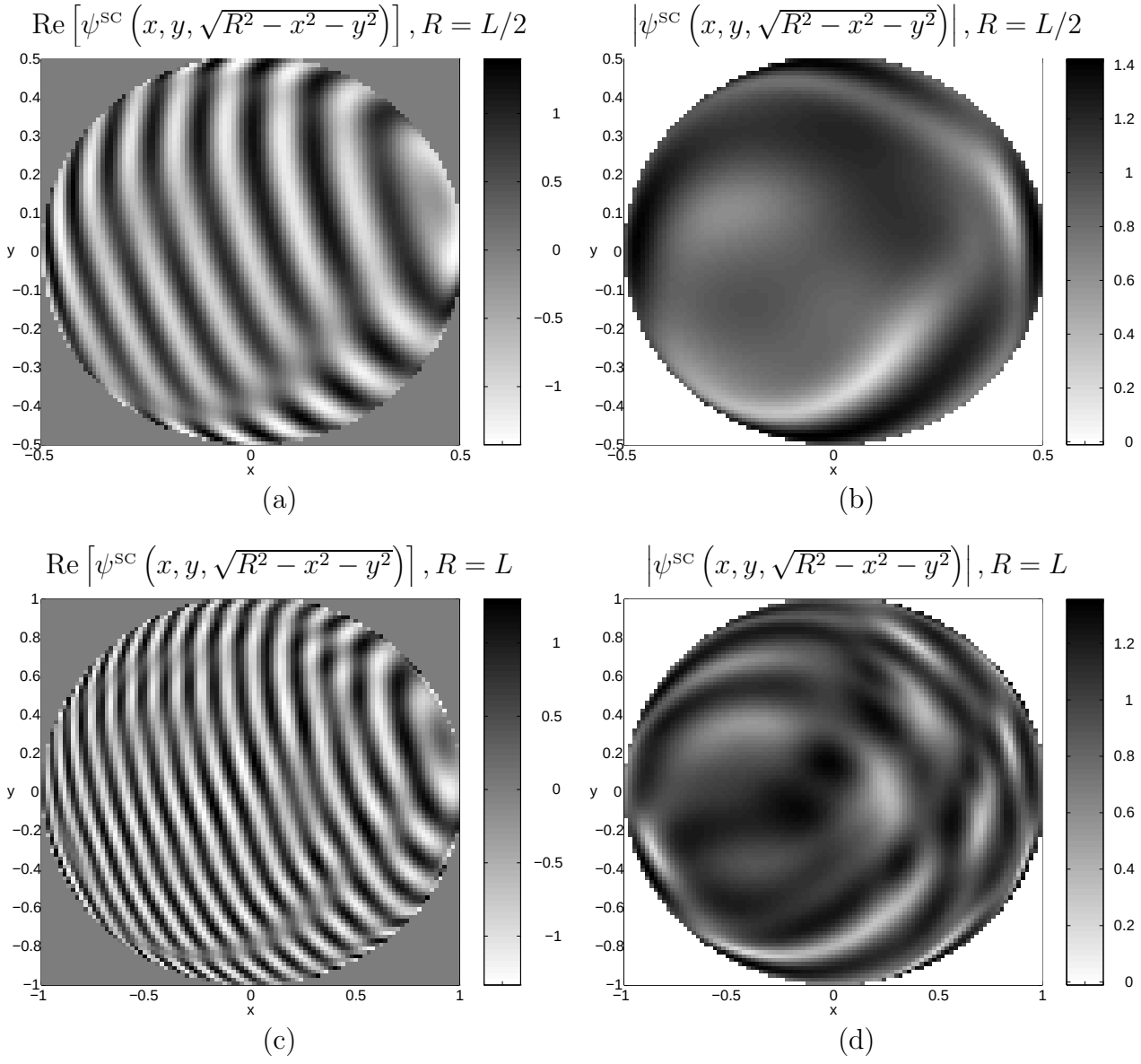

Figure 10: Example 1, Case B for the Dirichlet problem and a matrix size of 729×729. The real part and magnitude of the scattered field plotted on a hemisphere of radius $R = L/2$ in (a) and (b), and radius $R = L$ in (c) and (d). Here $L = L_1 = L_2$ and the resolution is 100×100.

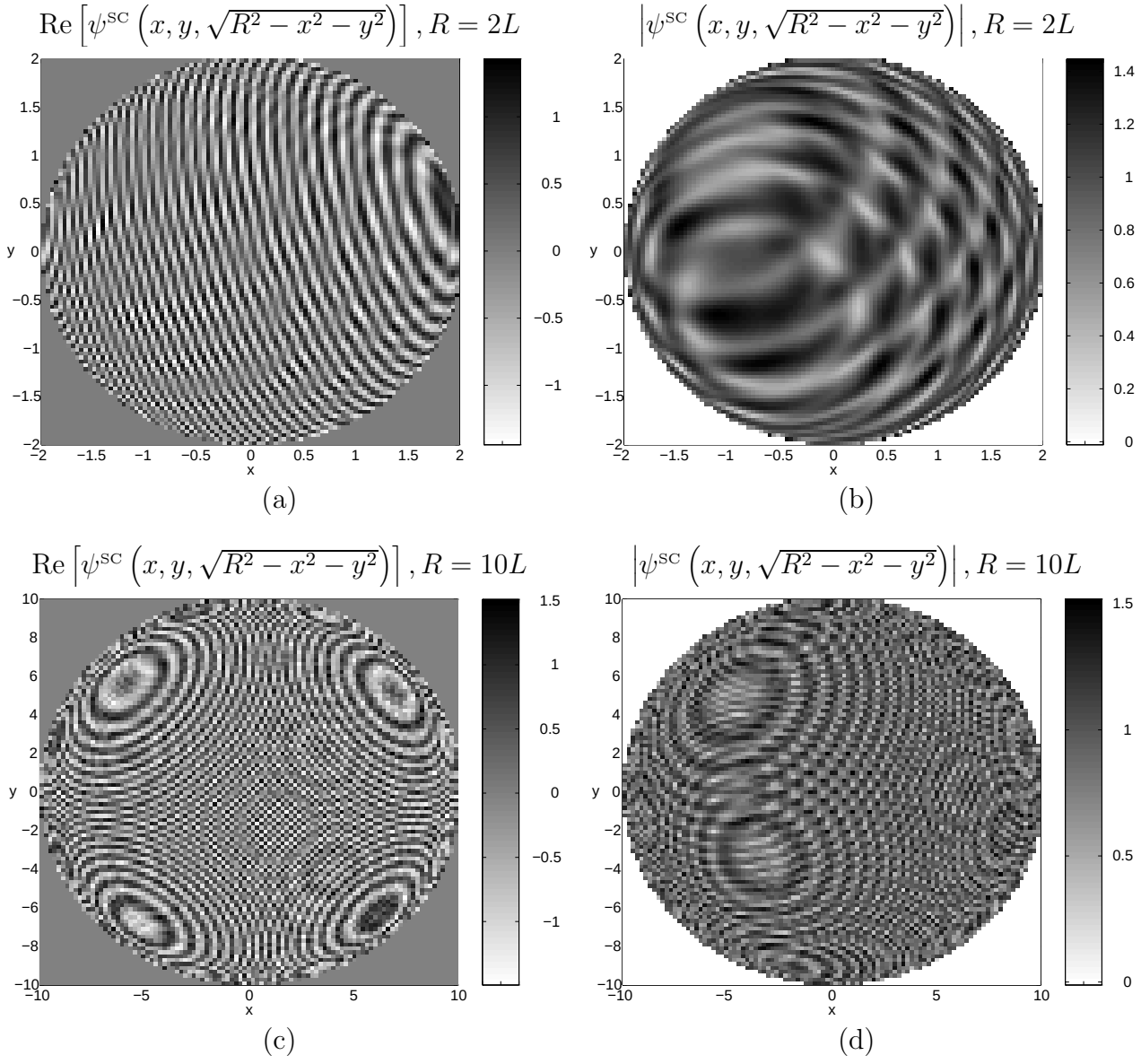

Figure 11: Example 1, Case B for the Dirichlet problem and a matrix size of 729×729. The real part and magnitude of the scattered field plotted on a hemisphere of radius $R = 2L$ in (a) and (b), and radius $R = 10L$ in (c) and (d). Here $L = L_1 = L_2$ and the resolution is 100×100.

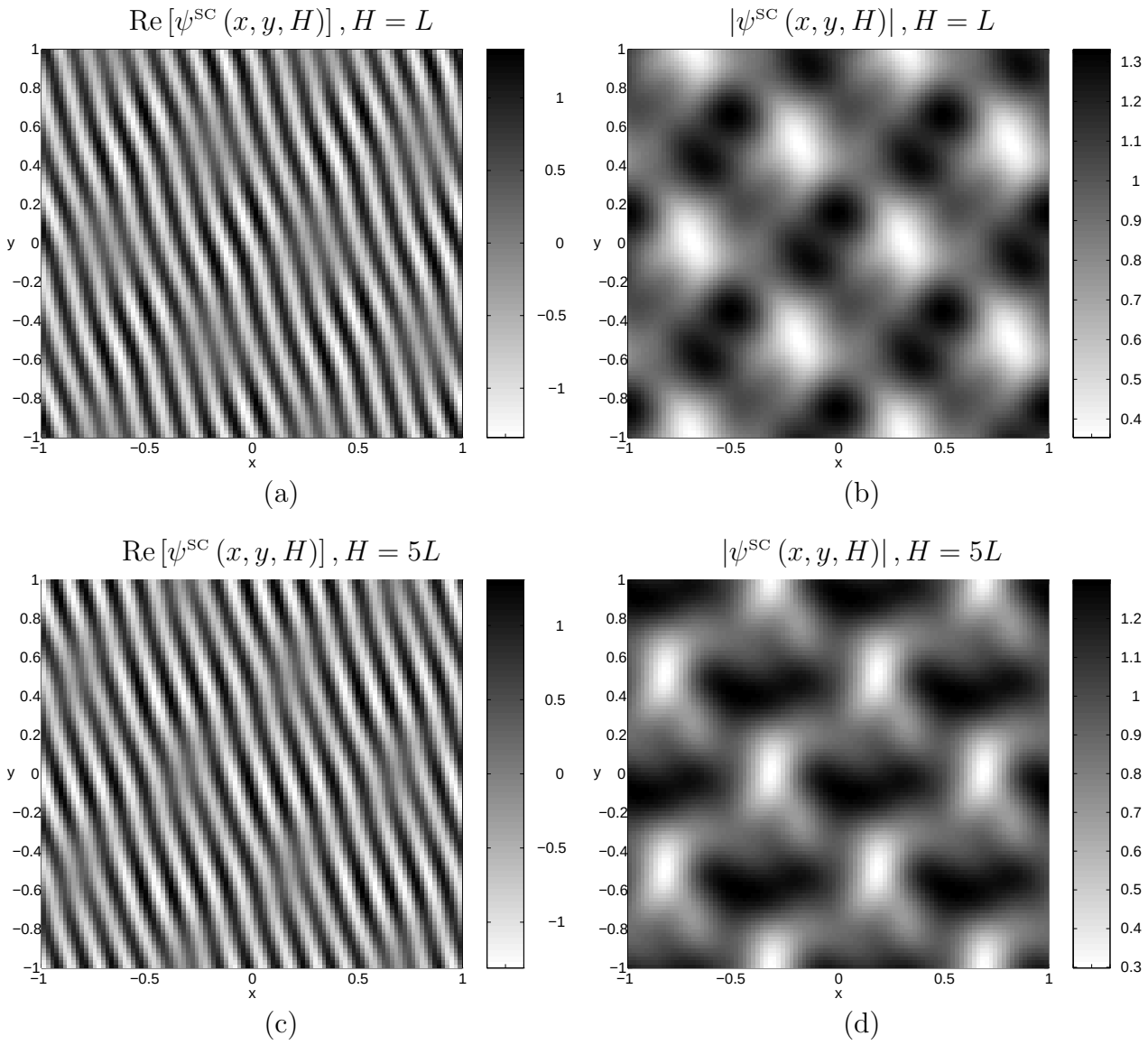

Figure 12: Example 1, Case B for the Dirichlet problem and a matrix size of 729×729. Real part and magnitude of the scattered field plotted on horizontal planes a distance $H = L$ above the surface in (a) and (b), and $H = 5L$ above the surface in (c) and (d). Again $L = L_1 = L_2$, with resolution 100×100. The plots hardly change. Compare with Fig. 6.

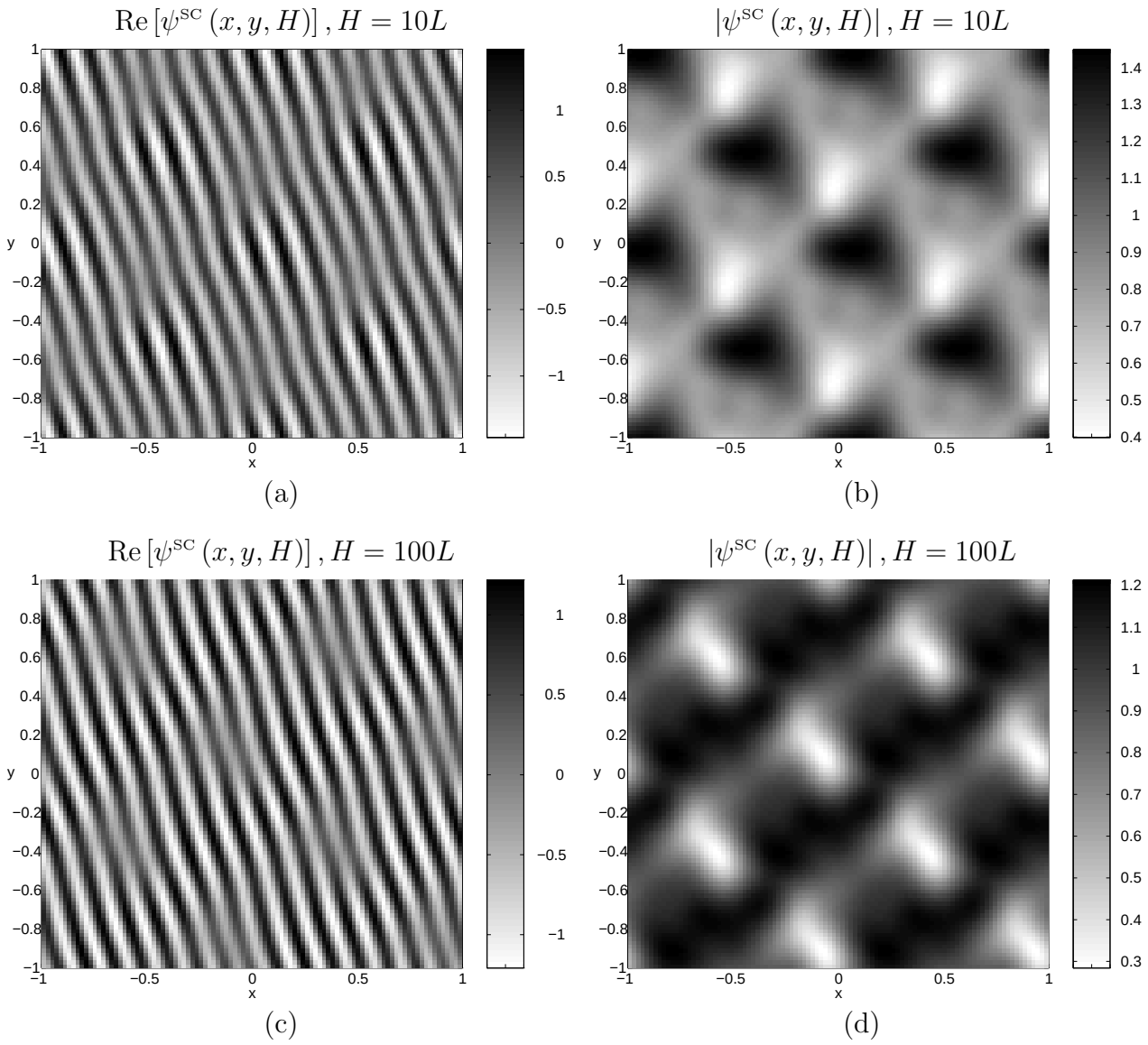

Figure 13: Example 1, Case B for the Dirichlet problem and a matrix size of 729×729. Real part and magnitude of the scattered field plotted on horizontal planes a distance $H = 10L$ above the surface in (a) and (b), and $H = 100L$ above the surface in (c) and (d). Again $L = L_1 = L_2$, with resolution 100×100. The plots hardly change. Compare with Fig. 7.

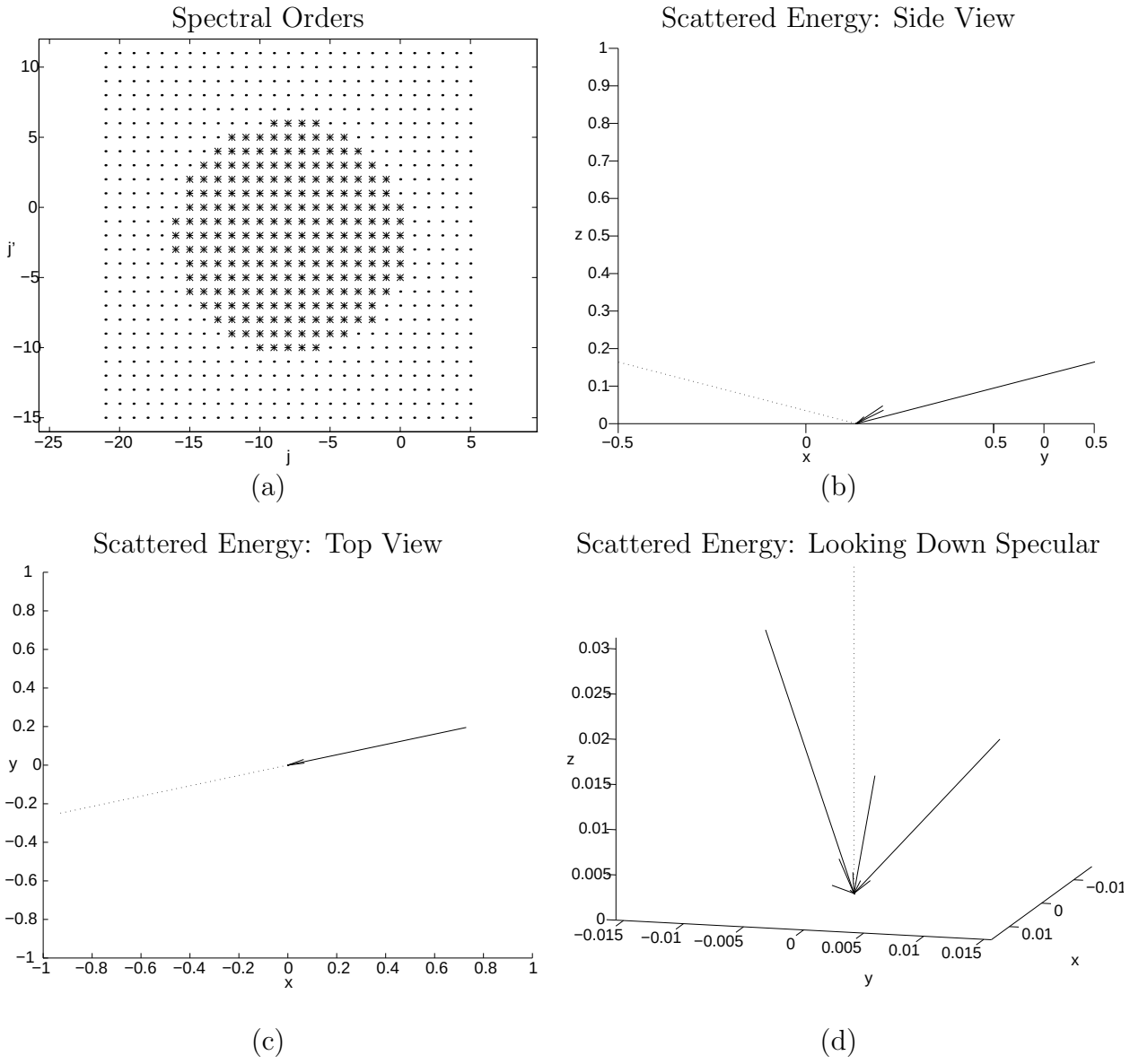

Figure 14: Example 1, Case B for the Dirichlet problem and a matrix size of 729×729. (a) Spectral orders with 27 samples in j and j'; star refers to radiating modes, dots to non-radiating modes. Scattered energy distribution viewed from (b) $\theta = 10°, \phi = -20°$, (c) $\theta = 0°, \phi = -90°$ and (d) $\theta = 20°, \phi = 15°$. Dashed line is incident field, solid lines are scattered Bragg modes. The magnitudes of the lines are proportional to the energy.

17.3 Example 2 Case A, No Grazing

$S(x,y)$	$-(d/2)\cos(2\pi x/L_1)\cos(2\pi y/L_2)$
(L_1, L_2)	(1,1)
$(d/L_1, d/L_2)$	(.25,.25)
$(\lambda/L_1, \lambda/L_2)$	(.95,.95)
Radiating Orders	3
θ^i	20°
ϕ^i	15°

Matrix Size	Number of Samples: Coord. x	Coord. y	Spectral j	Spectral j'	$\lambda/\Delta x$	$\lambda/\Delta y$	Fill Time (s)	Linear Solution Time (s)	Condition Number	Error
4×4	2	2	2	2	1.9000	1.9000	0.0200	0.0100	1.0000	< -15.9
16×16	4	4	4	4	3.8000	3.8000	0.0800	0.0100	4.0760	-15.6536
36×36	6	6	6	6	5.7000	5.7000	0.2000	0.0300	30.9213	-15.1764
64×64	8	8	8	8	7.6000	7.6000	0.4100	0.1200	246.8125	-14.8754
100×100	10	10	10	10	9.5000	9.5000	0.7100	0.3300	$1.9495 \cdot 10^3$	< -15.9
144×144	12	12	12	12	11.4000	11.4000	1.1900	0.8400	$1.5440 \cdot 10^4$	-15.1764
196×196	14	14	14	14	13.3000	13.3000	1.9400	2.0600	$1.2364 \cdot 10^5$	-14.5074
256×256	16	16	16	16	15.2000	15.2000	2.9400	4.3100	$1.0023 \cdot 10^6$	-14.0515
324×324	18	18	18	18	17.1000	17.1000	4.3200	8.1000	$8.2295 \cdot 10^6$	-13.9212
400×400	20	20	20	20	19.0000	19.0000	6.7100	15.4300	$6.8267 \cdot 10^7$	-13.8977
484×484	22	22	22	22	20.9000	20.9000	8.7200	26.8900	$5.7220 \cdot 10^8$	-12.8754

Table 7: Parameters and computational results for the Dirichlet problem, Example 2, Case B. Angle parameters are chosen to avoid grazing incidence and reflection. Only square systems were considered. The table is mostly self-explanatory with additional definitions in Section 16. The wavelength λ is comparable to the two equal periods. Note that the surface is much rougher than in Example 1 and the convergence is better (see Table 3).

Matrix Size	Number of Samples: Coord. x	Coord. y	Spectral j	Spectral j'	$\lambda/\Delta x$	$\lambda/\Delta y$	Fill Time (s)	Linear Solution Time (s)	Condition Number	Error
4×16	4	4	2	2	3.8000	3.8000	0.0200	0.0100	1.2248	-0.3984
16×36	6	6	4	4	5.7000	5.7000	0.0800	0.0700	2.9395	-1.1017
16×64	8	8	4	4	7.6000	7.6000	0.0900	0.1500	3.0644	-1.1116
36×64	8	8	6	6	7.6000	7.6000	0.2100	0.5500	9.5595	-1.8423
36×144	12	12	6	6	11.4000	11.4000	0.2800	1.3000	9.5955	-1.7480
16×4	2	2	4	4	1.9000	1.9000	0.0600	0.0100	1.0000	-0.0280
36×16	4	4	6	6	3.8000	3.8000	0.1700	0.0500	7.9633	-0.5672
36×25	5	5	6	6	4.7500	4.7500	0.1800	0.1100	29.9996	-1.5526
100×64	8	8	10	10	7.6000	7.6000	0.5800	2.0800	627.2538	-0.9794
144×100	10	10	12	12	9.5000	9.5000	0.9600	4.8400	$5.0441 \cdot 10^3$	-1.0740

Table 8: Parameters and computational results for the Dirichlet problem, Example 2, Case A. Angle parameters are chosen to avoid grazing incidence and reflection. Only non-square systems are included by using additional coordinate sampling. The convergence results are quite poor for the non-square systems considered.

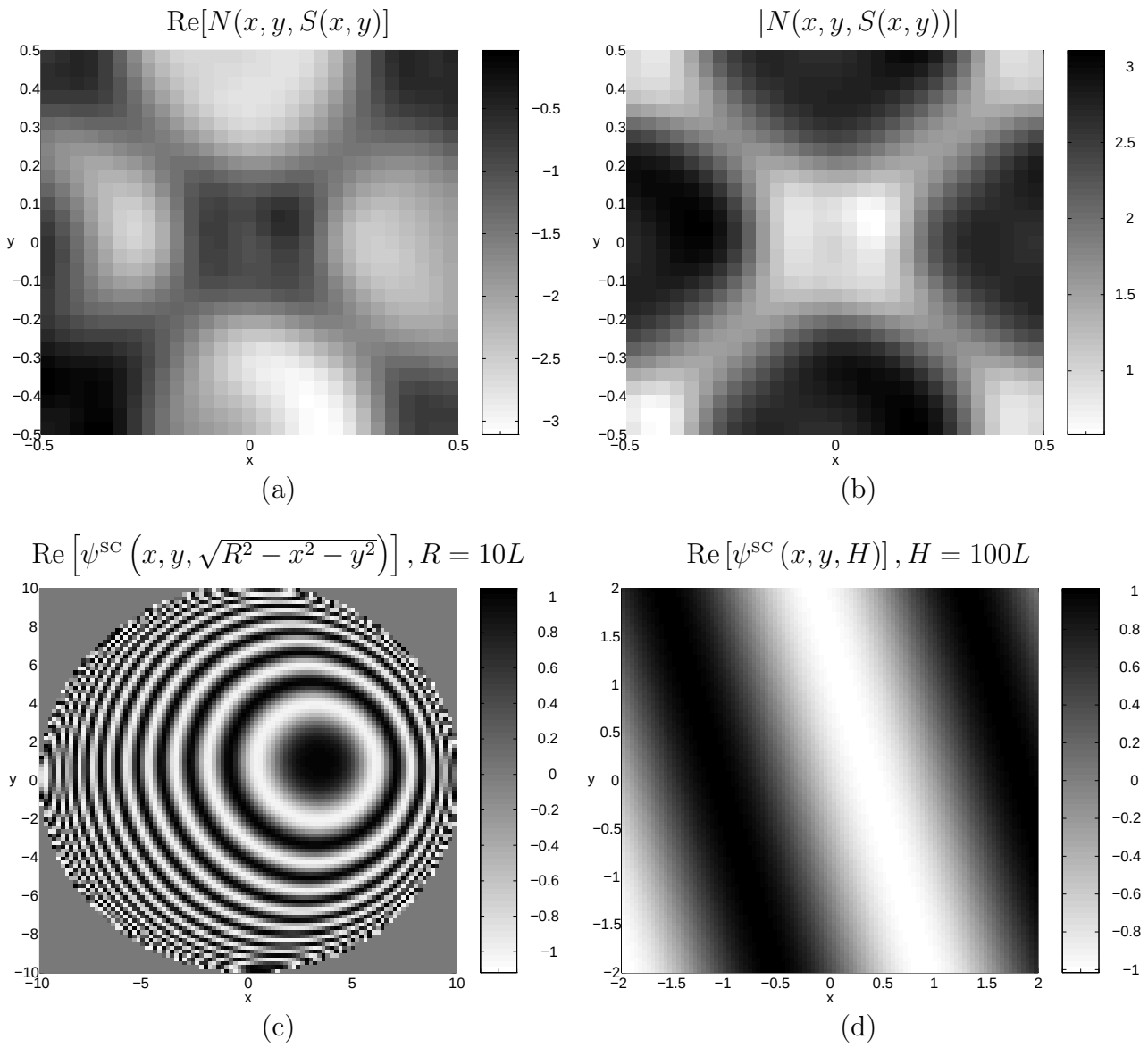

Figure 15: Example 2, Case A for the Dirichlet problem. Real part (a) and magnitude (b) of the surface current N, matrix size 36×900 with an error of -1.7498. and the real part of the scattered field in (c) and (d) for a matrix size 484×484, plotted on a hemisphere of radius $R = 10L$ (where $L = L_1 = L_2$) looking down from above and on a plane (d) a distance $H = 100L$ above the surface. The resolution is 100×100. The 900 size of the coordinate sampling was to get higher resolution in these pictures (30×30 pixels).

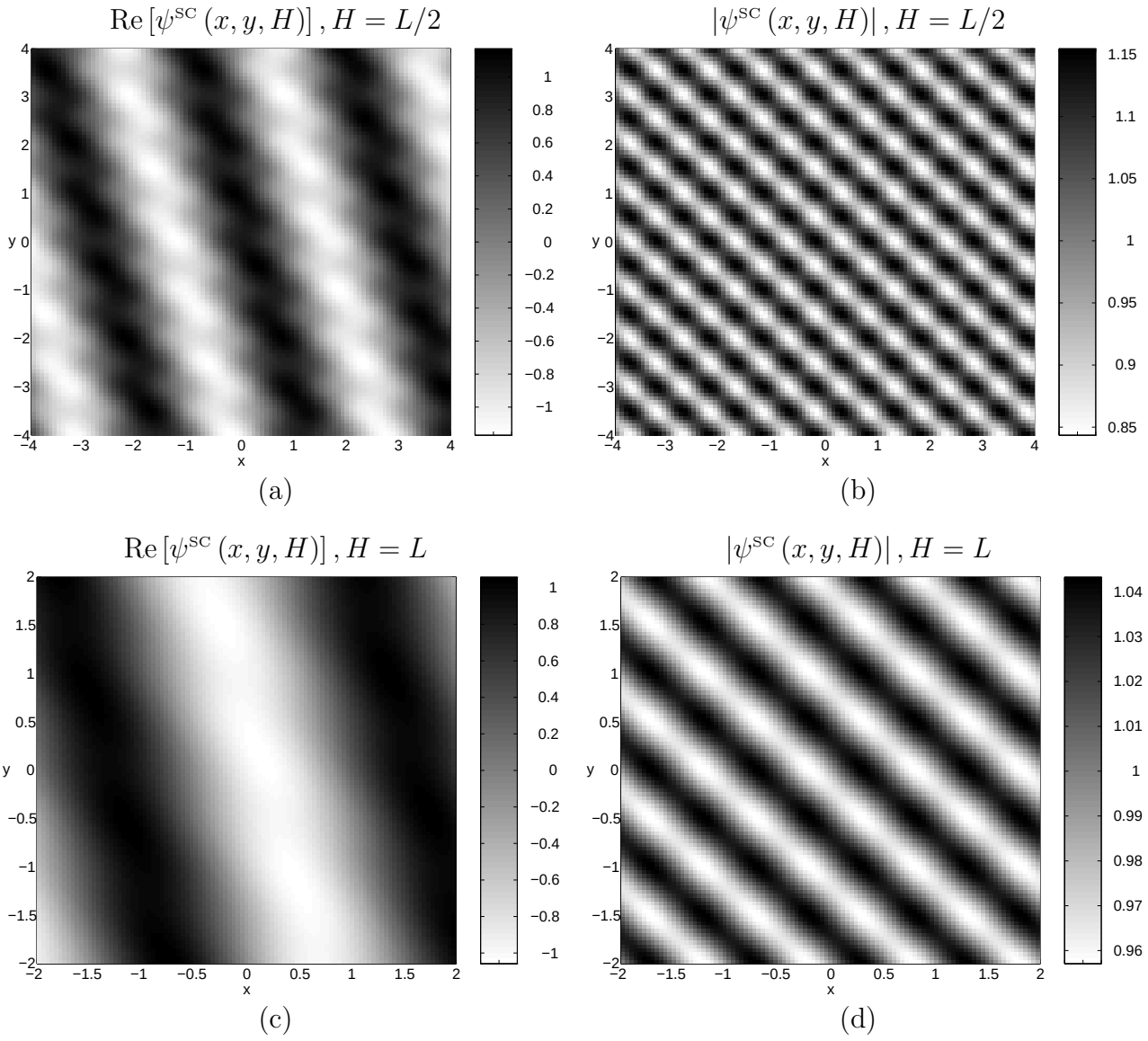

Figure 16: Example 2, Case A for the Dirichlet problem and a matrix size of 484×484. Real part ((a) and (c)) and magnitudes ((b) and (d)) of the scattered field plotted on a horizontal plane a distance $H = L/2$ ((a) and (b)) and $H = L$ ((c) and (d)) above the surface. Again, $L = L_1 = L_2$. In (a) and (b) the width of the plane is $8L$ and in (c) and (d) the width is $4L$.

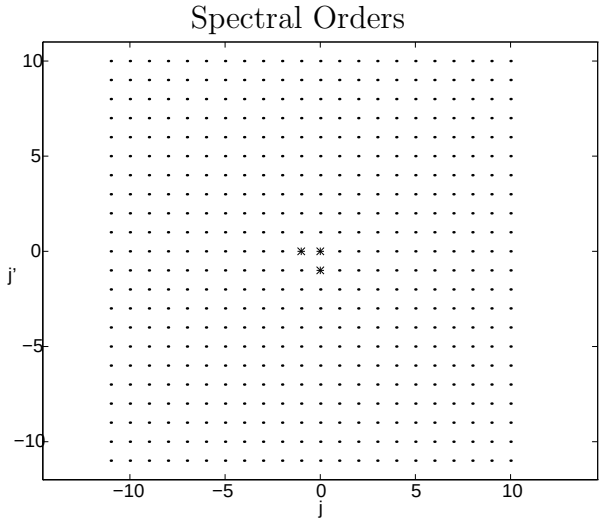

(a)

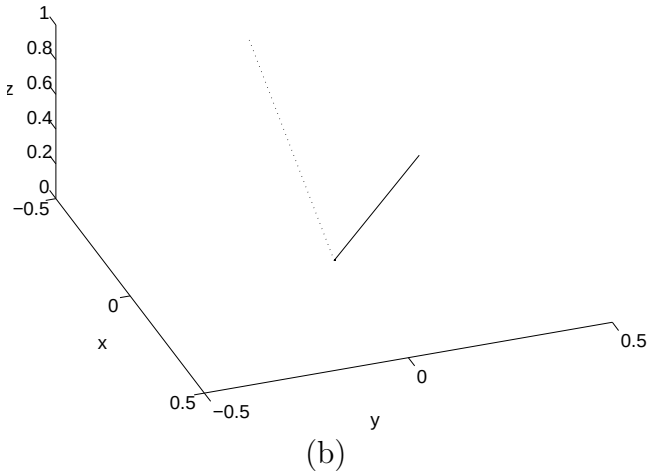

(b)

Figure 17: Example 2, Case A for the Dirichlet problem with a matrix size of 484×484. (a) Spectral orders with 22 samples in j and j'; stars refer to radiating modes, and dots to non-radiating modes. (b) Scattered energy distribution viewed from $\theta = 40°, \phi = -20°$. Dashed line is incident field, solid lines are scattered Bragg modes. The magnitudes of the lines are proportional to the energy.

17.4 Example 2 Case B, Near-Grazing Incidence/Reflection

$S(x,y)$	$-(d/2)\cos(2\pi x/L_1)\cos(2\pi y/L_2)$
(L_1, L_2)	(1,1)
$(d/L_1, d/L_2)$	(.25,.25)
$(\lambda/L_1, \lambda/L_2)$	(.95,.95)
Radiating Orders	4
θ^i	75°
ϕ^i	15°

Matrix Size	Number of Samples: Coord. x	Coord. y	Spectral j	Spectral j'	$\lambda/\Delta x$	$\lambda/\Delta y$	Fill Time (s)	Linear Solution Time (s)	Condition Number	Error
6×6	3	2	3	2	2.8500	1.9000	0.0300	0.0100	1.0000	< -15.9
16×16	4	4	4	4	3.8000	3.8000	0.0700	0.0100	4.3221	-2.8789
36×36	6	6	6	6	5.7000	5.7000	0.1800	0.0300	32.4522	-3.5466
64×64	8	8	8	8	7.6000	7.6000	0.3600	0.1100	258.9573	-3.7416
100×100	10	10	10	10	9.5000	9.5000	0.6600	0.2900	$2.0444 \cdot 10^3$	-3.8465
144×144	12	12	12	12	11.4000	11.4000	1.1100	0.8200	$1.6185 \cdot 10^4$	-3.8987
196×196	14	14	14	14	13.3000	13.3000	1.7500	1.8200	$1.2956 \cdot 10^5$	-3.8942
256×256	16	16	16	16	15.2000	15.2000	2.7700	3.9000	$1.0499 \cdot 10^6$	-3.8663
324×324	18	18	18	18	17.1000	17.1000	4.0700	7.8900	$8.6189 \cdot 10^6$	-3.7994
400×400	20	20	20	20	19.0000	19.0000	5.8500	13.7300	$7.1485 \cdot 10^7$	-3.7253
484×484	22	22	22	22	20.9000	20.9000	8.2900	23.8900	$5.9908 \cdot 10^8$	-3.6150

Table 9: Parameters and computational results for the Dirichlet problem, Example 2, Case B. Angle parameters were chosen so that near-grazing incidence and reflection occurred. Only square systems were considered. Note that although in principle there are 6 possible combinations of j and j' values which radiate, only four modes in fact radiate. The wavelength λ was approximately equal to the two (equal) periods. Convergence was still very good but nowhere near as good as when grazing was avoided (compare with Table 7).

Matrix Size	Number of Samples: Coord. x	Coord. y	Spectral j	Spectral j'	$\lambda/\Delta x$	$\lambda/\Delta y$	Fill Time (s)	Linear Solution Time (s)	Condition Number	Error
6×16	4	4	3	2	3.8000	3.8000	0.0300	0.0200	1.3892	-1.4403
16×36	6	6	4	4	5.7000	5.7000	0.0900	0.0700	3.2232	-2.0552
16×64	8	8	4	4	7.6000	7.6000	0.1200	0.1700	3.3733	-2.0159
36×64	8	8	6	6	7.6000	7.6000	0.2200	0.6600	10.4975	-2.5849
36×144	12	12	6	6	11.4000	11.4000	0.3000	1.4700	10.7216	-2.4863
16×4	2	2	4	4	1.9000	1.9000	0.0700	0.0100	1.0000	-0.2149
36×16	4	4	6	6	3.8000	3.8000	0.1600	0.0500	8.3064	-0.9023
36×25	5	5	6	6	4.7500	4.7500	0.1800	0.1200	30.7104	-1.8978
100×64	8	8	10	10	7.6000	7.6000	0.5700	2.0500	648.6537	-1.5177
144×100	10	10	12	12	9.5000	9.5000	0.9500	4.9000	$5.2162 \cdot 10^3$	-1.6022

Table 10: Parameters and computational results for the Dirichlet problem, Example 2, Case B. Angle parameters were chosen so that near-grazing incidence and reflection occurred. Only non-square systems were considered. Note that although in principle there are 6 possible combinations of j and j' values which radiate, only four modes in fact radiate. Convergence was not as good as for the square systems in Table 9.

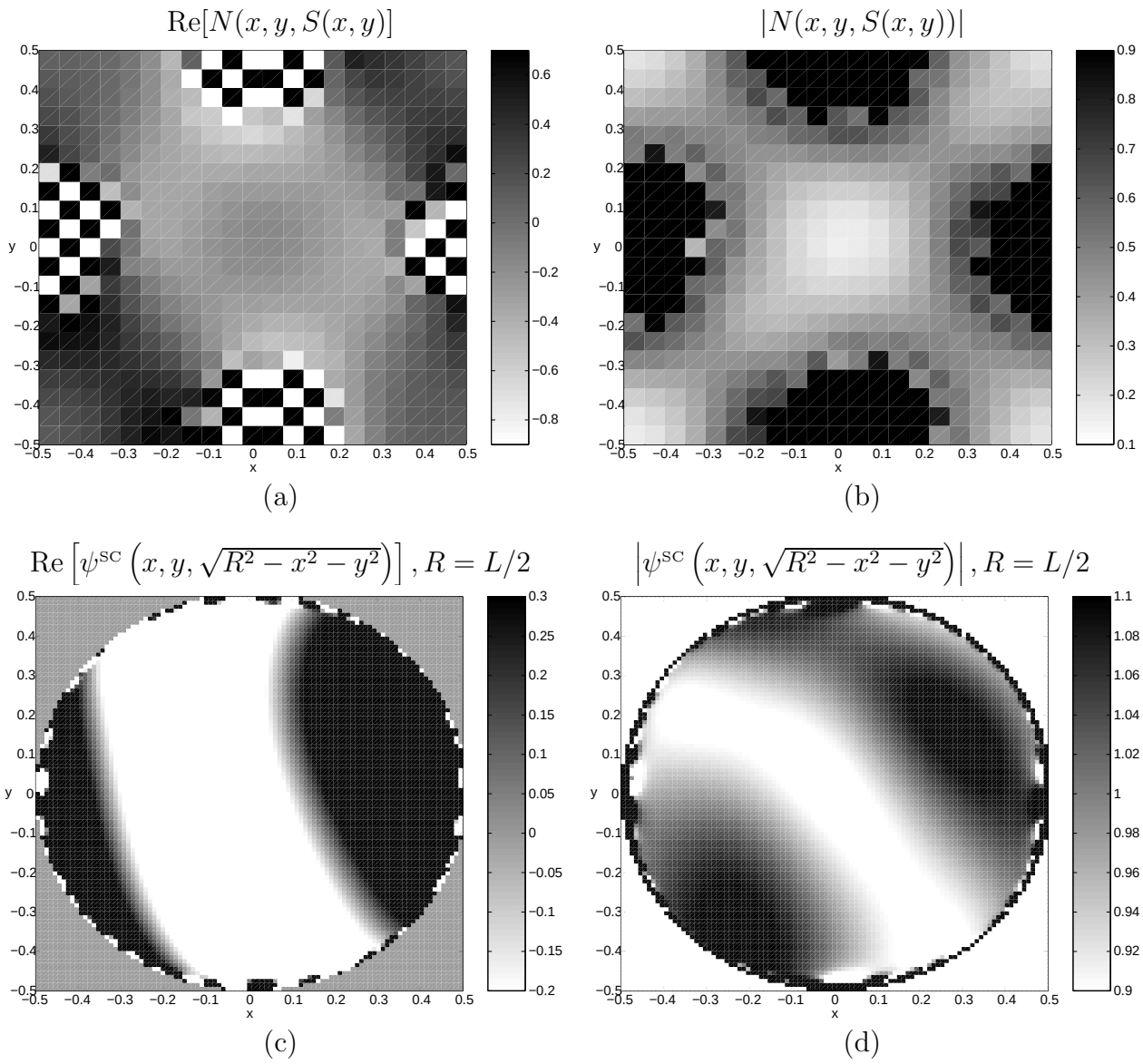

Figure 18: Example 2, Case B for the Dirichlet problem. Real part (a) and magnitude (b) of the surface current or normal derivative N generated with a matrix of size 484×484. Real part (c) and magnitude (d) of the scattered field plotted on a hemisphere of radius $R = L/2$ ($L = L_1 = L_2$) with a matrix of size 484×484 and resolution 100×100. Structure in the scattered field only becomes visible at larger radii (see Fig. 19).

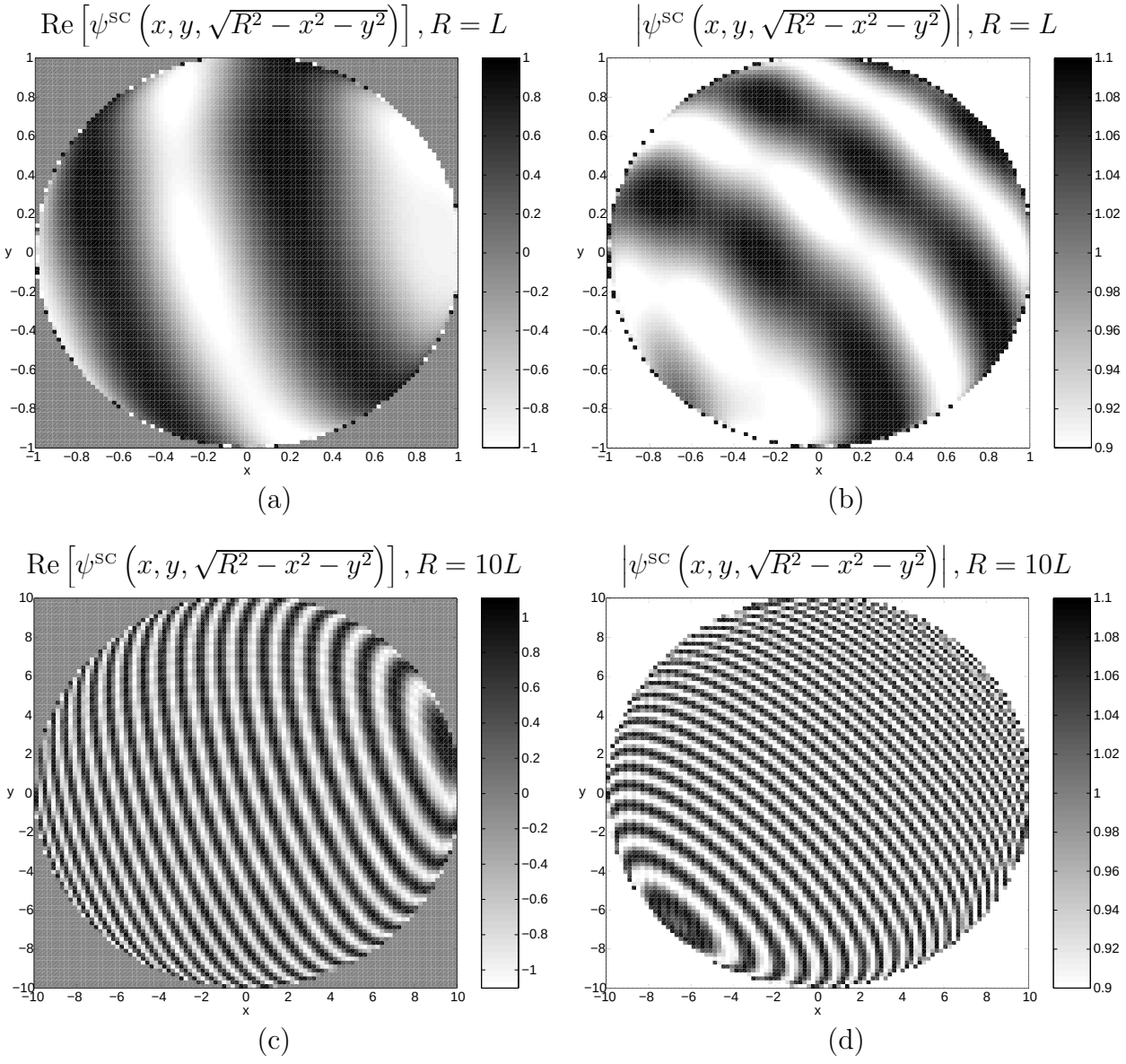

Figure 19: Example 2, Case B for the Dirichlet problem with a matrix size of 484×484. Real part ((a) and (c)) and magnitude ((b) and (d)) of the scattered field plotted on hemispheres of radius $R = L$ ((a) and (b)) and $R = 10L$ ((c) and (d)) where $L = L_1 = L_2$. The resolution is 100×100.

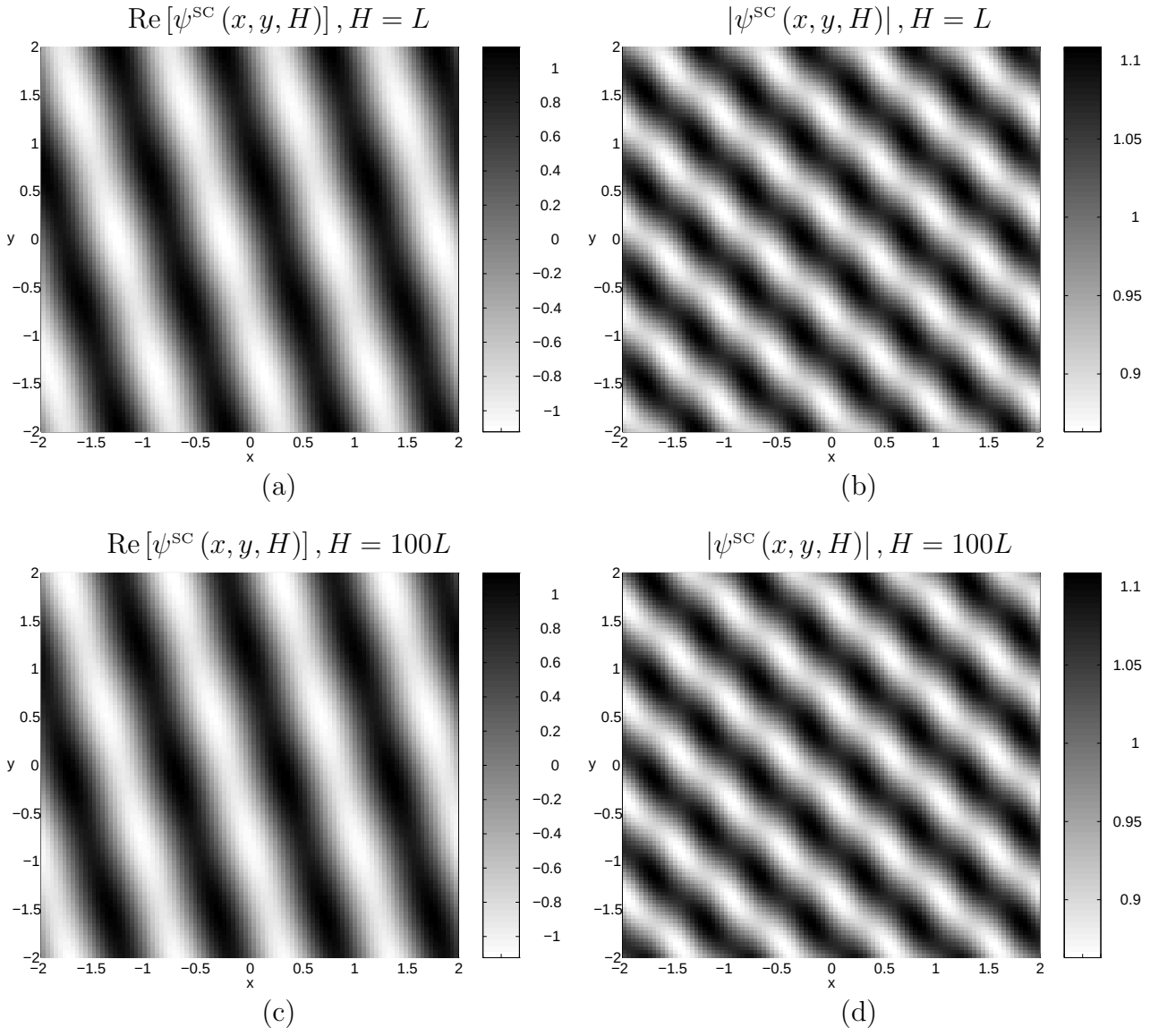

Figure 20: Example 2, Case B for the Dirichlet problem with a matrix size of 484×484. Real part ((a) and (c)) and magnitude ((b) and (d)) of the scattered field plotted on a horizontal plane a distance $H = L$ above the surface in (a) and (b), and $H = 100L$ above the surface in (c) and (d). Here $L = L_1 = L_2$ and the resolution is 100×100. The width of the plane is $4L$ for all plots.

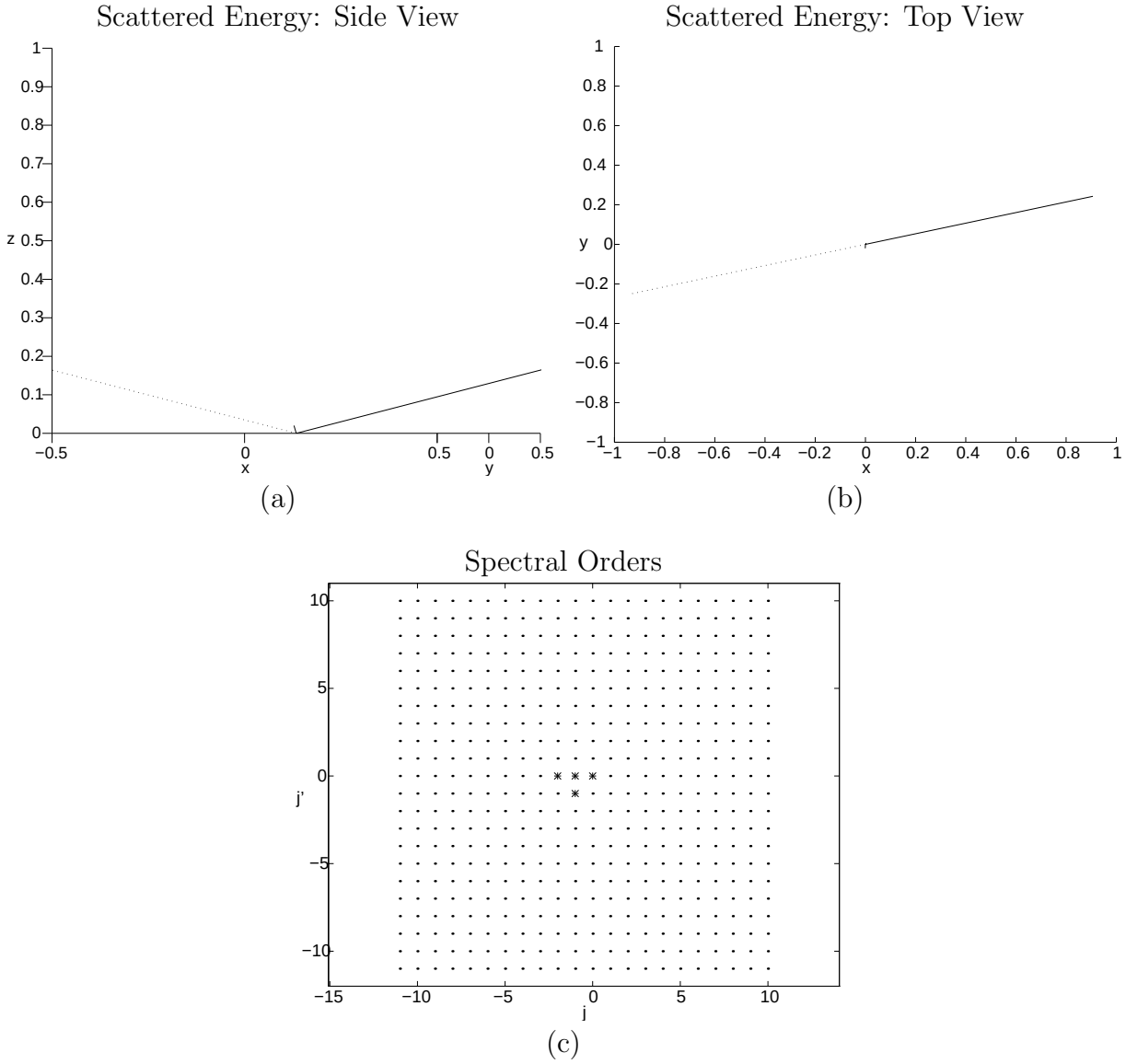

Figure 21: Example 2, Case B for the Dirichlet problem. Scattered energy distribution viewed from (a) $\theta = 90°, \phi = -75°$ and (b) $\theta = 0°, \phi = -90°$. Dashed line is incident field, solid lines are scattered Bragg modes. The magnitudes of the lines are proportional to the energy. (c) Spectral Orders with 22 samples in j and j'; stars refer to radiating modes, and dots to non-radiating modes illustrating the four real Bragg modes.

17.5 Example 3 Case A, No Grazing

$S(x,y)$	$-(d/2)\cos(2\pi x/L_1)\cos(2\pi y/L_2)$
(L_1, L_2)	(1,1)
$(d/L_1, d/L_2)$	(2.5,2.5)
$(\lambda/L_1, \lambda/L_2)$	(100,100)
Radiating Orders	1
θ^i	20°
ϕ^i	15°

Matrix Size	Number of Samples Coord. x	Coord. y	Spectral j	Spectral j'	$\lambda/\Delta x$	$\lambda/\Delta y$	Fill Time (s)	Linear Solution Time (s)	Condition Number	Error
1×1	1	1	1	1	100	100	0.0100	0.0100	1.0000	-15.6536
4×4	2	2	2	2	200	200	0.0100	0.0100	1.0000	< -15.9
9×9	3	3	3	3	300	300	0.0400	0.0100	$3.9291 \cdot 10^{6}$	-15.6536
16×16	4	4	4	4	400	400	0.0800	0.0100	$3.1261 \cdot 10^{8}$	-15.3525
25×25	5	5	5	5	500	500	0.1200	0.0100	$3.8499 \cdot 10^{13}$	-15.6536
36×36	6	6	6	6	600	600	0.1900	0.0200	$6.7856 \cdot 10^{17}$	-12.8255
49×49	7	7	7	7	700	700	0.2700	0.0600	$2.1576 \cdot 10^{20}$	-15.6536
64×64	8	8	8	8	800	800	0.3800	0.0900	$8.2161 \cdot 10^{22}$	-15.3525
81×81	9	9	9	9	900	900	0.5000	0.1700	$4.2876 \cdot 10^{27}$	-15.1764
100×100	10	10	10	10	1000	1000	0.6600	0.3000	$2.2935 \cdot 10^{31}$	-14.3313
121×121	11	11	11	11	1100	1100	0.8800	0.5000	$4.7088 \cdot 10^{33}$	-12.1127

Table 11: Parameters and computational results for the Dirichlet problem, Example 3, Case A. Angle parameters were chosen to avoid grazing incidence and reflection. Only square systems were considered. The wavelength λ is much greater than either of the (equal) surface periods and only one radiating mode exists. The errors were extremely small even for very large condition numbers.

Matrix Size	Number of Samples: Coord. x	Coord. y	Spectral j	Spectral j'	$\lambda/\Delta x$	$\lambda/\Delta y$	Fill Time (s)	Linear Solution Time (s)	Condition Number	Error
1×4	2	2	1	1	200	200	0.0100	$< 10^{-3}$	1.0000	-15.3525
1×9	3	3	1	1	300	300	0.0100	$< 10^{-3}$	1.0000	-2.2649
25×36	6	6	5	5	600	600	0.1300	0.1100	$2.0992 \cdot 10^{10}$	-7.6275
25×49	7	7	5	5	700	700	0.1400	0.1500	$9.6463 \cdot 10^{9}$	-2.7063
49×81	9	9	7	7	900	900	0.3100	0.7000	$4.9957 \cdot 10^{15}$	$-1.9556 \cdot 10^{-5}$
9×4	2	2	3	3	200	200	0.0400	$< 10^{-3}$	2.0000	-15.3525
49×16	4	4	7	7	400	400	0.2200	0.0500	$5.6658 \cdot 10^{10}$	-4.5227
81×16	4	4	9	9	400	400	0.3900	0.0700	$2.8913 \cdot 10^{13}$	-4.5227
121×16	4	4	11	11	400	400	0.5700	0.1000	$3.6543 \cdot 10^{15}$	-4.5224
169×16	4	4	13	13	400	400	0.7800	0.1400	$4.0784 \cdot 10^{17}$	$< 10^{-6}$

Table 12: Parameters and computational results for the Dirichlet problem, Example 3, Case A. Angle parameters were chosen to avoid grazing incidence and reflection. Only non-square systems were considered. The wavelength λ is much greater than either of the (equal) surface periods and only one radiating mode exists. The errors were small but not nearly as small as for the square systems in Table 11.

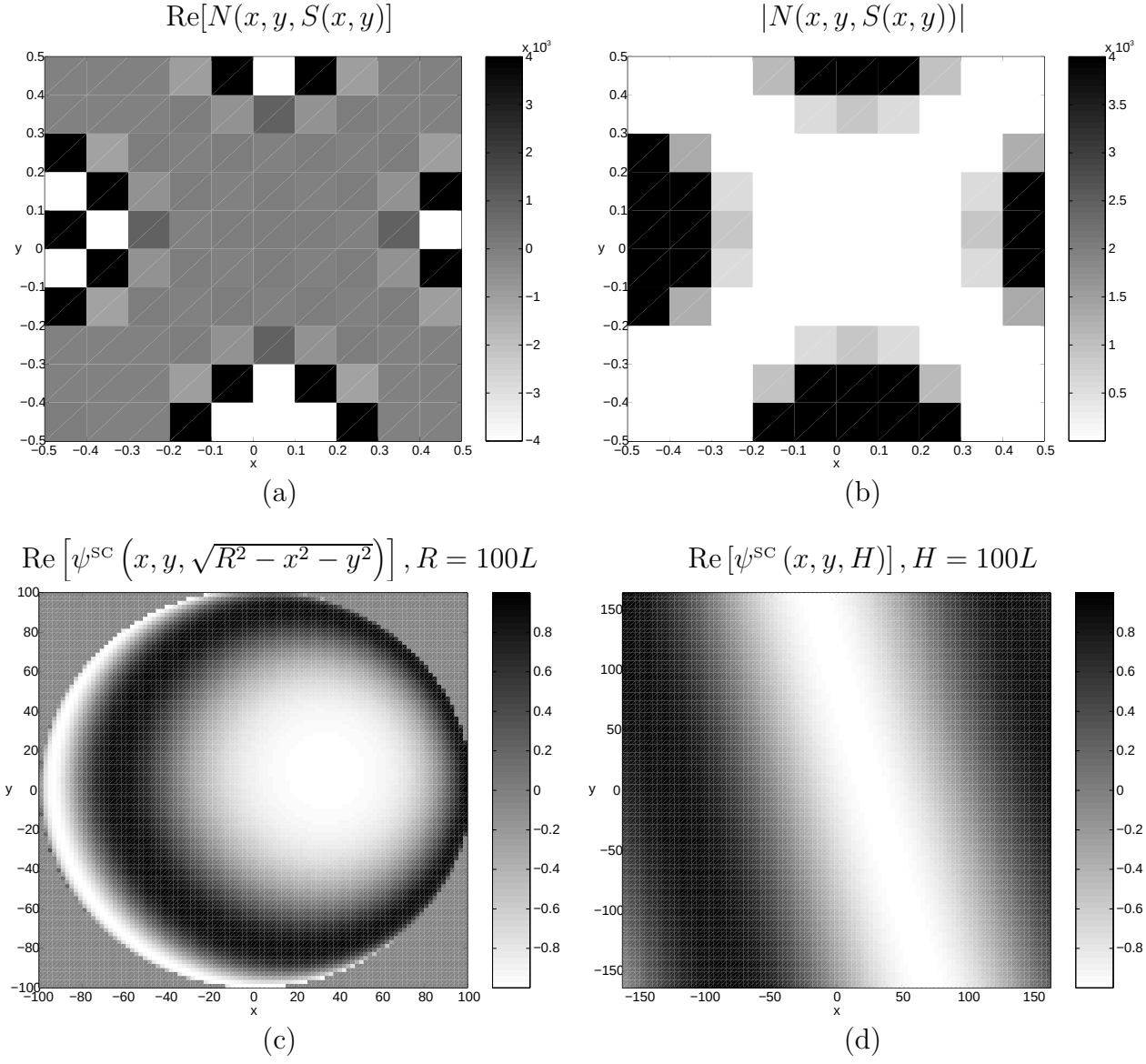

Figure 22: Example 3, Case A for the Dirichlet problem. Real part (a) and magnitude (b) of the surface current or normal derivative N generated with a matrix size of 121×121. Real part of the scattered field plotted on a hemisphere (c) of radius $R = 100L$ and on a plane (d) at height $H = 100L$ above the surface. Here $L = L_1 = L_2$. In (c) and (d) the matrix size was 121×121 and the images have a resolution of 100×100.

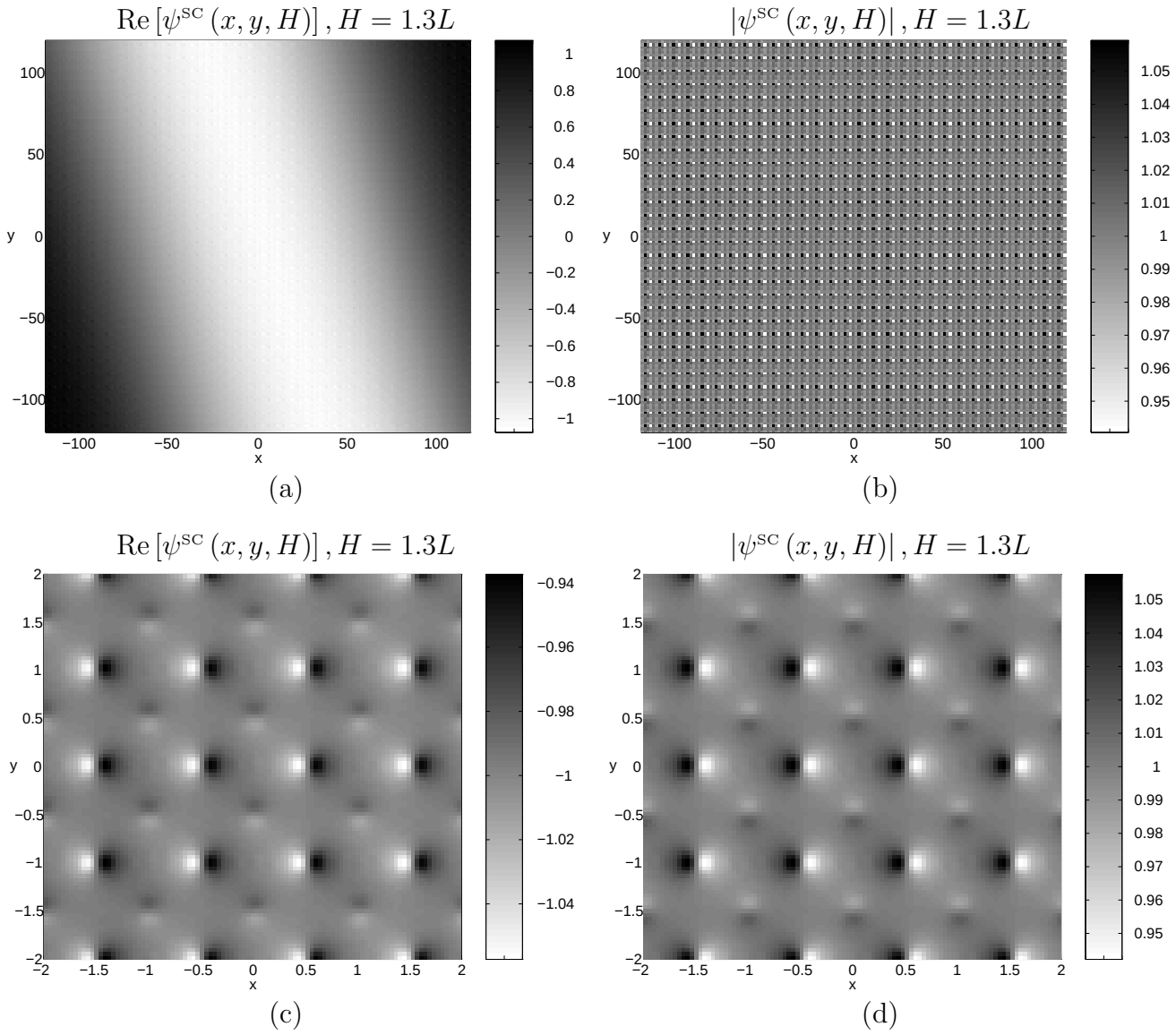

Figure 23: Example 3, Case A for the Dirichlet problem with a matrix size of 121×121. Real part ((a) and (c)) and magnitudes ((b) and (d)) of the scattered field plotted on a plane at distance $H = 1.3L$ above the surface. Here $L = L_1 = L_2$. Parts (c) and (d) are zoomed-in images of (a) and (b), respectively. Parts (a) and (b) have resolution 150×150 and parts (c) and (d) have resolution 100×100.

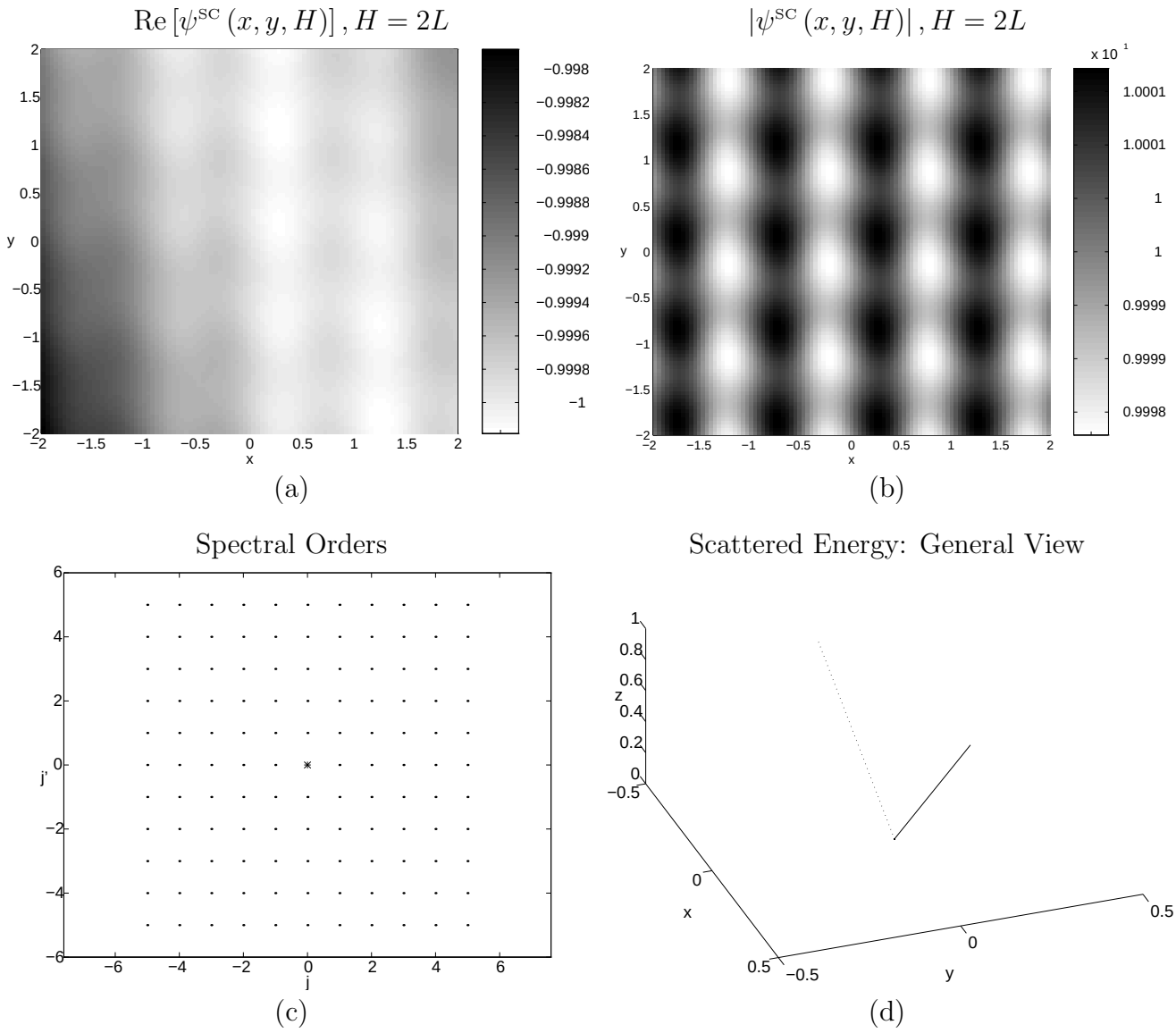

Figure 24: Example 3, Case A for the Dirichlet problem with a matrix size of 121×121. Real part (a) and magnitude (b) of the scattered field plotted on a plane at distance $H = 2L$ above the surface. Here $L = L_1 = L_2$ and the resolution is 100×100. Note the darkness scale in both cases. (c) Spectral orders with 11 samples in j and j'; stars refer to radiating modes and dots to non-radiating modes. (d) Scattered energy distribution viewed from $\theta = 40°, \phi = -20°$. Dashed line is incident field, solid lines are scattered Bragg modes. The magnitudes of the lines are proportional to the energy.

17.6 Example 3 Case B, Near-Grazing Incidence/Reflection

$S(x,y)$	$-(d/2)\cos(2\pi x/L_1)\cos(2\pi y/L_2)$
(L_1, L_2)	(1,1)
$(d/L_1, d/L_2)$	(2.5,2.5)
$(\lambda/L_1, \lambda/L_2)$	(100,100)
Radiating Orders	1
θ^i	75°
ϕ^i	15°

Matrix Size	Number of Samples: Coord. x	Coord. y	Spectral j	Spectral j'	$\lambda/\Delta x$	$\lambda/\Delta y$	Fill Time (s)	Linear Solution Time (s)	Condition Number	Error
1×1	1	1	1	1	100	100	0.0100	$< 10^{-3}$	1.0000	< -15.9
4×4	2	2	2	2	200	200	0.0200	$< 10^{-3}$	1.0000	< -15.9
9×9	3	3	3	3	300	300	0.0400	0.0100	$3.9429 \cdot 10^{6}$	-15.3525
16×16	4	4	4	4	400	400	0.0800	$< 10^{-3}$	$3.2356 \cdot 10^{8}$	-15.6536
25×25	5	5	5	5	500	500	0.1200	0.0100	$4.6186 \cdot 10^{13}$	< -15.9
36×36	6	6	6	6	600	600	0.1800	0.0300	$1.5418 \cdot 10^{18}$	-14.5744
49×49	7	7	7	7	700	700	0.2600	0.0500	$1.8373 \cdot 10^{20}$	-15.3525
64×64	8	8	8	8	800	800	0.3600	0.1000	$1.3722 \cdot 10^{23}$	-15.3525
81×81	9	9	9	9	900	900	0.5000	0.1700	$8.8589 \cdot 10^{27}$	-15.6536
100×100	10	10	10	10	1000	1000	0.6500	0.2900	$2.7528 \cdot 10^{31}$	-15.6536
121×121	11	11	11	11	1100	1100	0.8800	0.5200	$4.5615 \cdot 10^{33}$	-13.9376
144×144	12	12	12	12	1200	1200	1.1200	0.8000	$3.9242 \cdot 10^{37}$	-14.2064
169×169	13	13	13	13	1300	1300	1.4500	1.2700	$6.4054 \cdot 10^{39}$	-11.4572
196×196	14	14	14	14	1400	1400	1.7600	1.9500	$8.3684 \cdot 10^{43}$	-10.5530
225×225	15	15	15	15	1500	1500	2.2300	2.7300	$3.3895 \cdot 10^{46}$	-12.6747
256×256	16	16	16	16	1600	1600	2.7200	4.0700	$1.1279 \cdot 10^{50}$	-9.0324

Table 13: Parameters and computational results for the Dirichlet problem, Example 3, Case B. Angle parameters were chosen to include near-grazing incidence and reflection. Only square systems were considered. The wavelength λ is much greater than either of the (equal) surface periods and only one radiating mode exists. The errors were extremely small even for every large condition numbers.

Matrix Size	Number of Samples: Coord. x	Coord. y	Spectral j	Spectral j'	$\lambda/\Delta x$	$\lambda/\Delta y$	Fill Time (s)	Linear Solution Time (s)	Condition Number	Error
1×4	2	2	1	1	200	200	0.0100	0.0100	1.0000	-15.0515
1×9	3	3	1	1	300	300	0.0100	$< 10^{-3}$	1.0000	-3.3839
25×36	6	6	5	5	600	600	0.1300	0.1100	$2.1027 \cdot 10^{10}$	-7.8476
25×49	7	7	5	5	700	700	0.1400	0.1600	$9.6713 \cdot 10^{9}$	-3.8260
49×81	9	9	7	7	900	900	0.3100	0.7100	$5.0074 \cdot 10^{15}$	$-1.8815 \cdot 10^{-5}$
9×4	2	2	3	3	200	200	0.0300	0.0100	2.0000	-15.0515
49×16	4	4	7	7	400	400	0.2200	0.0600	$5.7839 \cdot 10^{10}$	-4.5233
81×16	4	4	9	9	400	400	0.3700	0.0700	$2.8914 \cdot 10^{13}$	-4.5233
121×16	4	4	11	11	400	400	0.5600	0.1100	$3.7704 \cdot 10^{15}$	-4.5220
169×16	4	4	13	13	400	400	0.7700	0.1400	$2.8722 \cdot 10^{17}$	$< 10^{-6}$

Table 14: Parameters and computational results for the Dirichlet problem, Example 3, Case B. Angle parameters were chosen to include near-grazing incidence and reflection. Only non-square systems were considered. The wavelength λ is much greater than either of the (equal) surface periods and only one radiating mode exists. The errors were generally small but not nearly as small as for the square systems in Table 13.

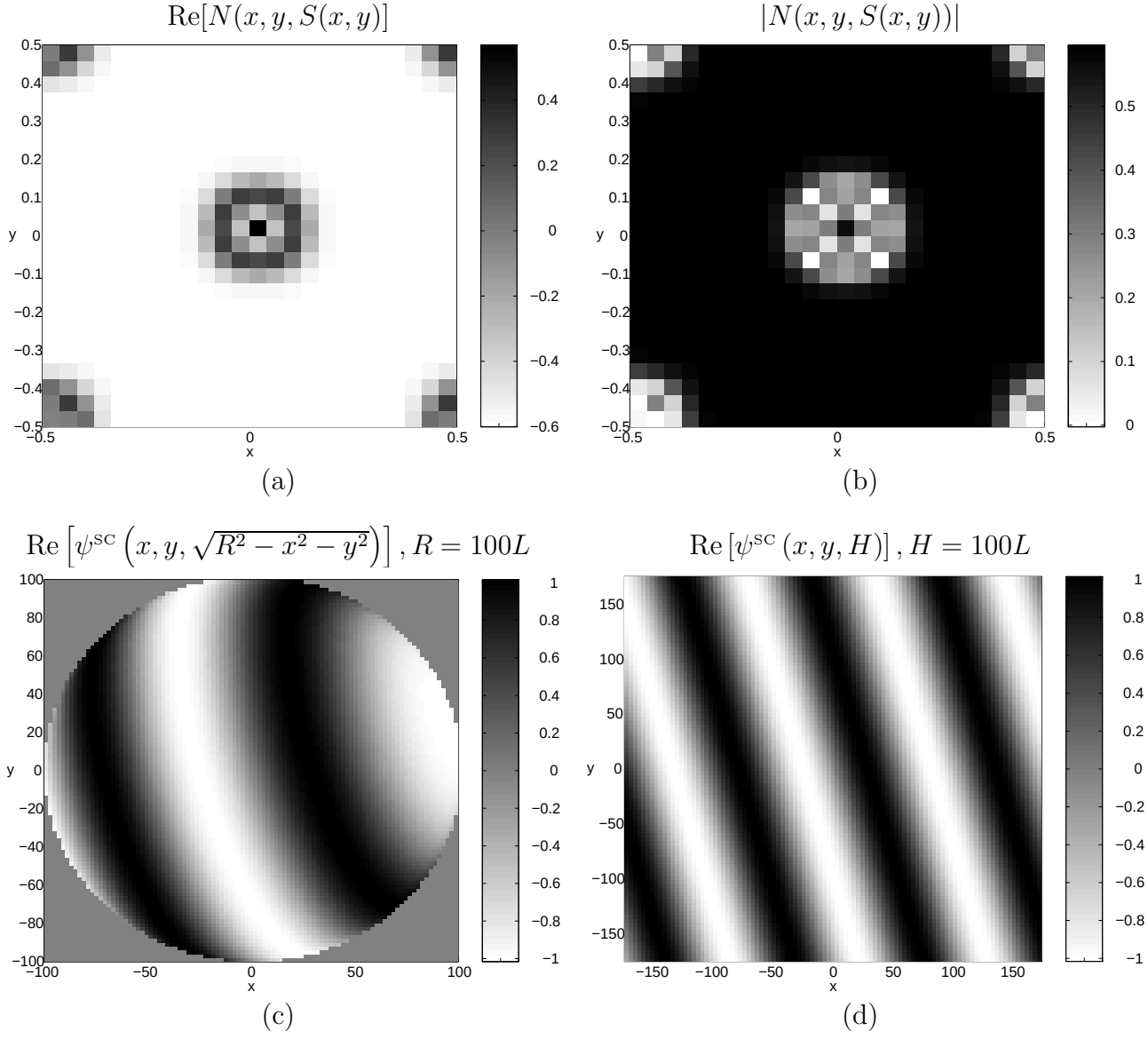

Figure 25: Example 3, Case B for the Dirichlet problem. Real part (a) and magnitude (b) of the surface current or normal derivative N generated with a matrix size of 25×625 and error of -3.5373. Real part of the scattered field plotted on a hemisphere (c) of radius $R = 100L$ and on a plane (d) at height $H = 100L$ above the surface. Here $L = L_1 = L_2$. The matrix size was 121×121 and the images have a resolution of 100×100.

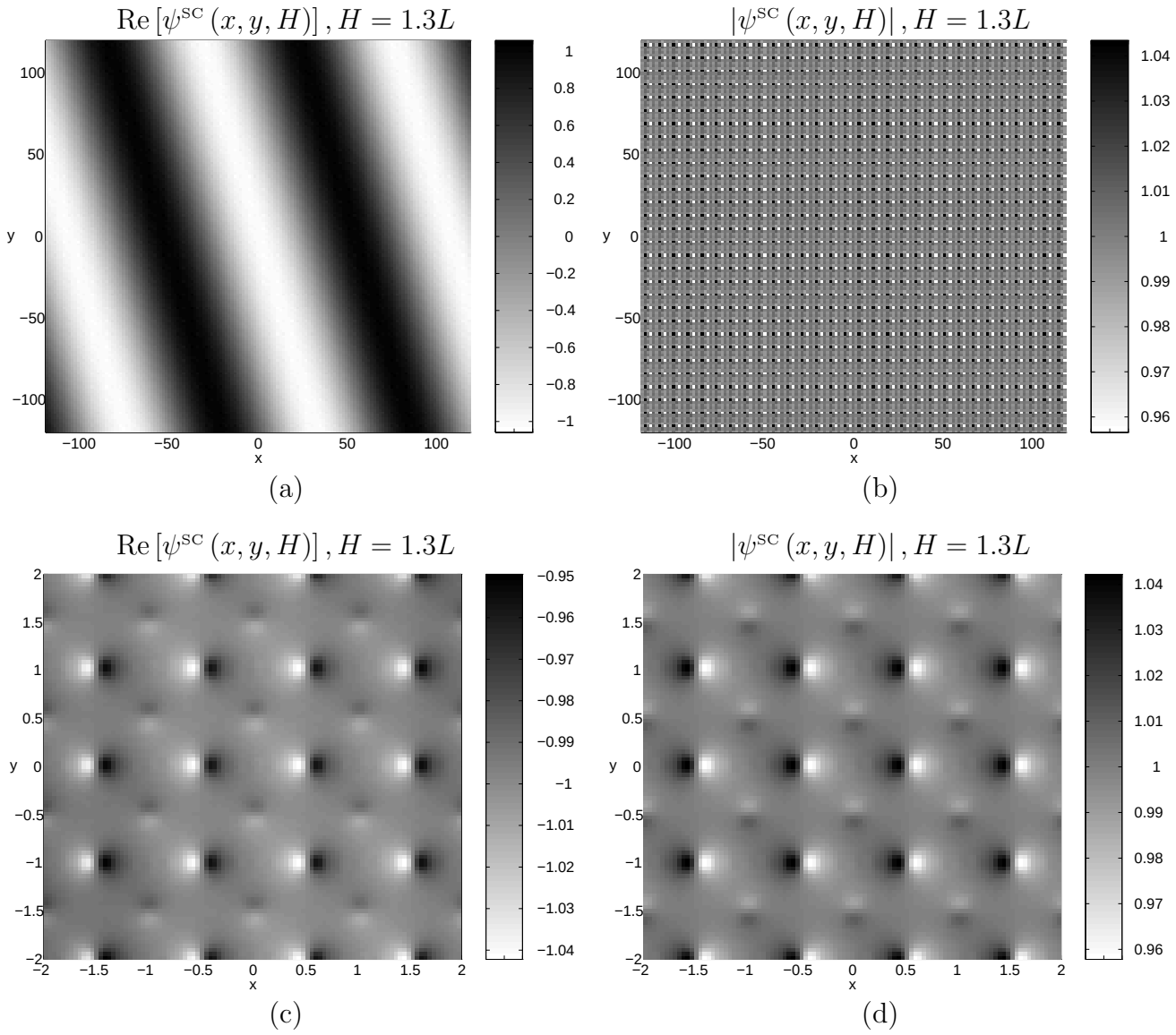

Figure 26: Example 3, Case B for the Dirichlet problem with a matrix size of 121×121. Real part ((a) and (c)) and magnitudes ((b) and (d)) of the scattered field plotted on a plane at distance $H = 1.3L$ above the surface. Here $L = L_1 = L_2$. Parts (c) and (d) are zoomed-in images of (a) and (b), respectively. Parts (a) and (b) have resolution 150×150 and parts (c) and (d) have resolution 100×100.

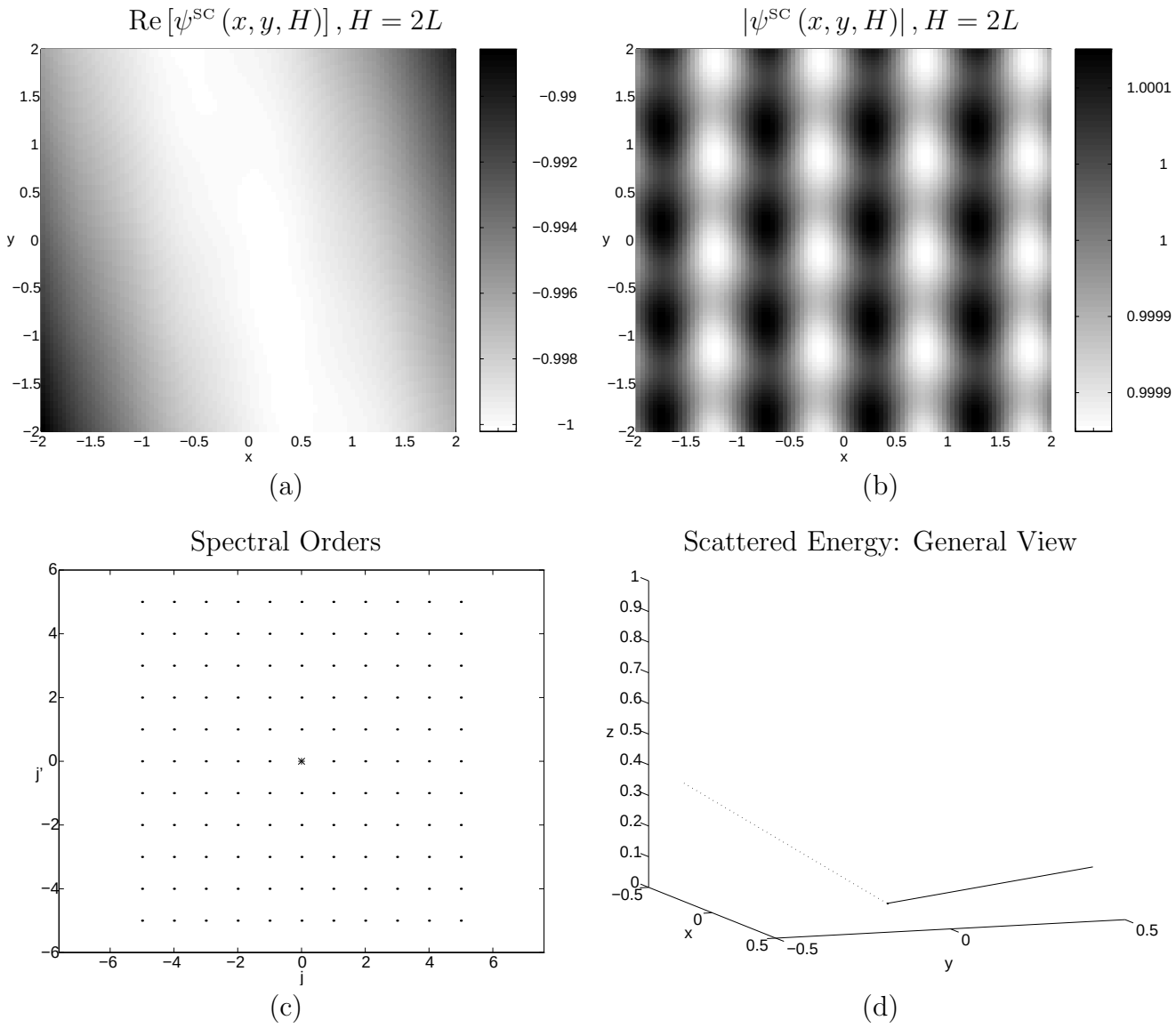

Figure 27: Example 3, Case B for the Dirichlet problem with a matrix size of 121×121. Real part (a) and magnitude (b) of the scattered field plotted on a plane at distance $H = 2L$ above the surface. Here $L = L_1 = L_2$ and the resolution is 100×100. (c) Spectral orders with 11 samples in j and j'; stars refer to radiating modes and dots to non-radiating modes. (d) Scattered energy distribution viewed from $\theta = 80°, \phi = -20°$. Dashed line is incident field, solid lines are scattered Bragg modes. The magnitudes of the lines are proportional to the energy.

17.7 Example 4 Case A, $L_1 > L_2$

$S(x,y)$	$-(d/2)\cos(2\pi x/L_1)\cos(2\pi y/L_2)$
(L_1, L_2)	(1,.5)
$(d/L_1, d/L_2)$	(.075,.15)
$(\lambda/L_1, \lambda/L_2)$	(.12,.24)
Radiating Orders	109
θ^i	20°
ϕ^i	15°

Matrix Size	Number of Samples Coord. x	Coord. y	Spectral j	Spectral j'	$\lambda/\Delta x$	$\lambda/\Delta y$	Fill Time (s)	Linear Solution Time (s)	Condition Number	Error
136 × 136	17	8	17	8	2.0400	0.9600	1.0100	0.7500	6.5692	-2.1767
162 × 162	18	9	18	9	2.1600	1.0800	1.3500	1.2200	13.6825	-3.4275
190 × 190	19	10	19	10	2.2800	1.2000	1.7100	1.8100	24.8239	-3.3970
220 × 220	20	11	20	11	2.4000	1.3200	2.1300	2.7100	47.5487	-4.4669
252 × 252	21	12	21	12	2.5200	1.4400	2.7100	4.2200	82.1995	-4.0164
286 × 286	22	13	22	13	2.6400	1.5600	3.3700	5.8600	150.6919	-5.2378
322 × 322	23	14	23	14	2.7600	1.6800	4.1800	8.4200	254.1110	-4.6674
360 × 360	24	15	24	15	2.8800	1.8000	4.8800	11.3600	455.5054	-5.7751
400 × 400	25	16	25	16	3.0000	1.9200	6.0800	15.7400	757.7690	-5.2450
442 × 442	26	17	26	17	3.1200	2.0400	7.2900	19.8300	$1.3413 \cdot 10^3$	-6.3786
486 × 486	27	18	27	18	3.2400	2.1600	8.1200	24.4200	$2.2137 \cdot 10^3$	-5.8237
289 × 289	17	17	17	17	2.0400	2.0400	4.0700	6.9500	421.6498	-7.0884
324 × 324	18	18	18	18	2.1600	2.1600	4.2100	8.2200	881.1838	-5.2715
361 × 361	19	19	19	19	2.2800	2.2800	4.7100	10.4400	$1.2789 \cdot 10^3$	-6.8717
400 × 400	20	20	20	20	2.4000	2.4000	5.7200	14.0500	$2.6245 \cdot 10^3$	-5.7603
441 × 441	21	21	21	21	2.5200	2.5200	7.1100	19.3600	$3.7883 \cdot 10^3$	-7.4819
484 × 484	22	22	22	22	2.6400	2.6400	8.3700	25.5800	$7.6819 \cdot 10^3$	-6.2522
529 × 529	23	23	23	23	2.7600	2.7600	10.2400	33.4700	$1.1057 \cdot 10^4$	-8.1226
576 × 576	24	24	24	24	2.8800	2.8800	11.8000	44.7200	$2.2233 \cdot 10^4$	-6.7411
625 × 625	25	25	25	25	3.0000	3.0000	14.5000	59.0800	$3.1955 \cdot 10^4$	-8.8479
676 × 676	26	26	26	26	3.1200	3.1200	15.5700	68.5500	$6.3852 \cdot 10^4$	-7.2294
729 × 729	27	27	27	27	3.2400	3.2400	17.7900	87.3400	$9.1725 \cdot 10^4$	-9.9348

Table 15: Parameters and computational results for the Dirichlet problem, Example 4, Case A. Here $L_1 = 2L_2$. Only square systems were considered. Convergence was quite good for this case of roughness values different in the two directions. The wavelength λ is much less than either period.

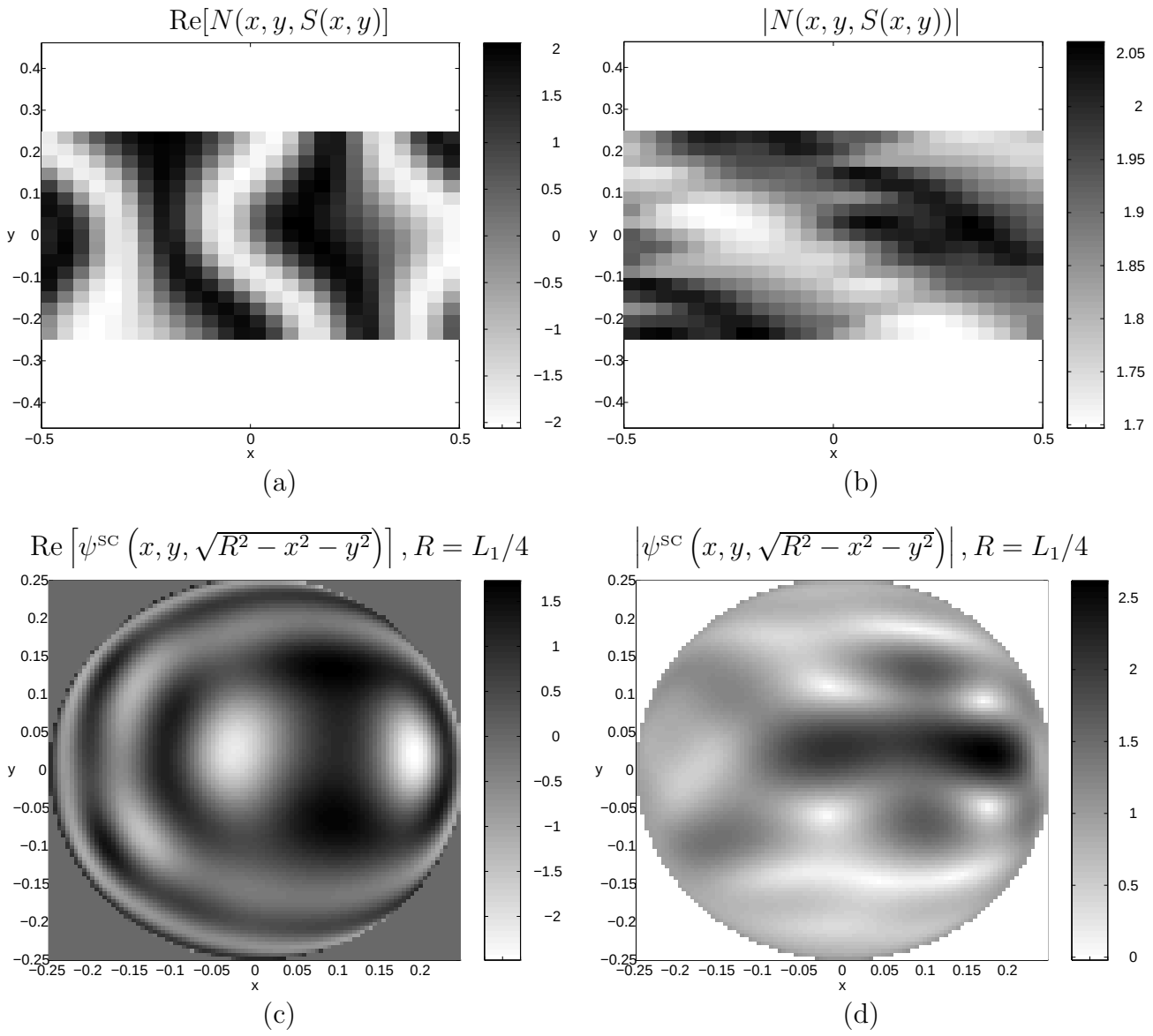

Figure 28: Example 4, Case A for the Dirichlet problem and a matrix size of 486×486. Real part (a) and magnitude (b) of the surface current or normal derivative N. Real part (c) and magnitude (d) of the scattered field plotted on a close-in hemisphere of radius $R = L_1/4$, i.e. one quarter of the period in the $x-$direction. The resolution is 100×100.

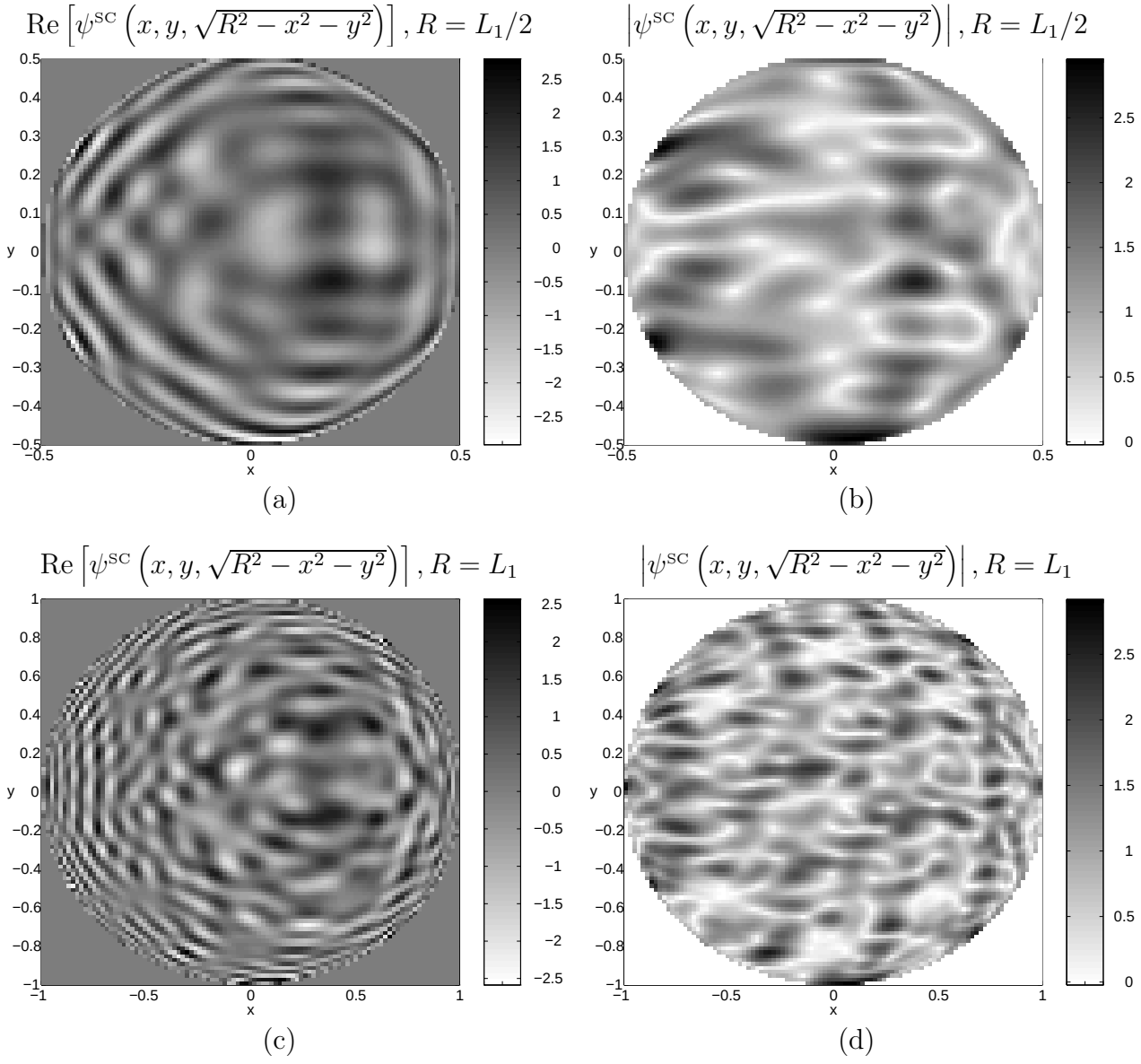

Figure 29: Example 4, Case A for the Dirichlet problem and a matrix size of 486×486. Real part ((a) and (c)) and magnitude ((b) and (d)) of the scattered field viewed on radially increasing hemispheres of radius $R = L_1/2$ in (a) and (b), and $R = L_1$ in (c) and (d) with a resolution of 100×100.

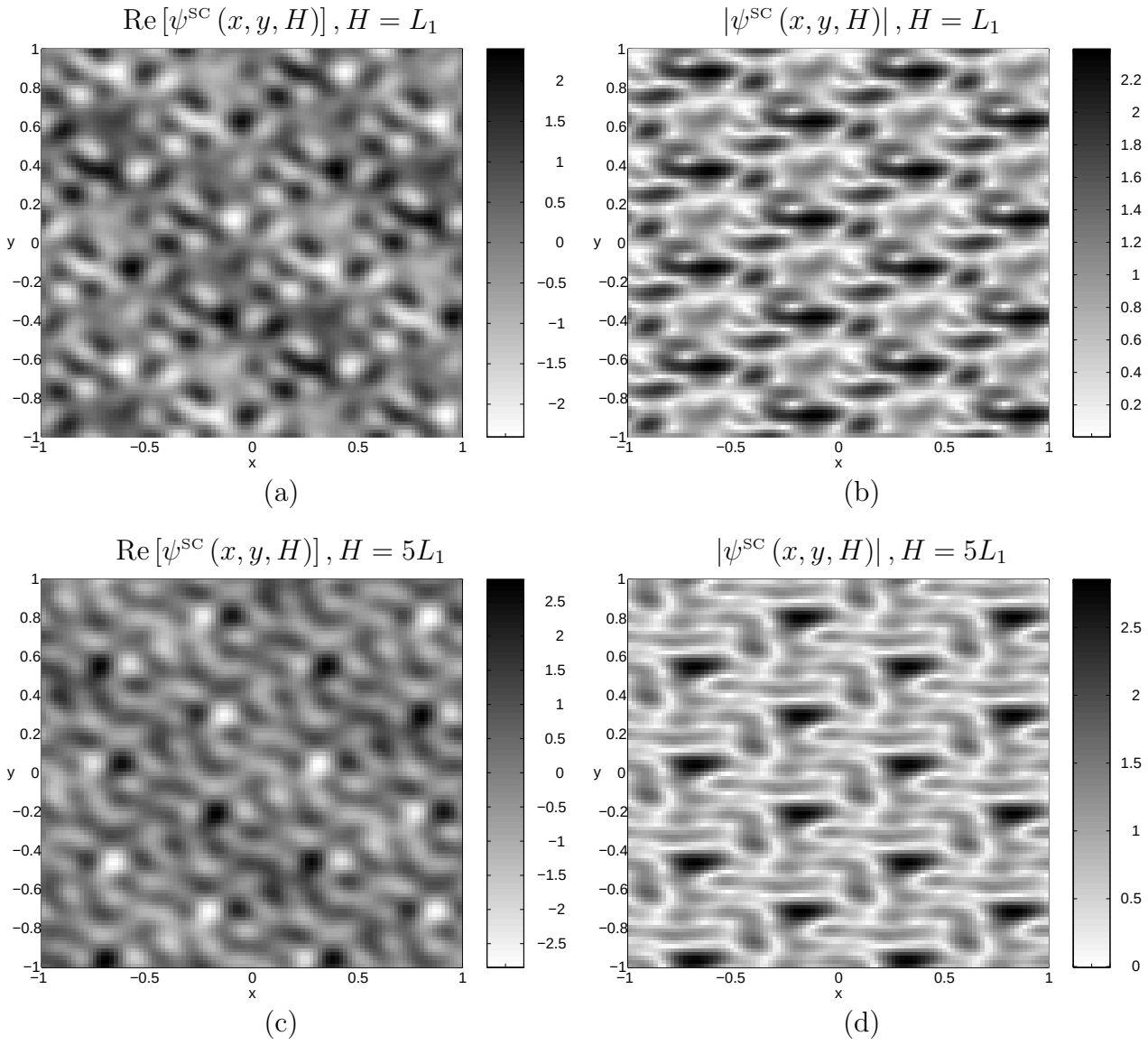

Figure 30: Example 4, Case A for the Dirichlet problem and a matrix size of 486×486. Real part ((a) and (c)) and magnitude ((b) and (d)) of the scattered field viewed on horizontal planes of increasing distance from the surface at $H = L_1$ in (a) and (b), and $H = 5L_1$ in (c) and (d).

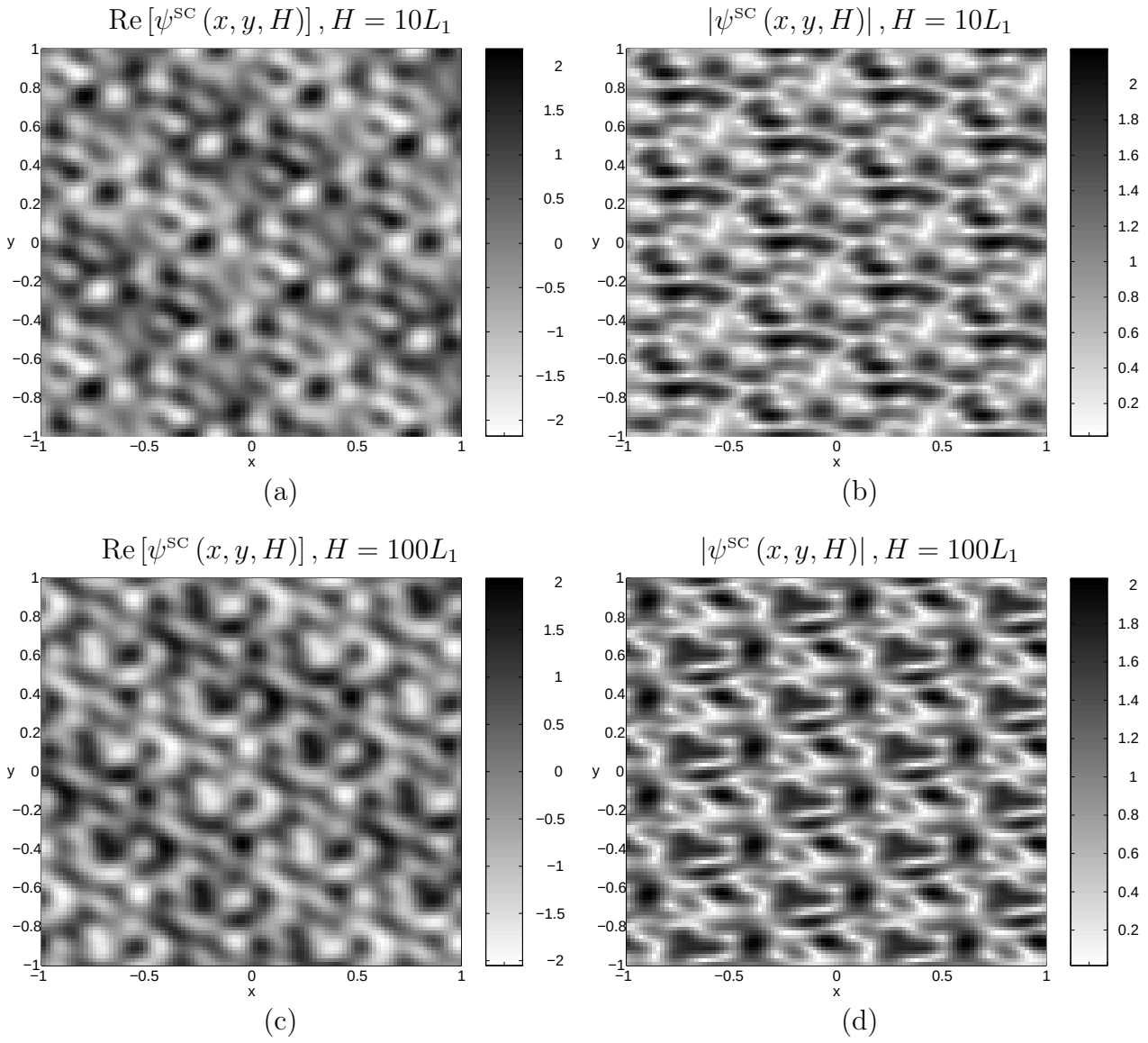

Figure 31: Example 4, Case A for the Dirichlet problem and a matrix size of 486×486. Real part ((a) and (c)) and magnitude ((b) and (d)) of the scattered field viewed on horizontal planes of increasing distance from the surface at $H = 10L_1$ in (a) and (b), and $H = 100L_1$ in (c) and (d).

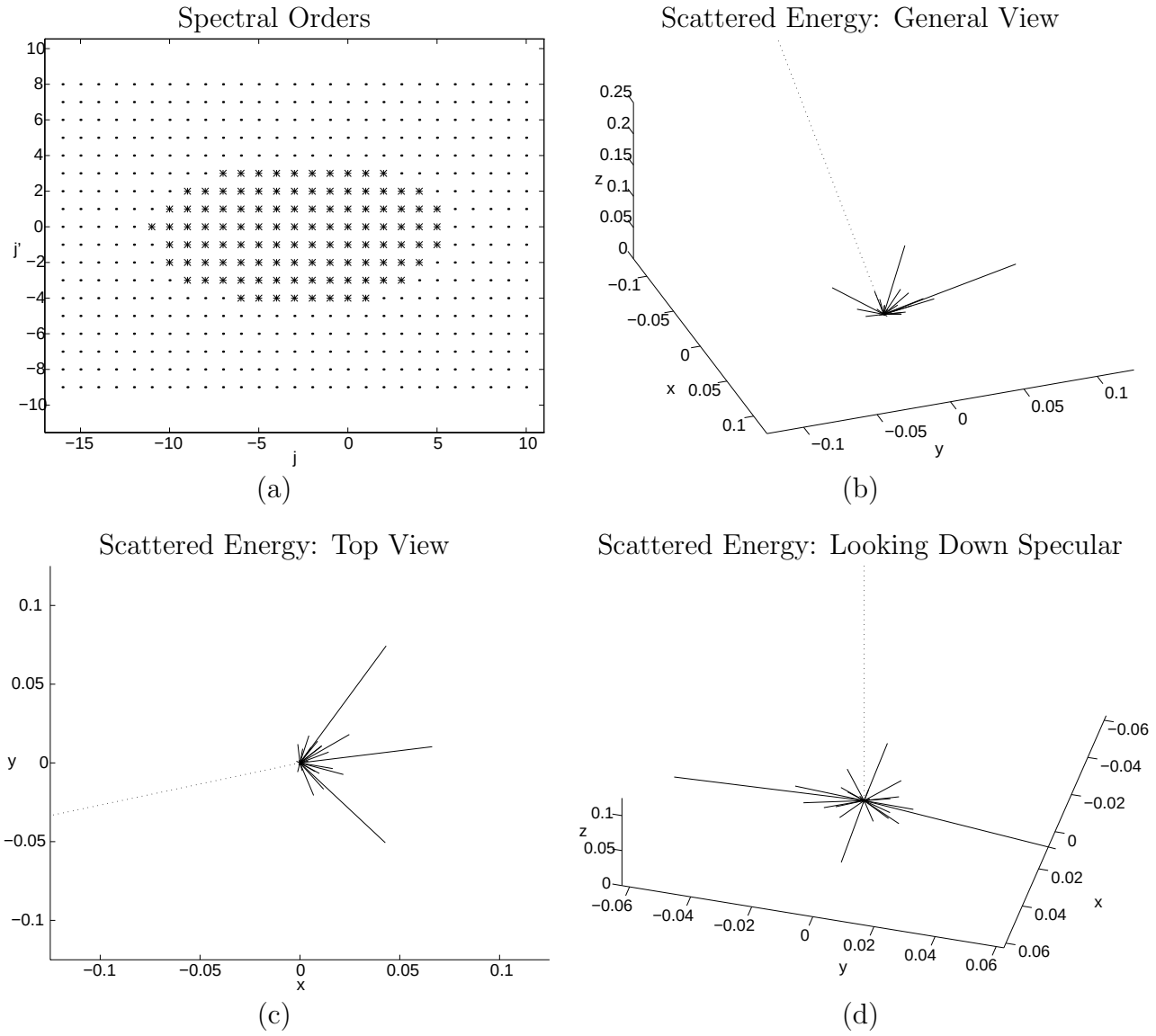

Figure 32: Example 4, Case A for the Dirichlet problem. (a) Spectral orders with 27 samples in j and 18 in j'; stars refer to radiating modes and dots to non-radiating modes. Scattered energy distribution viewed from (b) $\theta = 40°, \phi = -20°$ (c) $\theta = 0°, \phi = -90°$ (d) $\theta = 20°, \phi = 15°$. Dashed line is incident field, solid lines are scattered Bragg modes. The magnitudes of the lines are proportional to the energy.

17.8 Example 4 Case B, $L_1 >> L_2$

$S(x,y)$	$-(d/2)\cos(2\pi x/L_1)\cos(2\pi y/L_2)$
(L_1, L_2)	(1,.05)
$(d/L_1, d/L_2)$	(.075,.150)
$(\lambda/L_1, \lambda/L_2)$	(.12,2.40)
Radiating Orders	17
θ^i	20°
ϕ^i	15°

Matrix Size	Number of Samples Coord. x	Coord. y	Spectral j	Spectral j'	$\lambda/\Delta x$	$\lambda/\Delta y$	Fill Time (s)	Linear Solution Time (s)	Condition Number	Error
17 × 17	17	1	17	1	2.0400	0.1200	0.0800	0.0200	1.6319	-4.9707
36 × 36	18	2	18	2	2.1600	0.2400	0.1900	0.0300	1.0000	< -15.9
57 × 57	19	3	19	3	2.2800	0.3600	0.3200	0.0900	786.0448	-2.5743
80 × 80	20	4	20	4	2.4000	0.4800	0.5500	0.2000	$2.0248 \cdot 10^4$	-2.7686
105 × 105	21	5	21	5	2.5200	0.6000	0.8000	0.3800	$7.2357 \cdot 10^5$	-1.3685
132 × 132	22	6	22	6	2.6400	0.7200	1.0400	0.7300	$3.3771 \cdot 10^8$	-1.0049
161 × 161	23	7	23	7	2.7600	0.8400	1.4000	1.2100	$4.3818 \cdot 10^9$	-1.6574
192 × 192	24	8	24	8	2.8800	0.9600	1.8300	1.9600	$5.4034 \cdot 10^{10}$	-1.6080
225 × 225	25	9	25	9	3.0000	1.0800	2.3900	3.0300	$4.1184 \cdot 10^{11}$	-1.6731
260 × 260	26	10	26	10	3.1200	1.2000	3.0100	4.5800	$2.4100 \cdot 10^{13}$	-1.6480
297 × 297	27	11	27	11	3.2400	1.3200	3.7200	6.4100	$1.2410 \cdot 10^{14}$	-1.5578
289 × 289	17	17	17	17	2.0400	2.0400	3.7800	6.2800	$7.7568 \cdot 10^{24}$	-0.5850
324 × 324	18	18	18	18	2.1600	2.1600	4.3700	8.3800	$2.0658 \cdot 10^{26}$	-1.4543
361 × 361	19	19	19	19	2.2800	2.2800	5.4500	11.3300	$3.9084 \cdot 10^{27}$	1.2890
400 × 400	20	20	20	20	2.4000	2.4000	6.4100	14.8600	$4.9564 \cdot 10^{28}$	-0.8009

Table 16: Parameters and computational results for the Dirichlet problem, Example 4, Case B where $L_1 = 20L_2$. Only square systems were considered. Convergence was better for smaller systems in this case of roughness values dramatically different in the two directions.

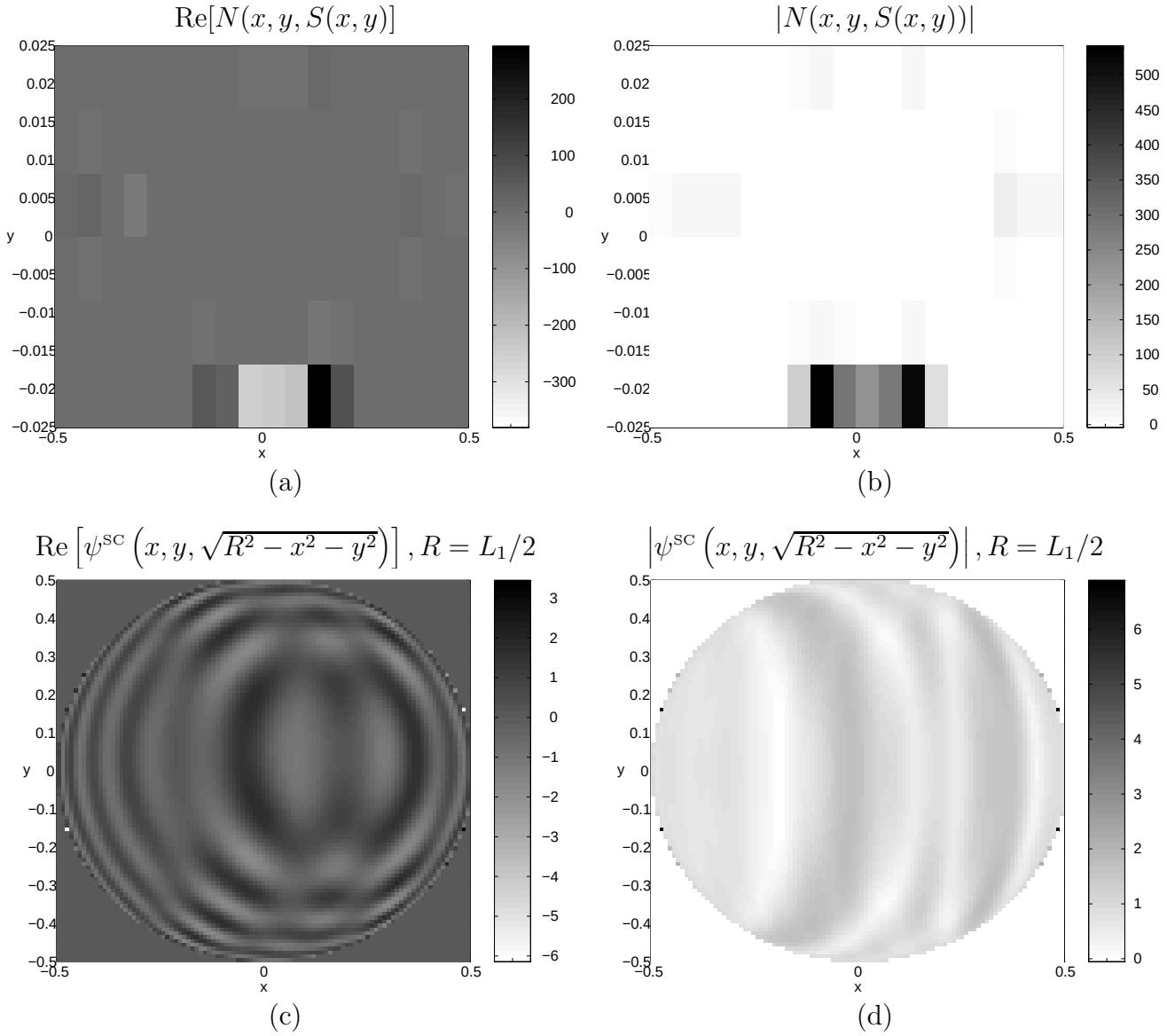

Figure 33: Example 4, Case B for the Dirichlet problem. Real part (a) and magnitude (b) of the surface current or normal derivative N with added non-radiating orders of 3 rows in y, above and below, and 1 column in x, left and right for a matrix size of 133×133 (where $133 = 19 \times 7 = jj'$). Real part (c) and magnitude (d) of the scattered field plotted on a close-in hemisphere of radius $R = L_1/2$, with a matrix size of 57×57 and a resolution of 100×100.

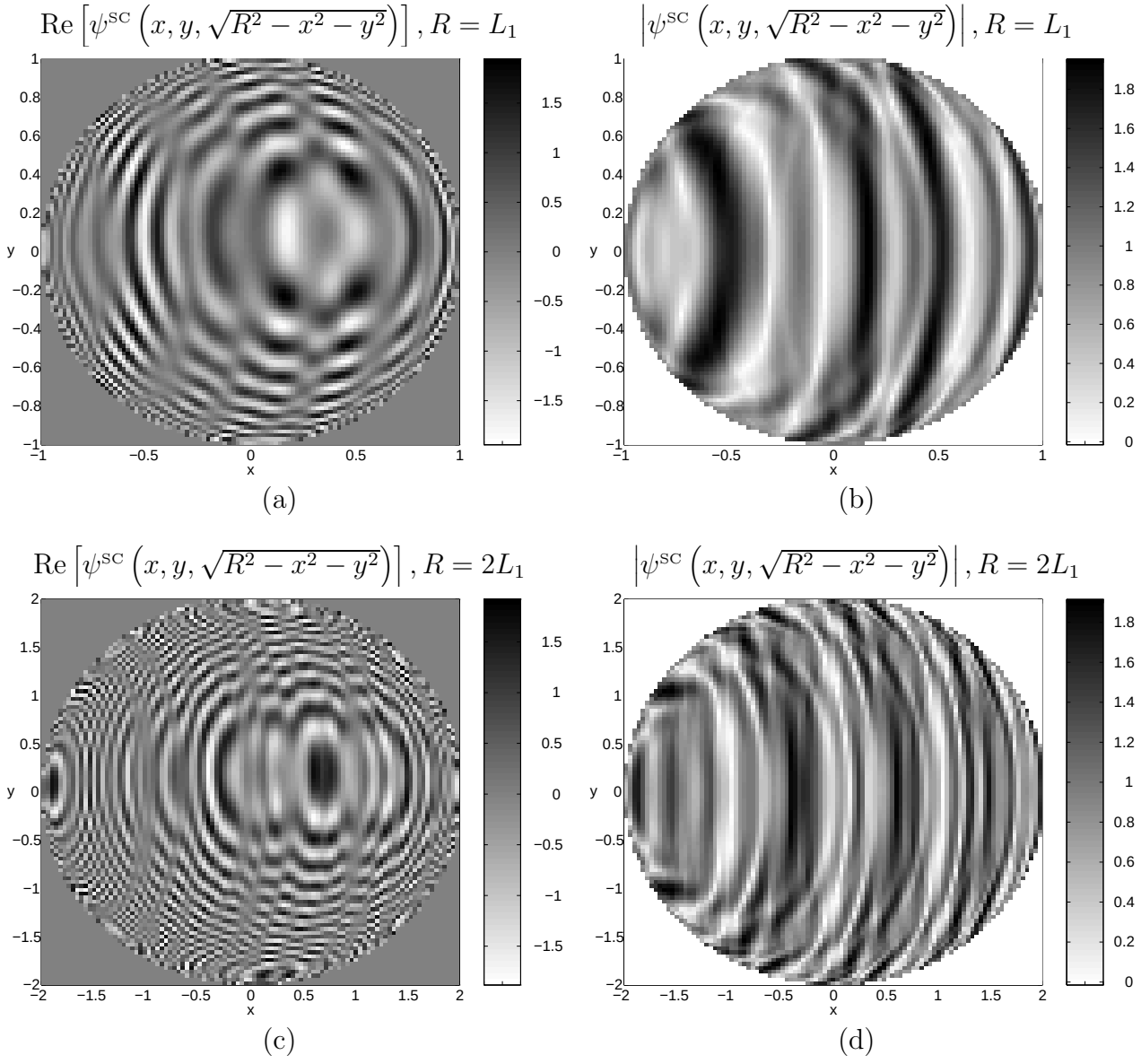

Figure 34: Example 4, Case B for the Dirichlet problem and a matrix size of 57×57. Real part ((a) and (c)) and magnitude ((b) and (d)) of the scattered field viewed on radially increasing hemispheres of radius $R = L_1$ in (a) and (b), and $R = 2L_1$ in (c) and (d) with a resolution of 100×100.

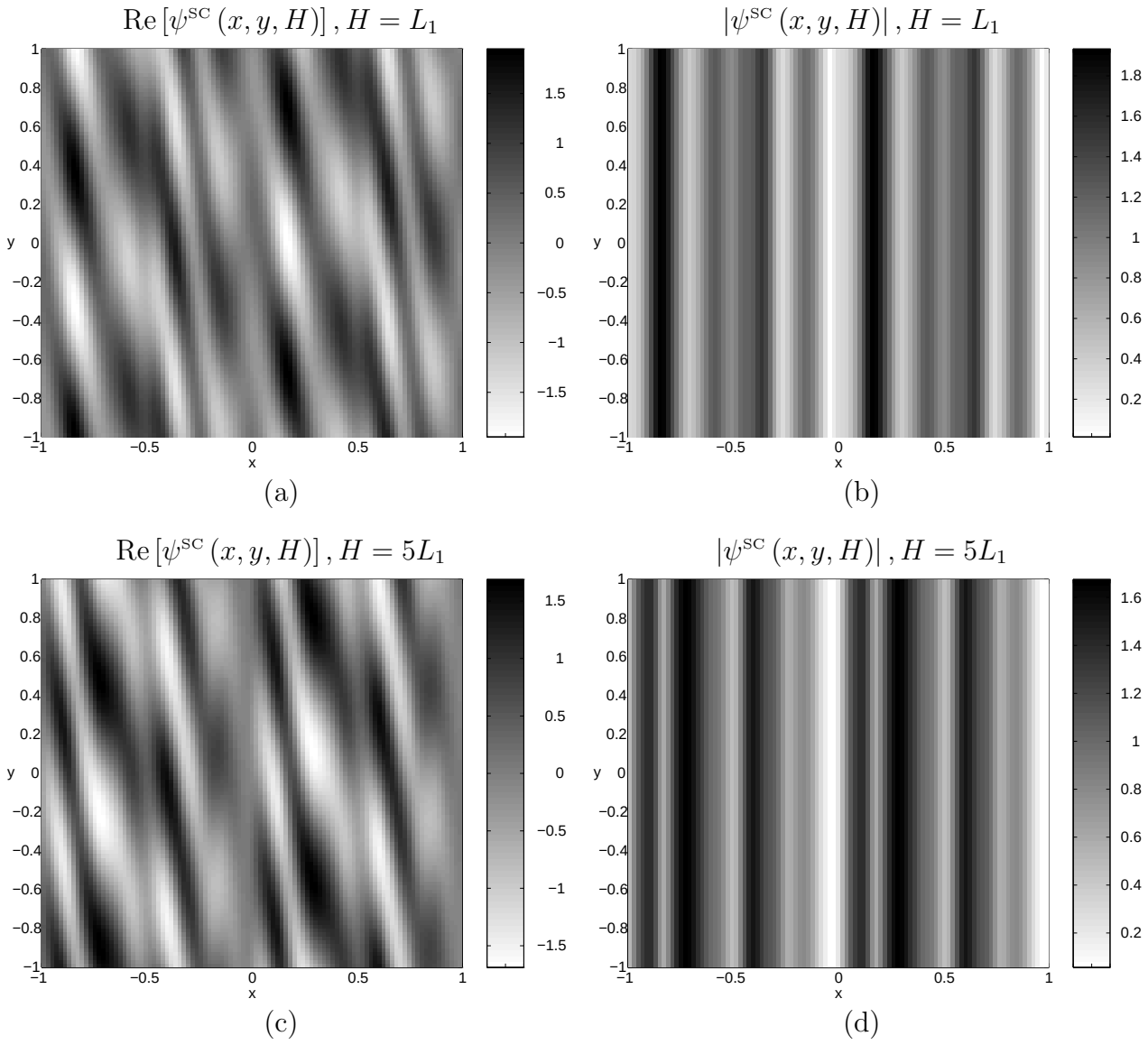

Figure 35: Example 4, Case B for the Dirichlet problem and a matrix size of 57×57. Real part ((a) and (c)) and magnitude ((b) and (d)) of the scattered field viewed on horizontal planes of increasing distance from the surface at $H = L_1$ in (a) and (b), and $H = 5L_1$ in (c) and (d).

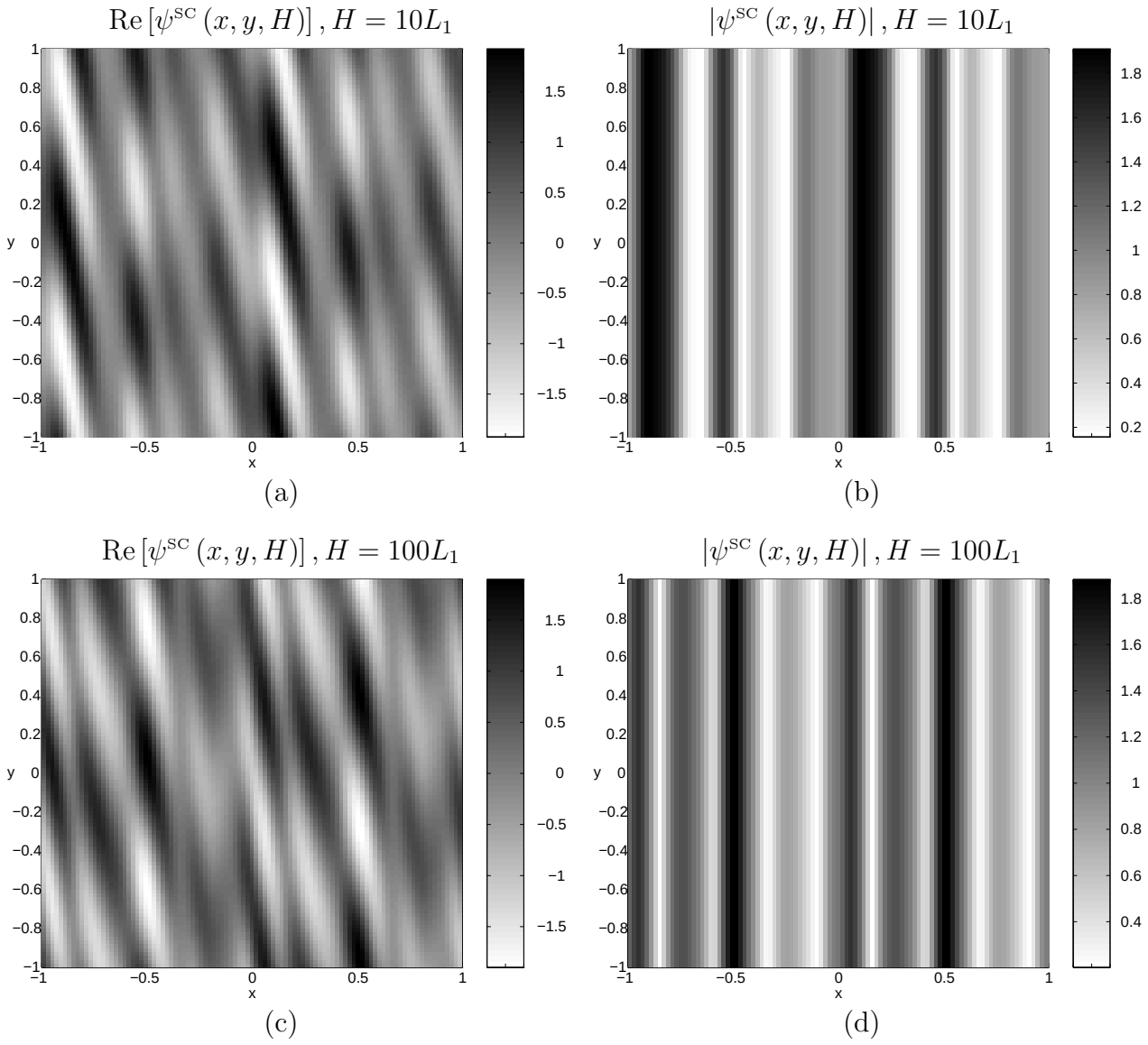

Figure 36: Example 4, Case B for the Dirichlet problem and a matrix size of 57×57. Real part ((a) and (c)) and magnitude ((b) and (d)) of the scattered field viewed on horizontal planes of increasing distance from the surface at $H = 10L_1$ in (a) and (b), and $H = 100L_1$ in (c) and (d).

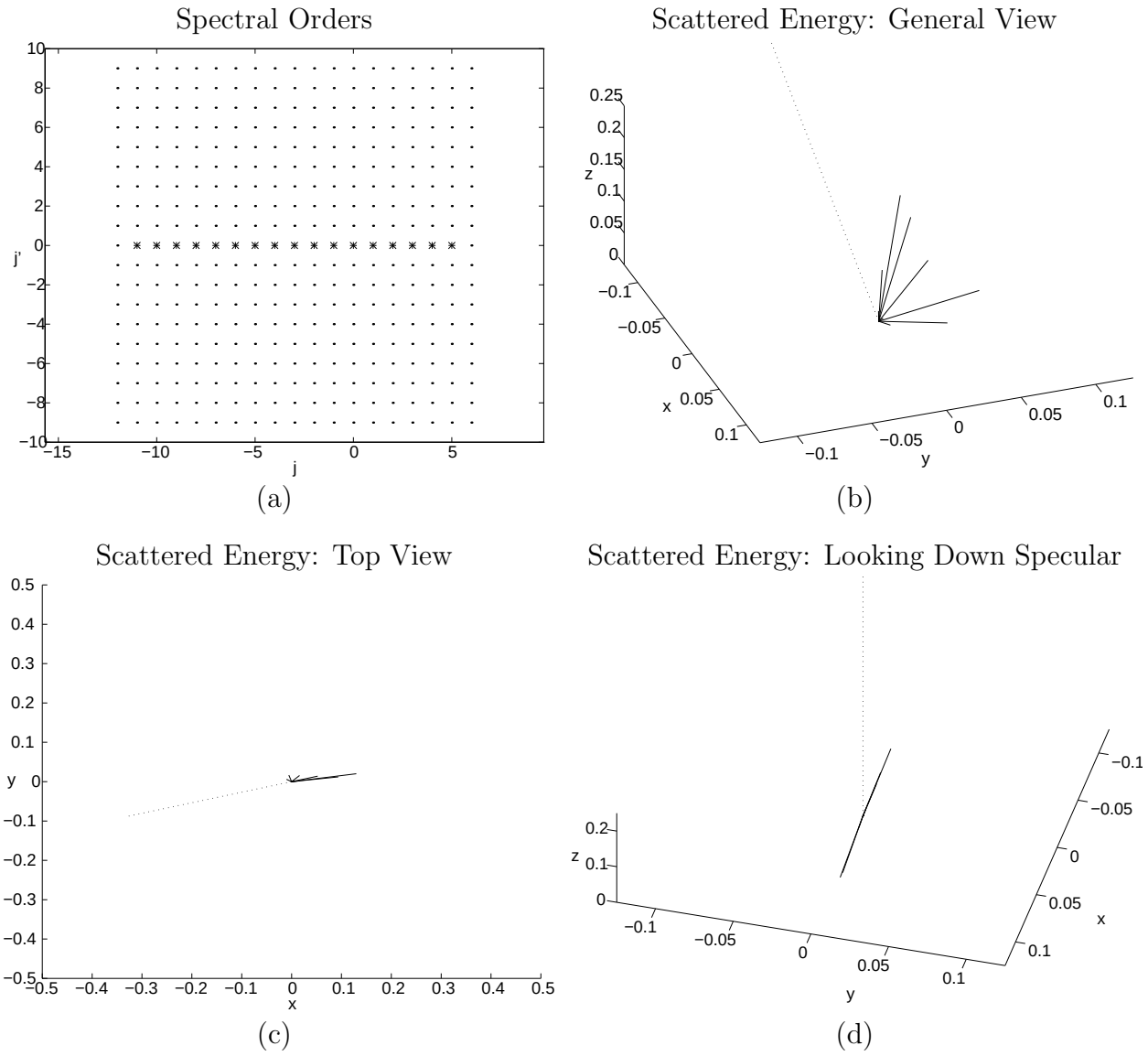

Figure 37: Example 4, Case B for the Dirichlet problem and a matrix size of 729×729. (a) Spectral orders with 19 samples in j and j'; stars refer to radiating modes, dots to non-radiating modes. Scattered energy distribution viewed from (b) $\theta = 40°, \phi = -20°$, (c) $\theta = 0°, \phi = -90°$ and (d) $\theta = 20°, \phi = 15°$. Dashed line is incident field, solid lines are scattered Bragg modes. The magnitudes of the lines are proportional to the energy. In (a), because of the difference in periods, the Bragg modes are confined to specular in the $y-$direction ($j' = 0$).

17.9 Saw-tooth Surface

$S(x,y)$	$2d\left(2\frac{\lfloor x \rfloor}{L_1}-\frac{1}{2}\right)\left(2\frac{\lfloor y \rfloor}{L_2}-\frac{1}{2}\right)$
(L_1, L_2)	(1,1)
$(d/L_1, d/L_2)$	(.075,.075)
$(\lambda/L_1, \lambda/L_2)$	(.12,.12)
Radiating Orders	218
θ^i	20°
ϕ^i	15°

Matrix Size	Number of Samples				$\lambda/\Delta x$	$\lambda/\Delta y$	Fill Time (s)	Linear Solution Time (s)	Condition Number	Error
	Coord.		Spectral							
	x	y	j	j'						
289 × 289	17	17	17	17	2.0400	2.0400	3.2600	5.8300	6.9791	-4.6422
324 × 324	18	18	18	18	2.1600	2.1600	3.9400	8.0500	9.3280	-4.5842
361 × 361	19	19	19	19	2.2800	2.2800	4.8100	10.9800	15.1707	-5.3309
400 × 400	20	20	20	20	2.4000	2.4000	5.8000	14.8500	19.1490	-4.6870
441 × 441	21	21	21	21	2.5200	2.5200	6.9900	19.9400	31.3842	-5.0115
484 × 484	22	22	22	22	2.6400	2.6400	8.4000	26.0200	37.9368	-5.0694
529 × 529	23	23	23	23	2.7600	2.7600	9.8000	33.9300	62.7203	-5.4834
576 × 576	24	24	24	24	2.8800	2.8800	11.8600	46.1900	73.4911	-4.8989
625 × 625	25	25	25	25	3.0000	3.0000	14.1100	60.2800	122.4601	-5.1393
676 × 676	26	26	26	26	3.1200	3.1200	16.6900	75.5400	140.3028	-5.7180
729 × 729	27	27	27	27	3.2400	3.2400	19.0700	101.4100	235.2732	-5.2314

Table 17: Parameters and computational results for the Dirichlet problem for the saw-tooth surface illustrated in Fig. 38. Only square systems were considered and convergence was quite good. Condition numbers were quite small.

$$S(x,y) = 2d\left(2\frac{|x|}{L_1} - \frac{1}{2}\right)\left(2\frac{|y|}{L_2} - \frac{1}{2}\right)$$

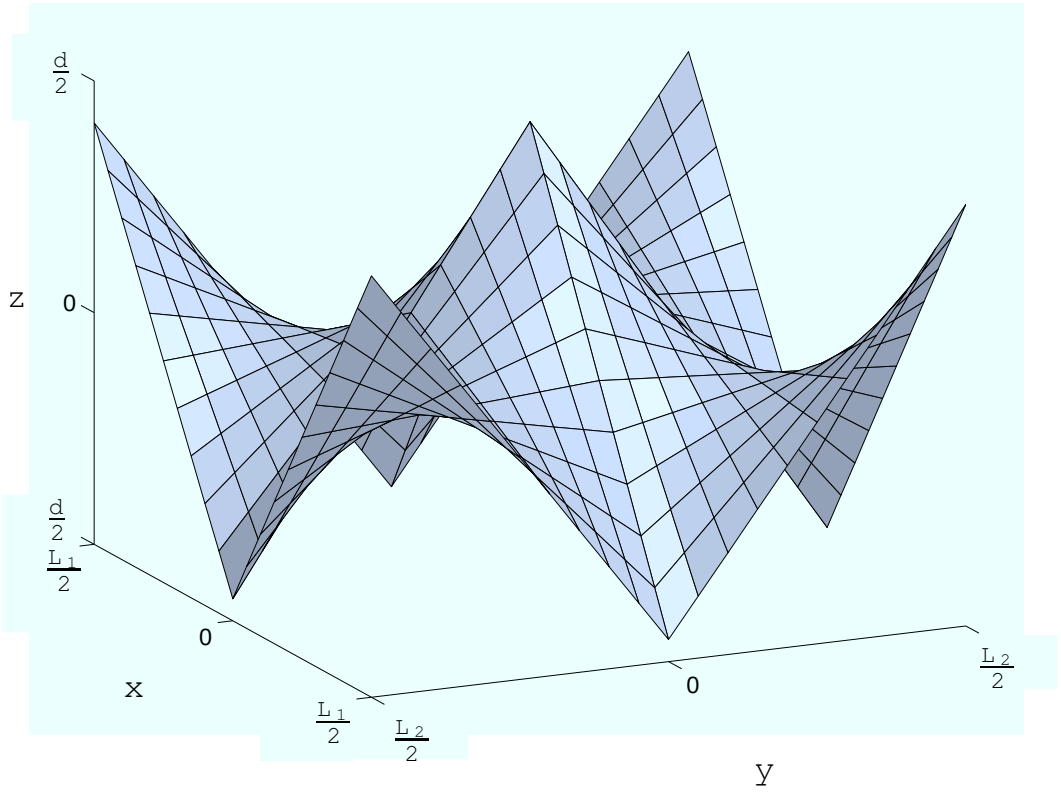

Figure 38: Saw-tooth Surface. The parameters are listed in Table 17.

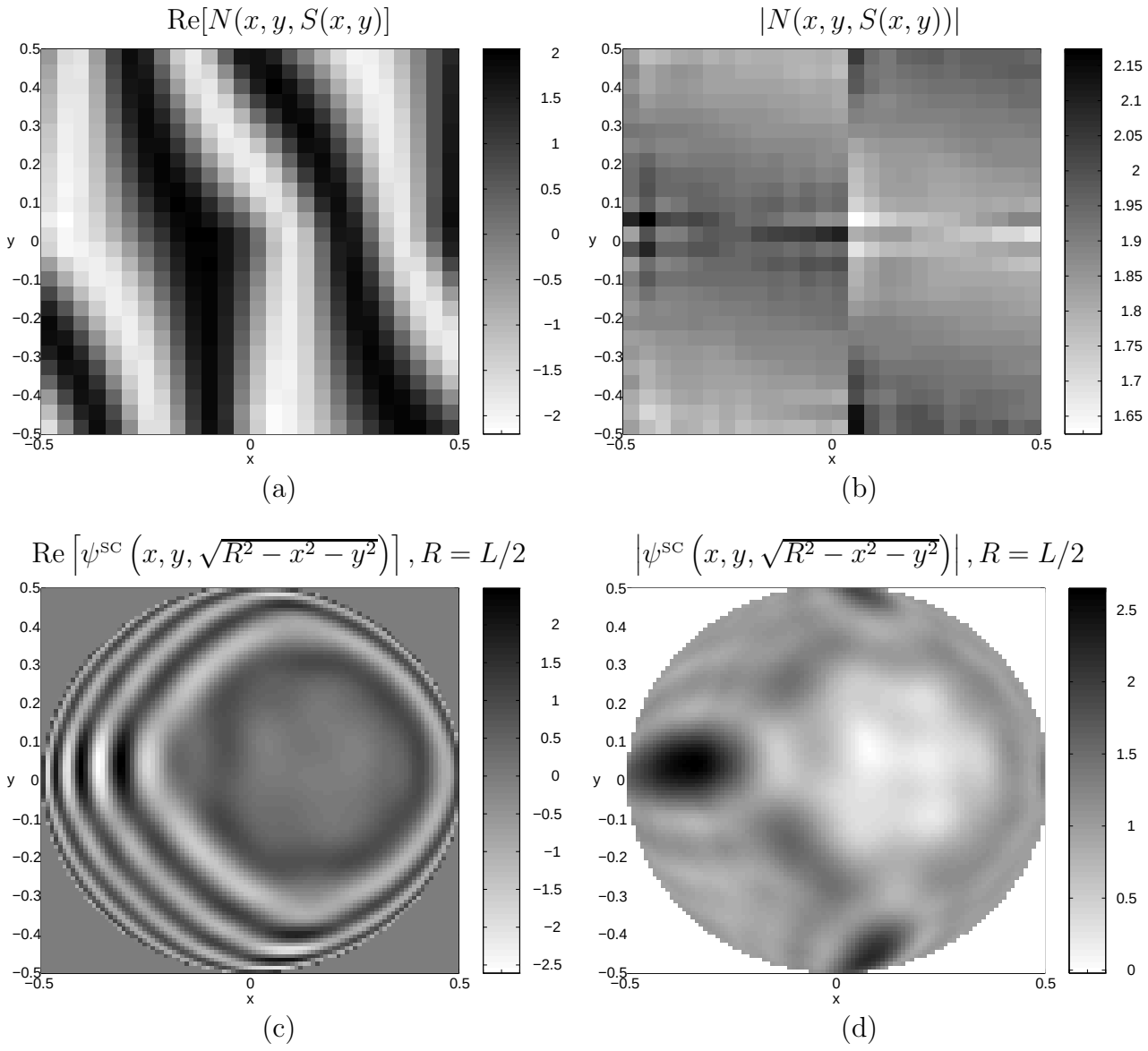

Figure 39: Saw-tooth surface for the Dirichlet problem and a matrix size of 729×729. Real part (a) and magnitude (b) of the surface current or normal derivative N and real part (c) and magnitude (d) of the scattered field plotted on a close-in hemisphere of radius $R = L/2$ (here $L = L_1 = L_2$) with a resolution of 100×100.

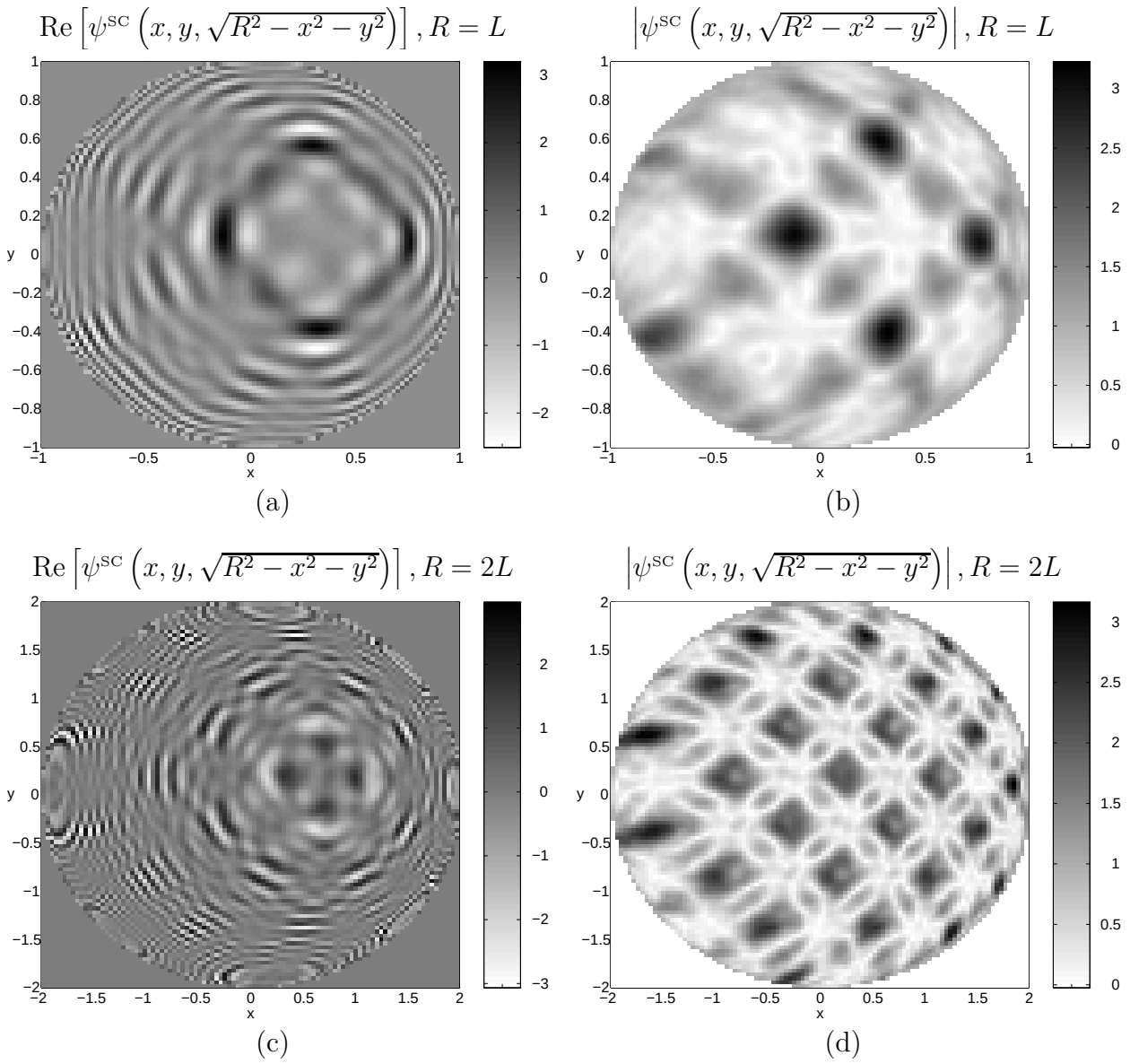

Figure 40: Saw-tooth surface for the Dirichlet problem and a matrix size of 729×729. Real part ((a) and (c)) and magnitudes ((b) and (d)) of the scattered field viewed on hemispheres of increasing radii $R = L$ in (a) and (b), and $R = 2L$ in (c) and (d) where $L = L_1 = L_2$ and with a resolution of 100×100. A sharper structure is evident in the field as the radius increases.

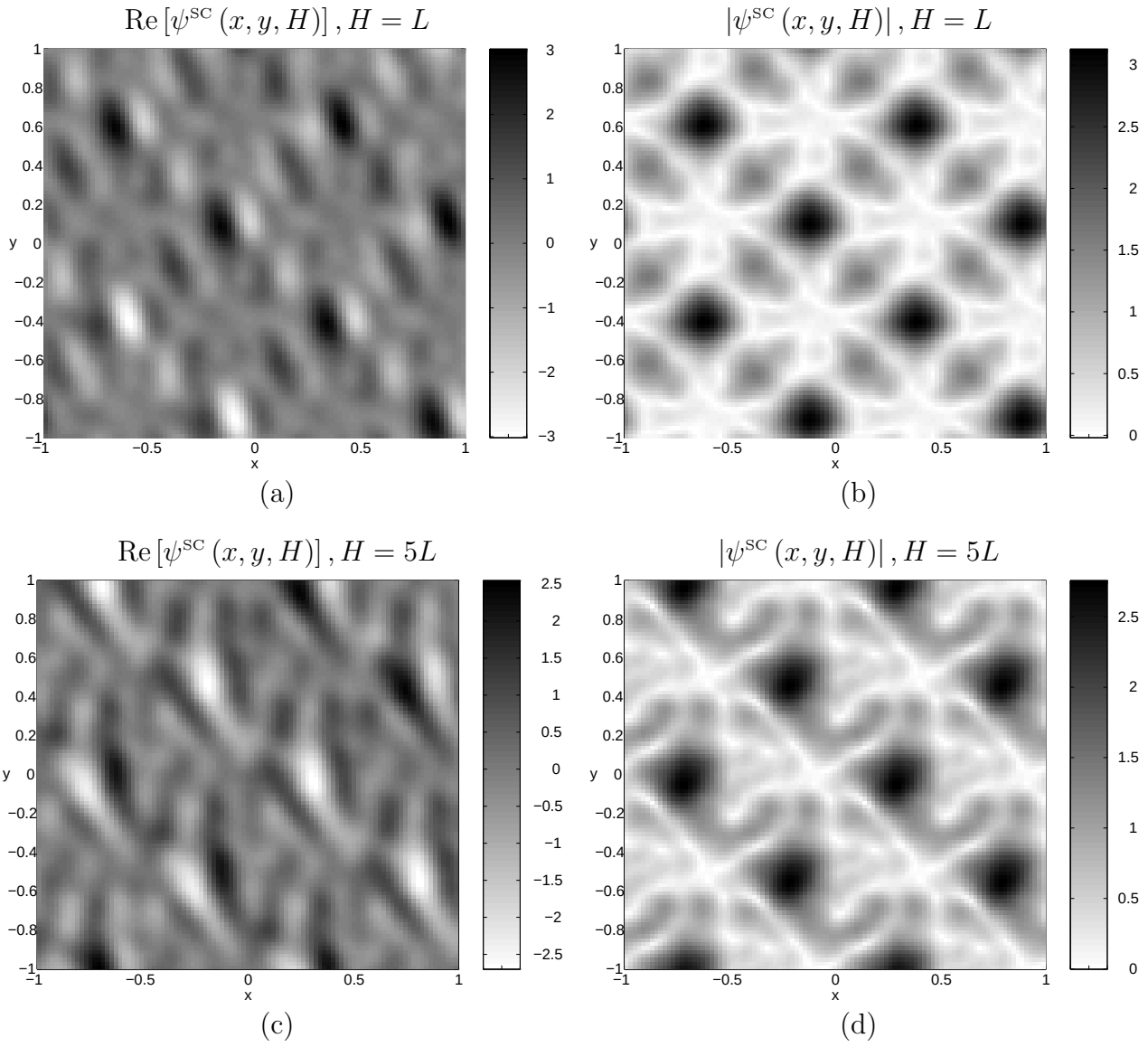

Figure 41: Saw-tooth surface for the Dirichlet problem and a matrix size of 729×729. Real part ((a) and (c)) and magnitudes ((b) and (d)) of the scattered field viewed on horizontal planes of increasing distance above the surface, at $H = L$ in (a) and (b), and $H = 5L$ in (c) and (d).

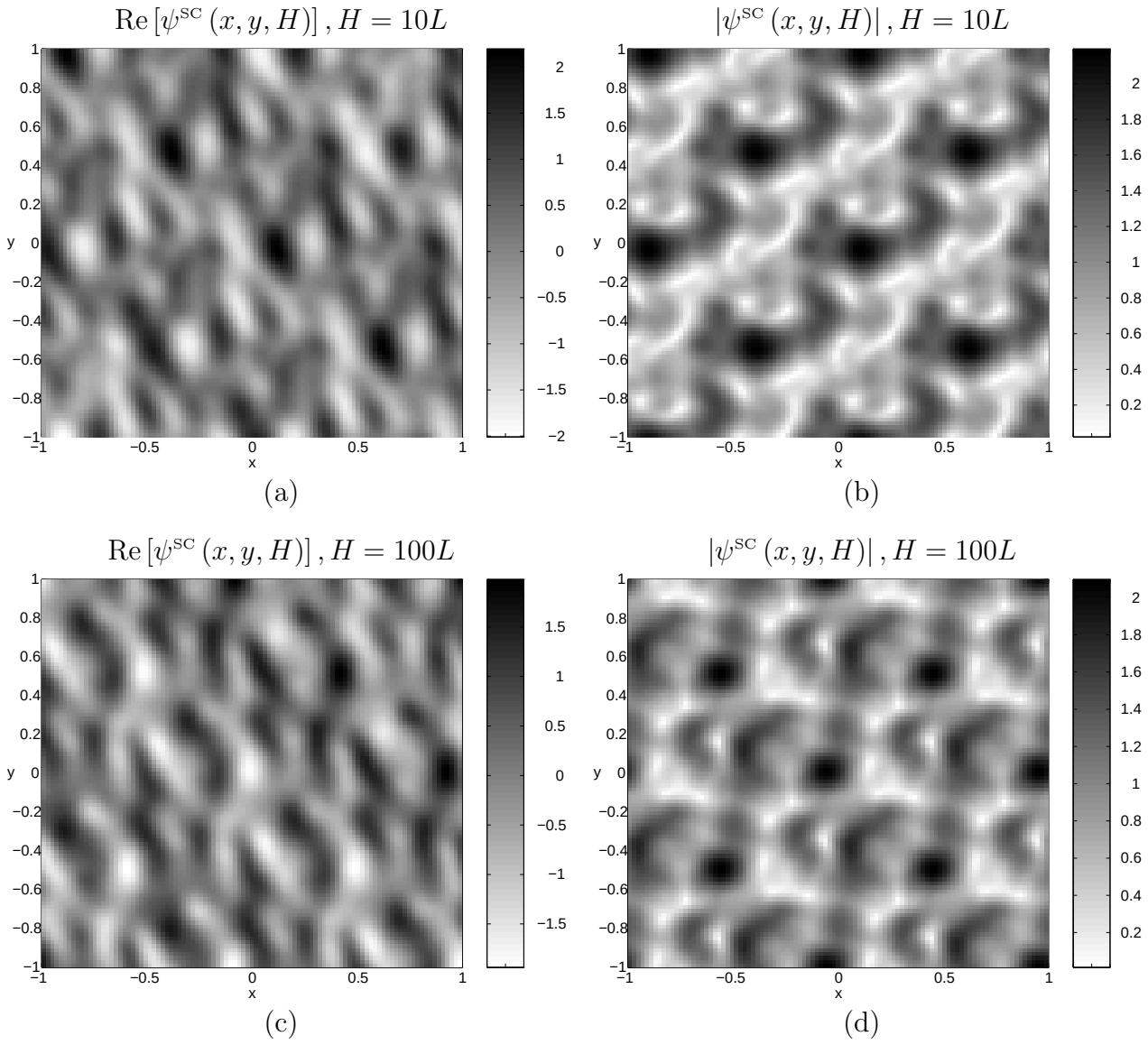

Figure 42: Saw-tooth surface for the Dirichlet problem and a matrix size of 729×729. Real part ((a) and (c)) and magnitudes ((b) and (d)) of the scattered field viewed on horizontal planes of increasing distance above the surface, at $H = 10L$ in (a) and (b), and $H = 100L$ in (c) and (d).

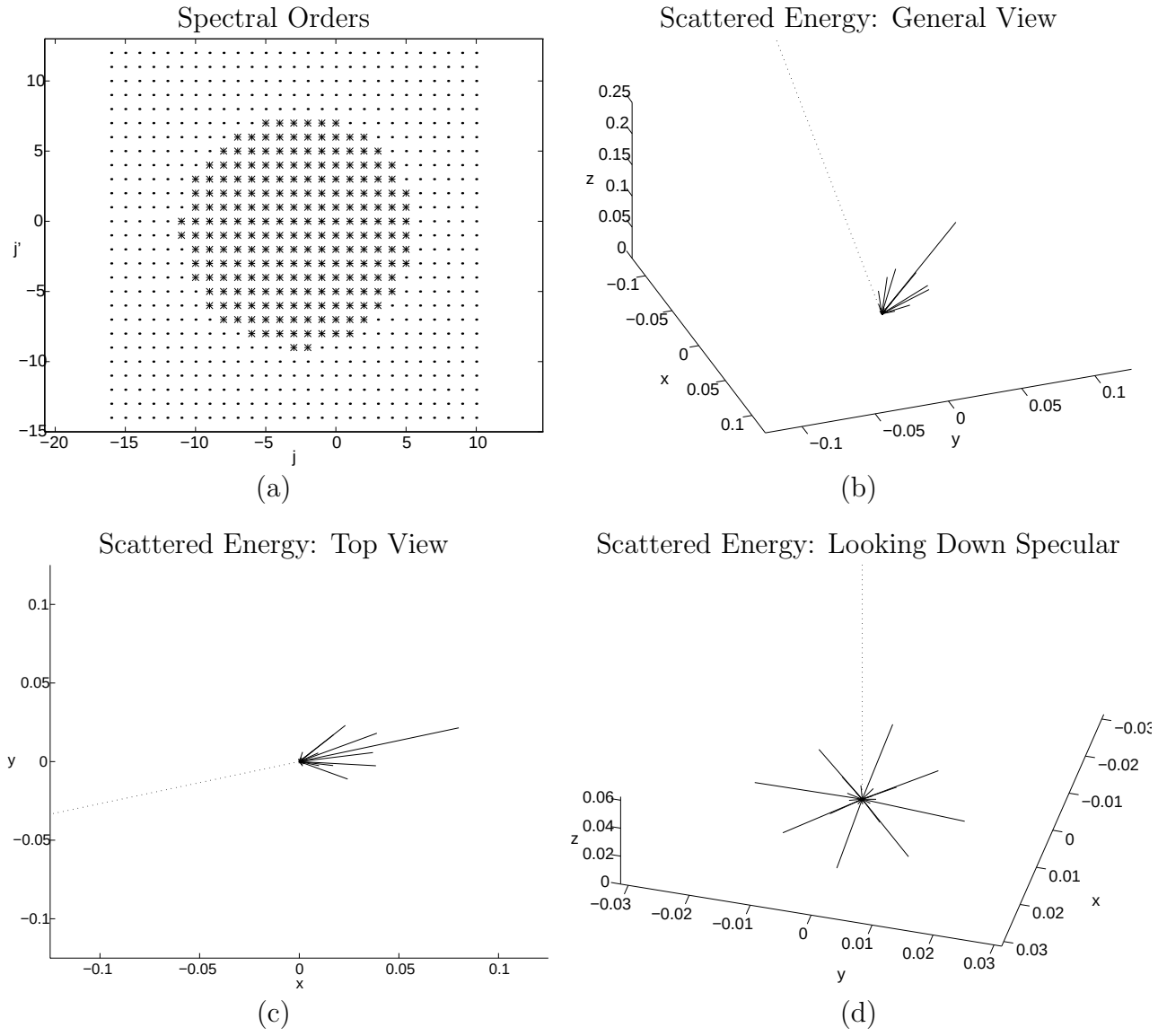

Figure 43: Saw-tooth surface for the Dirichlet problem and a matrix size of 729×729. (a) Spectral orders with 27 samples in j and j'; stars refer to radiating modes, and dots to non-radiating modes. Scattered energy distribution viewed from (b) $\theta = 40°, \phi = -20°$ (c) $\theta = 0°, \phi = -90°$ (d) $\theta = 20°, \phi = 15°$. Dashed line is incident field, solid lines are scattered Bragg modes. The magnitudes of the lines are proportional to the energy.

17.10 Suite of ϕ^i values (azimuthal angles of incidence)

$S(x,y)$	$-(d/2)\cos(2\pi x/L_1)\cos(2\pi y/L_2)$
(L_1, L_2)	(1,1)
$(d/L_1, d/L_2)$	(.075,.075)
$(\lambda/L_1, \lambda/L_2)$	(.12,.12)
θ^i	75°
Coordinate Sampling (x,y)	(19,19)

Matrix Size	ϕ^i	Radiating Orders	Spectral Sampling j	Spectral Sampling j'	Fill Time (s)	Linear Solution Time (s)	Condition Number	Error
361 × 361	0	221	19	19	4.5200	10.1100	31.0986	-3.0615
361 × 361	5	220	19	19	4.5400	10.1400	31.4446	-3.0616
342 × 361	10	220	19	18	4.1900	449.8600	16.7692	-3.1014
361 × 361	15	220	19	19	4.5400	10.4000	31.3239	-3.2300
342 × 361	20	217	18	19	4.5700	481.1000	16.9834	-1.9265
342 × 361	25	217	19	18	4.2100	473.0100	17.0979	-4.2997
361 × 361	30	221	19	19	4.5200	10.8000	31.0950	-4.2530
324 × 361	35	213	18	18	4.0100	403.6700	9.8004	-3.1581
361 × 361	40	220	19	19	4.7800	11.2700	31.3299	-4.9944
361 × 361	45	216	19	19	4.6900	11.7900	31.8821	-4.7223
361 × 361	50	220	19	19	4.8400	11.0400	31.3299	-4.9944
324 × 361	55	213	18	18	4.2800	454.1000	9.8004	-3.1581
361 × 361	60	221	19	19	4.8500	11.3000	31.0950	-4.2530
342 × 361	65	217	18	19	4.5100	500.8500	17.0979	-4.2997
342 × 361	70	217	19	18	4.2200	440.8000	16.9834	-1.9265
361 × 361	75	220	19	19	4.4200	10.1700	31.3239	-3.2300
342 × 361	80	220	18	19	4.1900	440.3000	16.7692	-3.1014
361 × 361	85	220	19	19	4.4400	10.1400	31.4446	-3.0616
361 × 361	90	221	19	19	4.4200	10.1300	31.0986	-3.0615

Table 18: Parameters and computational results for the Dirichlet problem where the incident azimuthal angle ϕ^i varies. The spectral sampling includes one extra row or column of non-radiating orders added to each side of the set of radiating orders. Convergence was good for all cases. The polar angle of incidence θ^i was near grazing.

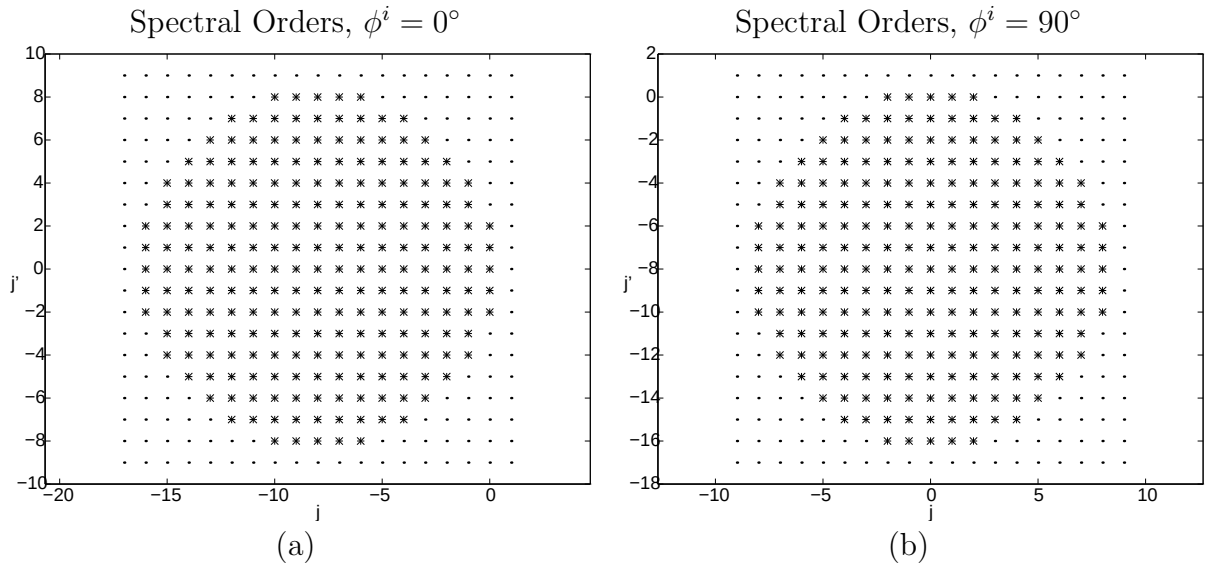

Figure 44: Spectral orders for incident angles (a) $\phi^i = 0°$ and (b) $\phi^i = 90°$ illustrating the shift of the radiating orders where stars refer to radiating modes, and dots to non-radiating modes. There were 19 samples in both j and j'.

17.11 Maximum Roughness with respect to incident polar angle θ^i

$S(x,y)$	$-(d/2)\cos(2\pi x/L_1)\cos(2\pi y/L_2)$
(L_1, L_2)	(1,1)
$(\lambda/L_1, \lambda/L_2)$	(.2,.2)
ϕ^i	50°

Line	Matrix Size	Added Non-radiating Rows and Columns on all Sides
Dash Dot	100×100	0
Solid	144×144	1
Dashed	196×196	2
Dotted	256×256	3

Table 19: Parameters for the Dirichlet example chosen to illustrate the maximum roughness $d/L\,(L = L_1 = L_2)$ of the surface $S(x,y)$ with respect to incident polar angle θ^i for error fixed at less than -2. Four different sampling schemes are illustrated and the results are plotted in Fig. 45. The different sampling schemes consist in adding non-radiating modes to the spectral sampling. Sampling is symmetric in x and y, and j and j'.

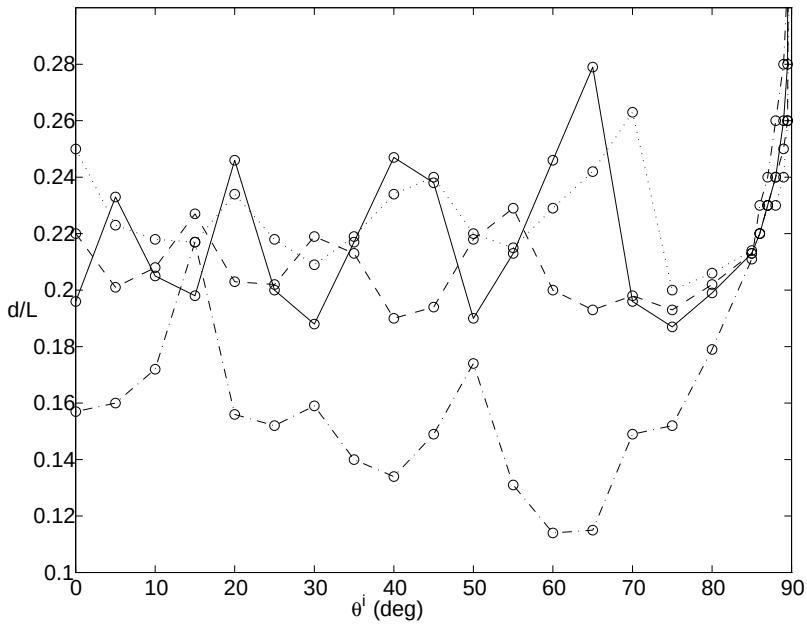

Figure 45: Maximum roughness for fixed error less than -2 with respect to incident polar angle θ^i for the Dirichlet problem. Data near $\theta^i = 0°$ is taken at .01° and data near $\theta^i = 90°$ is taken at 89.99°. The sampling schemes are explained in Table 19. The best overall results were achieved by adding a non-radiating row in the spectral sampling (solid curve). An expanded view near 90° is illustrated in Fig. 46.

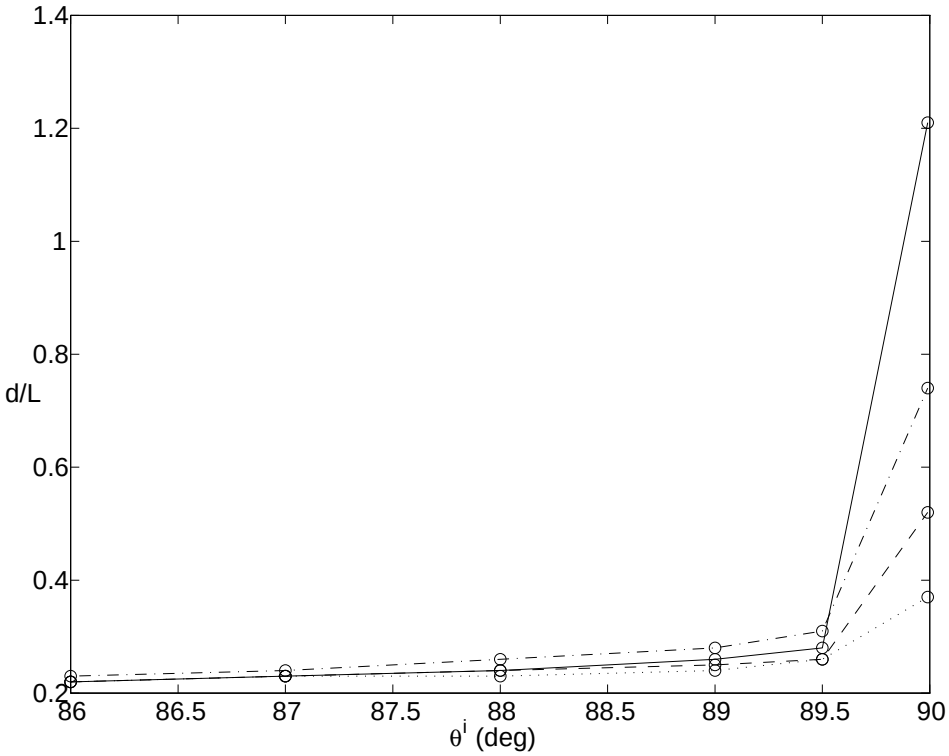

Figure 46: Maximum roughness for fixed error less than -2 with respect to incident polar angle θ^i for the Dirichlet problem. Expanded view near $\theta^i = 90°$ of Fig. 45. Data near $\theta^i = 90°$ is taken at 89.99°. Large increases in maximum roughness were noted near grazing incidence in several examples.

17.12 Maximum Roughness with respect to λ/L

$S(x,y)$	$-(d/2)\cos(2\pi x/L_1)\cos(2\pi y/L_2)$
(L_1, L_2)	(1,1)
θ^i	20°
ϕ^i	15°

Line	j left	j right	j' above	j' below
Dash Dot	0	0	0	0
Solid	1	1	1	1
Dashed	2	2	2	2
Dotted	3	3	3	3

Table 20: Parameters for the Dirichlet example chosen to illustrate the maximum roughness $d/L\,(L = L_1 = L_2)$ of the surface $S(x,y)$ with respect to λ/L, the ratio of the wavelength to surface period. Four different sampling schemes are illustrated and the results are plotted in Fig. 47. The schemes refer to additional spectral orders added in the left (or back scatter) direction or right (forward) scattered direction. Sampling is symmetric in x and y, and j and j'.

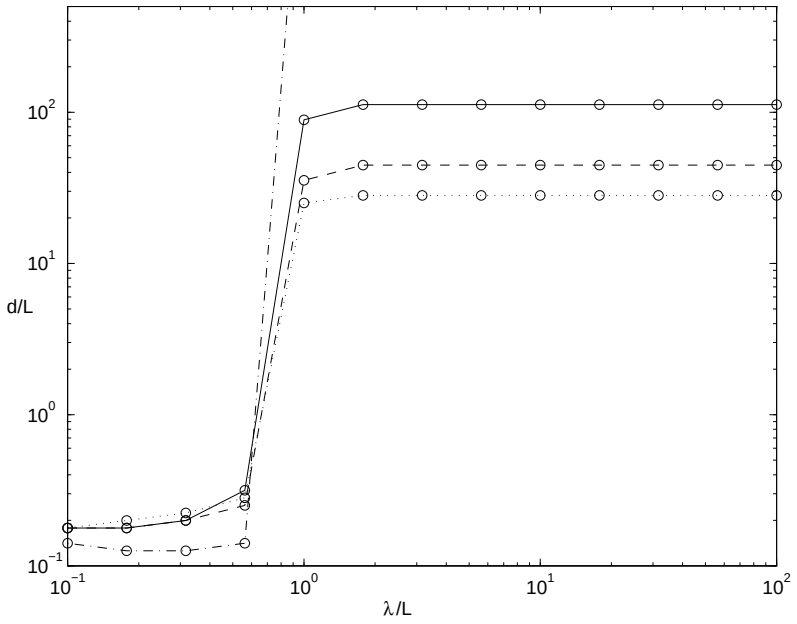

Figure 47: Maximum roughness for fixed error less than -2 with respect to λ/L ($L = L_1 = L_2$) for the Dirichlet problem. The spectral sampling schemes are explained in Table 19. Dash-dot line extends above graph to unknown height. The maximum roughness dramatically increased as λ/L approached 1 from below.

17.13 Complexity Analysis: Square Systems using Gaussian Elimination

$S(x, y)$	$-(d/2)\cos(2\pi x/L_1)\cos(2\pi y/L_2)$
(L_1, L_2)	(1,1)
$(d/L_1, d/L_2)$	(.05,.05)
$(\lambda/L_1, \lambda/L_2)$	(.2,.2)
Radiating Orders	77
θ^i	15°
ϕ^i	50°

n	Matrix Size	Fill Time (s)	Linear Solution Time (s)	Total Time (s)	Linear Solution Flops	Total Flops	Condition Number	Error
100	100 × 100	0.6600	0.3400	2.6100	2979571	3560327	2.1330	-7.7161
121	121 × 121	0.8800	0.5500	3.2500	5178093	6049260	3.1777	-10.3480
144	144 × 144	1.1400	0.8600	4.2200	8605675	9861692	3.7395	-9.9487
169	169 × 169	1.4400	1.3100	5.4500	13754205	15507736	5.3574	-12.0391
196	196 × 196	1.8000	2.0600	7.0900	21262891	23646400	6.2403	-11.1569
225	225 × 225	2.2700	3.0300	9.1500	31943271	35110606	8.6709	-13.2635
256	256 × 256	2.7200	4.2300	11.5100	46770283	50898260	10.0677	-12.3227
289	289 × 289	3.4600	5.8200	14.6800	66932735	72222722	13.7504	-14.9546
324	324 × 324	4.0800	8.4400	18.8700	93942291	100621792	15.9553	-13.6579
361	361 × 361	5.0500	11.0000	23.5300	129450199	137774438	21.5627	-15.6536
400	400 × 400	6.0000	15.6300	30.2800	175596267	185849772	25.0302	-15.1764
441	441 × 441	7.2200	19.7100	36.9900	234674363	247172550	33.5881	-15.9546
484	484 × 484	8.5500	27.2000	47.4200	309523963	324614720	39.0217	-15.2556
529	529 × 529	10.1200	33.6200	57.2800	403387983	421453254	52.0996	-15.3525
576	576 × 576	11.9600	46.5700	74.1100	519860667	541318036	60.5890	-14.9546
625	625 × 625	13.9400	58.7300	90.4700	663052481	688356756	80.5903	-14.9546
676	676 × 676	16.1800	81.3100	117.7300	837802955	867447752	93.8228	-15.0515
729	729 × 729	18.8000	95.4900	137.4300	$1.0495 \cdot 10^9$	$1.0840 \cdot 10^9$	124.4313	-15.1764
784	784 × 784	22.2800	128.5100	177.0600	$1.3039 \cdot 10^9$	$1.3439 \cdot 10^9$	145.0188	-15.1764
841	841 × 841	25.7300	152.2500	207.9600	$1.6080 \cdot 10^9$	$1.6540 \cdot 10^9$	191.8829	-14.9546
900	900 × 900	29.9400	207.3200	270.7500	$1.9690 \cdot 10^9$	$2.0217 \cdot 10^9$	223.8669	-15.2556

Table 21: Total time and flops for a complexity analysis of a Dirichlet problem. The graphical presentation is in Fig. 48. Only square systems are included, and total time and flops do not include condition number computation. Convergence was excellent for all cases.

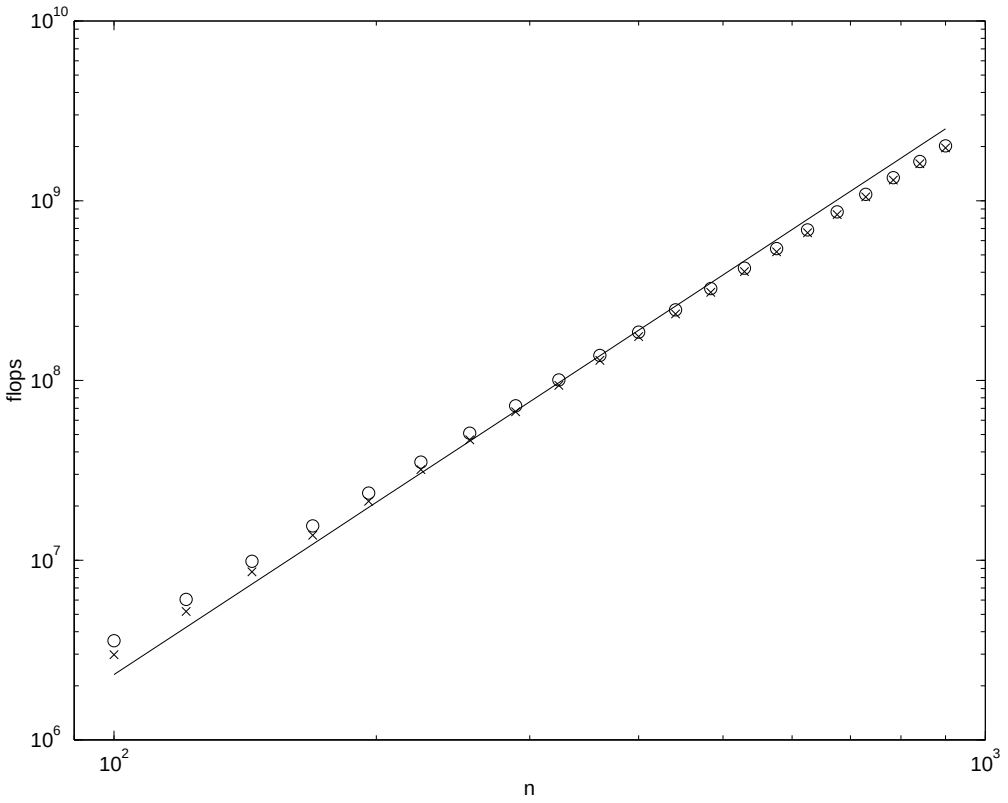

Figure 48: Complexity for the square system of the Dirichlet example in Table 21. o refers to total flops and $\times$ to linear flops. The solid line is a linear regression with slope 3.1818.

17.14 Complexity Analysis: Non-Square Systems using Pseudo-inverse

$S(x,y)$	$-(d/2)\cos(2\pi x/L_1)\cos(2\pi y/L_2)$
(L_1, L_2)	(1,1)
$(d/L_1, d/L_2)$	(.05,.05)
$(\lambda/L_1, \lambda/L_2)$	(.2,.2)
Radiating Orders	77
Spectral Samples (j,j')	(10,10)
θ^i	15°
ϕ^i	50°

n	Matrix Size	Fill Time (s)	Linear Solution Time (s)	Total Time (s)	Linear Solution Flops	Total Flops	Condition Number	Error
121	100 × 121	0.7600	6.6000	9.0500	76546056	77246449	1.6095	-8.0314
144	100 × 144	0.7600	10.3900	12.7700	91613110	92444523	1.5684	-7.9983
169	100 × 169	0.8400	11.6800	14.1800	111729654	112703479	1.5679	-7.9949
196	100 × 196	0.9100	15.0900	17.7400	134446511	135574140	1.5679	-7.9948
225	100 × 225	0.9500	18.0400	20.8000	161463948	162756773	1.5679	-7.9948
256	100 × 256	1.0500	29.6600	32.6200	195673238	197142651	1.5679	-7.9948
289	100 × 289	1.1700	28.8500	31.9600	233786404	235443797	1.5679	-7.9948
324	100 × 324	1.1700	35.3800	38.6300	278082076	279938841	1.5679	-7.9948
361	100 × 361	1.2800	41.2100	44.6400	328977394	331044923	1.5679	-7.9948
400	100 × 400	1.4700	57.0000	60.7800	387560989	389850674	1.5679	-7.9948
441	100 × 441	1.4900	61.6900	65.6000	454432455	456955688	1.5679	-7.9948
484	100 × 484	1.7100	74.5700	78.8100	530296741	533064914	1.5679	-7.9948
529	100 × 529	1.7200	88.1300	92.4900	616028707	619053212	1.5679	-7.9948
576	100 × 576	1.8800	115.9600	120.6800	712148268	715440497	1.5679	-7.9948
625	100 × 625	2.0300	116.7100	121.7000	820886393	824457738	1.5679	-7.9948
676	100 × 676	2.1800	138.6400	143.8900	942159666	946021519	1.5679	-7.9948
729	100 × 729	2.4800	158.6000	164.3600	$1.0764 \cdot 10^9$	$1.0806 \cdot 10^9$	1.5679	-7.9948
784	100 × 784	2.7600	191.4000	197.6500	$1.2253 \cdot 10^9$	$1.2297 \cdot 10^9$	1.5679	-7.9948
841	100 × 841	2.6500	200.0200	206.2500	$1.3878 \cdot 10^9$	$1.3926 \cdot 10^9$	1.5679	-7.9948
900	100 × 900	2.9000	233.8300	240.4500	$1.5688 \cdot 10^9$	$1.5740 \cdot 10^9$	1.5679	-7.9948

Table 22: Total time and flops for a complexity analysis of a Dirichlet problem. The graphical presentation is in Fig. 49. Only non-square systems are included, and total time and flops do not include condition number computation. Convergence was excellent for all cases although not as good as for the square systems in Table 21.

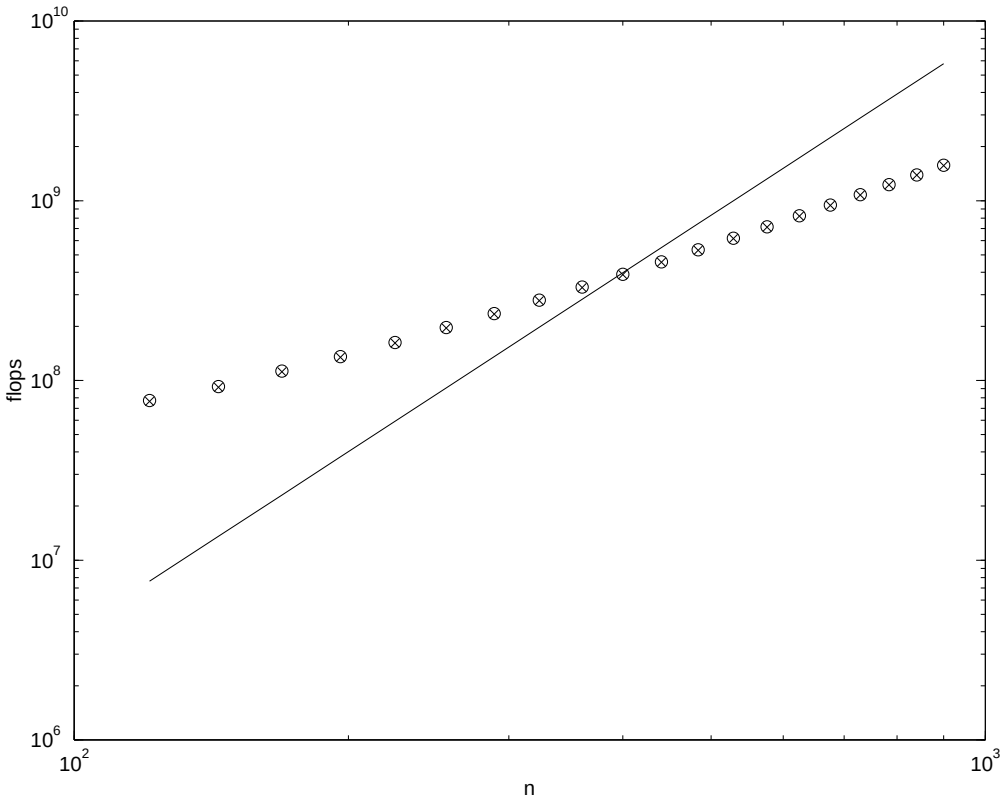

Figure 49: Complexity for the non-square system of the Dirichlet example in Table 22. o refers to total flops and $\times$ to linear flops. The solid line is a linear regression with slope 3.3046.

18 Neumann Computations

In this section we present results for the perfectly reflecting Neumann boundary value problem which corresponds electromagnetically to TM-polarization. The theoretical development is summarized in Section 10. Three sinusoidal surface examples are presented in Secs. 18.1 -18.6. Each example was investigated under non-grazing and near-grazing incidence and reflection conditions.

In Example 1, the wavelength was much less than the surface periods. In Example 2 the wavelength was approximately equal to the surface periods, and in Example 3 the wavelength was much greater than the surface periods. In addition, in Secs. 18.7 and 18.8 we present studies of the maximum roughness (d/L) for error less than -2 as a function of incident polar angle (Sec. 18.7) and wavelength to period ratio (Sec. 18.8). In the last two sections we briefly plot the complexity analysis for solving both square systems (Sec. 18.9) using Gaussian elimination and for non-square systems (Sec. 18.10) using pseudo-inverse techniques.

18.1 Example 1 Case A, No Grazing

$S(x,y)$	$-(d/2)\cos(2\pi x/L_1)\cos(2\pi y/L_2)$
(L_1, L_2)	(1,1)
$(d/L_1, d/L_2)$	(.075,.075)
$(\lambda/L_1, \lambda/L_2)$	(.12,.12)
Radiating Orders	218
θ^i	20°
ϕ^i	15°

Matrix Size	Number of Samples: Coord. x	Coord. y	Spectral j	Spectral j'	$\lambda/\Delta x$	$\lambda/\Delta y$	Fill Time (s)	Linear Solution Time (s)	Condition Number	Error
289 × 289	17	17	17	17	2.0400	2.0400	4.5400	6.2600	71.6735	-5.3770
324 × 324	18	18	18	18	2.1600	2.1600	5.6300	8.2700	264.7948	-7.1146
361 × 361	19	19	19	19	2.2800	2.2800	6.4400	11.4100	176.0992	-6.7235
400 × 400	20	20	20	20	2.4000	2.4000	8.0700	14.9700	214.8385	-7.6919
441 × 441	21	21	21	21	2.5200	2.5200	8.9100	18.8600	319.5200	-9.2915
484 × 484	22	22	22	22	2.6400	2.6400	10.6200	24.6100	425.0522	-8.3856
529 × 529	23	23	23	23	2.7600	2.7600	12.4000	31.9900	533.5915	-7.9052
576 × 576	24	24	24	24	2.8800	2.8800	16.2200	49.9800	681.1928	-8.9625
625 × 625	25	25	25	25	3.0000	3.0000	16.3700	53.4300	870.0316	-8.5241
676 × 676	26	26	26	26	3.1200	3.1200	19.2600	68.4200	$1.0996 \cdot 10^3$	-9.9120
729 × 729	27	27	27	27	3.2400	3.2400	22.0200	86.8900	$1.3827 \cdot 10^3$	-9.2995

Table 23: Parameters and computational results for the Neumann problem, Example 1, Case A. Angle parameters are chosen so that grazing incidence and reflection are avoided. Only square systems were considered. The parameters are the same as for the Dirichlet problem in Table 3. The results are comparable with both condition numbers and errors slightly larger here. The wavelength λ is much less than either of the (equal) surface periods. Convergence was excellent for all cases considered.

Matrix Size	Number of Samples				$\lambda/\Delta x$	$\lambda/\Delta y$	Fill Time (s)	Linear Solution Time (s)	Condition Number	Error
	Coord.		Spectral							
	x	y	j	j'						
289 × 324	18	18	17	17	2.1600	2.1600	4.6500	261.4700	35.9695	-6.2911
289 × 361	19	19	17	17	2.2800	2.2800	4.8600	284.9600	28.0875	-6.4678
289 × 400	20	20	17	17	2.4000	2.4000	5.1800	347.1100	27.5702	-6.5425
289 × 441	21	21	17	17	2.5200	2.5200	5.5500	431.0700	27.0242	-6.5551
289 × 484	22	22	17	17	2.6400	2.6400	6.2500	473.7800	27.0161	-6.5561
324 × 289	17	17	18	18	2.0400	2.0400	4.9100	239.5500	48.4037	-5.8041
361 × 289	17	17	19	19	2.0400	2.0400	5.4100	284.6200	51.5707	-5.9067
400 × 289	17	17	20	20	2.0400	2.0400	6.7300	305.4700	59.3619	-6.0161
441 × 289	17	17	21	21	2.0400	2.0400	6.7900	290.4100	58.9058	-3.3230
484 × 289	17	17	22	22	2.0400	2.0400	7.4600	334.3800	58.5645	-3.3227

Table 24: Parameters and computational results for the Neumann problem, Example 1, Case A. Angle parameters are chosen so that grazing incidence and reflection are avoided. Only non-square systems were considered. The parameters are the same as for the Dirichlet problem in Table 4. The results are comparable with the condition numbers slightly larger here. The wavelength λ is much less than either of the (equal) surface periods. The error was larger than for the square systems (Table 23) and deteriorated as more non-radiating modes were added.

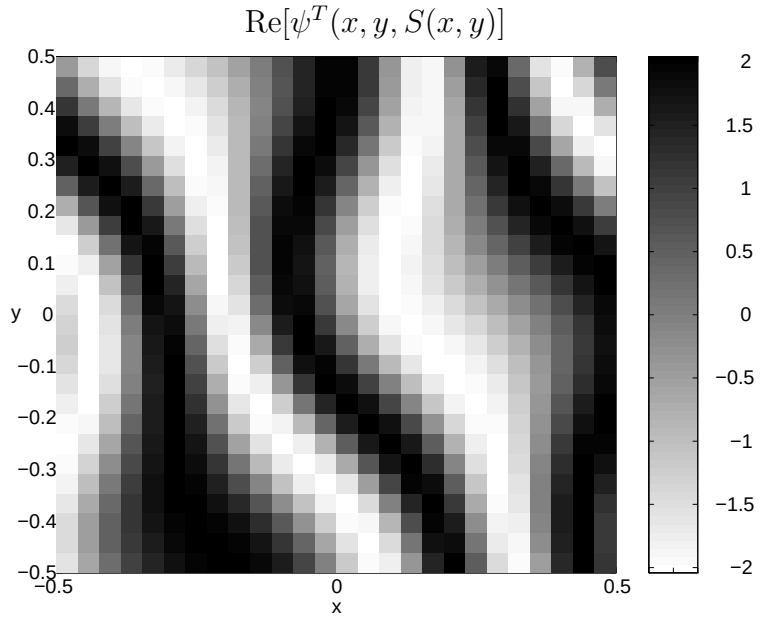

(a)

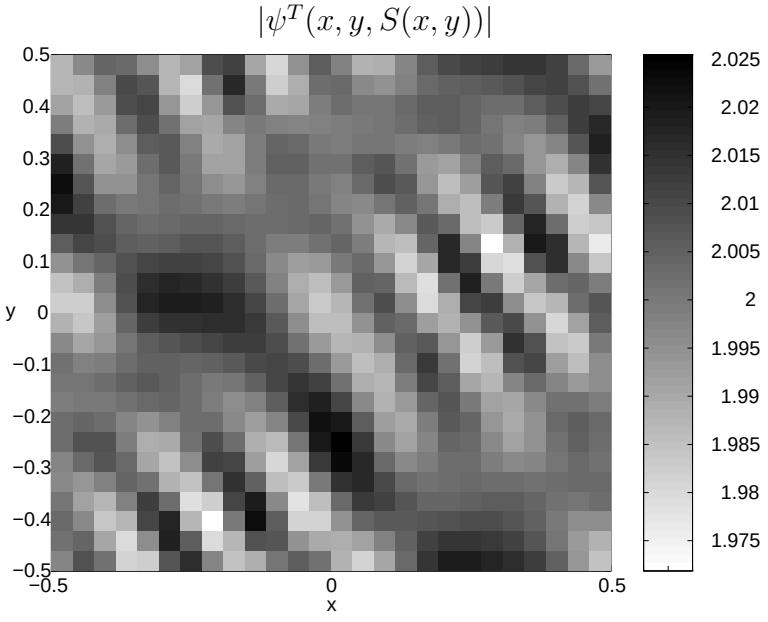

(b)

Figure 50: Example 1, Case A for the Neumann problem with a matrix size of 729×729 with an error of -9.2995. Real part (a) and magnitude (b) of the total field on the surface.

18.2 Example 1 Case B, Near-Grazing Incidence/Reflection

$S(x,y)$	$-(d/2)\cos(2\pi x/L_1)\cos(2\pi y/L_2)$
(L_1, L_2)	(1,1)
$(d/L_1, d/L_2)$	(.075,.075)
$(\lambda/L_1, \lambda/L_2)$	(.12,.12)
Radiating Orders	220
θ^i	75°
ϕ^i	15°

Matrix Size	Number of Samples				$\lambda/\Delta x$	$\lambda/\Delta y$	Fill Time (s)	Linear Solution Time (s)	Condition Number	Error
	Coord.		Spectral							
	x	y	j	j'						
289 × 289	17	17	17	17	2.0400	2.0400	4.3300	5.5800	86.0076	-0.4139
324 × 324	18	18	18	18	2.1600	2.1600	5.1000	7.6100	89.5040	-2.5973
361 × 361	19	19	19	19	2.2800	2.2800	6.1700	10.3800	87.4948	-1.6433
400 × 400	20	20	20	20	2.4000	2.4000	7.3400	13.7800	130.8250	-3.6024
441 × 441	21	21	21	21	2.5200	2.5200	8.5800	18.2600	167.8446	-3.1785
484 × 484	22	22	22	22	2.6400	2.6400	10.3200	25.4000	222.3018	-4.1685
529 × 529	23	23	23	23	2.7600	2.7600	11.9700	31.3500	276.9816	-3.6104
576 × 576	24	24	24	24	2.8800	2.8800	14.0500	42.5200	366.8100	-4.9838
625 × 625	25	25	25	25	3.0000	3.0000	16.2600	53.4500	452.7573	-4.4744
676 × 676	26	26	26	26	3.1200	3.1200	18.7300	73.3500	588.2078	-5.8107
729 × 729	27	27	27	27	3.2400	3.2400	21.5900	86.3000	801.8589	-5.3146

Table 25: Parameters and computational results for the Neumann problem, Example 1, Case B. Angle parameters are chosen to include grazing incidence and reflection. Only square systems were considered. The parameters are the same as for the Dirichlet problem in Table 5. The results are comparable with both condition numbers and errors slightly larger here. The wavelength λ is much less than either of the (equal) surface periods. Convergence improved by adding evanescent waves.

Matrix Size	Number of Samples Coord. x	Coord. y	Spectral j	Spectral j'	$\lambda/\Delta x$	$\lambda/\Delta y$	Fill Time (s)	Linear Solution Time (s)	Condition Number	Error
289 × 324	18	18	17	17	2.1600	2.1600	4.4800	251.7200	36.7048	-1.3732
289 × 361	19	19	17	17	2.2800	2.2800	4.7800	282.1300	26.9270	-1.2551
289 × 400	20	20	17	17	2.4000	2.4000	5.1400	342.0800	26.0958	-1.2489
289 × 441	21	21	17	17	2.5200	2.5200	5.4300	400.7700	25.1324	-1.2486
324 × 289	17	17	18	18	2.0400	2.0400	4.7700	238.5300	66.9280	-1.5271
361 × 289	17	17	19	19	2.0400	2.0400	5.3500	255.5300	58.0662	-0.0593
400 × 289	17	17	20	20	2.0400	2.0400	6.0200	273.9500	79.8781	-0.0532
441 × 289	17	17	21	21	2.0400	2.0400	6.6500	292.6200	59.8022	-0.0324

Table 26: Parameters and computational results for the Neumann problem, Example 1, Case B. Angle parameters are chosen to include grazing incidence and reflection. Only non-square systems were considered. The parameters are the same as for the Dirichlet problem in Table 6. The convergence results are poor and comparable to the Dirichlet results in Table 6 for these non-square systems. The wavelength λ is much less than either of the (equal) surface periods.

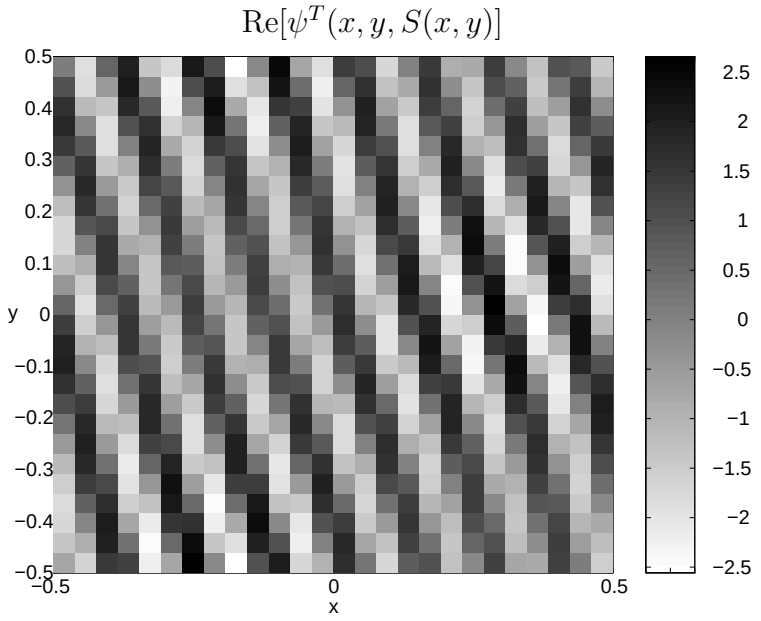

(a)

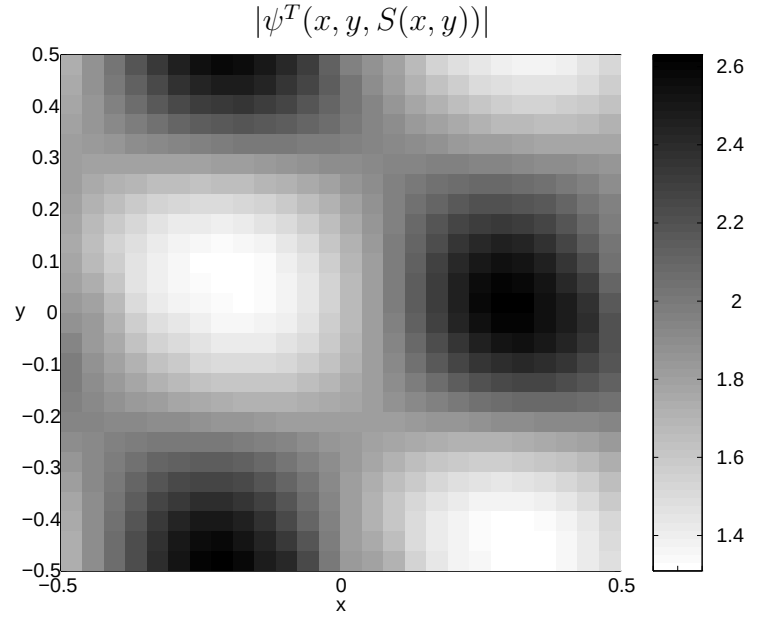

(b)

Figure 51: Example 1, Case B for the Neumann problem with a matrix size of 729×729 and an error of -5.3146. Real part (a) and magnitude (b) of the total field on the surface.

18.3 Example 2 Case A, No Grazing

$S(x,y)$	$-(d/2)\cos(2\pi x/L_1)\cos(2\pi y/L_2)$
(L_1, L_2)	(1,1)
$(d/L_1, d/L_2)$	(.25,.25)
$(\lambda/L_1, \lambda/L_2)$	(.95,.95)
Radiating Orders	3
θ^i	20°
ϕ^i	15°

Matrix Size	Number of Samples: Coord. x	Coord. y	Spectral j	Spectral j'	$\lambda/\Delta x$	$\lambda/\Delta y$	Fill Time (s)	Linear Solution Time (s)	Condition Number	Error
4×4	2	2	2	2	1.9000	1.9000	0.0200	0.0200	2.6463	< -15.9
16×16	4	4	4	4	3.8000	3.8000	0.1700	0.0100	86.5420	-15.0003
36×36	6	6	6	6	5.7000	5.7000	0.4100	0.0300	191.9474	-12.2171
64×64	8	8	8	8	7.6000	7.6000	0.8400	0.1300	$4.8087 \cdot 10^3$	-14.4775
100×100	10	10	10	10	9.5000	9.5000	1.3400	0.3700	$2.5102 \cdot 10^4$	-11.3225
144×144	12	12	12	12	11.4000	11.4000	2.2300	1.0100	$2.1760 \cdot 10^5$	-11.1530
196×196	14	14	14	14	13.3000	13.3000	3.3900	2.5000	$5.9507 \cdot 10^6$	-10.7172
256×256	16	16	16	16	15.2000	15.2000	3.8900	4.0100	$3.4245 \cdot 10^7$	-12.7071
324×324	18	18	18	18	17.1000	17.1000	5.5900	7.8200	$5.9760 \cdot 10^8$	-10.9631
400×400	20	20	20	20	19.0000	19.0000	8.0100	15.2300	$1.3403 \cdot 10^{10}$	-8.9165
484×484	22	22	22	22	20.9000	20.9000	11.7000	26.8200	$3.0515 \cdot 10^{10}$	-10.6510

Table 27: Parameters and computational results for the Neumann problem, Example 2, Case A. Angle parameters were chosen so that grazing incidence and reflection are avoided. Only square systems were considered. The parameters are the same as for the Dirichlet problem in Table 7. The results are comparable with both condition numbers and errors slightly larger here. The wavelength λ is much less than either of the two equal surface periods. Note that the surface is much rougher than Example 1.

Matrix Size	Number of Samples Coord. x	Coord. y	Spectral j	Spectral j'	$\lambda/\Delta x$	$\lambda/\Delta y$	Fill Time (s)	Linear Solution Time (s)	Condition Number	Error
4×16	4	4	2	2	3.8000	3.8000	0.0400	0.0100	2.1004	-0.2583
16×36	6	6	4	4	5.7000	5.7000	0.1500	0.0700	12.7005	-0.4986
16×64	8	8	4	4	7.6000	7.6000	0.1800	0.1700	12.6872	-0.5093
36×64	8	8	6	6	7.6000	7.6000	0.4000	0.6300	63.0013	-0.8613
36×144	12	12	6	6	11.4000	11.4000	0.4900	1.5200	58.2659	-0.7731
16×4	2	2	4	4	1.9000	1.9000	0.1300	$< 10^{-3}$	1.6042	-0.0038
36×16	4	4	6	6	3.8000	3.8000	0.3400	0.0500	19.2954	-0.0537
36×25	5	5	6	6	4.7500	4.7500	0.3300	0.1200	123.7270	-0.0858
100×64	8	8	10	10	7.6000	7.6000	1.0700	2.6200	$1.2963 \cdot 10^3$	-0.0763
144×100	10	10	12	12	9.5000	9.5000	1.6800	5.3600	$1.0412 \cdot 10^4$	-0.0818

Table 28: Parameters and computational results for the Neumann problem, Example 2, Case A. Angle parameters were chosen so that grazing incidence and reflection are avoided. Only non-square systems were considered. The parameters are the same as for the Dirichlet problem in Table 8. The error results are much poorer than the corresponding Dirichlet results. The wavelength λ is much less than either of the two equal surface periods. Note that the surface is much rougher than Example 1. For non-square systems of these types the error was very poor for all cases considered.

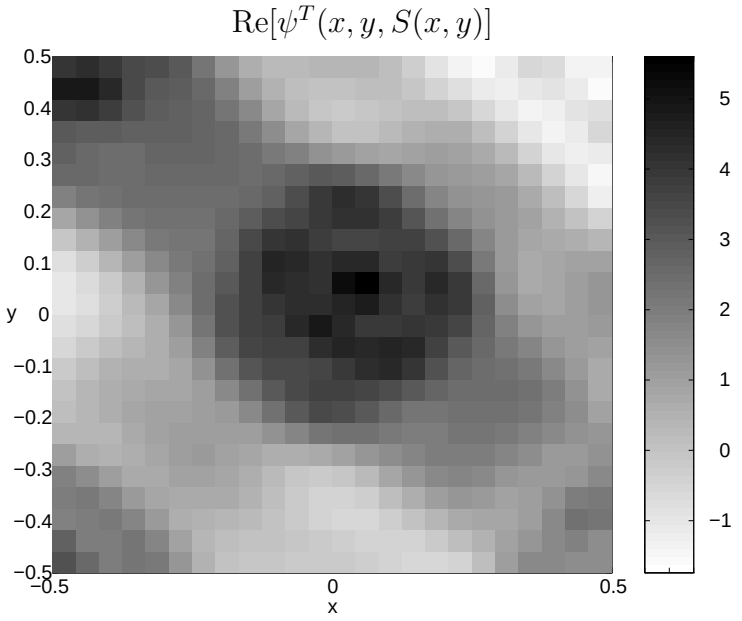

(a)

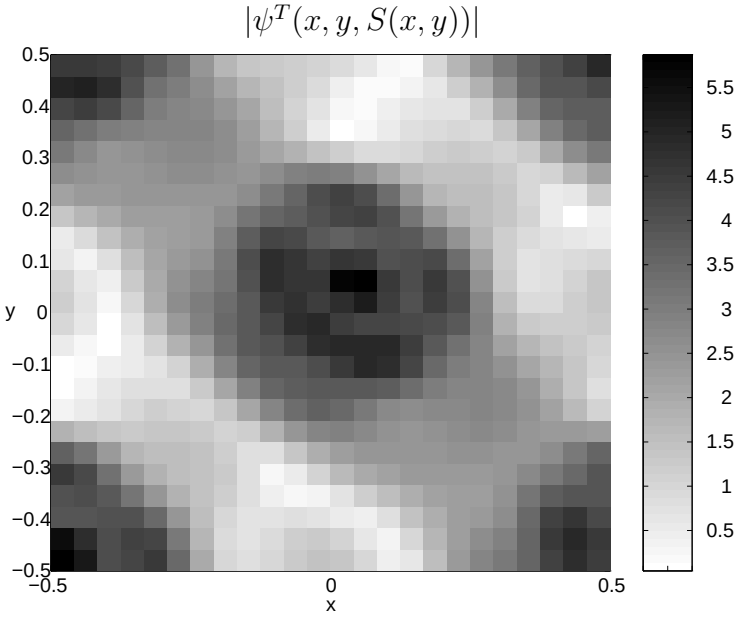

(b)

Figure 52: Example 2, Case A for the Neumann problem with matrix size of 64×625 and an error of -1.0708. Real part (a) and magnitude (b) of the total field on the surface.

18.4 Example 2 Case B, Near-Grazing Incidence/Reflection

$S(x,y)$	$-(d/2)\cos(2\pi x/L_1)\cos(2\pi y/L_2)$
(L_1, L_2)	(1,1)
$(d/L_1, d/L_2)$	(.25,.25)
$(\lambda/L_1, \lambda/L_2)$	(.95,.95)
Radiating Orders	4
θ^i	75°
ϕ^i	15°

Matrix Size	Number of Samples: Coord. x	Coord. y	Spectral j	Spectral j'	$\lambda/\Delta x$	$\lambda/\Delta y$	Fill Time (s)	Linear Solution Time (s)	Condition Number	Error
6 × 6	3	2	3	2	2.8500	1.9000	0.0400	0.0100	13.7189	-0.4203
16 × 16	4	4	4	4	3.8000	3.8000	0.1600	0.0100	26.7158	-0.9917
36 × 36	6	6	6	6	5.7000	5.7000	0.3900	0.0400	290.3924	-1.0087
64 × 64	8	8	8	8	7.6000	7.6000	0.7700	0.1300	$2.1112 \cdot 10^3$	-0.3907
100 × 100	10	10	10	10	9.5000	9.5000	1.3300	0.3900	$2.2048 \cdot 10^4$	-1.8794
144 × 144	12	12	12	12	11.4000	11.4000	2.1400	1.0400	$2.4370 \cdot 10^5$	0.1103
196 × 196	14	14	14	14	13.3000	13.3000	3.2300	2.4000	$2.5337 \cdot 10^6$	-0.7912
256 × 256	16	16	16	16	15.2000	15.2000	4.8500	5.0900	$4.0569 \cdot 10^7$	0.7296
324 × 324	18	18	18	18	17.1000	17.1000	7.1800	9.9200	$3.3593 \cdot 10^8$	-0.4512
400 × 400	20	20	20	20	19.0000	19.0000	8.7000	14.6100	$5.2406 \cdot 10^9$	0.5100
484 × 484	22	22	22	22	20.9000	20.9000	12.3700	27.1200	$5.3707 \cdot 10^{10}$	-0.4749

Table 29: Parameters and computational results for the Neumann problem, Example 2, Case B. Angle parameters were chosen so that grazing incidence and reflection are included. Only square systems were considered. The parameters are the same as for the Dirichlet problem in Table 9. Except for one case, the convergence results are very poor, much poorer than for the Dirichlet problem. The surface was also very rough and the wavelength was comparable to the (equal) surface periods.

Matrix Size	Number of Samples Coord. x	Coord. y	Spectral j	Spectral j'	$\lambda/\Delta x$	$\lambda/\Delta y$	Fill Time (s)	Linear Solution Time (s)	Condition Number	Error
6×16	4	4	3	2	3.8000	3.8000	0.0400	0.0200	3.2595	-0.1398
16×36	6	6	4	4	5.7000	5.7000	0.1400	0.0600	20.4915	-0.2428
16×64	8	8	4	4	7.6000	7.6000	0.1500	0.1500	18.8569	-0.2112
36×64	8	8	6	6	7.6000	7.6000	0.3400	0.5500	126.5558	-0.5375
36×144	12	12	6	6	11.4000	11.4000	0.4200	1.3000	101.4699	-0.3302
16×4	2	2	4	4	1.9000	1.9000	0.1200	0.0100	1.7423	$-8.1994 \cdot 10^{-5}$
36×16	4	4	6	6	3.8000	3.8000	0.2900	0.0500	21.3568	-0.0160
36×25	5	5	6	6	4.7500	4.7500	0.2900	0.1200	102.0965	-0.0200
100×64	8	8	10	10	7.6000	7.6000	0.9300	2.0200	$1.3979 \cdot 10^{3}$	-0.0182
144×100	10	10	12	12	9.5000	9.5000	1.4900	4.7700	$1.1137 \cdot 10^{4}$	-0.0192

Table 30: Parameters and computational results for the Neumann problem, Example 2, Case B. Only non-square systems were considered. The convergence results are very poor.

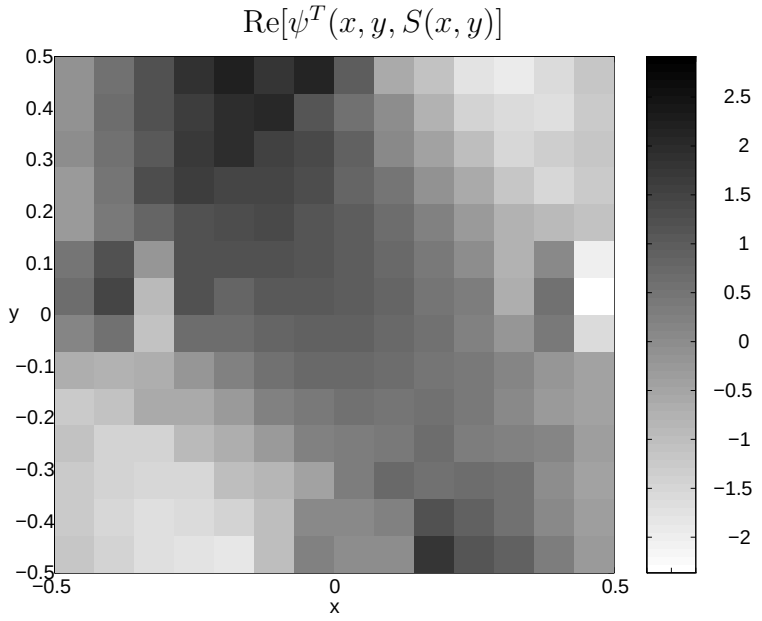

(a)

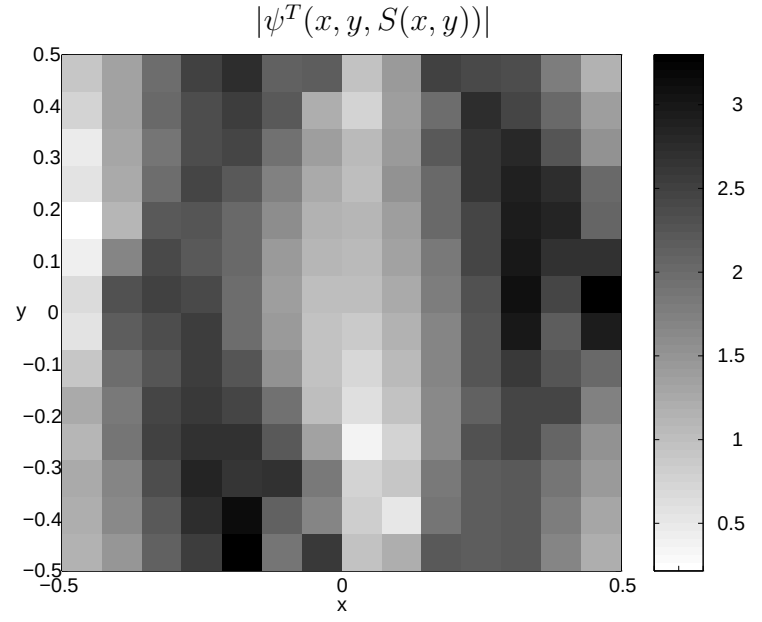

(b)

Figure 53: Example 2, Case B for the Neumann problem with a matrix size of 144×225 and error of -1.0815. Real part (a) and magnitude (b) of the total field ψ^{T} on the surface.

18.5 Example 3 Case A, No Grazing

$S(x,y)$	$-(d/2)\cos(2\pi x/L_1)\cos(2\pi y/L_2)$
(L_1, L_2)	(1,1)
$(d/L_1, d/L_2)$	(2.5,2.5)
$(\lambda/L_1, \lambda/L_2)$	(100,100)
Radiating Orders	1
θ^i	20°
ϕ^i	15°

Matrix Size	Number of Samples Coord. x	Coord. y	Spectral j	Spectral j'	$\lambda/\Delta x$	$\lambda/\Delta y$	Fill Time (s)	Linear Solution Time (s)	Condition Number	Error
1×1	1	1	1	1	100	100	0.0200	0.0100	1.0000	-15.6536
4×4	2	2	2	2	200	200	0.0400	0.0100	150.8090	< -15.9
9×9	3	3	3	3	300	300	0.0700	$< 10^{-3}$	$1.1223 \cdot 10^{7}$	-11.6853
16×16	4	4	4	4	400	400	0.1300	0.0100	$1.2199 \cdot 10^{10}$	-14.8754
25×25	5	5	5	5	500	500	0.1900	0.0200	$1.5243 \cdot 10^{13}$	-11.0679
36×36	6	6	6	6	600	600	0.3000	0.0200	$5.4403 \cdot 10^{18}$	-11.4632
49×49	7	7	7	7	700	700	0.4400	0.0600	$3.2937 \cdot 10^{19}$	-11.5722
64×64	8	8	8	8	800	800	0.6000	0.1000	$1.0084 \cdot 10^{25}$	-10.8135
81×81	9	9	9	9	900	900	0.8000	0.1800	$8.2139 \cdot 10^{26}$	-11.2613
100×100	10	10	10	10	1000	1000	1.0100	0.3100	$9.3545 \cdot 10^{30}$	-11.0669
121×121	11	11	11	11	1100	1100	1.3300	0.5200	$1.7865 \cdot 10^{33}$	-9.0654

Table 31: Parameters and computational results for the Neumann problem, Example 3, Case A. Angle parameters are chosen so that grazing incidence and reflection are avoided. Only square systems were considered. The parameters are the same as for the Dirichlet problem in Table 11. The results are comparable. Note the very large roughness of the surface and the very large ratio of wavelength λ to surface period.

Matrix Size	Number of Samples: Coord. x	Coord. y	Spectral j	Spectral j'	$\lambda/\Delta x$	$\lambda/\Delta y$	Fill Time (s)	Linear Solution Time (s)	Condition Number	Error
1×4	2	2	1	1	200	200	0.0200	$< 10^{-3}$	1.0000	-15.3525
1×9	3	3	1	1	300	300	0.0200	$< 10^{-3}$	1.0000	-0.0544
25×36	6	6	5	5	600	600	0.2100	0.1100	$1.8443 \cdot 10^{10}$	-0.0196
25×49	7	7	5	5	700	700	0.2200	0.1600	$3.0348 \cdot 10^{11}$	-0.0388
49×81	9	9	7	7	900	900	0.4900	0.6900	$2.7864 \cdot 10^{16}$	$< 10^{-6}$
9×4	2	2	3	3	200	200	0.0700	$< 10^{-6}$	300.9883	-15.3525
49×16	4	4	7	7	400	400	0.3900	0.0600	$9.2010 \cdot 10^{11}$	-0.5169
81×16	4	4	9	9	400	400	0.6300	0.0800	$2.6837 \cdot 10^{14}$	-0.5169
121×16	4	4	11	11	400	400	0.9400	0.1100	$2.8679 \cdot 10^{16}$	$< 10^{-6}$
169×16	4	4	13	13	400	400	1.3100	0.1400	$3.0469 \cdot 10^{18}$	$< 10^{-6}$

Table 32: Parameters and computational results for the Neumann problem, Example 3, Case A. Angle parameters are chosen so that grazing incidence and reflection are avoided. Only non-square systems were considered. The parameters are the same as for the Dirichlet problem in Table 12. The error results are comparable to the Dirichlet example only for two systems (1×4 and 9×4). Otherwise adding more non-radiating modes for the Neumann problem caused the error to severely deteriorate. Note the very large roughness of the surface and the very large ratio of wavelength λ to surface period.

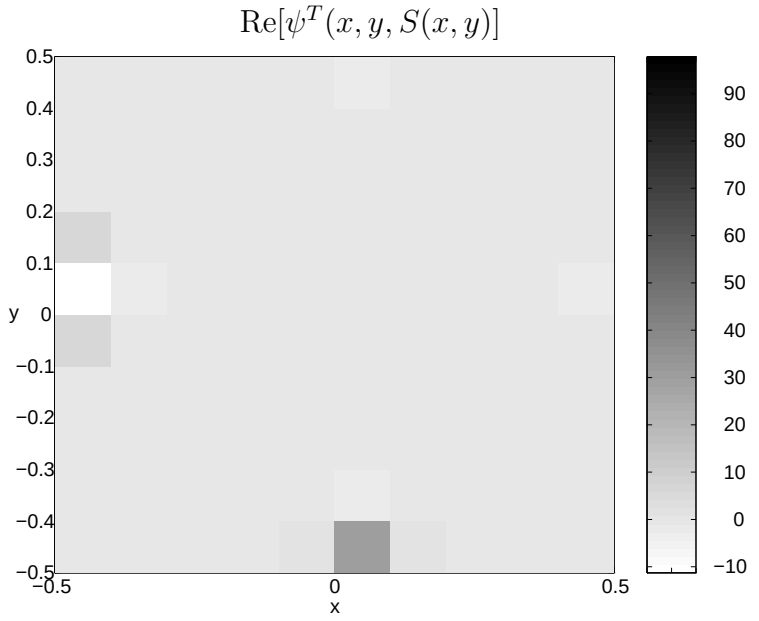

(a)

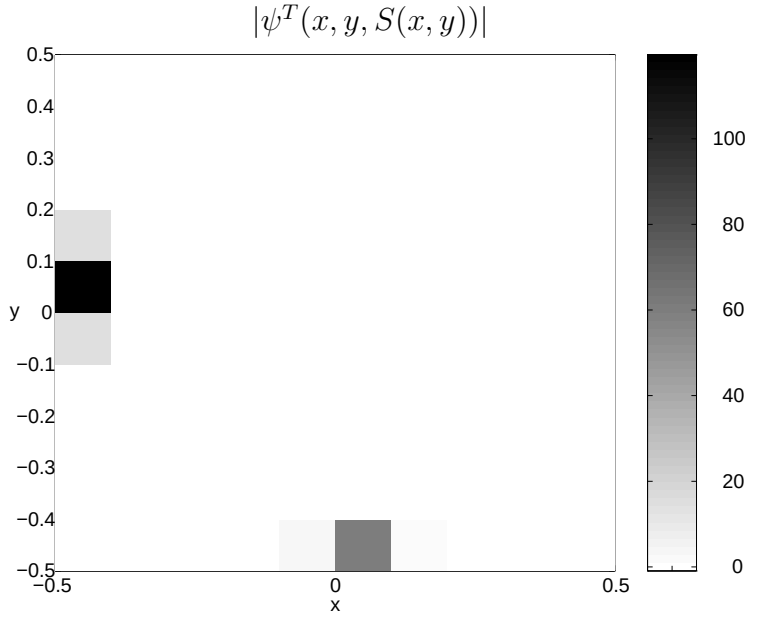

(b)

Figure 54: Example 3, Case B for the Neumann problem with a matrix of size 64×625 and an error of -1.0708. Real part (a) and magnitude (b) of the total field ψ^{T} on the surface.

18.6 Example 3 Case B, Near-Grazing Incidence/Reflection

$S(x,y)$	$-(d/2)\cos(2\pi x/L_1)\cos(2\pi y/L_2)$
(L_1, L_2)	(1,1)
$(d/L_1, d/L_2)$	(2.5,2.5)
$(\lambda/L_1, \lambda/L_2)$	(100,100)
Radiating Orders	1
θ^i	75°
ϕ^i	15°

Matrix Size	Number of Samples: Coordinate x	Coordinate y	Spectral j	Spectral j'	$\lambda/\Delta x$	$\lambda/\Delta y$	Fill Time (sec)	Linear Solution Time (sec)	Condition Number	Error
1×1	1	1	1	1	100	100	0.0200	0.0100	1.0000	< -15.9
4×4	2	2	2	2	200	200	0.0300	0.0100	549.6318	< -15.9
9×9	3	3	3	3	300	300	0.0800	0.0100	$2.4487 \cdot 10^{7}$	-11.4872
16×16	4	4	4	4	400	400	0.1400	$< 10^{-3}$	$1.9106 \cdot 10^{10}$	-15.0515
25×25	5	5	5	5	500	500	0.2200	0.0200	$2.8038 \cdot 10^{13}$	-10.2382
36×36	6	6	6	6	600	600	0.3300	0.0400	$4.4693 \cdot 10^{18}$	-12.6217
49×49	7	7	7	7	700	700	0.5000	0.0600	$4.6066 \cdot 10^{19}$	-10.9173
64×64	8	8	8	8	800	800	0.6500	0.1100	$5.1819 \cdot 10^{24}$	-12.3248
81×81	9	9	9	9	900	900	0.8600	0.2000	$6.7276 \cdot 10^{26}$	-10.6541
100×100	10	10	10	10	1000	1000	1.1000	0.3200	$2.6052 \cdot 10^{31}$	-12.0901
121×121	11	11	11	11	1100	1100	1.4300	0.5700	$1.1520 \cdot 10^{33}$	-10.2995

Table 33: Parameters and computational results for the Neumann problem, Example 3, Case B. Angle parameters are chosen so that grazing incidence and reflection are included. Only square systems were considered. The parameters are the same as for the Dirichlet problem in Table 13. The results are comparable. Note the very large roughness of the surface and the very large ratio of wavelength λ to surface period.

Matrix Size	Number of Samples				$\lambda/\Delta x$	$\lambda/\Delta y$	Fill Time (sec)	Linear Solution Time (sec)	Condition Number	Error
	Coordinate		Spectral							
	x	y	j	j'						
1×4	2	2	1	1	200	200	0.0200	0.0100	1.0000	-15.0515
1×9	3	3	1	1	300	300	0.0100	$< 10^{-3}$	1.0000	-1.7293
25×36	6	6	5	5	600	600	0.2300	0.1300	$8.3850 \cdot 10^{9}$	-1.6105
25×49	7	7	5	5	700	700	0.2500	0.1600	$1.3370 \cdot 10^{11}$	-1.6842
49×81	9	9	7	7	900	900	0.5300	0.7500	$1.2489 \cdot 10^{16}$	$-1.7840 \cdot 10^{-15}$
9×4	2	2	3	3	200	200	0.0700	$< 10^{-3}$	$1.0928 \cdot 10^{3}$	-14.8754
49×16	4	4	7	7	400	400	0.4100	0.0500	$9.2096 \cdot 10^{11}$	-1.3718
81×16	4	4	9	9	400	400	0.6800	0.0800	$2.6875 \cdot 10^{14}$	-1.3718
121×16	4	4	11	11	400	400	1.0400	0.1200	$4.2683 \cdot 10^{16}$	$< 10^{-6}$
169×16	4	4	13	13	400	400	1.4400	0.1500	$1.9399 \cdot 10^{18}$	$< 10^{-6}$

Table 34: Parameters and computational results for the Neumann problem, Example 3, Case A. Angle parameters are chosen so that grazing incidence and reflection are avoided. Only non-square systems were considered. The parameters are the same as for the Dirichlet problem in Table 14. The error results are comparable to the Dirichlet example only for two systems (1×4 and 9×4). Otherwise adding more non-radiating modes for the Neumann problem caused the error to severely deteriorate. Note the very large roughness of the surface and the very large ratio of wavelength λ to surface period.

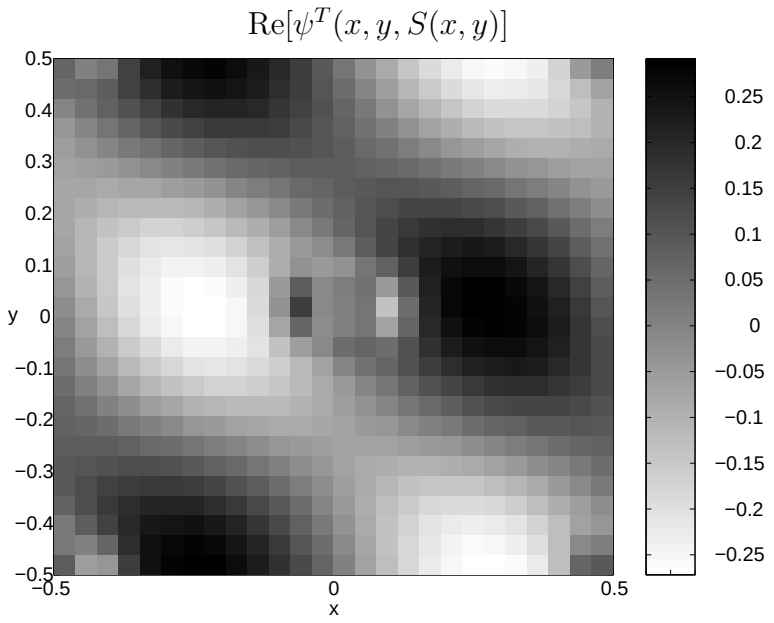

(a)

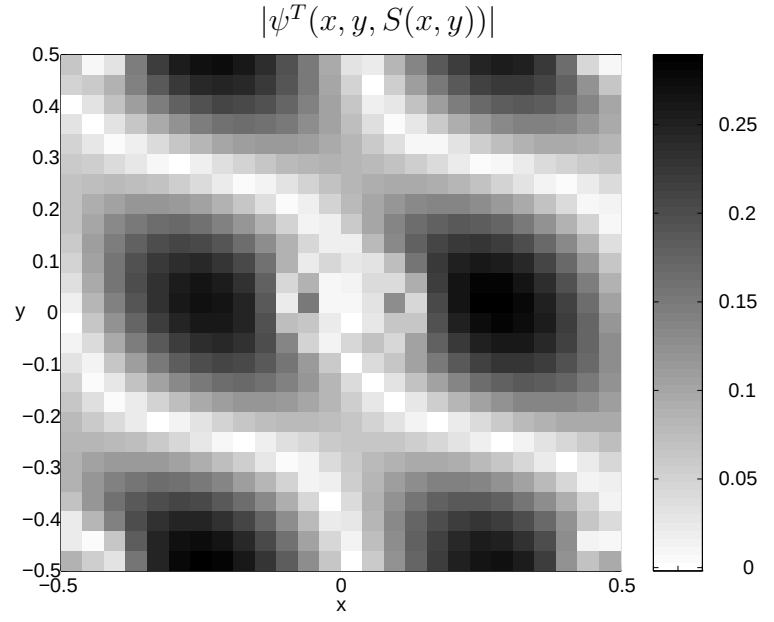

(b)

Figure 55: Example 3, Case B for the Neumann problem with matrix size of 25×729 and an error of -1.7037. Real part (a) and magnitude (b) of the total field ψ^{T} on the surface.

18.7 Maximum Roughness with respect to incident polar angle θ^i

$S(x,y)$	$-(d/2)\cos(2\pi x/L_1)\cos(2\pi y/L_2)$
(L_1, L_2)	(1,1)
$(\lambda/L_1, \lambda/L_2)$	(.2,.2)
ϕ^i	50°

Line	Matrix Size	Added Non-radiating Rows and Columns on all Sides
Dash Dot	100×100	0
Solid	144×144	1
Dashed	196×196	2
Dotted	256×256	3

Table 35: Parameters for the Neumann example chosen to illustrate the maximum roughness d/L ($L = L_1 = L_2$) of the surface $S(x,y)$ with respect to incident polar angle θ^i for fixed error less than -2. Four different sampling schemes are illustrated and the results are plotted in Fig. 56. The different sampling schemes consist in adding non-radiating modes to the spectral sampling. Sampling is symmetric in x and y, and j and j'.

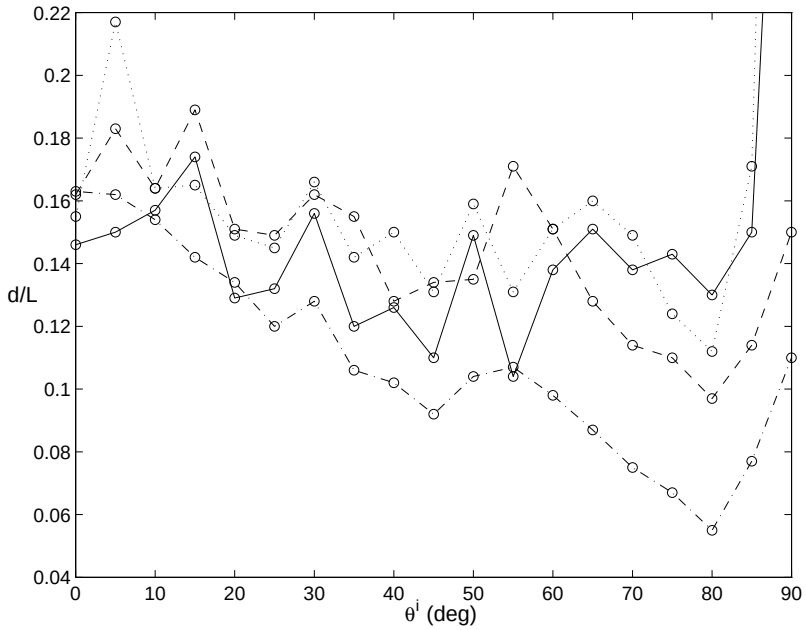

Figure 56: Maximum roughness for error less than -2 with respect to the incident polar angle θ^i for the Neumann problem. Data near $\theta^i = 0°$ is taken at .01° and data near $\theta^i = 90°$ is taken at 89.99°. The sampling schemes are explained in Table 35. The best overall results were achieved by adding at least one non-radiating row in the spectral sampling. An expanded view near 90° is illustrated in Fig. 57. The roughness values were not as large as those for the Dirichlet example (compare with Fig. 45).

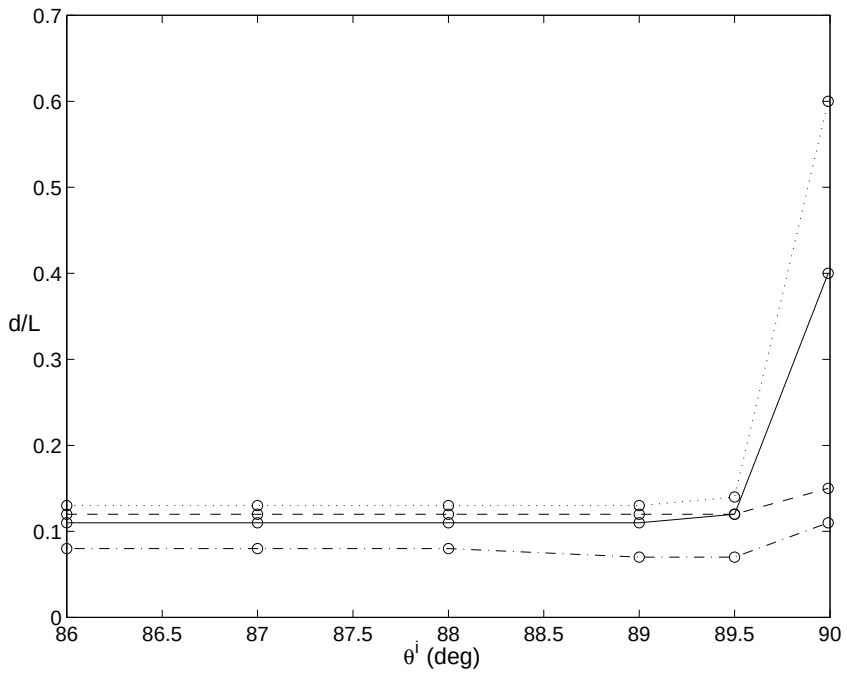

Figure 57: Maximum roughness for error less than -2 with respect to incident polar angle θ^i for the Neumann problem. Expanded view near $\theta^i = 90°$ of Fig. 56. Data near $\theta^i = 90°$ is taken at 89.99°. Large increases in maximum roughness were noted near grazing incidence for the Dirichlet problem also (see Fig. 46).

18.8 Maximum Roughness with respect to λ/L

$S(x,y)$	$-(d/2)\cos(2\pi x/L_1)\cos(2\pi y/L_2)$
(L_1, L_2)	(1,1)
θ^i	20°
ϕ^i	15°

Line	j left	j right	j' above	j' below
Dash Dot	0	0	0	0
Solid	1	1	1	1
Dashed	2	2	2	2
Dotted	3	3	3	3

Table 36: Parameters for the Neumann example chosen to illustrate the maximum roughness d/L ($L = L_1 = L_2$) of the surface $S(x,y)$ with respect λ/L, the ratio of the wavelength to surface period. Four different sampling schemes are illustrated and the results are plotted in Fig. 58. The schemes refer to additional spectral orders added in the left (or back scatter) direction or right (forward) scattered direction. Sampling is symmetric in x and y, and j and j'.

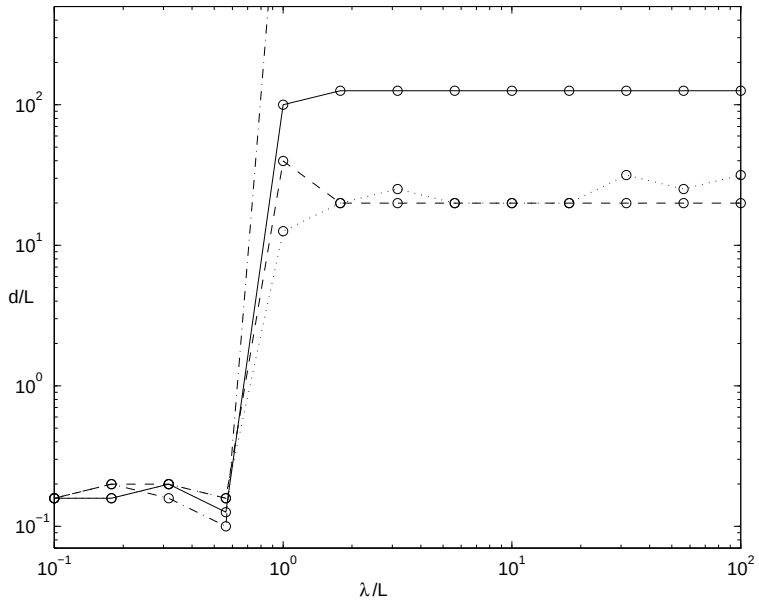

Figure 58: Maximum roughness for error less than -2 with respect to λ/L ($L = L_1 = L_2$) for the Neumann problem. The spectral sampling schemes are explained in Table 36. Dash-dot line extends above graph to unknown height. The maximum roughness dramatically increased as λ/L approached 1 from below.

18.9 Complexity Analysis: Square Systems using Gaussian Elimination

$S(x,y)$	$-(d/2)\cos(2\pi x/L_1)\cos(2\pi y/L_2)$
(L_1, L_2)	(1,1)
$(d/L_1, d/L_2)$	(.05,.05)
$(\lambda/L_1, \lambda/L_2)$	(.2,.2)
Radiating Orders	77
θ^i	15°
ϕ^i	50°

n	Matrix Size	Fill Time (s)	Linear Solution Time (s)	Total Time (s)	Linear Solution Flops	Total Flops	Condition Number	Error
100	100 × 100	1.0900	0.3300	3.5400	2983555	3747420	25.9228	-6.3102
121	121 × 121	1.4300	0.5900	4.5900	5194085	6348039	38.4574	-7.9452
144	144 × 144	1.7800	0.9300	5.6800	8620995	10293268	51.2732	-8.6658
169	169 × 169	2.1600	1.3200	6.9800	13771475	16115137	75.4129	-9.4168
196	196 × 196	2.6600	2.0500	8.8500	21287883	24483004	70.5720	-10.3954
225	225 × 225	3.2900	2.8700	11.1300	31960955	36216765	96.7695	-10.4603
256	256 × 256	3.9400	4.1200	13.8700	46788611	52345660	107.9030	-10.3744
289	289 × 289	5.1500	6.5600	19.1500	66999163	74131481	142.5696	-10.4739
324	324 × 324	5.8400	8.0300	21.9000	93985331	103002588	158.3785	-10.4788
361	361 × 361	6.8600	10.9000	27.4400	129526733	140776399	204.1964	-10.4705
400	400 × 400	8.9000	16.3900	36.4400	175621219	189490724	226.2025	-10.4705
441	441 × 441	9.7700	20.3400	43.1700	234739869	251658763	286.6307	-10.4707
484	484 × 484	11.5100	25.7700	52.8000	309632403	330074516	316.8435	-10.4704
529	529 × 529	14.3200	33.6700	65.5600	403483403	427969005	396.3320	-10.4706
576	576 × 576	16.0600	46.9100	83.3900	519886307	548984268	437.3828	-10.4707
625	625 × 625	18.9600	60.0900	103.2400	663118281	697448231	541.6599	-10.4705
676	676 × 676	21.7700	82.6200	130.1200	837985899	878220388	596.9795	-10.4706
729	729 × 729	26.6500	101.1300	156.9500	$1.0496 \cdot 10^9$	$1.0965 \cdot 10^9$	733.4159	-10.4707
784	784 × 784	29.4000	124.3100	188.4600	$1.3040 \cdot 10^9$	$1.3583 \cdot 10^9$	807.4657	-10.4706
841	841 × 841	35.0100	166.2200	239.8700	$1.6081 \cdot 10^9$	$1.6707 \cdot 10^9$	985.5373	-10.4703
900	900 × 900	40.8200	215.0700	299.6600	$1.9692 \cdot 10^9$	$2.0409 \cdot 10^9$	$1.0841 \cdot 10^3$	-10.4705

Table 37: Total time and flops for a complexity analysis of a Neumann problem using Gaussian elimination. The graphical presentation is in Fig. 59. Only square systems are included, and total time and flops do not include condition number computation. Convergence was excellent in all cases but not as good as for the Dirichlet problem (see Table 21).

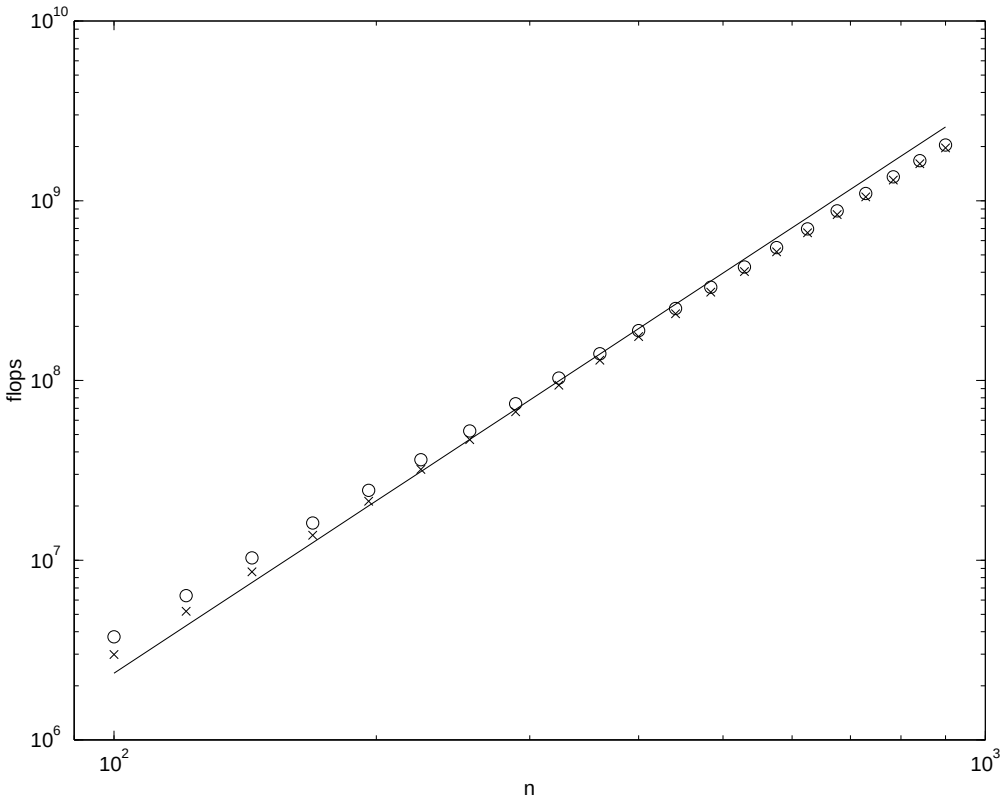

Figure 59: Complexity for the square system of the Neumann example in Table 37. o refers to total flops and × to linear flops. The solid line is a linear regression with slope 3.1855.

18.10 Complexity Analysis: Non-Square Systems using Pseudo-inverse

$S(x,y)$	$-(d/2)\cos(2\pi x/L_1)\cos(2\pi y/L_2)$
(L_1, L_2)	(1,1)
$(d/L_1, d/L_2)$	(.05,.05)
$(\lambda/L_1, \lambda/L_2)$	(.2,.2)
Radiating Orders	77
Spectral Samples (j,j')	(10,10)
θ^i	15°
ϕ^i	50°

n	Matrix Size	Fill Time (s)	Linear Solution Time (s)	Total Time (s)	Linear Solution Flops	Total Flops	Condition Number	Error
121	100 × 121	1.0700	6.6100	9.8000	77092355	78013501	15.5743	-6.4439
144	100 × 144	1.1500	9.7300	12.9200	93443434	94536839	14.9025	-6.4177
169	100 × 169	1.2100	11.7600	15.1700	112960043	114240685	14.8993	-6.4146
196	100 × 196	1.4100	14.8600	18.5000	136598375	138081232	14.8983	-6.4146
225	100 × 225	1.3800	18.3400	21.9800	164617868	166317918	14.8983	-6.4146
256	100 × 256	1.4700	29.9900	33.8200	197401820	199334041	14.8983	-6.4146
289	100 × 289	1.5600	27.9700	31.9500	235654991	237834361	14.8983	-6.4146
324	100 × 324	1.6500	36.1400	40.3900	280135407	282576904	14.8983	-6.4146
361	100 × 361	1.7800	41.8300	46.2900	331431661	334150263	14.8983	-6.4146
400	100 × 400	1.8800	58.2700	63.0400	389955928	392966613	14.8983	-6.4146
441	100 × 441	1.9900	62.1800	67.4100	456988126	460305872	14.8983	-6.4146
484	100 × 484	2.4100	73.1200	78.6800	532568291	536208076	14.8983	-6.4146
529	100 × 529	2.2800	86.4800	92.1900	619053350	623030152	14.8983	-6.4146
576	100 × 576	2.7100	118.5900	124.7700	715764172	720092969	14.8983	-6.4146
625	100 × 625	2.5600	114.8400	120.9800	824110130	828805900	14.8983	-6.4146
676	100 × 676	2.7400	134.8400	141.5200	945054596	950132317	14.8983	-6.4146
729	100 × 729	3.3000	154.4300	161.7600	$1.0798 \cdot 10^9$	$1.0853 \cdot 10^9$	14.8983	-6.4146
784	100 × 784	3.3800	189.6300	197.1900	$1.2289 \cdot 10^9$	$1.2348 \cdot 10^9$	14.8983	-6.4146
841	100 × 841	3.2200	202.1300	209.9100	$1.3938 \cdot 10^9$	$1.4001 \cdot 10^9$	14.8983	-6.4146
900	100 × 900	3.5100	231.5600	239.6200	$1.5753 \cdot 10^9$	$1.5820 \cdot 10^9$	14.8983	-6.4146

Table 38: Total time and flops for a complexity analysis of a Neumann problem. The graphical presentation is in Fig. 60. Only non-square systems are included, and total time and flops do not include condition number computation. Convergence was excellent for all cases, but still not quite as good as for the Dirichlet problem (see Table 22).

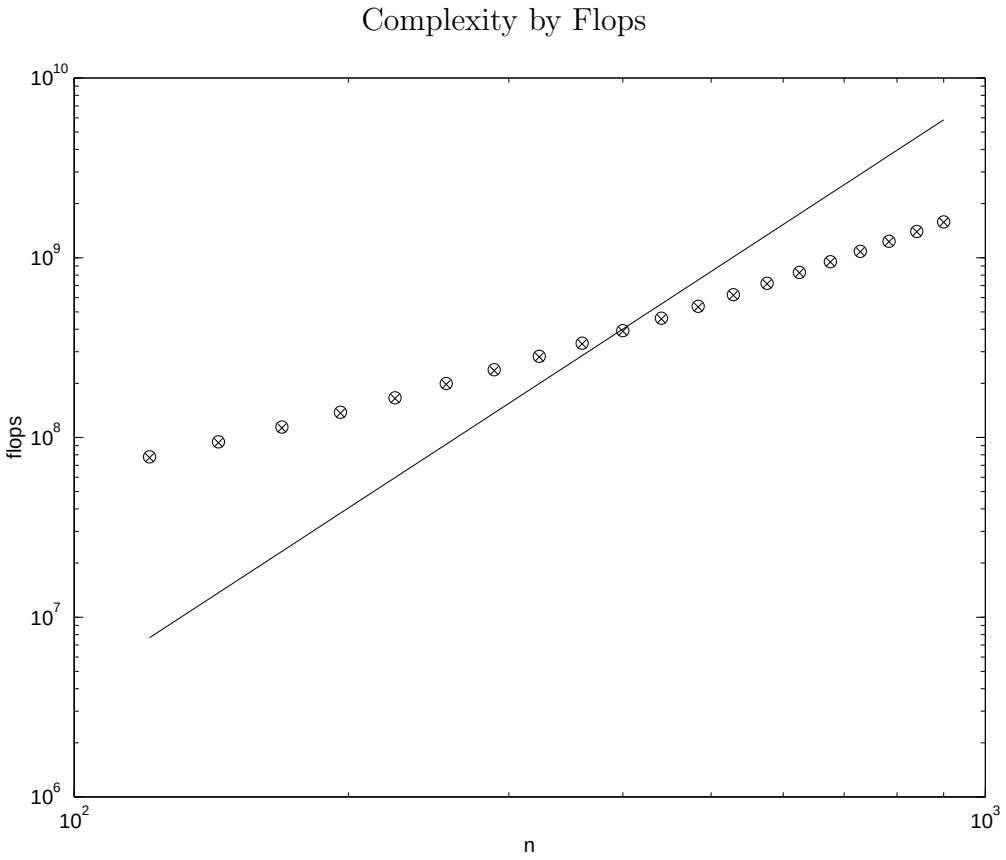

Figure 60: Complexity for the non-square system of the Neumann example in Table 38. o refers to total flops and $\times$ to linear flops. The solid line is a linear regression with slope 3.3061

19 Transmission Interface Computations

In this section we present results for the full transmission case using the theoretical results from Sections 13-15. In particular, we base the solution on Eq. (15.24) with the subsequent discussion in Section 15 which refers to the condition number and the numerical treatment of non-square systems using pseudo-inverse techniques.

Two parameter examples are presented in Secs. 19.1 and 19.2 (wavelength less than surface periods), Secs. 19.3 and 19.4 (wavelength approximately the same as the periods) under conditions of no grazing and grazing incidence and reflection, and Secs. 19.5 and 19.6 (wavelength much greater than the surface periods).

We present tables of results for both square and non-square systems of equations and plots of the boundary unknowns and scattered fields. The square systems results are a degenerate case of transmission where only the density changes in the lower region. The non-square systems also involved a change in wavenumber ($\kappa \neq 1$) and consequently a different number of radiating orders above and below the surface. Although even these systems could be made square by appropriate coordinate sampling, the non-square systems resulted in smaller condition numbers and better error results which was in direct contrast to the results for the Dirichlet and Neumann problems in Sections 17 and 18.

Extensive suites of parameters are presented in Secs. 19.7-19.9. In Sec. 19.7, the azimuthal angle of incidence ϕ^i is varied from 0° to 90° in 5° increments using different spectral and coordinate sampling schemes. Convergence was excellent and nearly uniform for all cases. In Sec. 19.8, we present a suite of κ-values ranging from 0.1 to slightly more than 5. The results for κ-values less than one amount to inverting the usual layer scattering problems since the medium of the incident field has the *higher* wavenumber. We include these examples to demonstrate the flexibility of the numerical codes. In Sec. 19.9 we present a suite of ρ-values ranging from 0.1 to 10, again with the values less than one representing incidence on a less dense medium. Again the flexibility of the numerical code is evident. For both κ- and ρ-variability we present an example of perfect transmission.

The maximum roughness (slope) values at fixed error are included in Sec. 19.10 (with respect to θ^i, the polar angle of incidence), Sec. 19.11 (with respect to ρ), Sec. 19.12 (with respect to ρ at near-grazing incidence), Sec. 19.13 (with respect to κ), and Sec. 19.14 (with respect to κ at near-grazing incidence).

Finally, in Secs. 19.15 and 19.16 we briefly present results on the complexity analysis of both square and non-square systems. The results are substantially the same as those for the Dirichlet and Neumann problems.

19.1 Example 1 Case A

$S(x,y)$	$-(d/2)\cos(2\pi x/L_1)\cos(2\pi y/L_2)$
(L_1, L_2)	(1,1)
$(d/L_1, d/L_2)$	(.075,.075)
$(\lambda/L_1, \lambda/L_2)$	(.25,.25)
ρ	2
θ^i	20°
ϕ^i	15°

κ	1
Radiating Orders Above	50
Radiating Orders Below	50
Fraction of Energy Reflected	.111

System Size	Number of Samples Coord. x	Coord. y	Spectral Above j	Above j'	Below j	Below j'	$\lambda/\Delta x$	$\lambda/\Delta y$	Fill Time (s)	Linear Solution Time (s)	Condition Number	Error
128 × 128	8	8	8	8	8	8	2.0000	2.0000	1.5500	0.7100	28.5260	-4.1255
162 × 162	9	9	9	9	9	9	2.2500	2.2500	2.1200	1.3200	41.4069	-5.2561
200 × 200	10	10	10	10	10	10	2.5000	2.5000	2.8300	2.5000	47.1880	-5.1305
242 × 242	11	11	11	11	11	11	2.7500	2.7500	3.5800	4.4600	60.6896	-7.1244
288 × 288	12	12	12	12	12	12	3.0000	3.0000	4.5300	7.0900	75.3934	-6.4628
338 × 338	13	13	13	13	13	13	3.2500	3.2500	5.0400	8.9900	96.0624	-7.6576
392 × 392	14	14	14	14	14	14	3.5000	3.5000	6.0400	14.0100	117.2922	-7.3163

Table 39: Parameters and computational results for Example 1, Case A of the transmission problem. Spectral modes in both x and y and both above and below the surface are present. The coordinate sampling is the product of the numbers in the columns "x" and "y" then doubled to cover both reflection and transmission regions. Only square systems were treated and the wavelength was 1/4 of the two equal surface periods.

κ	1.5
Radiating Orders Above	50
Radiating Orders Below	116
Fraction of Energy Reflected	.0149

System Size	Number of Samples						$\lambda/\Delta x$	$\lambda/\Delta y$	Fill Time (s)	Linear Solution Time (s)	Condition Number	Error
	Coord.		Spectral									
			Above		Below							
	x	y	j	j'	j	j'						
208 × 288	12	12	8	8	12	12	3.0000	3.0000	2.4700	31.6100	10.4720	-6.4737
250 × 338	13	13	9	9	13	13	3.2500	3.2500	3.4200	46.9800	15.1591	-6.8363
296 × 392	14	14	10	10	14	14	3.5000	3.5000	4.1500	93.3000	19.3543	-8.8283
346 × 450	15	15	11	11	15	15	3.7500	3.7500	5.4600	192.0100	26.4751	-8.1641
400 × 512	16	16	12	12	16	16	4.0000	4.0000	7.0600	335.0800	33.1836	-7.9554
458 × 578	17	17	13	13	17	17	4.2500	4.2500	8.1000	409.9800	43.9118	-9.9717
520 × 648	18	18	14	14	18	18	4.5000	4.5000	9.6800	661.1100	54.4365	-10.0931

Table 40: Parameters and computational results for Example 1, Case A of the transmission problem. Spectral modes in both x and y and both above and below the surface are present. The numbers of modes above and below are different since $\kappa \neq 1$. Additional coordinate samples were added to make the linear system non-square. For this transmission case the non-square systems performed slightly better than the square systems.

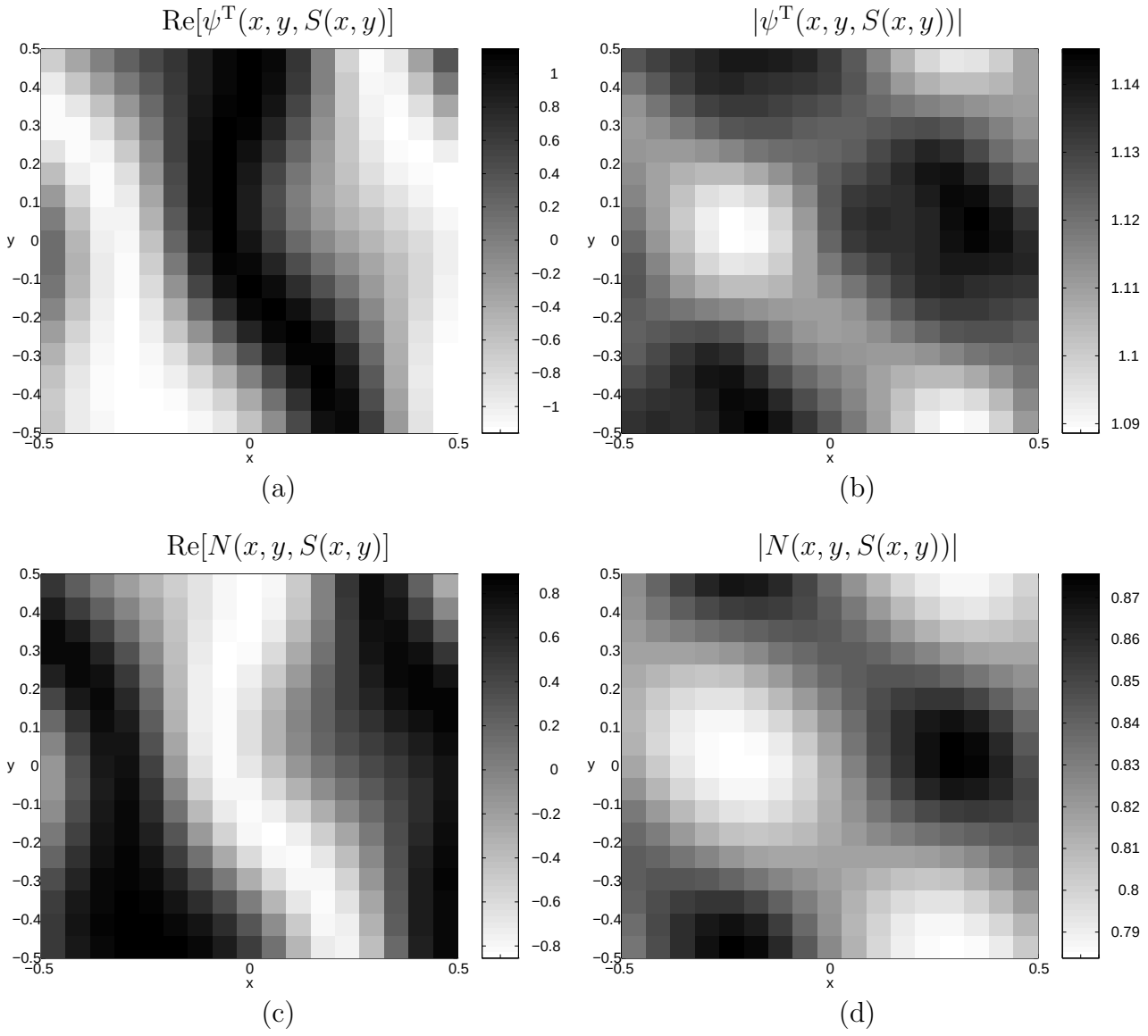

Figure 61: Example 1, Case A for the transmission problem with a square system of size 520×648 and $\kappa = 1.5$. Real part (a) and magnitude (b) of the total field ψ^{T} on the surface and real part (c) and magnitude (d) of the surface current or normal derivative N on the surface.

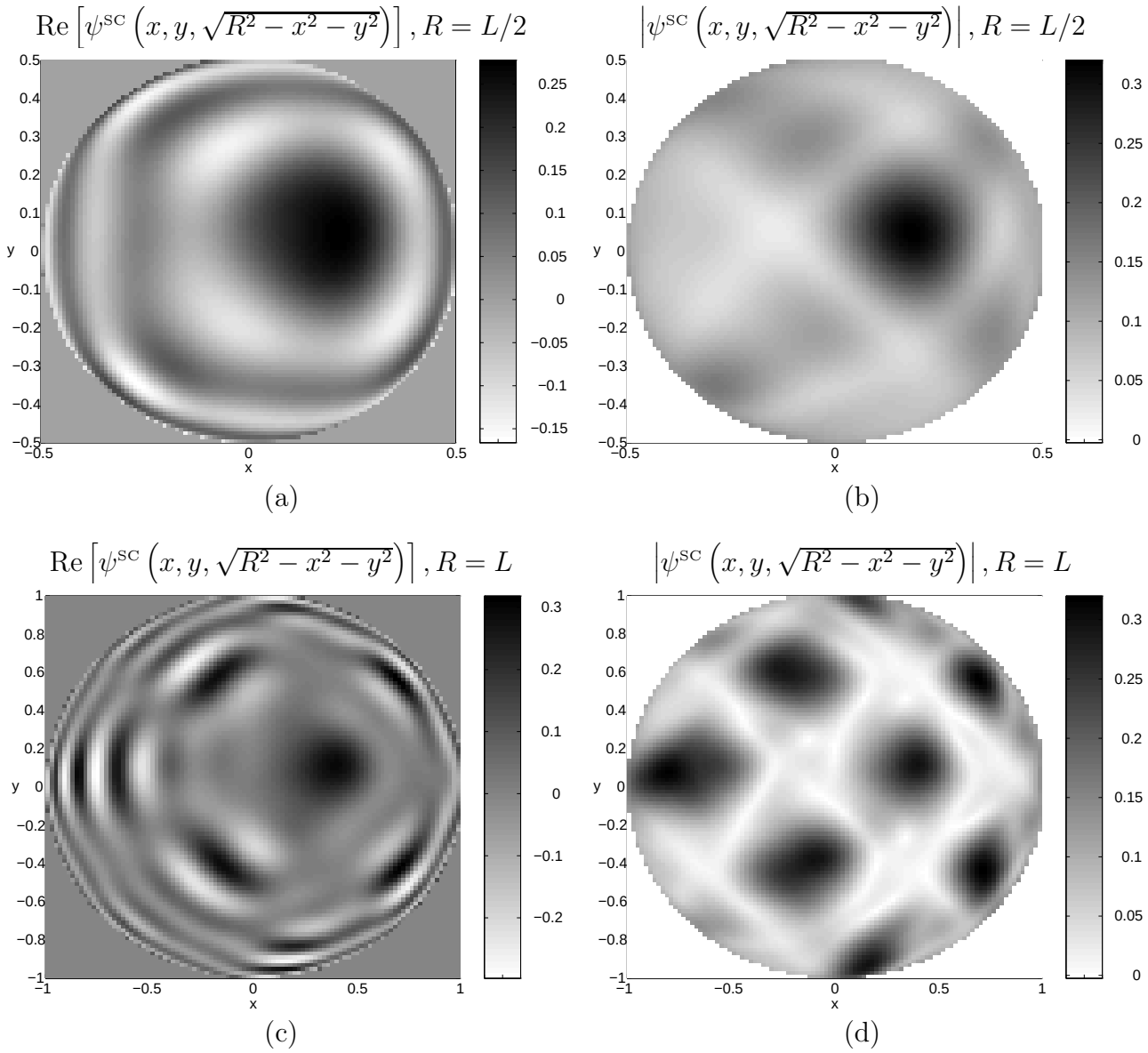

Figure 62: Example 1, Case A for the transmission problem with a non-square system of size 520×648 and $\kappa = 1.5$. Real part ((a) and (c)) and magnitude ((b) and (d)) of the scattered field plotted on hemispheres of radius $R = L/2$ ((a) and (b)) and $R = L$ ((c) and (d)) looking down. Here $L = L_1 = L_2$. The resolution of the pictures is 100×100.

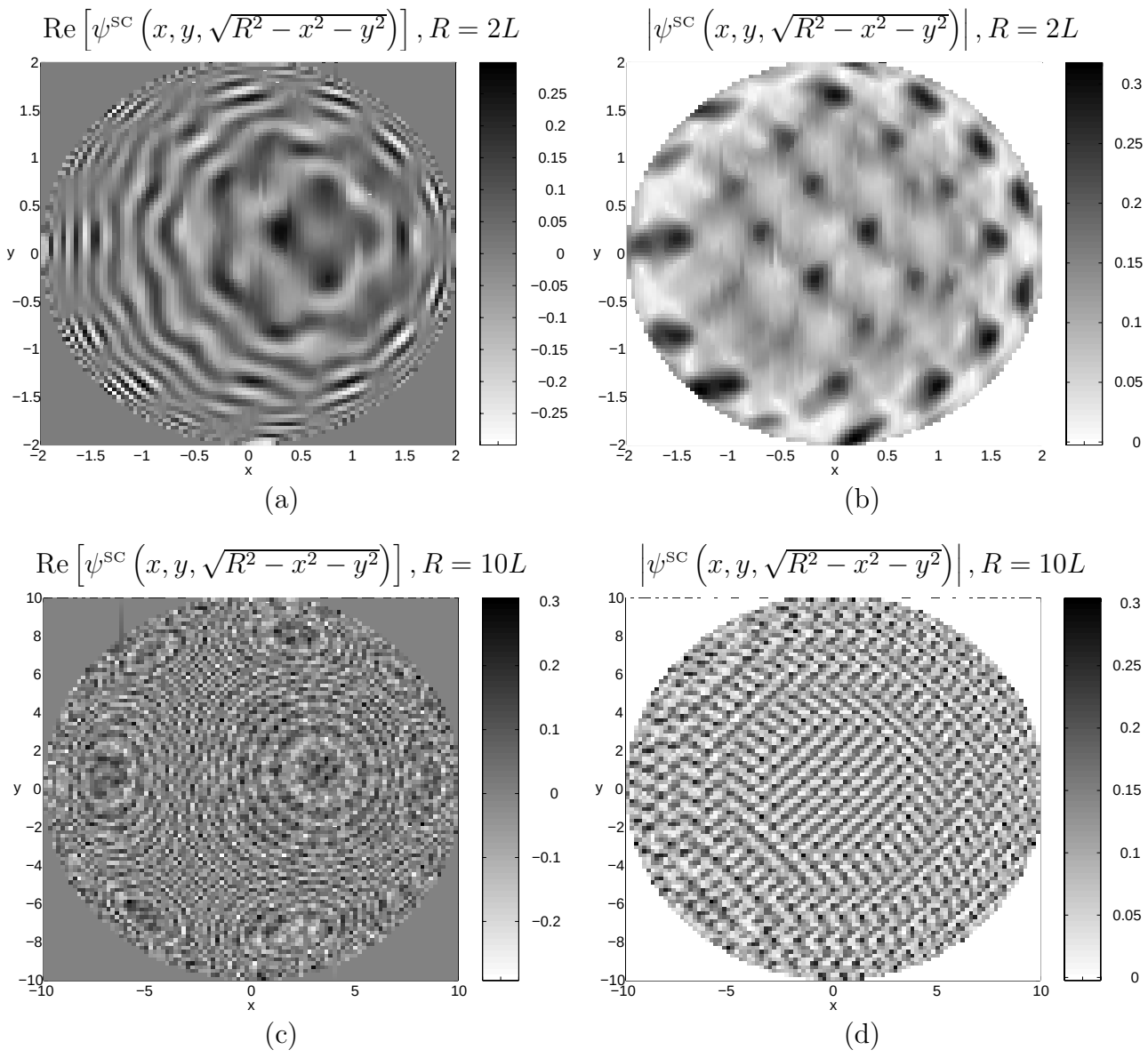

Figure 63: Example 1, Case A for the transmission problem with a non-square system of size 520×648 and $\kappa = 1.5$. Real part ((a) and (c)) and magnitude ((b) and (d)) of the scattered field plotted on hemispheres of radius $R = 2L$ ((a) and (b)) and $R = 10L$ ((c) and (d)) looking down. Here $L = L_1 = L_2$. The resolution is 100×100.

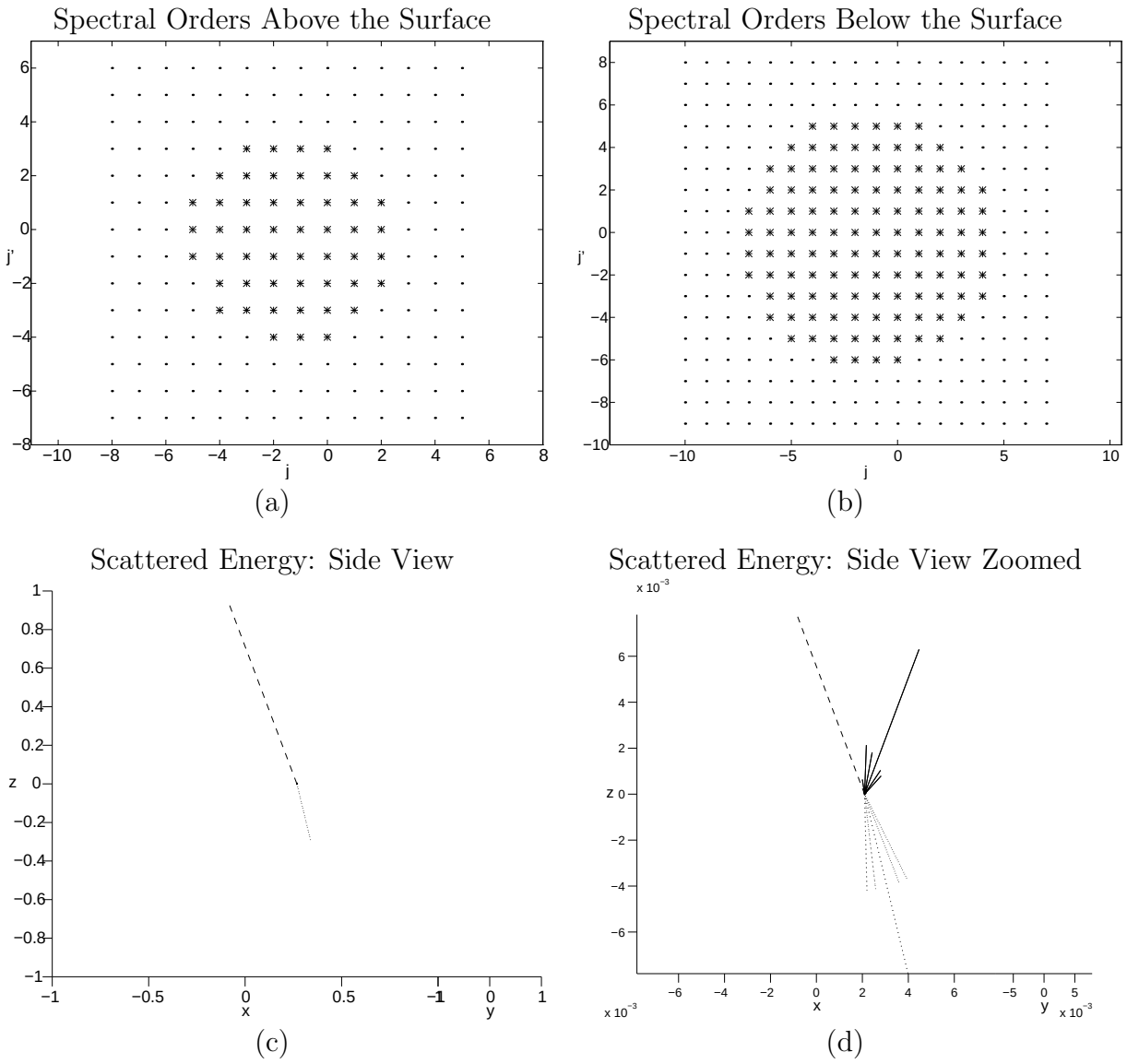

Figure 64: Example 1, Case A for the transmission problem with a non-square system of size 520×648 and $\kappa = 1.5$. (a) Spectral orders above the surface with 14 samples in j and j'. (b) Spectral orders below the surface with 18 samples in j and j'. (c) and (d) Scattered energy distribution viewed from $\theta = 90°$ and $\phi = -75°$. Incident field is dashed, reflected field is solid and transmitted field is dotted. (c) is an unscaled side view and (d) is a zoomed view with scale of 10^{-3} in both x and y.

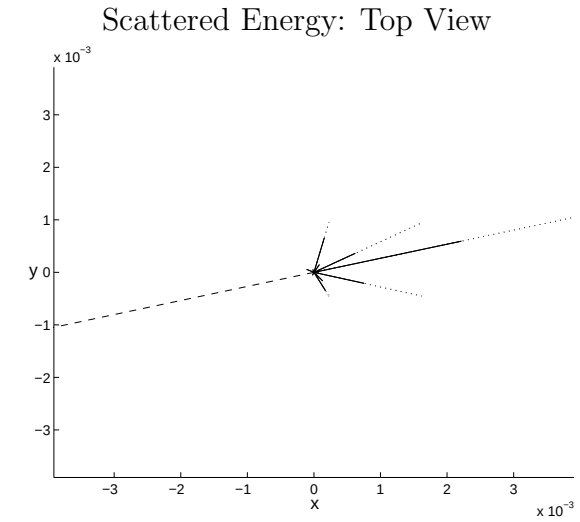

(a)

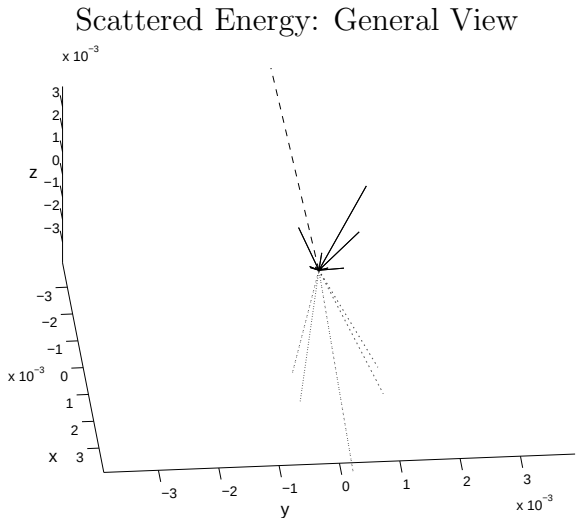

(b)

Figure 65: Example 1, Case A for the transmission problem with a non-square system of size 520×648 and $\kappa = 1.5$. Scattered energy distribution viewed from (a) $\theta = 0°$ and $\phi = -90°$, and (b) $\theta = 40°$ and $\phi = -5°$. Incident field is dashed, reflected field is solid and transmitted field is dotted. Zoomed views with 10^{-3} scale in all directions.

19.2 Example 1 Case B

$S(x,y)$	$-(d/2)\cos(2\pi x/L_1)\cos(2\pi y/L_2)$
(L_1, L_2)	(1,1)
$(d/L_1, d/L_2)$	(.075,.075)
$(\lambda/L_1, \lambda/L_2)$	(.25,.25)
ρ	2
θ^i	75°
ϕ^i	15°

κ	1
Radiating Orders Above	48
Radiating Orders Below	48
Fraction of Energy Reflected	.12

System Size	Number of Samples Coord. x	Coord. y	Spectral Above j	Above j'	Below j	Below j'	$\lambda/\Delta x$	$\lambda/\Delta y$	Fill Time (s)	Linear Solution Time (s)	Condition Number	Error
112 × 112	8	7	8	7	8	7	2.0000	1.7500	0.1400	0.0400	12.6264	-1.7273
144 × 144	9	8	9	8	9	8	2.2500	2.0000	0.1900	0.0800	42.1853	-2.8514
180 × 180	10	9	10	9	10	9	2.5000	2.2500	0.2500	0.1400	55.1987	-2.7312
220 × 220	11	10	11	10	11	10	2.7500	2.5000	0.3200	0.3100	85.5216	-4.1872
264 × 264	12	11	12	11	12	11	3.0000	2.7500	0.3900	0.6200	83.3558	-3.4966
312 × 312	13	12	13	12	13	12	3.2500	3.0000	0.4900	1.1200	112.6966	-4.7103
364 × 364	14	13	14	13	14	13	3.5000	3.2500	0.6000	1.8300	131.1395	-4.2105

Table 41: Parameters and computational results for Example 1, Case B of the transmission problem. Spectral modes in both x and y and both above and below the surface are present. The coordinate sampling is the product of the numbers in the columns "x" and "y" then doubled to cover both reflection and transmission regions. Only square systems were treated and the wavelength was 1/4 of the two equal surface periods. (Computations were done on a customized Pentium III 500 MHz PC).

κ	1.5
Radiating Orders Above	48
Radiating Orders Below	110
Fraction of Energy Reflected	.14

System Size	Number of Samples: Coord. x	Coord. y	Spectral: Above j	Above j'	Below j	Below j'	$\lambda/\Delta x$	$\lambda/\Delta y$	Fill Time (s)	Linear Solution Time (s)	Condition Number	Error
188 × 264	12	11	8	7	12	11	3.0000	2.7500	0.2700	1.7100	8.9023	-1.6685
228 × 312	13	12	9	8	13	12	3.2500	3.0000	0.3500	3.0900	14.1219	-2.7058
272 × 364	14	13	10	9	14	13	3.5000	3.2500	0.4400	5.5300	16.9178	-2.7201
320 × 420	15	14	11	10	15	14	3.7500	3.5000	0.5500	9.6900	24.7115	-2.7495
372 × 480	16	15	12	11	16	15	4.0000	3.7500	0.6700	15.1700	29.3392	-2.7355
428 × 544	17	16	13	12	17	16	4.2500	4.0000	0.8300	23.8800	41.0368	-3.6475
488 × 612	18	17	14	13	18	17	4.5000	4.2500	0.9900	34.9300	48.5162	-3.6489

Table 42: Parameters and computational results for Example 1, Case B of the transmission problem. Spectral modes in both x and y and both above and below the surface are present. The numbers of modes above and below are different since $\kappa \neq 1$. Additional coordinate samples were added to make the linear system non-square. For this transmission case the non-square systems performed about as well as the square systems. (Computations were done on a customized Pentium III 500 MHz PC).

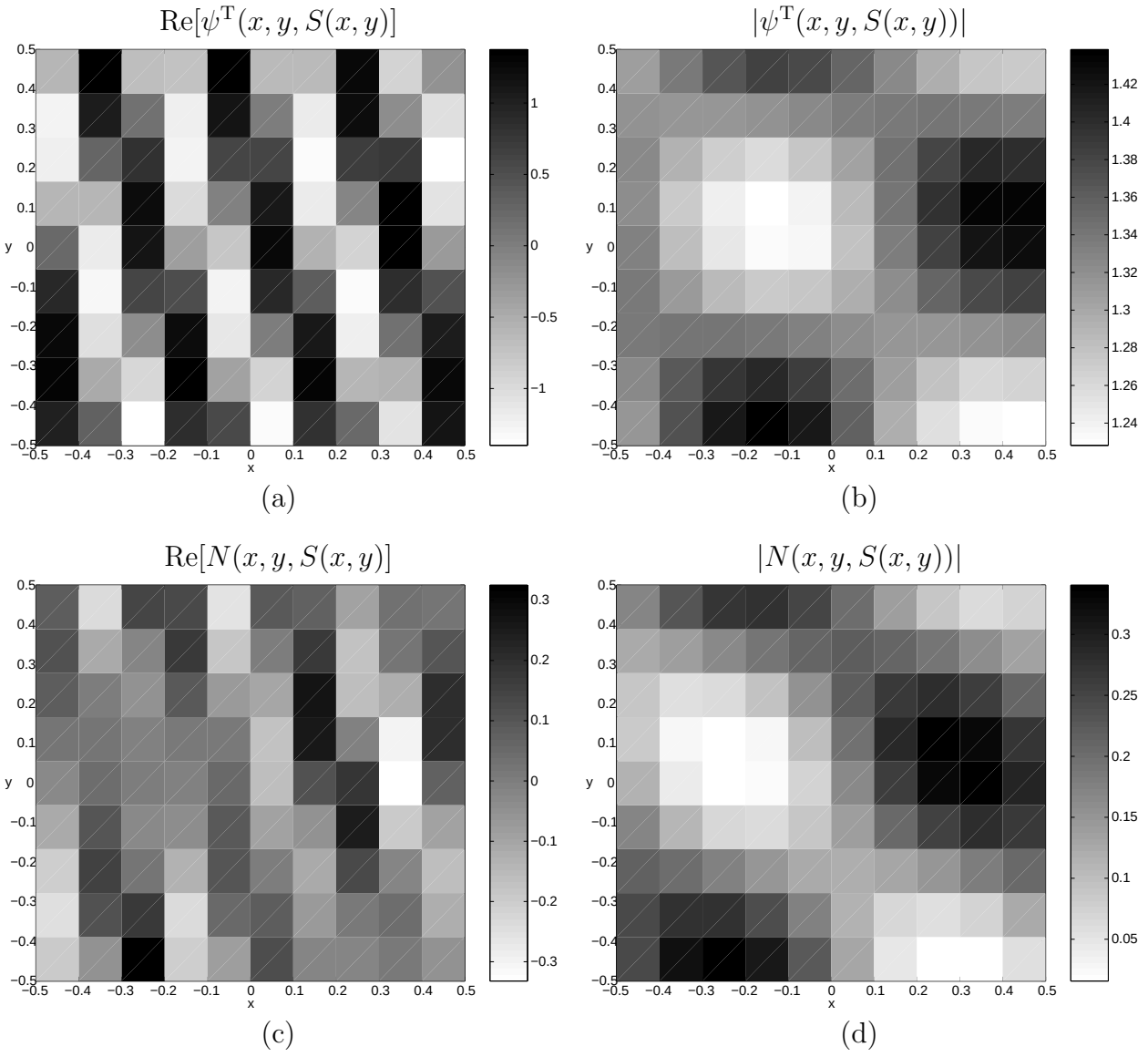

Figure 66: Example 1, Case B for the transmission problem with a square system of size 220×220 and $\kappa = 1$. Real part (a) and magnitude (b) of the total field ψ^{T} on the surface and real part (c) and magnitude (d) of the surface current or normal derivative N on the surface.

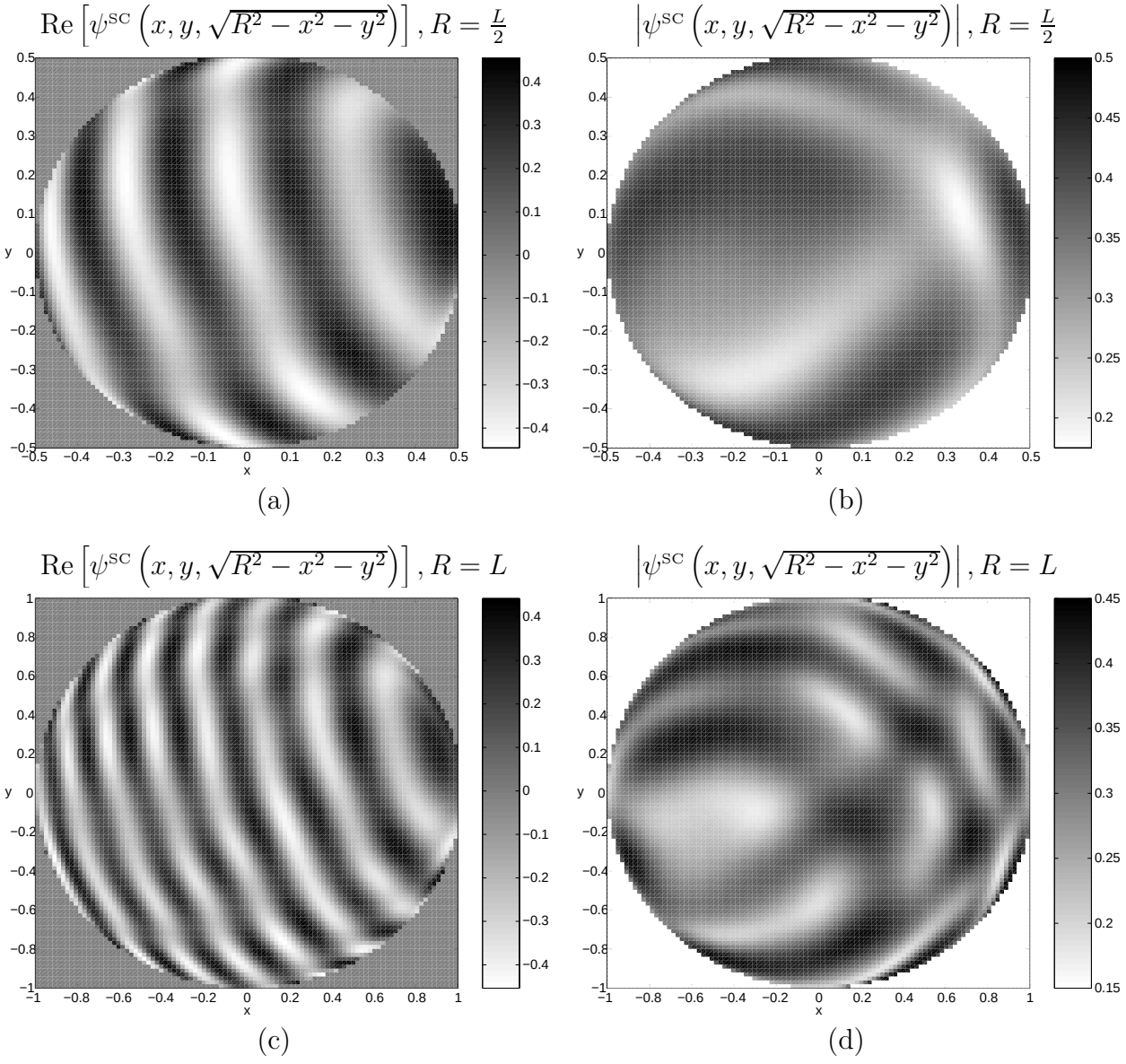

Figure 67: Example 1, Case B for the transmission problem with a square system of size 220×220 and $\kappa = 1$. Real part ((a) and (c)) and magnitude ((b) and (d)) of the scattered field plotted on hemispheres of radius $R = L/2$ ((a) and (b)) and $R = L$ ((c) and (d)) looking down. Here $L = L_1 = L_2$. The resolution of the pictures is 100×100.

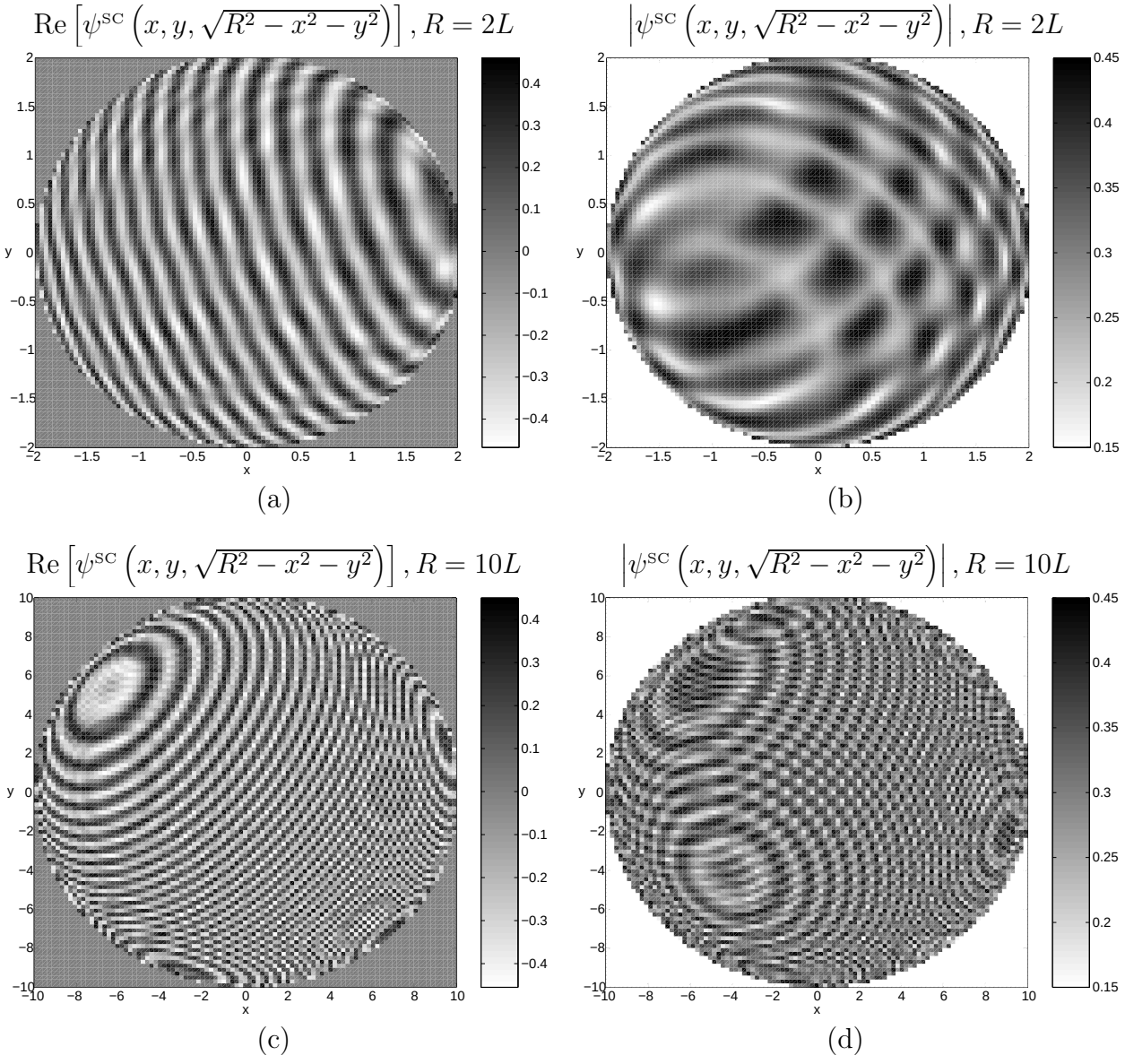

Figure 68: Example 1, Case B for the transmission problem with a square system of size 220×220 and $\kappa = 1$. Real part ((a) and (c)) and magnitude ((b) and (d)) of the scattered field plotted on hemispheres of radius $R = 2L$ ((a) and (b)) and $R = 10L$ ((c) and (d)) looking down. Here $L = L_1 = L_2$. The resolution is 100×100.

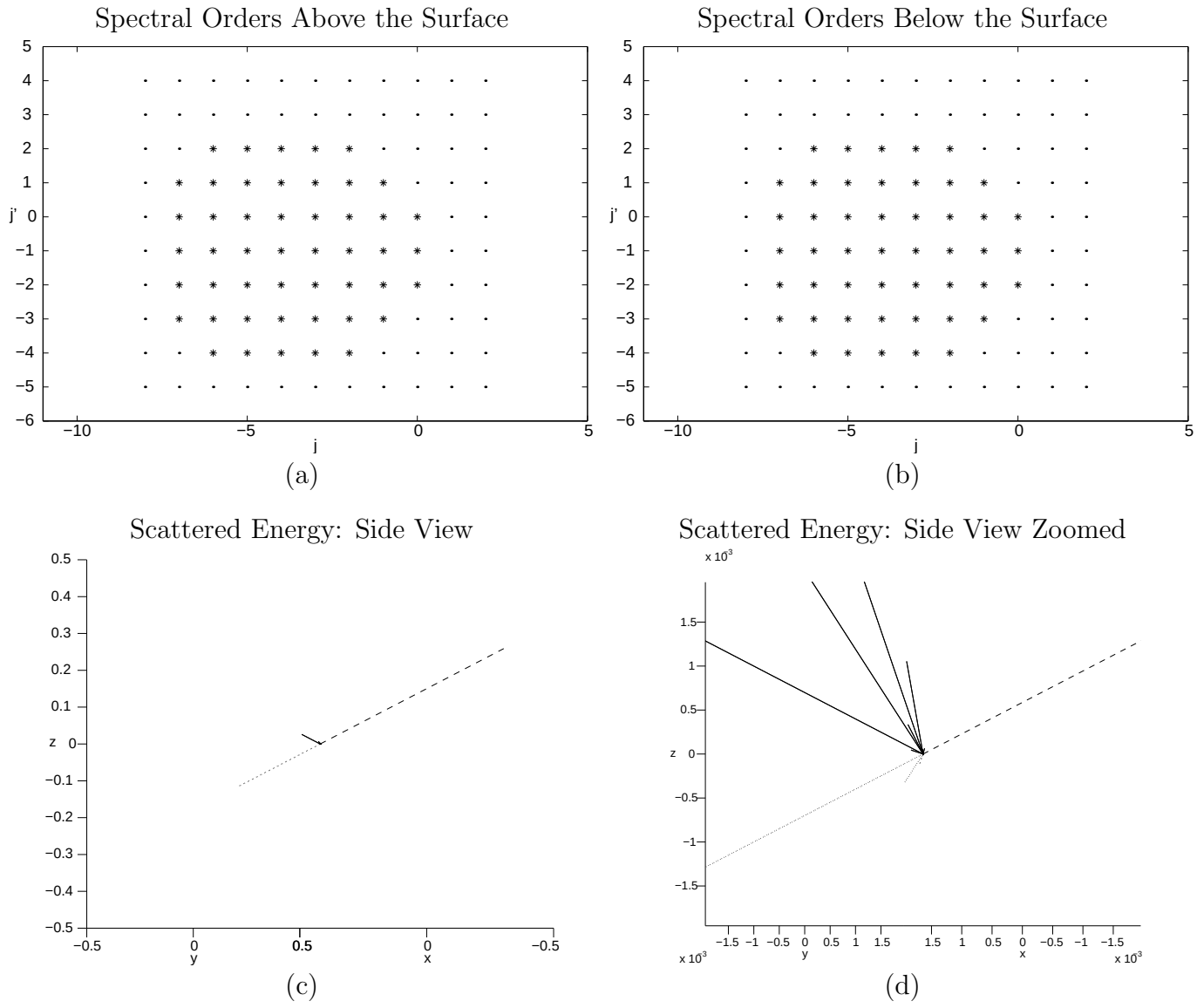

Figure 69: Example 1, Case B for the transmission problem with a square system of size 220×220 and $\kappa = 1$. (a) Spectral orders above the surface with 11 samples in j and 10 samples in j'. (b) Spectral orders below the surface with 11 samples in j and 10 samples in j'. (c) and (d) Scattered energy distribution viewed from $\theta = 90°$ and $\phi = -75°$. Incident field is dashed, reflected field is solid and transmitted field is dotted. (c) is an unscaled side view and (d) is a zoomed view with scale of 10^{-3} in both x and y.

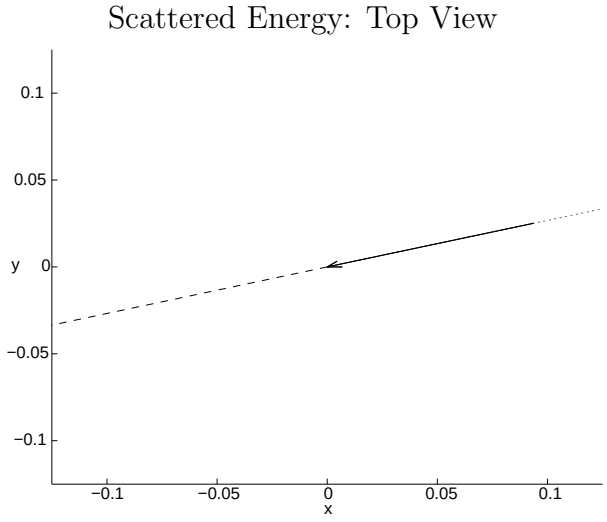

(a)

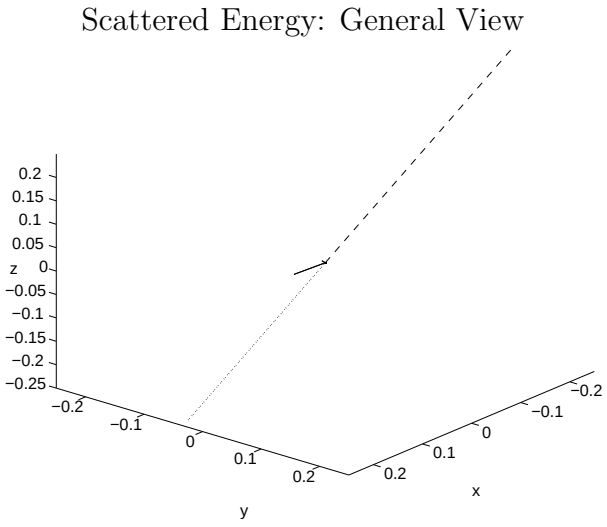

(b)

Figure 70: Example 1, Case B for the transmission problem with a square system of size 220×220 and $\kappa = 1$. Scattered energy distribution viewed from (a) $\theta = 0°$ and $\phi = -90°$, and (b) $\theta = 40°$ and $\phi = -5°$. Incident field is dashed, reflected field is solid and transmitted field is dotted. Zoomed views with 10^{-3} scale in all directions.

19.3 Example 2 Case A

$S(x,y)$	$-(d/2)\cos(2\pi x/L_1)\cos(2\pi y/L_2)$
(L_1, L_2)	(1,1)
$(d/L_1, d/L_2)$	(.075,.075)
$(\lambda/L_1, \lambda/L_2)$	(.95,.95)
ρ	2
θ^i	20°
ϕ^i	15°

κ	1
Radiating Orders Above	3
Radiating Orders Below	3
Fraction of Energy Reflected	.1058

System Size	Number of Samples						$\lambda/\Delta x$	$\lambda/\Delta y$	Fill Time (s)	Linear Solution Time (s)	Condition Number	Error
	Coord.		Spectral									
			Above		Below							
	x	y	j	j'	j	j'						
8 × 8	2	2	2	2	2	2	1.9000	1.9000	0.0700	0.0100	4.8237	-15.1764
18 × 18	3	3	3	3	3	3	2.8500	2.8500	0.1500	0.0100	5.7868	-3.3657
32 × 32	4	4	4	4	4	4	3.8000	3.8000	0.3000	0.0200	7.6518	-3.7671
50 × 50	5	5	5	5	5	5	4.7500	4.7500	0.4400	0.0500	10.3837	-4.4897
72 × 72	6	6	6	6	6	6	5.7000	5.7000	0.6500	0.1300	14.0583	-5.0138
98 × 98	7	7	7	7	7	7	6.6500	6.6500	0.9400	0.2800	18.3491	-5.8853
128 × 128	8	8	8	8	8	8	7.6000	7.6000	1.2600	0.6000	24.0675	-5.8788
162 × 162	9	9	9	9	9	9	8.5500	8.5500	1.6800	1.1300	30.9155	-6.8809
200 × 200	10	10	10	10	10	10	9.5000	9.5000	2.2000	1.9300	39.9777	-7.1344
242 × 242	11	11	11	11	11	11	10.4500	10.4500	2.8600	3.3900	50.7290	-8.1988
288 × 288	12	12	12	12	12	12	11.4000	11.4000	3.8800	5.9200	64.7536	-8.0051
338 × 338	13	13	13	13	13	13	12.3500	12.3500	4.9400	9.2000	82.3364	-9.0085
392 × 392	14	14	14	14	14	14	13.3000	13.3000	5.6700	13.3400	136.4801	-9.3196

Table 43: Parameters and computational results for Example 2, Case A of the transmission problem. Spectral modes in both x and y and both above and below the surface are present. The coordinate sampling is the product of the numbers in the columns "x" and "y" then doubled to cover both reflection and transmitted regions. Only square systems were treated and the wavelength was approximately equal to the two equal surface periods.

κ	1.5
Radiating Orders Above	3
Radiating Orders Below	7
Fraction of Energy Reflected	.0144

System Size	Number of Samples: Coord. x	Coord. y	Spectral: Above j	Above j'	Below j	Below j'	$\lambda/\Delta x$	$\lambda/\Delta y$	Fill Time (s)	Linear Solution Time (s)	Condition Number	Error
13 × 18	3	3	2	2	3	3	2.8500	2.8500	0.1100	0.0400	4.8332	-2.0469
25 × 32	4	4	3	3	4	4	3.8000	3.8000	0.2100	0.0700	7.3181	-3.4925
41 × 50	5	5	4	4	5	5	4.7500	4.7500	0.3600	0.2000	8.1715	-3.6294
61 × 72	6	6	5	5	6	6	5.7000	5.7000	0.5400	0.5600	13.0734	-4.6987
85 × 98	7	7	6	6	7	7	6.6500	6.6500	0.8000	1.3800	15.4007	-4.9841
113 × 128	8	8	7	7	8	8	7.6000	7.6000	1.1000	3.9300	22.9436	-5.7298
145 × 162	9	9	8	8	9	9	8.5500	8.5500	1.5200	6.7900	26.8406	-6.4673
181 × 200	10	10	9	9	10	10	9.5000	9.5000	2.0000	11.0500	38.3842	-6.9135
221 × 242	11	11	10	10	11	11	10.4500	10.4500	2.6100	22.6600	44.7170	-7.5939
265 × 288	12	12	11	11	12	12	11.4000	11.4000	3.4200	56.9100	62.2186	-8.0072
313 × 338	13	13	12	12	13	13	12.3500	12.3500	4.2000	89.7300	72.2816	-9.3706
365 × 392	14	14	13	13	14	14	13.3000	13.3000	5.2300	150.2100	98.5735	-9.0700
421 × 450	15	15	14	14	15	15	14.2500	14.2500	6.5000	256.7600	114.2766	-10.0657

Table 44: Parameters and computational results for Example 2, Case A of the transmission problem. Spectral modes in both x and y and both above and below the surface are present. The numbers of modes above and below are different since $\kappa \neq 1$. Additional coordinate samples were added to make the linear system non-square.

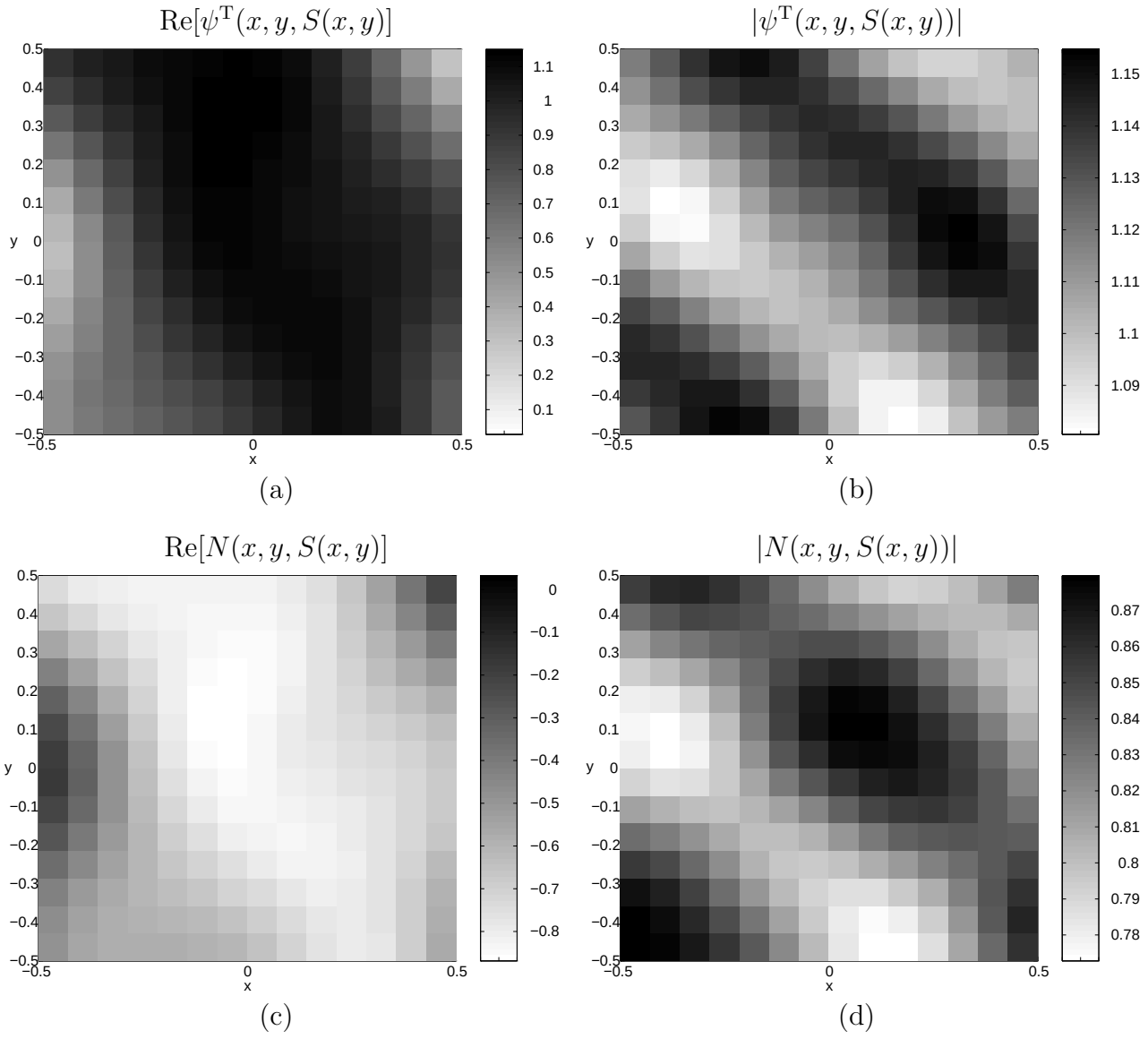

Figure 71: Example 2, Case A for the transmission problem with a non-square system of size 421×450 and $\kappa = 1.5$. Real part (a) and magnitude (b) of the total field ψ^{T} on the surface and real part (c) and magnitude (d) of the surface current or normal derivative N on the surface.

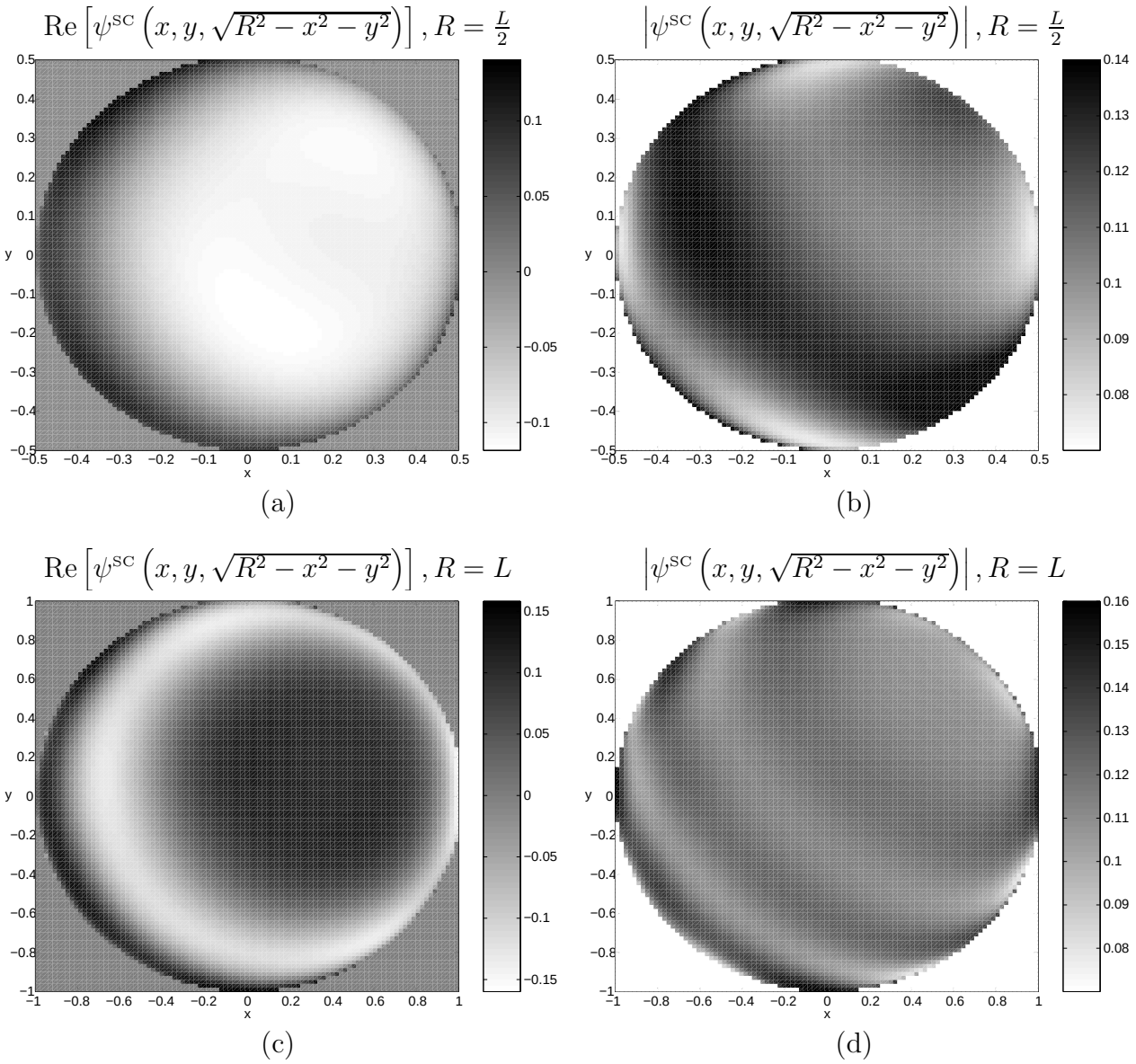

Figure 72: Example 2, Case A for the transmission problem with a square system of size 392×392 and $\kappa = 1$. Real part ((a) and (c)) and magnitude ((b) and (d)) of the scattered field plotted on hemispheres of radius $R = L/2$ ((a) and (b)) and $R = L$ ((c) and (d)) looking down. Here $L = L_1 = L_2$. The resolution of the pictures is 100×100.

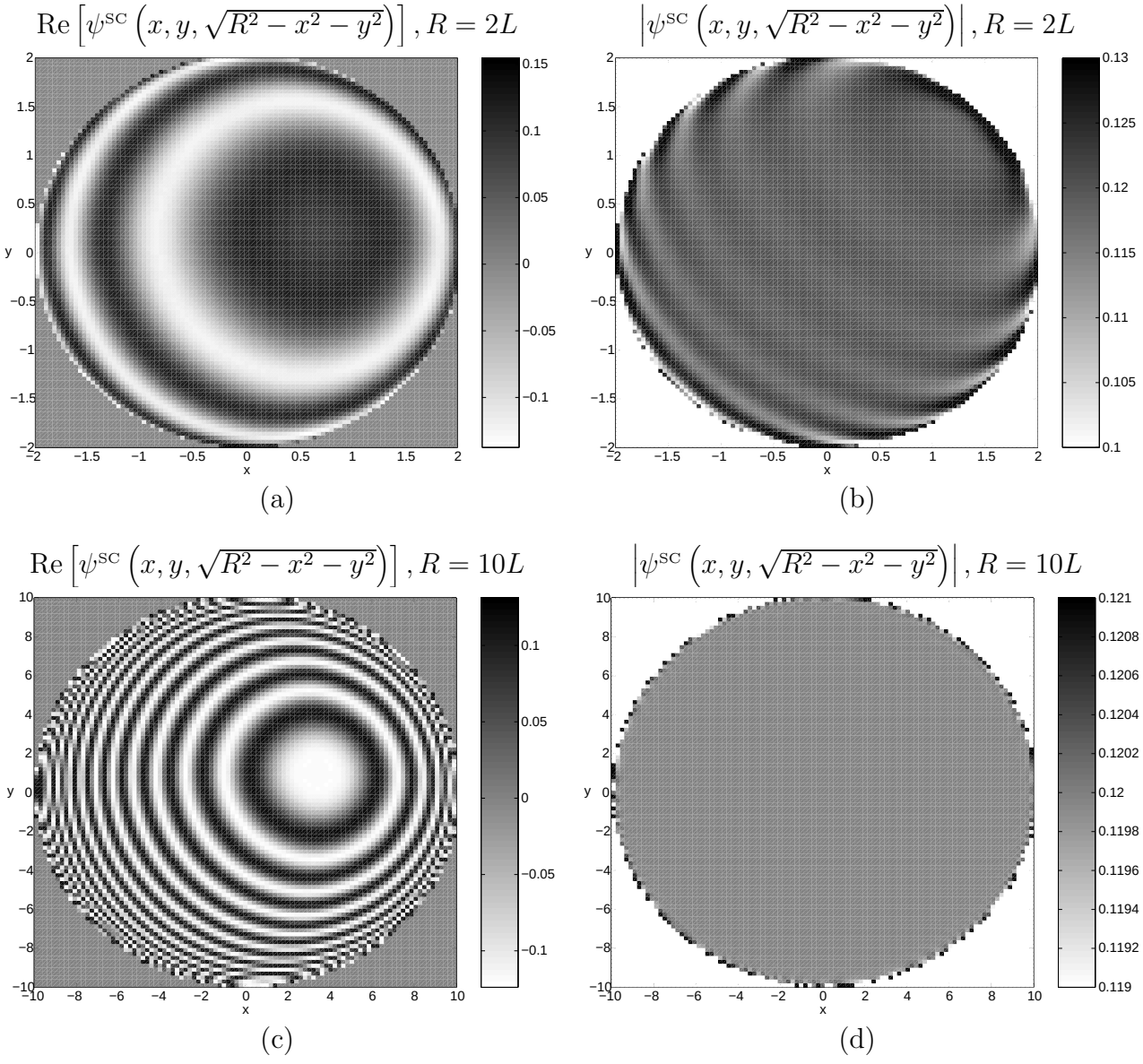

Figure 73: Example 2, Case A for the transmission problem with a square system of size 392×392 and $\kappa = 1$. Real part ((a) and (c)) and magnitude ((b) and (d)) of the scattered field plotted on hemispheres of radius $R = 2L$ ((a) and (b)) and $R = 10L$ ((c) and (d)) looking down. Here $L = L_1 = L_2$. The resolution is 100×100.

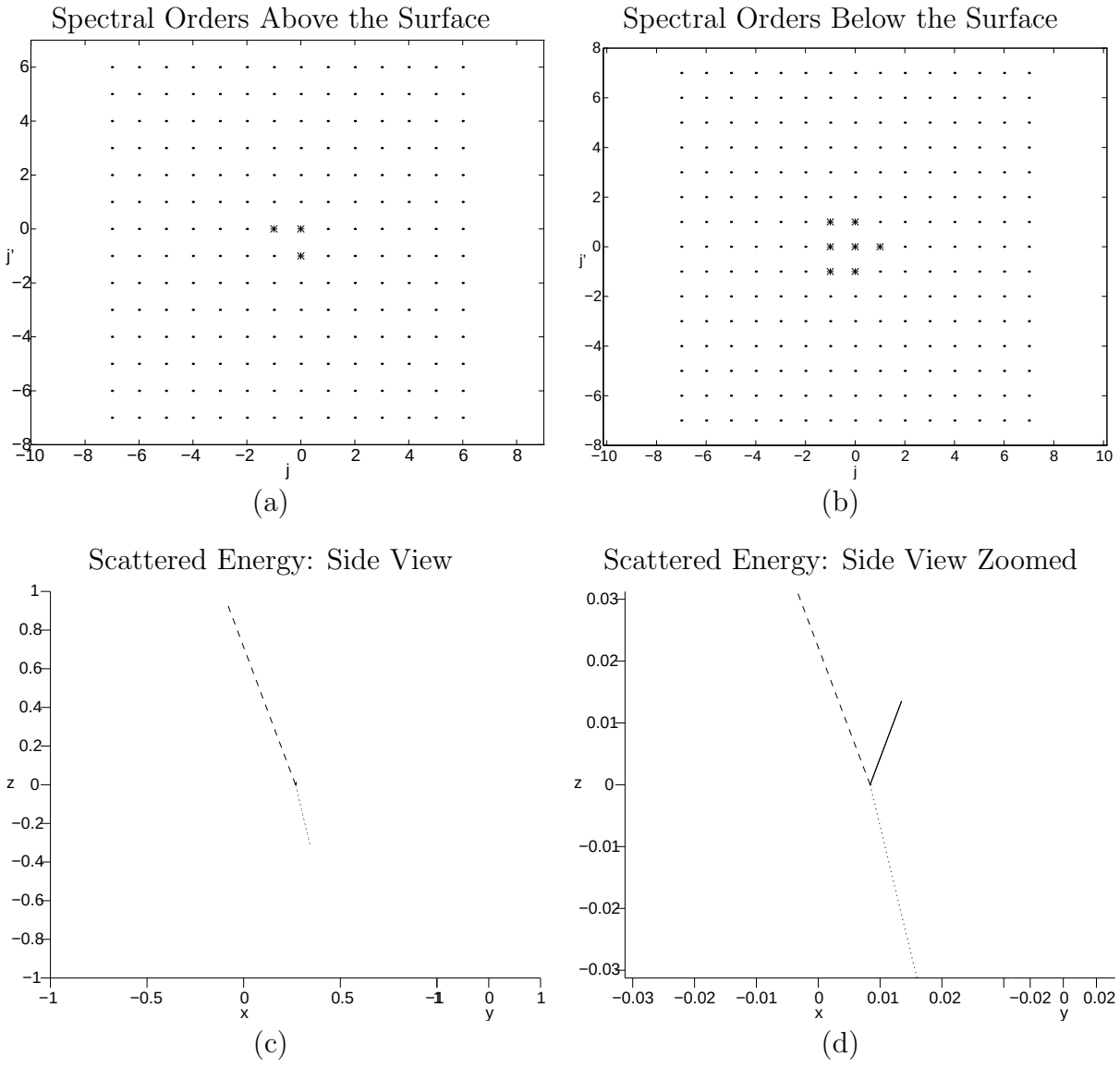

Figure 74: Example 2, Case A for the transmission problem with a non-square system of size 421×450 and $\kappa = 1.5$. (a) Spectral orders above the surface with 14 samples in j and j'. (b) Spectral orders below the surface with 15 samples in j and j'. (c) and (d) Scattered energy distribution viewed from $\theta = 90^\circ$ and $\phi = -75^\circ$. Incident field is dashed, reflected field is solid and transmitted field is dotted. (c) is an unscaled side view and (d) is a zoomed view with scale as indicated.

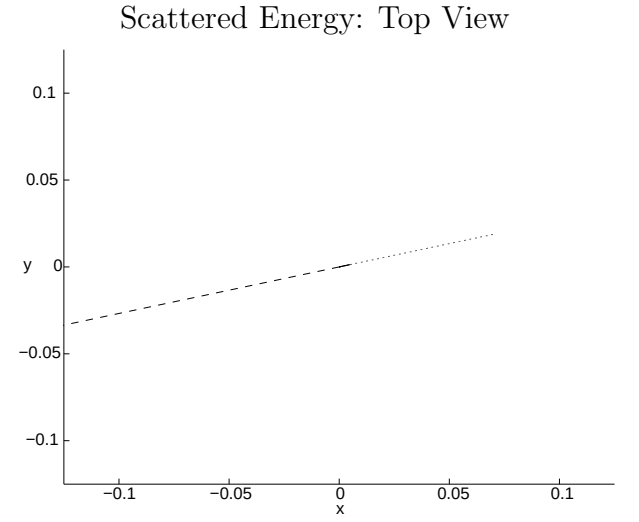

(a)

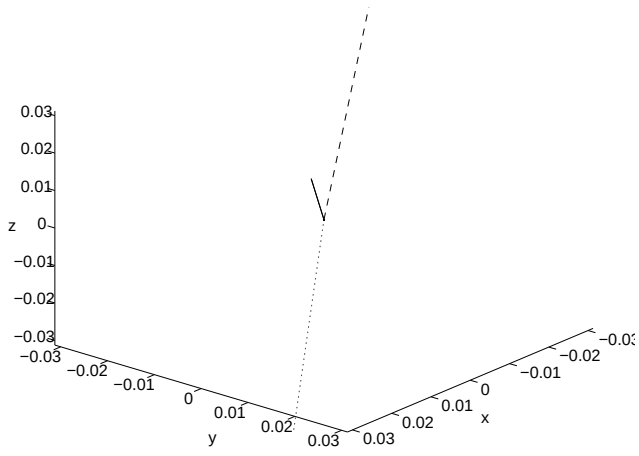

(b)

Figure 75: Example 2, Case A for the transmission problem with a square system of size 392×392 and $\kappa = 1$. Scattered energy distribution viewed from (a) $\theta = 0°$ and $\phi = -90°$, and (b) $\theta = 40°$ and $\phi = -5°$. Incident field is dashed, reflected field is solid and transmitted field is dotted. Zoomed views with 10^{-3} scale in all directions.

19.4 Example 2 Case B

$S(x,y)$	$-(d/2)\cos(2\pi x/L_1)\cos(2\pi y/L_2)$
(L_1, L_2)	(1,1)
$(d/L_1, d/L_2)$	(.075,.075)
$(\lambda/L_1, \lambda/L_2)$	(.95,.95)
ρ	2
θ^i	75°
ϕ^i	15°

κ	1
Radiating Orders Above	4
Radiating Orders Below	4
Fraction of Energy Reflected	.11

System Size	Number of Samples Coord. x	Coord. y	Spectral Above j	Above j'	Below j	Below j'	$\lambda/\Delta x$	$\lambda/\Delta y$	Fill Time (s)	Linear Solution Time (s)	Condition Number	Error
12 × 12	3	2	3	2	3	2	2.8500	1.9000	0.0100	$< 10^{-3}$	34.7746	-2.1621
24 × 24	4	3	4	3	4	3	3.8000	2.8500	0.0300	$< 10^{-3}$	52.7117	-3.4689
40 × 40	5	4	5	4	5	4	4.7500	3.8000	0.0400	0.0100	60.3039	-3.1177
60 × 60	6	5	6	5	6	5	5.7000	4.7500	0.0700	0.0100	90.5124	-4.1825
84 × 84	7	6	7	6	7	6	6.6500	5.7000	0.1000	0.0200	110.6209	-4.0941
112 × 112	8	7	8	7	8	7	7.6000	6.6500	0.1400	0.0300	153.7470	-5.1166
144 × 144	9	8	9	8	9	8	8.5500	7.6000	0.1600	0.0900	189.8261	-5.0248
180 × 180	10	9	10	9	10	9	9.5000	8.5500	0.2600	0.1600	254.0543	-6.1993
220 × 220	11	10	11	10	11	10	10.4500	9.5000	0.3300	0.3500	314.5013	-6.0961
264 × 264	12	11	12	11	12	11	11.4000	10.4500	0.4000	0.6300	411.8188	-7.1622
312 × 312	13	12	13	12	13	12	12.3500	11.4000	0.5000	1.1200	507.3954	-7.0568
364 × 364	14	13	14	13	14	13	13.3000	12.3500	0.6200	1.7900	654.5029	-8.2714
420 × 420	15	14	15	14	15	14	14.2500	13.3000	0.7600	2.7100	801.7465	-8.1616

Table 45: Parameters and computational results for Example 2, Case B of the transmission problem. Spectral modes in both x and y and both above and below the surface are present. The coordinate sampling is the product of the numbers in the columns "x" and "y" then doubled to cover both reflection and transmission regions. Only square systems were treated and the wavelength was approximately equal to the two equal surface periods. (Computations were done on a customized Pentium III 500 MHz PC).

κ	1.5
Radiating Orders Above	4
Radiating Orders Below	7
Fraction of Energy Reflected	.14

System Size	Number of Samples: Coord. x	Coord. y	Spectral: Above j	Above j'	Below j	Below j'	$\lambda/\Delta x$	$\lambda/\Delta y$	Fill Time (s)	Linear Solution Time (s)	Condition Number	Error
15 × 18	3	3	3	2	3	3	2.8500	2.8500	0.0100	0.0100	5.0194	-1.5588
28 × 32	4	4	4	3	4	4	3.8000	3.8000	0.0300	0.0100	7.5752	-5.2495
45 × 50	5	5	5	4	5	5	4.7500	4.7500	0.0600	0.0300	8.4449	-3.2745
66 × 72	6	6	6	5	6	6	5.7000	5.7000	0.0800	0.0700	13.1800	-4.2016
91 × 98	7	7	7	6	7	7	6.6500	6.6500	0.1200	0.1700	15.9756	-3.9552
120 × 128	8	8	8	7	8	8	7.6000	7.6000	0.1600	0.3600	23.2795	-5.4933
153 × 162	9	9	9	8	9	9	8.5500	8.5500	0.2000	0.6900	27.8386	-5.6419
190 × 200	10	10	10	9	10	10	9.5000	9.5000	0.2700	1.3600	39.0782	-6.3917
231 × 242	11	11	11	10	11	11	10.4500	10.4500	0.3400	2.6100	46.4069	-6.2535
276 × 288	12	12	12	11	12	12	11.4000	11.4000	0.4300	4.3400	63.5278	-7.5003
325 × 338	13	13	13	12	13	13	12.3500	12.3500	0.5200	7.7300	75.0610	-7.4449
378 × 392	14	14	14	13	14	14	13.3000	13.3000	0.6600	13.2400	106.8442	-8.5236
435 × 450	15	15	15	14	15	15	14.2500	14.2500	0.8000	21.9400	134.3711	-8.4689

Table 46: Parameters and computational results for Example 2, Case B of the transmission problem. Spectral modes in both x and y and both above and below the surface are present. The numbers of modes above and below are different since $\kappa \neq 1$. Additional coordinate samples were added to make the linear system non-square. For this transmission case the non-square systems performed about the same as the square systems. (Computations were done on a customized Pentium III 500 MHz PC).

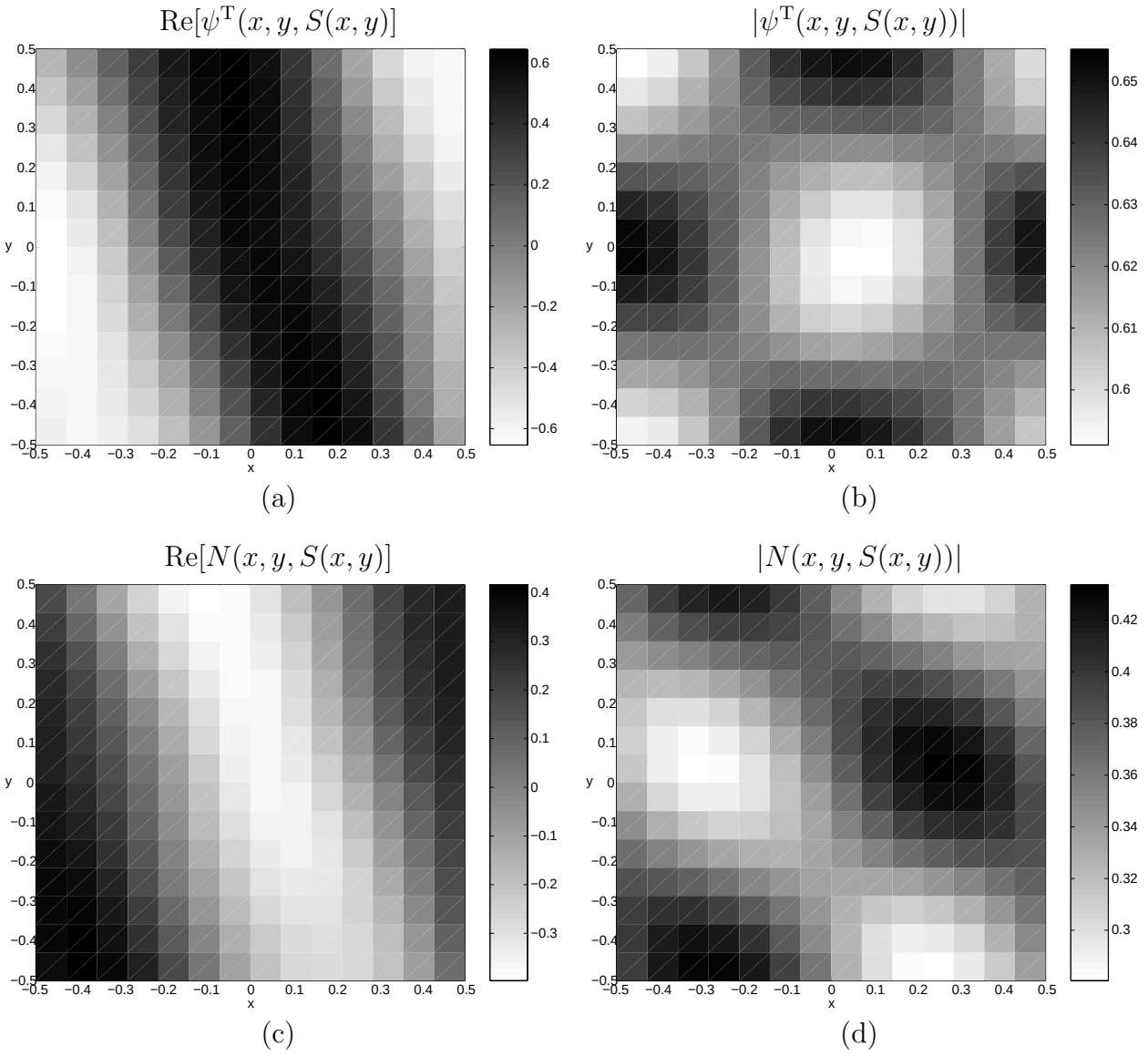

Figure 76: Example 1, Case B for the transmission problem with a non-square system of size 435×450 and $\kappa = 1.5$. Real part (a) and magnitude (b) of the total field ψ^{T} on the surface and real part (c) and magnitude (d) of the surface current or normal derivative N on the surface.

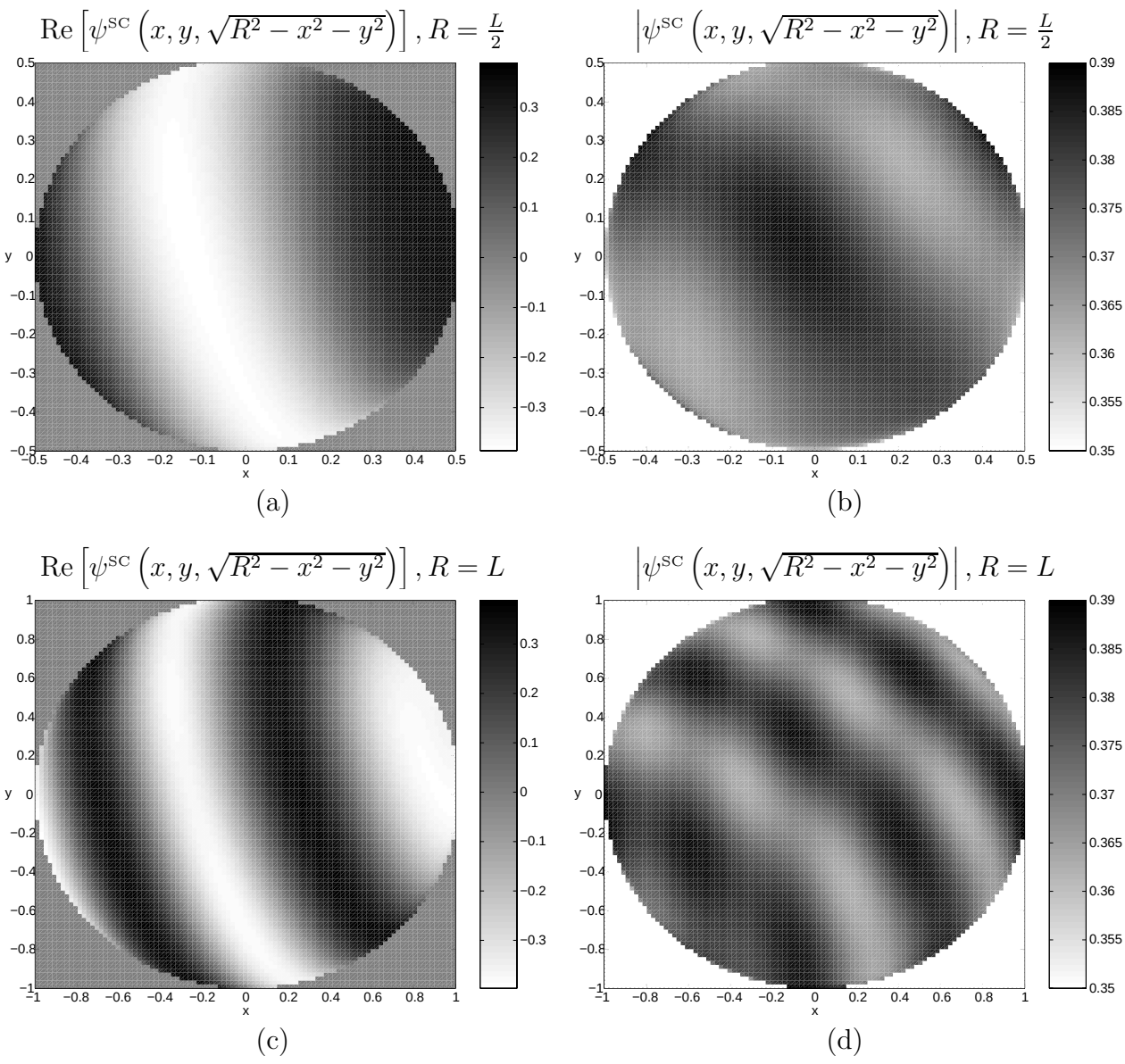

Figure 77: Example 2, Case B for the transmission problem with a non-square system of size 435×450 and $\kappa = 1.5$. Real part ((a) and (c)) and magnitude ((b) and (d)) of the scattered field plotted on hemispheres of radius $R = L/2$ ((a) and (b)) and $R = L$ ((c) and (d)) looking down. Here $L = L_1 = L_2$. The resolution of the pictures is 100×100.

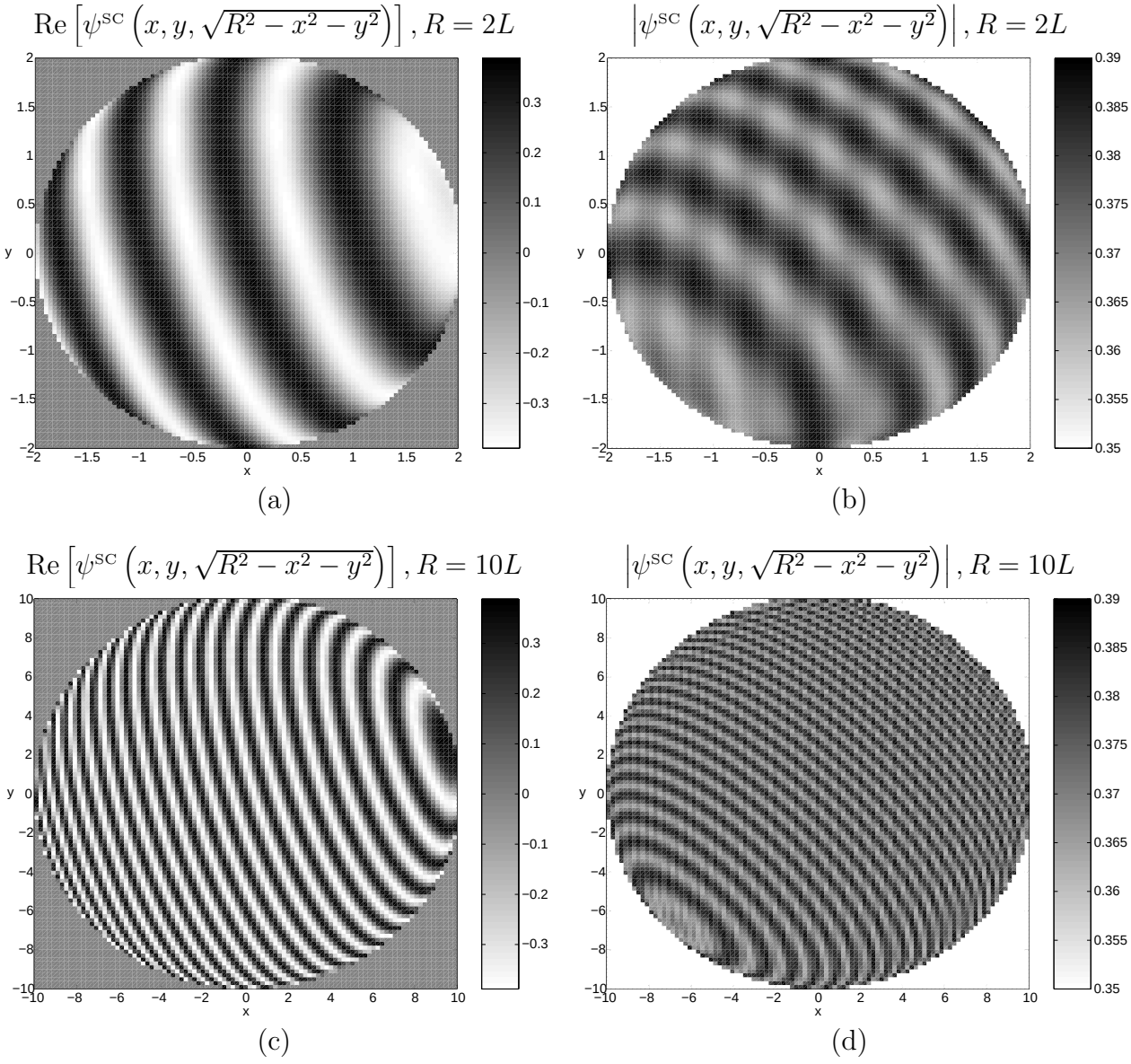

Figure 78: Example 2, Case B for the transmission problem with a non-square system of size 435×450 and $\kappa = 1.5$. Real part ((a) and (c)) and magnitude ((b) and (d)) of the scattered field plotted on hemispheres of radius $R = 2L$ ((a) and (b)) and $R = 10L$ ((c) and (d)) looking down. Here $L = L_1 = L_2$. The resolution is 100×100.

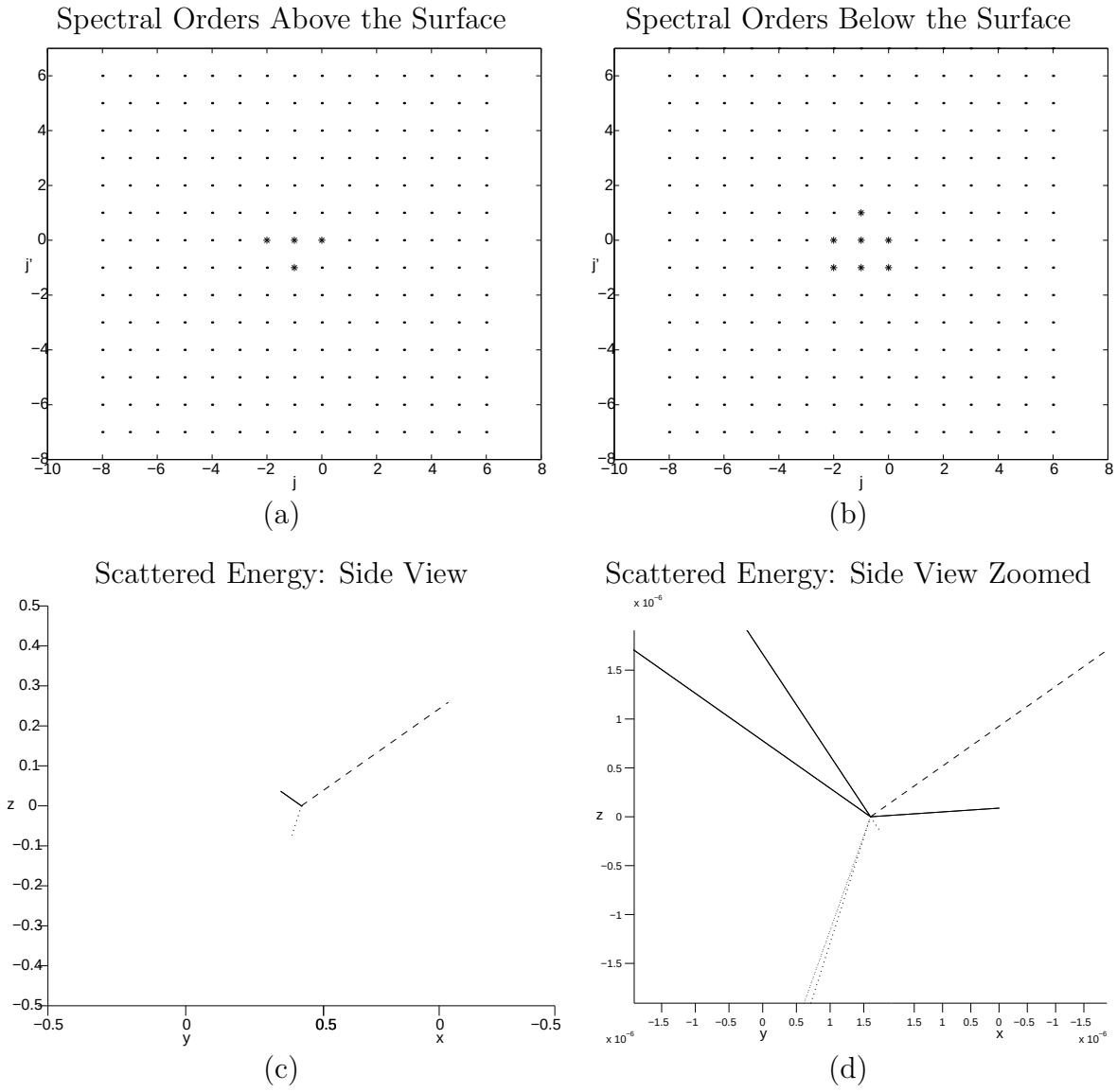

Figure 79: Example 2, Case B for the transmission problem with a non-square system of size 435×450 and $\kappa = 1.5$. (a) Spectral orders above the surface with 15 samples in j and 14 samples in j'. (b) Spectral orders below the surface with 15 samples in j and 15 samples in j'. (c) and (d) Scattered energy distribution viewed from $\theta = 90°$ and $\phi = -75°$. Incident field is dashed, reflected field is solid and transmitted field is dotted. (c) is an unscaled side view and (d) is a zoomed view with scale of 10^{-3} in both x and y.

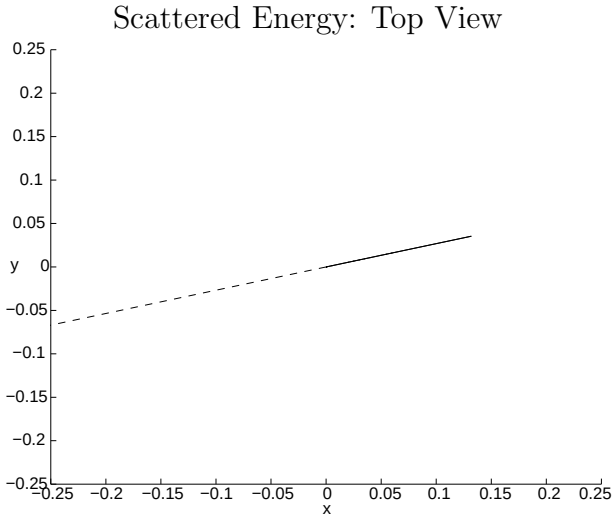

(a)

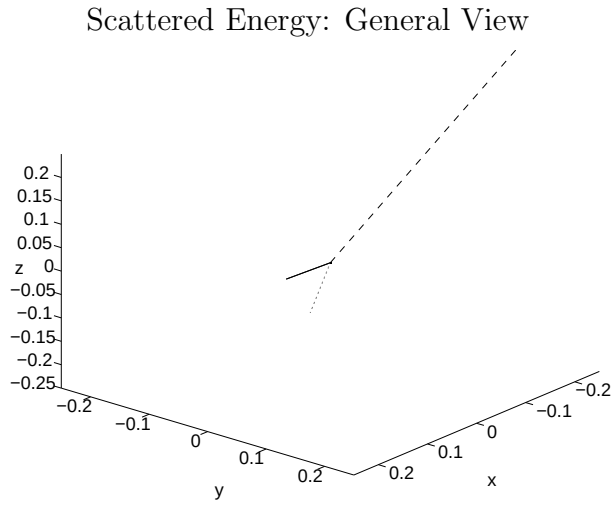

(b)

Figure 80: Example 2, Case B for the transmission problem with a non-square system of size 435×450 and $\kappa = 1.5$. Scattered energy distribution viewed from (a) $\theta = 0°$ and $\phi = -90°$, and (b) $\theta = 40°$ and $\phi = -5°$. Incident field is dashed, reflected field is solid and transmitted field is dotted. Zoomed views with 10^{-3} scale in all directions.

19.5 Example 3 Case A

For this example only two real modes were present, the scattered mode in specular and the transmitted mode as if no roughness were present. The resulting 2×2 system worked very well. Adding avanescent modes symmetrically worked well only through one example. Adding them unsymmetrically produced incorrent results.

$S(x,y)$	$-(d/2)\cos(2\pi x/L_1)\cos(2\pi y/L_2)$
(L_1, L_2)	(1,1)
$(d/L_1, d/L_2)$	(2.5,2.5)
$(\lambda/L_1, \lambda/L_2)$	(100,100)
ρ	2
θ^i	20°
ϕ^i	15°

κ	1
Radiating Orders Above	1
Radiating Orders Below	1
Fraction of Energy Reflected	.11

System Size	Number of Samples: Coord. x	Coord. y	Spectral: Above j	Above j'	Below j	Below j'	$\lambda/\Delta x$	$\lambda/\Delta y$	Fill Time (s)	Linear Solution Time (s)	Condition Number	Error
2×2	1	1	1	1	1	1	100	100	$< 10^{-3}$	$< 10^{-3}$	1.8635	-15.9546
8×8	2	2	2	2	2	2	200	200	0.0100	$< 10^{-3}$	162.9433	-15.4775
18×18	3	3	3	3	3	3	300	300	0.0200	0.0100	2.3402e+08	-1.0730

Table 47: Parameters and computational results for Example 3, Case A of the transmission problem for non-grazing incidence. Spectral modes in both x and y and both above and below the surface are present. The coordinate sampling is the product of the numbers in the columns "x" and "y" then doubled to cover both reflection and transmission regions. Only square systems were treated and the wavelength was 100 times larger than the two equal surface periods. Small system sizes worked very well in terms of error. For larger system sizes the error became even worse than that for the 18×18 example. Adding evanescent modes had to be done symmetrically as in the 8×8 example.

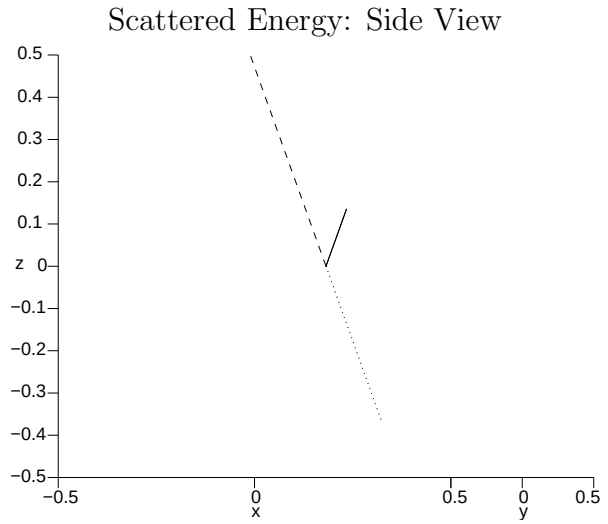

(a)

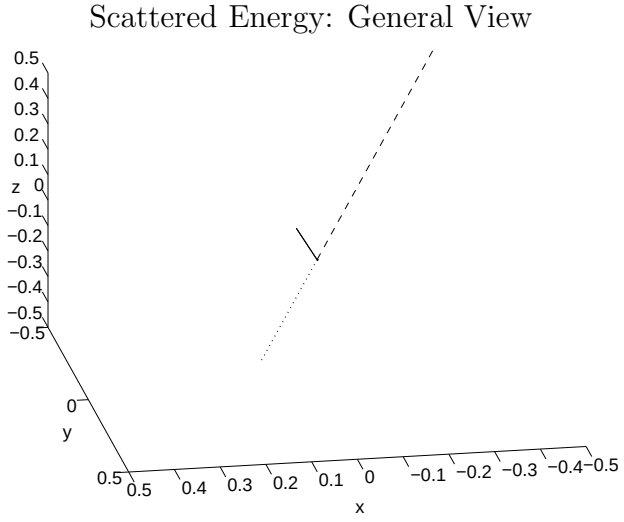

(b)

Figure 81: Example 3, Case A for the transmission problem with a square system of size 8×8 and $\kappa = 1$. Scattered energy distribution viewed from (a) $\theta = 90°$ and $\phi = -75°$ and (b) $\theta = 40°$ and $\phi = -5°$. Incident field is dashed, reflected field is solid and transmitted field is dotted.

19.6 Example 3 Case B

For this example only two real modes were present, the scattered mode in specular and the transmitted mode as if no roughness were present. The resulting 2×2 system worked very well. Adding avanescent modes symmetrically worked well only through one example. Adding them unsymmetrically produced incorrent results.

$S(x,y)$	$-(d/2)\cos(2\pi x/L_1)\cos(2\pi y/L_2)$
(L_1, L_2)	(1,1)
$(d/L_1, d/L_2)$	(2.5,2.5)
$(\lambda/L_1, \lambda/L_2)$	(100,100)
ρ	2
θ^i	75°
ϕ^i	15°

κ	1
Radiating Orders Above	1
Radiating Orders Below	1
Fraction of Energy Reflected	.11

System Size	Number of Samples: Coord. x	Coord. y	Spectral: Above j	Above j'	Below j	Below j'	$\lambda/\Delta x$	$\lambda/\Delta y$	Fill Time (s)	Linear Solution Time (s)	Condition Number	Error
2×2	1	1	1	1	1	1	100	100	0.0100	$< 10^{-3}$	6.4572	-15.3525
8×8	2	2	2	2	2	2	200	200	0.0100	$< 10^{-3}$	580.1612	-15.6536
18×18	3	3	3	3	3	3	300	300	0.0200	$< 10^{-3}$	1.6554e+09	-1.4002

Table 48: Parameters and computational results for Example 3, Case B of the transmission problem. Spectral modes in both x and y and both above and below the surface are present. The coordinate sampling is the product of the numbers in the columns "x" and "y" then doubled to cover both reflection and transmission regions. Only square systems were treated and the wavelength was 100 larger than the two equal surface periods. This is a case of near-grazing incidence.

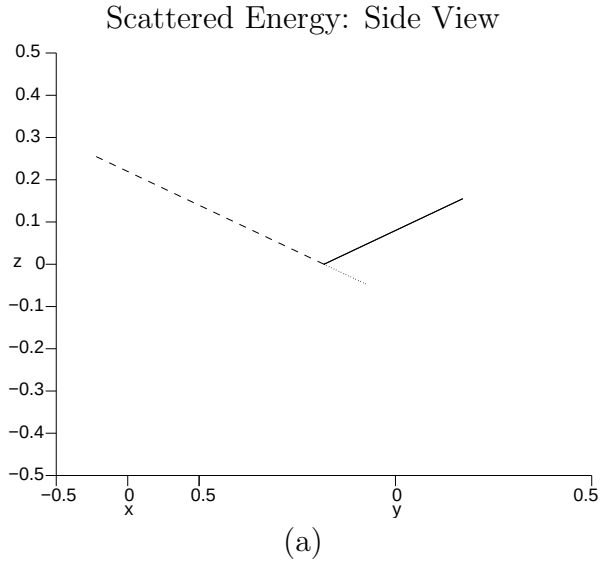

(a)

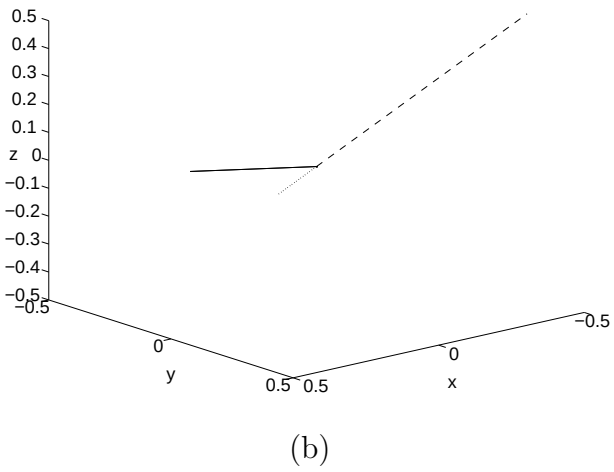

(b)

Figure 82: Example 3, Case B for the transmission problem with a square system of size 8×8 and $\kappa = 1$. Scattered energy distribution viewed from (a) $\theta = 90°$ and $\phi = -75°$ and (b) $\theta = 40°$ and $\phi = -5°$. Incident field is dashed, reflected field is solid and transmitted field is dotted.

19.7 Suite of ϕ^i Values, Azimuthal Angle of Incidence

$S(x,y)$	$-(d/2)\cos(2\pi x/L_1)\cos(2\pi y/L_2)$
(L_1, L_2)	(1,1)
$(d/L_1, d/L_2)$	(.075,.075)
$(\lambda/L_1, \lambda/L_2)$	(.25,.25)
ρ	2
κ	1.5
θ^i	20°

System Size	ϕ^i	Number of Samples: Coord. x	Coord. y	Spectral: Above j	Above j'	Below j	Below j'	Radiating Orders Above	Radiating Orders Below	Fill Time (s)	Linear Solution Time (s)	Condition Number	Error
188 × 264	0	12	11	8	7	12	11	50	110	2.4900	22.8200	8.3152	-6.3184
208 × 288	5	12	12	8	8	12	12	51	111	2.7400	37.5800	10.3545	-6.2158
208 × 288	10	12	12	8	8	12	12	51	114	2.6500	38.2400	10.4438	-6.2521
208 × 288	15	12	12	8	8	12	12	50	116	2.8100	37.3700	10.4720	-6.4737
208 × 288	20	12	12	8	8	12	12	51	116	2.7300	38.0900	10.4174	-7.6779
208 × 288	25	12	12	8	8	12	12	50	115	2.6200	39.9500	10.4660	-5.8449
208 × 288	30	12	12	8	8	12	12	51	112	2.6500	37.9700	10.4311	-7.6051
208 × 288	35	12	12	8	8	12	12	50	112	2.8100	37.0300	11.3118	-7.0022
208 × 288	40	12	12	8	8	12	12	48	113	2.6700	38.7700	11.0444	-6.7487
208 × 288	45	12	12	8	8	12	12	47	111	2.6400	38.5300	10.8652	-6.5637
208 × 288	50	12	12	8	8	12	12	48	113	2.8500	36.5900	11.0444	-6.7487
208 × 288	55	12	12	8	8	12	12	50	112	2.6300	38.5300	11.3118	-7.0022
208 × 288	60	12	12	8	8	12	12	51	112	2.6400	39.2000	10.4311	-7.6051
208 × 288	65	12	12	8	8	12	12	50	115	2.8200	37.6300	10.4660	-5.8449
208 × 288	70	12	12	8	8	12	12	51	116	2.7000	37.3900	10.4174	-7.6779
208 × 288	75	12	12	8	8	12	12	50	116	2.6300	39.5700	10.4720	-6.4737
208 × 288	80	12	12	8	8	12	12	51	114	2.6400	38.4500	10.4438	-6.2521
208 × 288	85	12	12	8	8	12	12	51	111	2.7900	37.3400	10.3545	-6.2158
188 × 264	90	11	12	7	8	11	12	50	110	2.3200	20.5900	8.3152	-6.3184
272 × 364	0	14	13	10	9	14	13	50	110	4.0500	76.4100	15.9388	-6.8955
296 × 292	5	14	14	10	10	14	14	51	111	4.3900	105.8800	19.3607	-7.8628
296 × 292	10	14	14	10	10	14	14	51	114	4.5300	104.5200	19.1891	-7.6142
296 × 292	15	14	14	10	10	14	14	50	116	4.3700	103.1300	19.3543	-8.8283
296 × 292	20	14	14	10	10	14	14	51	116	4.5900	103.0700	19.1041	-7.3425
296 × 292	25	14	14	10	10	14	14	50	115	4.3300	103.1300	19.4425	-6.8943
296 × 292	30	14	14	10	10	14	14	51	112	4.3000	103.0300	19.1593	-6.8839
296 × 292	35	14	14	10	10	14	14	50	112	4.3600	102.4400	20.2358	-6.5479
296 × 292	40	14	14	10	10	14	14	48	113	4.6000	103.7500	20.0768	-6.7477
296 × 292	45	14	14	10	10	14	14	47	111	4.3400	104.7000	19.9000	-6.9865
296 × 292	50	14	14	10	10	14	14	48	113	4.4400	103.6500	20.0768	-6.7477
296 × 292	55	14	14	10	10	14	14	50	112	4.3800	101.6900	20.2358	-6.5479
296 × 292	60	14	14	10	10	14	14	51	112	4.5800	103.1800	19.1593	-6.8839
296 × 292	65	14	14	10	10	14	14	50	115	4.3200	104.0700	19.4425	-6.8943
296 × 292	70	14	14	10	10	14	14	51	116	4.2900	104.5800	19.1041	-7.3425
296 × 292	75	14	14	10	10	14	14	50	116	4.4900	98.1500	19.3543	-8.8283
296 × 292	80	14	14	10	10	14	14	51	114	4.5200	102.1400	19.1891	-7.6142
296 × 292	85	14	14	10	10	14	14	51	111	4.2200	99.0300	19.3607	-7.8628
272 × 364	90	13	14	9	10	13	14	50	110	3.8800	75.2700	15.9388	-6.8955

Table 49: Parameters and computational results for parameters mostly similar to those of Example 1 of the transmission problem for different values of the azimuthal angle of incidence ϕ^i, in 5° increments, and using different spectral and coordinate sampling schemes. The error numbers were roughly uniform over the full azimuthal range and for all the different sampling schemes.

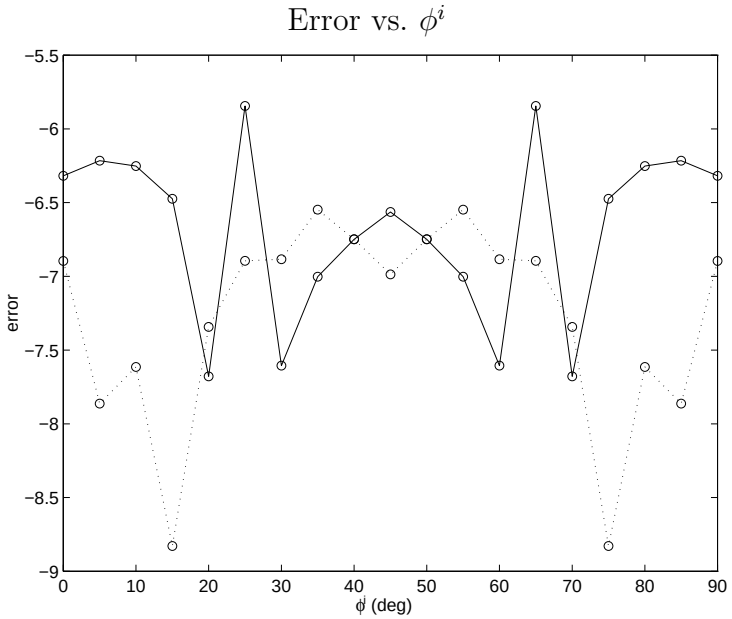

(a)

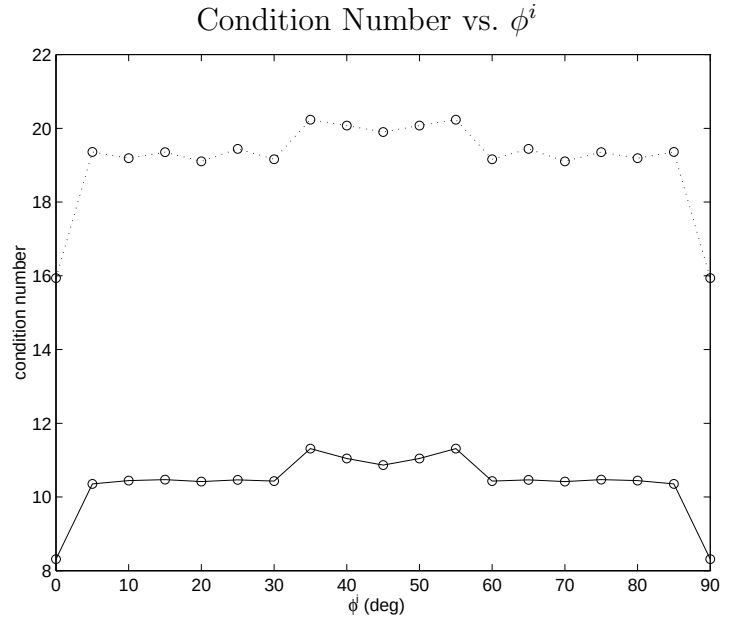

(b)

Figure 83: (a) Error and (b) condition number vs. ϕ^i, the azimuthal angle of incidence for Example 1 of the transmission problem. Solid lines mean no added non-radiating rows or columns, and dotted lines mean one added non-radiating row and column on all sides above the surface and below the surface. Error is down by approximately six orders of magnitude over the entire azimuthal angular variability.

19.8 Suite of κ Values

$S(x,y)$	$-(d/2)\cos(2\pi x/L_1)\cos(2\pi y/L_2)$
(L_1, L_2)	(1,1)
$(d/L_1, d/L_2)$	(.02,.02)
$(\lambda/L_1, \lambda/L_2)$	(.7,.7)
ρ	2
θ^i	20°
ϕ^i	15°
Radiating Orders Above	6

System Size	κ	Number of Samples: Coord. x	Coord. y	Spectral: Above j	Above j'	Below j	Below j'	Fraction of Energy Reflected	Radiating Orders Below	Fill Time (s)	Linear Solution Time (s)	Condition Number	Error
7×12	0.1000	2	3	2	3	1	1	1.0000	0	0.0700	0.0200	2.7807	-2.3049
7×12	0.1259	2	3	2	3	1	1	1.0000	0	0.0700	0.0100	2.7801	-2.2798
7×12	0.1585	2	3	2	3	1	1	1.0000	0	0.0700	0.0200	2.7791	-2.2369
7×12	0.1995	2	3	2	3	1	1	1.0000	0	0.0700	0.0100	2.7776	-2.1594
7×12	0.2512	2	3	2	3	1	1	1.0000	0	0.0600	0.0100	2.7751	-2.0006
7×12	0.3162	2	3	2	3	1	1	1.0000	0	0.0700	0.0200	2.7713	-1.4946
8×12	0.3981	2	3	2	3	2	1	0.6511	2	0.0700	0.0100	2.5972	-1.9012
8×12	0.5012	2	3	2	3	2	1	0.4557	2	0.0800	0.0200	2.3059	-2.4285
8×12	0.6310	2	3	2	3	2	1	0.3144	2	0.0800	0.0200	2.1262	-2.7674
10×12	0.7943	2	3	2	3	2	2	0.2007	4	0.1000	0.0200	2.8825	-3.3906
12×12	1.0000	2	3	2	3	2	3	0.1112	6	0.1200	$< 10^{-3}$	3.4941	-4.8057
18×24	1.2589	4	3	2	3	4	3	0.0502	10	0.1800	0.0400	2.9246	-2.7676
26×40	1.5849	4	5	2	3	4	5	0.0095	16	0.2700	0.1000	2.7249	-4.1560
36×60	1.9953	6	5	2	3	6	5	0.0005	26	0.3900	0.2200	2.7497	-3.9722
62×112	2.5119	8	7	2	3	8	7	0.0194	41	0.7000	1.2000	2.9692	-3.6141
87×162	3.1623	9	9	2	3	9	9	0.0632	62	1.0600	3.2600	3.3818	-3.3691
138×264	3.9811	12	11	2	3	12	11	0.1272	102	1.7800	15.1900	4.0906	-3.1805
216×420	5.0119	14	15	2	3	14	15	0.2054	162	3.7400	85.6100	5.4669	-3.0325
29×40	0.1000	4	5	4	5	3	3	1.0000	0	0.2700	0.1300	4.4465	-5.3817
29×40	0.1259	4	5	4	5	3	3	1.0000	0	0.2800	0.1300	4.4499	-5.3510
29×40	0.1585	4	5	4	5	3	3	1.0000	0	0.2600	0.1300	4.4553	-5.3013
29×40	0.1995	4	5	4	5	3	3	1.0000	0	0.2900	0.1400	4.4640	-5.2183
29×40	0.2512	4	5	4	5	3	3	1.0000	0	0.2800	0.1300	4.4780	-5.0681
29×40	0.3162	4	5	4	5	3	3	1.0000	0	0.2800	0.1300	4.5008	-4.6845
32×40	0.3981	4	5	4	5	4	3	0.6470	2	0.3000	0.1400	4.6656	-5.2144
32×40	0.5012	4	5	4	5	4	3	0.4540	2	0.3000	0.1400	4.7354	-5.3304
32×40	0.6310	4	5	4	5	4	3	0.3137	2	0.3000	0.1400	4.8686	-5.3351
36×40	0.7943	4	5	4	5	4	4	0.2006	4	0.3300	0.1600	5.5010	-5.5439
40×40	1.0000	4	5	4	5	4	5	0.1109	6	0.4300	0.0500	7.4499	-6.3845
50×60	1.2589	6	5	4	5	6	5	0.0465	10	0.5500	0.3700	7.7222	-5.9901
62×84	1.5849	6	7	4	5	6	7	0.0093	16	0.7000	0.7600	6.2782	-7.2055
76×112	1.9953	8	7	4	5	8	7	0.0005	26	0.8800	1.4900	5.5584	-6.0970
110×180	2.5119	10	9	4	5	10	9	0.0194	41	1.4200	4.8200	6.1465	-7.2767
141×242	3.1623	11	11	4	5	11	11	0.0633	62	1.7400	12.4800	6.4060	-6.4826
202×364	3.9811	14	13	4	5	14	13	0.1274	102	3.3600	55.9600	7.4543	-6.2676
292×544	5.0119	16	17	4	5	16	17	0.2056	162	5.5500	267.6600	9.2238	-6.1307

Table 50: Parameters and computational results for the transmission problem for a suite of values of $\kappa = k_2/k_1$, the ratio of wavenumbers. Different coordinate and spectral sampling schemes are presented, nearly all for non-square systems. The upper part of the table is plotted as the solid line in Fig. 84(a) and includes no added non-radiating rows and columns. The lower part of the table (dotted line in Fig. 84(a) consists of one added non-radiating row and column on all sides of the matrix both above and below the surface which improved the error numbers.

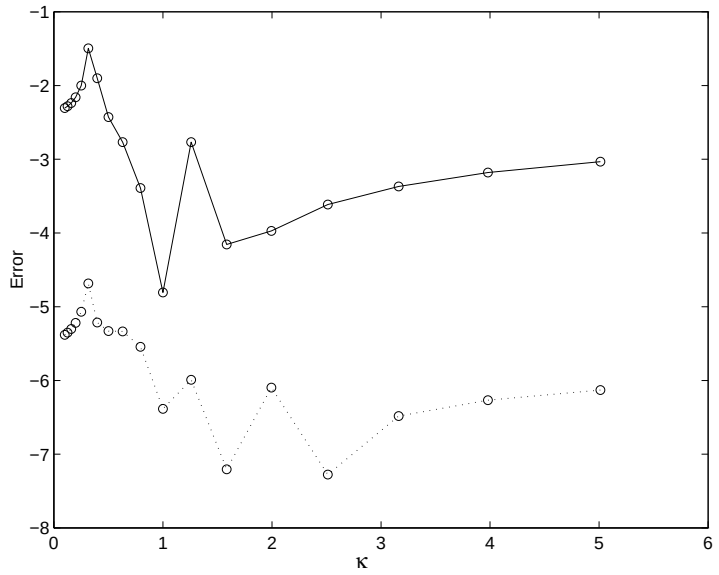

(a)

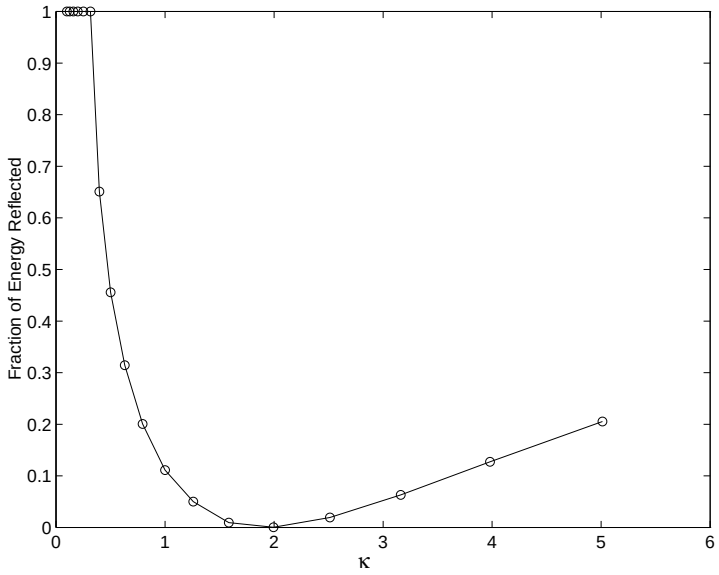

(b)

Figure 84: (a) Error vs. κ for the transmission problem. The surface parameters are listed in Table 50. Solid line refers to no added non-radiating rows or columns. The dotted line corresponds to one added non-radiating row and column on all sides above the surface and below the surface. (b) Shows the fraction of reflected energy vs. κ, with no added non-radiating rows or columns. The minimum of the curve illustrates an example of perfect transmission.

19.9 Suite of ρ Values

$S(x, y)$	$-(d/2)\cos(2\pi x/L_1)\cos(2\pi y/L_2)$
(L_1, L_2)	(1,1)
$(d/L_1, d/L_2)$	(.075,.075)
$(\lambda/L_1, \lambda/L_2)$	(.25,.25)
κ	1.5
θ^i	20°
ϕ^i	15°
Radiating Orders Above	50
Radiating Orders Below	116

System Size	ρ	Number of Samples						Fraction of Energy Reflected	Fill Time (s)	Linear Solution Time (s)	Condition Number	Error
		Coord.		Spectral								
				Above		Below						
		x	y	j	j'	j	j'					
208 × 288	0.1000	12	12	8	8	12	12	0.7742	2.9800	36.2500	16.9260	-4.9444
208 × 288	0.1259	12	12	8	8	12	12	0.7244	2.8700	37.6600	15.2338	-4.9919
208 × 288	0.1585	12	12	8	8	12	12	0.6661	2.6100	37.4000	13.3747	-5.0543
208 × 288	0.1995	12	12	8	8	12	12	0.5989	2.7000	38.7600	11.4855	-5.1375
208 × 288	0.2512	12	12	8	8	12	12	0.5234	2.6700	39.2400	9.6972	-5.2511
208 × 288	0.3162	12	12	8	8	12	12	0.4408	2.6000	39.6700	8.1086	-5.4128
208 × 288	0.3981	12	12	8	8	12	12	0.3535	2.6000	36.2500	6.9839	-5.6627
208 × 288	0.5012	12	12	8	8	12	12	0.2653	2.6300	35.8800	6.3893	-6.1587
208 × 288	0.6310	12	12	8	8	12	12	0.1812	2.6400	37.7000	5.9837	-6.3934
208 × 288	0.7943	12	12	8	8	12	12	0.1070	2.6400	38.6400	5.6171	-5.9992
208 × 288	1.0000	12	12	8	8	12	12	0.0488	2.6000	38.0600	5.3084	-5.9485
208 × 288	1.2589	12	12	8	8	12	12	0.0120	2.6400	40.2300	6.2400	-6.0001
208 × 288	1.5849	12	12	8	8	12	12	0.0002	2.6100	37.3900	7.8840	-6.0610
208 × 288	1.9953	12	12	8	8	12	12	0.0146	2.6500	39.1700	10.4389	-6.4576
208 × 288	2.5119	12	12	8	8	12	12	0.0538	2.6300	42.0300	14.4321	-5.5776
208 × 288	3.1623	12	12	8	8	12	12	0.1137	2.6300	39.1600	20.5077	-4.9103
208 × 288	3.9811	12	12	8	8	12	12	0.1890	2.6300	37.7000	29.6333	-4.4868
208 × 288	5.0119	12	12	8	8	12	12	0.2735	2.8800	37.3500	43.0853	-4.2055
208 × 288	6.3096	12	12	8	8	12	12	0.3615	2.8200	36.6500	62.4316	-4.0380
208 × 288	7.9433	12	12	8	8	12	12	0.4483	2.6300	40.9900	89.4511	-3.9742
208 × 288	10.0000	12	12	8	8	12	12	0.5301	2.7000	38.7200	126.0280	-4.0219
296 × 392	0.1000	14	14	10	10	14	14	0.7742	4.3700	106.7200	38.2908	-5.7059
296 × 392	0.1259	14	14	10	10	14	14	0.7244	4.3800	106.8200	34.2838	-5.7338
296 × 392	0.1585	14	14	10	10	14	14	0.6660	4.6800	103.5800	29.9761	-5.7703
296 × 392	0.1995	14	14	10	10	14	14	0.5989	4.8000	104.7600	26.7792	-5.8174
296 × 392	0.2512	14	14	10	10	14	14	0.5234	4.6800	106.9500	23.9234	-5.8772
296 × 392	0.3162	14	14	10	10	14	14	0.4408	4.3800	103.8200	20.8751	-5.9496
296 × 392	0.3981	14	14	10	10	14	14	0.3535	4.6300	105.0700	17.9190	-6.0297
296 × 392	0.5012	14	14	10	10	14	14	0.2653	4.3100	108.5700	15.2993	-6.1039
296 × 392	0.6310	14	14	10	10	14	14	0.1811	4.5000	105.2700	13.6450	-6.1529
296 × 392	0.7943	14	14	10	10	14	14	0.1070	4.3400	106.6100	12.9722	-6.1726
296 × 392	1.0000	14	14	10	10	14	14	0.0488	4.8200	103.8400	12.3741	-6.1912
296 × 392	1.2589	14	14	10	10	14	14	0.0120	4.3800	106.3500	12.8357	-6.2625
296 × 392	1.5849	14	14	10	10	14	14	0.0002	4.3900	106.1300	15.2528	-6.4863
296 × 392	1.9953	14	14	10	10	14	14	0.0146	4.5200	104.7200	19.3033	-8.3088
296 × 392	2.5119	14	14	10	10	14	14	0.0537	4.3800	104.3800	25.7208	-6.6114
296 × 392	3.1623	14	14	10	10	14	14	0.1136	4.4100	105.8700	35.9192	-7.4531
296 × 392	3.9811	14	14	10	10	14	14	0.1888	4.3700	104.3100	51.5533	-5.7810
296 × 392	5.0119	14	14	10	10	14	14	0.2733	4.3700	106.2200	75.2297	-5.2654
296 × 392	6.3096	14	14	10	10	14	14	0.3612	4.5400	101.2500	110.4746	-4.9484
296 × 392	7.9433	14	14	10	10	14	14	0.4478	4.9800	106.2900	161.7675	-4.7560
296 × 392	10.0000	14	14	10	10	14	14	0.5296	4.3400	106.1900	234.3887	-4.6631

Table 51: Parameters and computational results for parameters mostly similar to Example 1 of the transmission problem for different values of ρ ranging from 0.1 to 10. Different spectral and coordinate sampling schemes are included. Slightly higher condition numbers occur (compare Tables 49 and 50) than for angle and wavenumber suites.

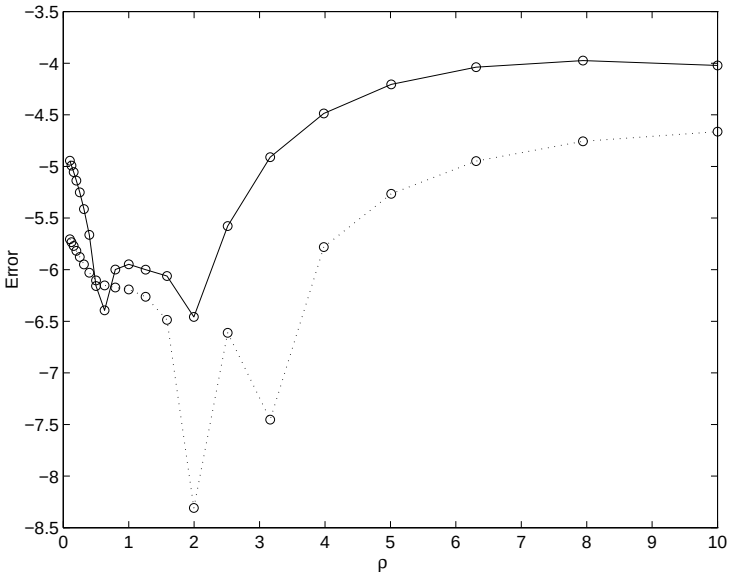

(a)

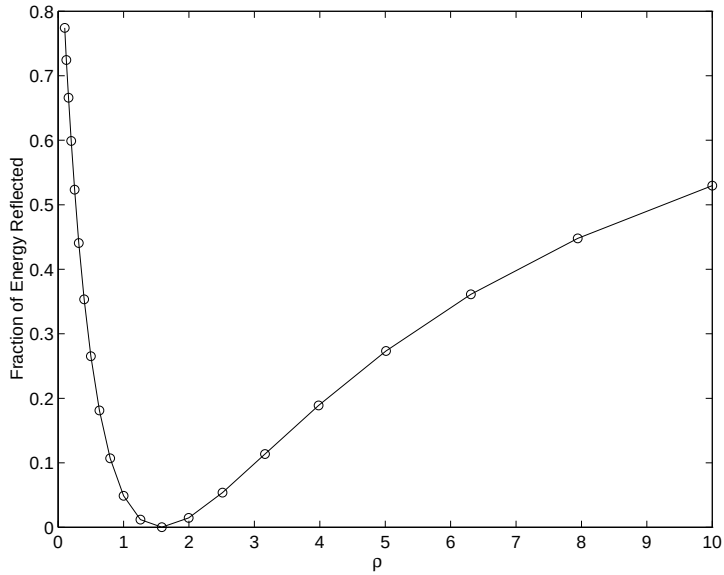

(b)

Figure 85: (a) Error vs. ρ for the transmission problem. The surface parameters are listed in Table 51. Solid line refers to no added non-radiating rows or columns. The dotted line corresponds to one added non-radiating row and column on all sides above the surface and below the surface. (b) Shows the fraction of reflected energy vs. ρ, with one added non-radiating row and column on all sides above the surface and below the surface. The minimum of the curve is an example of perfect transmission.

19.10 Maximum Roughness with Respect to Incident Polar Angle θ^i

$S(x,y)$	$-(d/2)\cos(2\pi x/L_1)\cos(2\pi y/L_2)$
(L_1, L_2)	(1,1)
$(\lambda/L_1, \lambda/L_2)$	(.25,.25)
ϕ^i	50°
ρ	1.5
κ	1.5

	Added Spectral Orders							
	Above Surface				Below Surface			
Line	L	R	T	B	L	R	T	B
Dash Dot	0	0	0	0	0	0	0	0
Solid	0	1	0	1	0	1	0	1
Dashed	1	1	1	1	1	1	1	1

Table 52: Parameters for Fig. 86, the maximum roughness (d/L) with respect to polar incident angle θ^i for the transmission problem and a fixed error less than -2. The box of added spectral orders refers to added columns (L = left, R = right) and added rows (T = top, B = bottom).

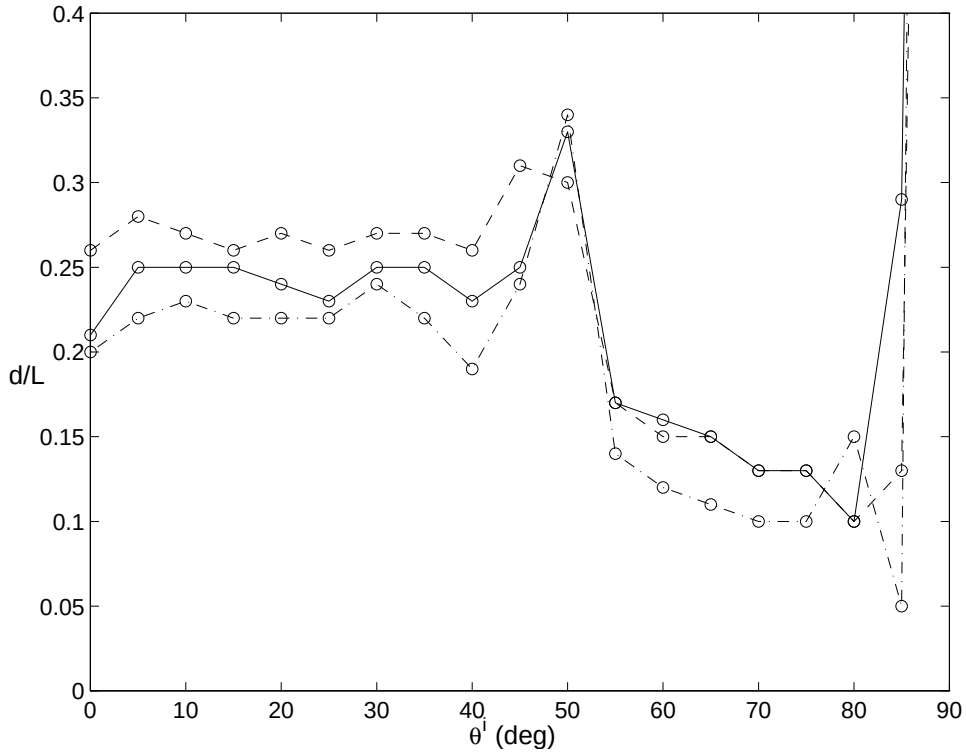

Figure 86: Maximum roughness (d/L) with respect to polar incident angle θ^i for the transmission problem and a fixed error less than -2. The curves are explained in Table 52.

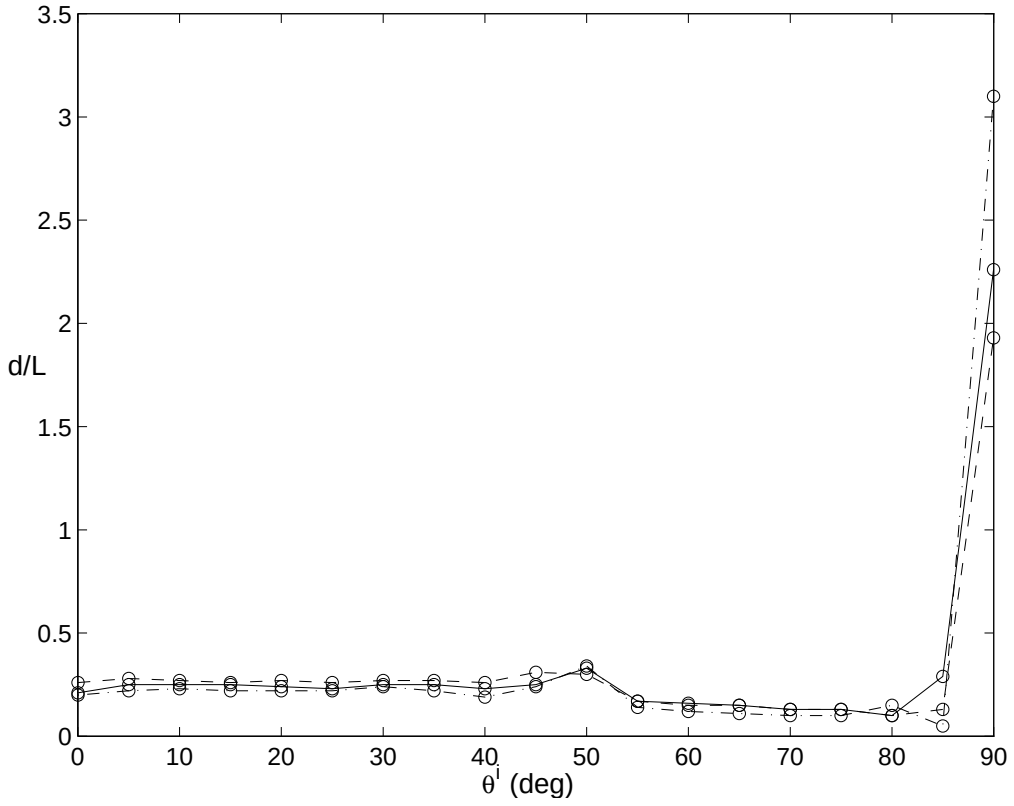

Figure 87: Unzoomed view of Fig. 86, maximum roughness (d/L) with respect to polar incident angle θ^i for the transmission problem and a fixed error less than -2. The curves are explained in Table 52.

19.11 Maximum Roughness with Respect to ρ

$S(x,y)$	$-(d/2)\cos(2\pi x/L_1)\cos(2\pi y/L_2)$
(L_1, L_2)	(1,1)
$(\lambda/L_1, \lambda/L_2)$	(.7,.7)
ϕ^i	15°
κ	2

Line	θ^i
Dash Dot	.01°
Solid	20°
Dashed	50°
Dotted	75°

Table 53: Parameters for Fig. 88, to compute the maximum roughness d/L ($L = L_1 = L_2$) with respect to the ratio of densities (or electromagnetic constants depending on the polarization) ρ for four different polar angles θ^i of incidence. One added row and column of non-radiating orders on all sides, above and below the surface. The fixed error is less than -2.

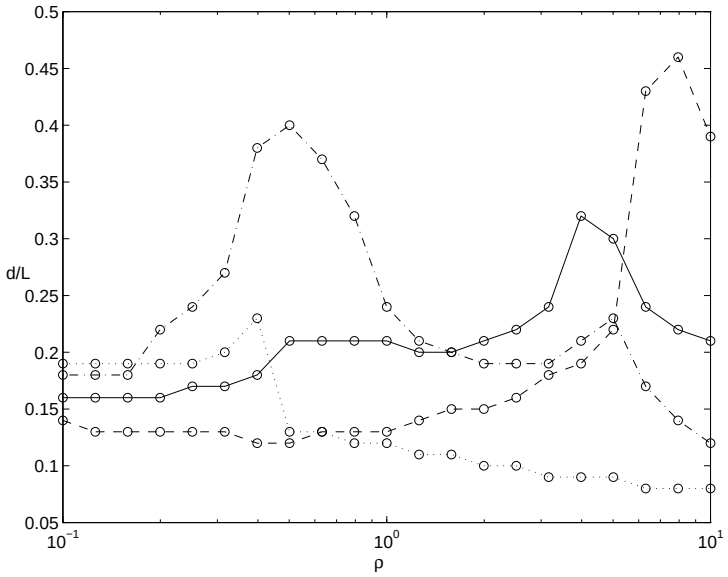

Figure 88: Maximum roughness for error less than -2 with respect to ρ at different values of incident polar angle θ^i for the transmission problem. The curves are defined in Table 53.

19.12 Maximum Roughness with Respect to ρ at Near-Grazing Incidence

$S(x,y)$	$-(d/2)\cos(2\pi x/L_1)\cos(2\pi y/L_2)$
(L_1, L_2)	(1,1)
$(\lambda/L_1, \lambda/L_2)$	(.7,.7)
ϕ^i	15°
θ^i	89.99°
κ	2
Radiating Orders Above	6
Radiating Orders Below	26

Line	System Size	Added Spectral Orders							
		Above Surface				Below Surface			
		L	R	T	B	L	R	T	B
Dash Dot	45×72	0	0	0	0	0	0	0	0
Solid	65×98	0	1	0	1	0	1	0	1
Dashed	89×128	1	1	1	1	1	1	1	1
Dotted	117×162	1	2	1	2	1	2	1	2

Table 54: Parameters for Fig. 89, to compute the maximum roughness d/L ($L = L_1 = L_2$) with respect ρ for fixed error less than -2 and for near grazing incidence ($\theta^i = 89.99^\circ$). The table for the four curves plotted in Fig. 89 indicates the system size with added spectral orders above the surface (added columns: L = left, R = right, and added rows: T = top and B = bottom) with an analogous interpretation for added spectral orders below the surface.

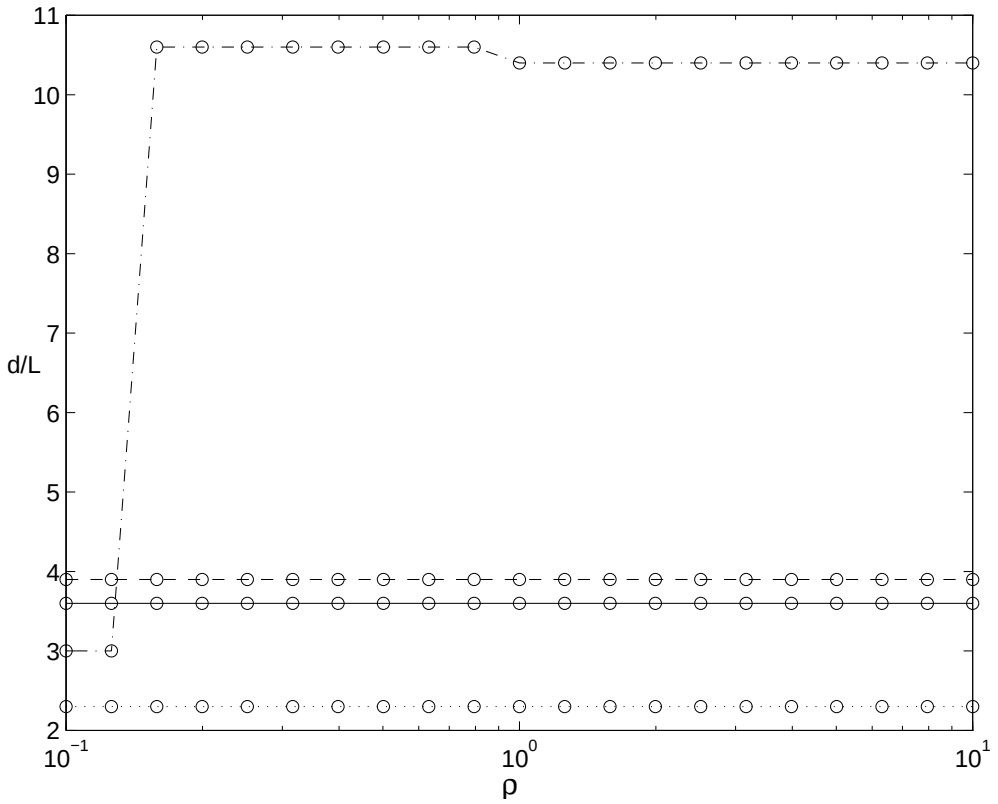

Figure 89: Maximum roughness for error less than -2 with respect to ρ at $\theta^i = 89.99°$ for the transmission problem. The curves are explained in Table 54. Very large values of roughness can be routinely computed as the polar angle of incidence approaches grazing.

19.13 Maximum Roughness with Respect to κ

$S(x,y)$	$-(d/2)\cos(2\pi x/L_1)\cos(2\pi y/L_2)$
(L_1, L_2)	(1,1)
$(\lambda/L_1, \lambda/L_2)$	(.7,.7)
ϕ^i	15°
ρ	2

Line	θ^i
Dash Dot (overlaps Solid)	.01°
Solid	20°
Dashed	50°
Dotted	75°

Table 55: Parameters for the maximum roughness d/L ($L = L_1 = L_2$) for the transmission problem with respect to κ at four different angles of incidence for error less than -2. One added row and column of non-radiating orders was included on all sides, both above and below the surface. The results are plotted in Fig. 90.

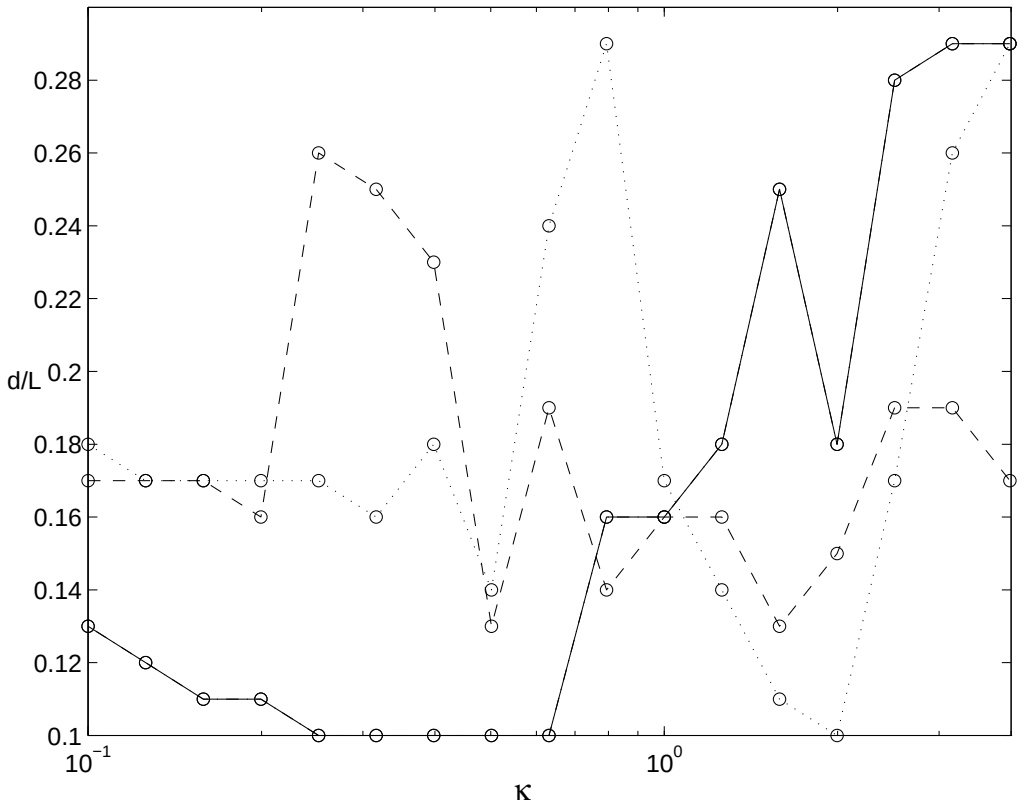

Figure 90: Maximum roughness d/L ($L = L_1 = L_2$) for the transmission problem as a function of κ for fixed error less than -2 at four different values of the polar incident angle θ^i. See Table 55 for the explanation of the curves.

19.14 Maximum Roughness with Respect to κ at Near-Grazing Incidence

$S(x,y)$	$-(d/2)\cos(2\pi x/L_1)\cos(2\pi y/L_2)$
(L_1, L_2)	(1,1)
$(\lambda/L_1, \lambda/L_2)$	(.7,.7)
ϕ^i	15°
θ^i	89.99°
ρ	2
Radiating Orders Above	6

	Added Spectral Orders							
	Above Surface				Below Surface			
Line	L	R	T	B	L	R	T	B
Dash Dot	0	0	0	0	0	0	0	0
Solid	0	1	0	1	0	1	0	1
Dashed	1	1	1	1	1	1	1	1
Dotted	1	2	1	2	1	2	1	2

Table 56: Parameters for the maximum roughness d/L ($L = L_1 = L_2$) for the transmission problem with respect to κ for four different sampling schemes and for fixed error is less than -2 at near-grazing incidence ($\theta^i = 89.99°$). The added spectral orders refer to added columns (L = left, R = right) and added rows (T = top, B = bottom) both above and below the surface.

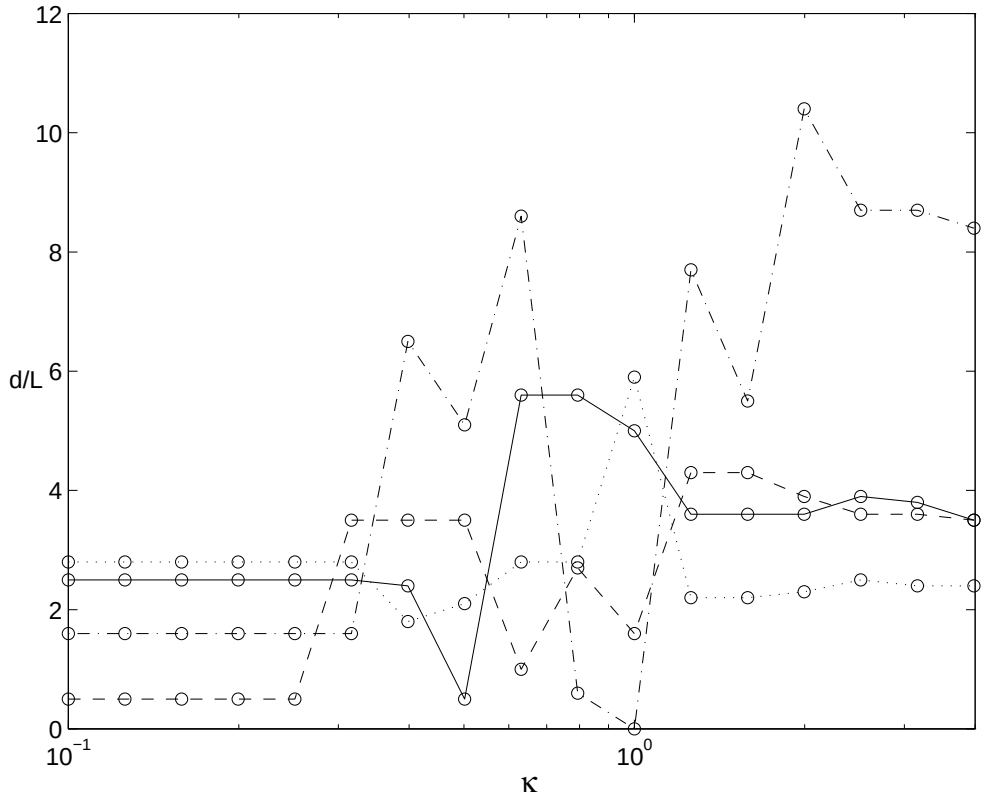

Figure 91: Maximum roughness for error less than -2 with respect to κ at $\theta^i = 89.99°$ for the transmission problem. Added columns (L = left, R = right) and added rows (T = top, B = bottom). Note the vertical scale. Very large values of roughness could be obtained at near-grazing incidence. The curves are defined in Table 56.

19.15 Complexity Analysis: Square Systems using Gaussian Elimination

$S(x,y)$	$-(d/2)\cos(2\pi x/L_1)\cos(2\pi y/L_2)$
(L_1, L_2)	(1,1)
$(d/L_1, d/L_2)$	(.05,.05)
$(\lambda/L_1, \lambda/L_2)$	(.7,.7)
Radiating Orders Above	6
Radiating Orders Below	6
θ^i	15°
ϕ^i	50°
κ	1
ρ	2

n	Matrix Size	Fill Time (s)	Linear Solution Time (s)	Total Time (s)	Linear Solution Flops	Total Flops	Condition Number	Error
18	18 × 18	0.1700	$< 10^{-3}$	0.9700	27355	45473	38.2400	-3.9057
32	32 × 32	0.2900	0.0200	1.1400	122779	177376	52.0596	-3.8400
50	50 × 50	0.4700	0.0500	1.6400	415859	545577	52.8477	-5.3779
72	72 × 72	0.7000	0.1400	2.3600	1164371	1429020	78.3249	-6.5385
98	98 × 98	1.0000	0.3100	3.2900	2816623	3301885	83.2941	-6.9563
128	128 × 128	1.3600	0.6100	4.6600	6111803	6933936	114.9821	-8.4267
162	162 × 162	1.8900	1.2300	6.5900	12164335	13474877	124.6712	-8.2562
200	200 × 200	2.5100	2.2500	9.4500	22581419	24571892	165.1655	-8.9655
242	242 × 242	3.2900	3.8000	13.0200	39609943	42516557	181.8529	-9.7378
288	288 × 288	4.3400	6.2500	18.0600	66280683	70389040	234.7397	-10.4554
338	338 × 338	5.0900	9.1600	23.2200	106516375	112166173	260.4395	-11.4624
392	392 × 392	6.2400	14.0600	31.4000	165396803	172986540	330.0770	-11.0926
450	450 × 450	7.8300	23.9100	45.8100	249260143	259251821	367.2704	-11.2560
512	512 × 512	9.6800	31.2200	58.9400	366078123	379001952	459.1127	-11.2866
578	578 × 578	12.1900	48.5800	84.2600	525261099	541720201	511.1221	-11.2795
648	648 × 648	14.4800	69.4000	114.7700	738607859	759282972	632.0961	-11.2784
722	722 × 722	17.5900	103.4200	158.9900	$1.0197{\cdot}10^9$	$1.0454{\cdot}10^9$	703.3761	-11.2788
800	800 × 800	22.2100	139.9100	212.7800	$1.3851{\cdot}10^9$	$1.4165{\cdot}10^9$	862.3475	-11.2790
882	882 × 882	26.2100	198.1300	289.8300	$1.8536{\cdot}10^9$	$1.8918{\cdot}10^9$	958.8002	-11.2784
968	968 × 968	29.9900	529.4500	642.3600	$2.4476{\cdot}10^9$	$2.4936{\cdot}10^9$	$1.1672{\cdot}10^3$	-11.2785
1058	1058 × 1058	35.7300	$1.0725{\cdot}10^3$	$1.2108{\cdot}10^3$	$3.1925{\cdot}10^9$	$3.2475{\cdot}10^9$	$1.2965{\cdot}10^3$	-11.2787

Table 57: Parameters and computational results for the complexity analysis of the transmission problem using square systems and Gaussian elimination. The results are presented graphically in Fig. 92. Total time and flops do not include condition number computation.

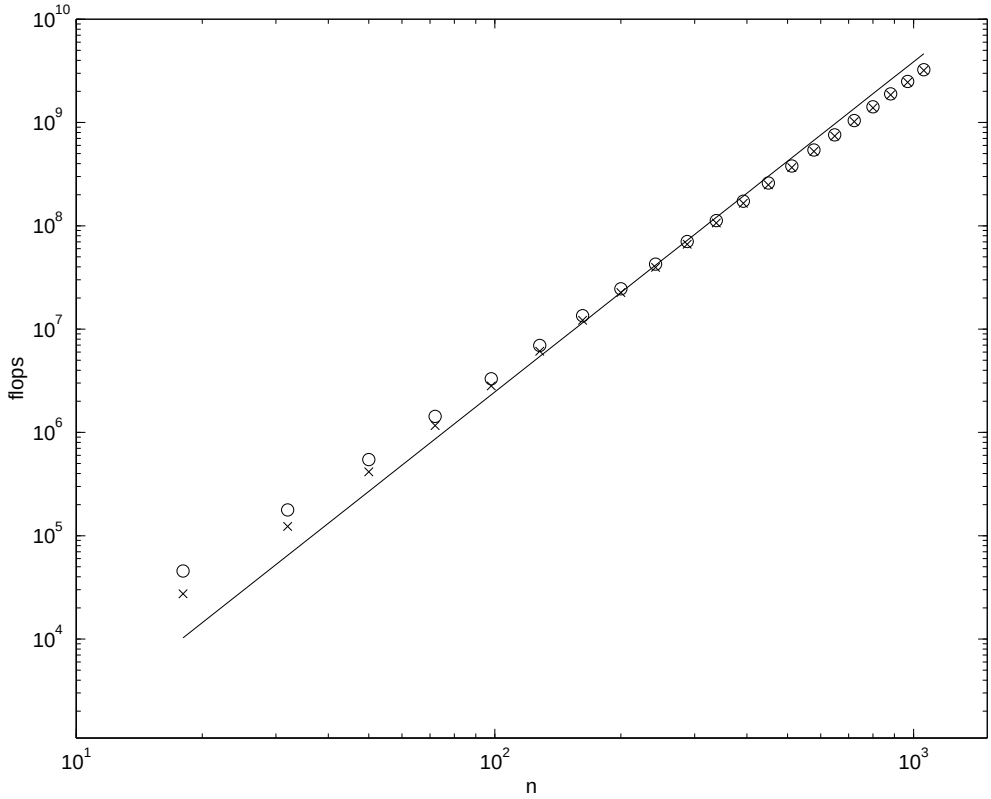

Figure 92: Complexity for the square system of the transmission example in Table 57. Flops vs. n is plotted for an $n \times n$ system using Gaussian elimination. Here o refers to total flops and $\times$ to linear flops. The solid line is a linear regression curve with respect to total flops with slope 3.1959

19.16 Complexity Analysis: Non-Square Systems using Pseudo-inverse

$S(x, y)$	$-(d/2)\cos(2\pi x/L_1)\cos(2\pi y/L_2)$
(L_1, L_2)	(1,1)
$(d/L_1, d/L_2)$	(.05,.05)
$(\lambda/L_1, \lambda/L_2)$	(.7,.7)
Radiating Orders Above	6
Radiating Orders Below	6
θ^i	15°
ϕ^i	50°
κ	1
ρ	2

n	Matrix Size	Fill Time (s)	Linear Solution Time (s)	Total Time (sec)	Linear Solution Flops	Total Flops	Condition Number	Error
32	18 × 32	0.0200	0.0100	0.0700	319958	505302	33.4515	-2.1438
50	18 × 50	0.0200	0.0100	0.1000	569101	871154	33.4541	-2.1693
72	18 × 72	0.0200	0.0100	0.0900	967683	1411978	33.4540	-2.1685
98	18 × 98	0.0200	0.0200	0.1000	1573507	2185904	33.4540	-2.1683
128	18 × 128	0.0200	0.0300	0.1100	2453935	3259915	33.4540	-2.1683
162	18 × 162	0.0300	0.0400	0.1400	3677232	4703034	33.4540	-2.1683
200	18 × 200	0.0200	0.0500	0.1500	5348016	6619500	33.4540	-2.1683
242	18 × 242	0.0300	0.0600	0.1700	7578200	9121226	33.4540	-2.1683
288	18 × 288	0.0200	0.1100	0.2300	10438940	12279368	33.4540	-2.1683
338	18 × 338	0.0200	0.1400	0.2400	14082123	16245761	33.4540	-2.1683
392	18 × 392	0.0300	0.2300	0.3500	18571731	21084491	33.4540	-2.1683
450	18 × 450	0.0300	0.2800	0.4100	24130335	27018077	33.4540	-2.1683
512	18 × 512	0.0300	0.4000	0.5400	30885429	34174013	33.4540	-2.1683
578	18 × 578	0.0300	0.4700	0.6100	38983137	42698423	33.4540	-2.1683
648	18 × 648	0.0400	0.5900	0.7600	48592495	52760343	33.4540	-2.1683
722	18 × 722	0.0300	0.7400	0.9000	59905615	64551885	33.4540	-2.1683
800	18 × 800	0.0400	0.9000	1.0800	73071216	78221768	33.4540	-2.1683
882	18 × 882	0.0400	1.0700	1.2800	88366512	94047206	33.4540	-2.1683
968	18 × 968	0.0400	1.2800	1.5000	105968304	112205000	33.4540	-2.1683
1058	18 × 1058	0.0400	1.5400	1.7700	126125447	132944005	33.4540	-2.1683

Table 58: Total time and flops for a complexity analysis of a transmission problem. The graphical presentation is in Fig. 93. Only non-square systems are included, and total time and flops do not include condition number computation. Convergence was excellent for all cases.

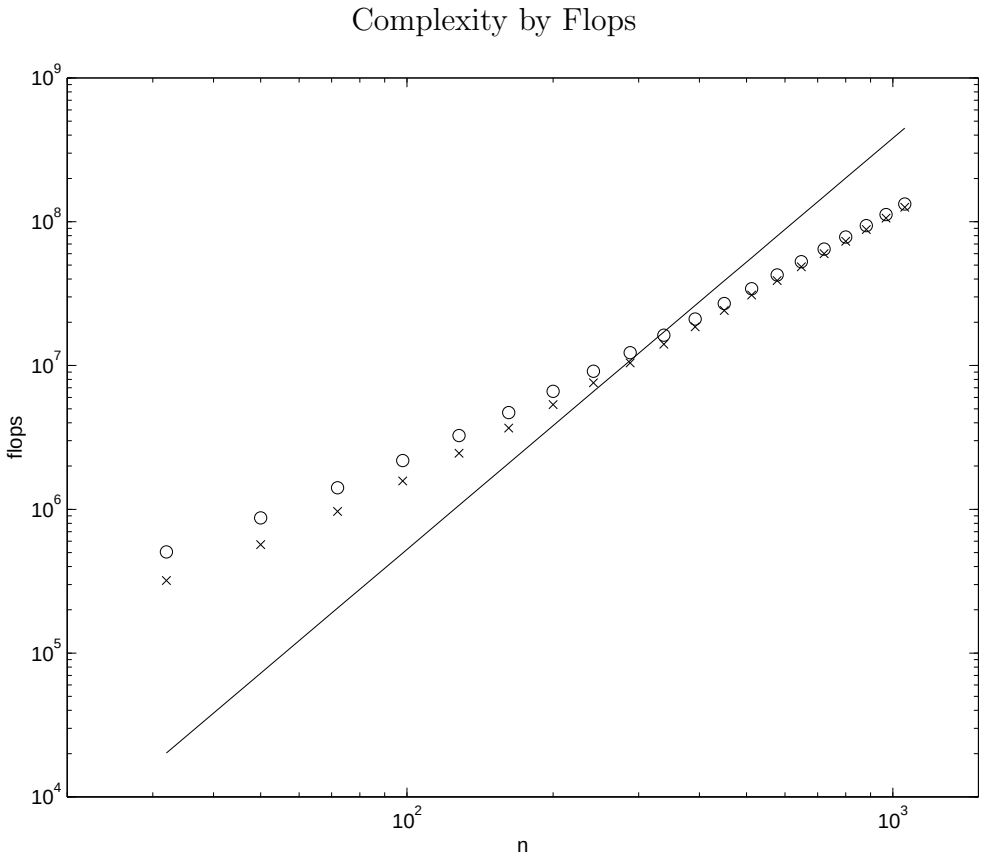

Figure 93: Complexity for the non-square system of the transmission example in Table 58. o refers to total flops and $\times$ to linear flops. The solid line is a linear regression curve with respect to total flops with slope 2.8605.

20 Summary and Conclusions

We presented theoretical and computational results to describe the scattering from and transmission through a two-dimensional periodic surface. The equations used to describe the scattering process were found using a reduction of the equations for an infinite surface. They were in a mixed spectral-coordinate (SC) representation.

Calculations were presented for both perfectly reflecting Dirichlet and Neumann examples as well as for the full transmission case where the rough interface separates two different homogeneous media. The computations were extensive, involving not only surfaces of different roughness under conditions of no grazing and near-grazing incidence and reflection, but also parameter studies over several orders of magnitude for density and wavenumber ratios as well as considerable variability in the incident angle.

The general conclusions are straightforward. The method is *very fast* as evidenced by the fill time of the matrix. Additional time savings can occur if different matrix solution methods are employed. We only used Gaussian (row reduction) or pseudo-inverse methods. The methods is *robust* as evidenced by the breath of parameter values we have computed. The include suites of values varying over two orders of magnitude in density ratio and wavenumber, and angular variation including near-grazing incidence and reflection. The method is highly *accurate* as evidenced by computation with energy checks. The only area where some poor performance was observed was in the Neumann results where we had a combination of *large* roughness, for both height and slope, grazing waves and the computations of the normal derivative of the periodic Green's function under these conditions and in Example 3 for the transmission case when we either added too many symmetric evanescant modes or did not add the evanescent modes symmetrically. Practically, most computations produced a lower error when the systems involved were square.

Acknowledgements

Effort sponsored by the Air Force Office of Scientific Research, Air Force Materials Command, USAF, under the Multi-University Research Initiative (MURI) program Grant # F49620-96-1-0039.

Erdmann's research was supported in part by an Undergraduate Research Grant from the Colorado Advanced Software Institute (CASI) and a Grant-in-Aid of Research from Sigma Xi, The Scientific Research Society.

We are grateful to Mr. Guy Somberg and Mr. Douglas Baldwin for technical assistance in the production of this report.

References

[1] Boag A., Leviatan Y., and Boag A., Analysis of electromagnetic scattering from doubly periodic nonplanar surfaces using a patch-current model. IEEE Trans. **AP-41**, 732–738 (1993).

[2] Bruce N.C., Calculations of the Mueller matrix for scattering of light from two-dimensional surfaces. Waves in Random Media **8**, 15–28 (1998).

[3] DeSanto J.A., Scattering from a perfectly reflecting arbitrary periodic surface: An exact theory, Radio Sci. **16**, 1315–1326 (1981).

[4] DeSanto J.A., Exact spectral formalism for rough-surface scattering, J. Opt. Soc. Am. A **2**, 2202–2207 (1985).

[5] DeSanto J.A., A new formulation of electromagnetic scattering from rough dielectric interfaces, J. Elect. Waves and Applications **1**, 1293–1306 (1993).

[6] DeSanto J.A., Erdmann G., Hereman W., and Misra M., Theoretical and Computational Aspects of Scattering from Rough Surfaces: One-dimensional Perfectly Reflecting Surfaces, Technical Report MCS-97-09, Report of Work in Progress, MURI Project, AFOSR Grant # F49620-96-1-0039, Department of Mathematical and Computer Sciences, Colorado School of Mines, Golden, Colorado (1997).

[7] DeSanto J.A., Erdmann G., Hereman W., and Misra M., Theoretical and Computational Aspects of Scattering from Rough Surfaces: One-dimensional Transmission Interface, Technical Report MCS-00-02, Report of Work in Progress, MURI Project, AFOSR Grant # F49620-96-1-0039, Department of Mathematical and Computer Sciences, Colorado School of Mines, Golden, Colorado (2000).

[8] DeSanto J.A., Erdmann G., Hereman W., and Misra M., Theoretical and computational aspects of scattering from rough surfaces: One-dimensional perfectly reflecting surfaces, Waves in Random Media **8**, 385–414 (1998).

[9] Kim M.-J., Berenyi H.M., and Burge R.E., Scattering of scalar waves by two-dimensional gratings of arbitrary shape: application to rough surfaces at near-grazing incidence. Proc. R. Soc. Lond. A **446**, 289–308 (1994).

[10] Kinsman B., Wind Waves, Their Generation and Propagation on the Ocean Surface. Dover, New York (1984).

[11] Tran P., and Maradudin A.A., The scattering of electromagnetic waves from a randomly rough 2D metallic surface. Opt. Comm. **110**, 269–273 (1994).

[12] Wagner R.L, Song J., and Chew W.C., Monte Carlo simulation of electromagnetic scattering from two-dimensional random rough surfaces, IEEE Trans. AP **45**, 235–245 (1997).